2015

Molecularly imprinted nanoparticles (MINPs) as antibody mimics

Joseph Khadori Awino
Iowa State University

Molecularly imprinted nanoparticles (MINPs) as antibody mimics

by

Joseph K. Awino

A dissertation submitted to the graduate faculty

in partial fulfillment of the requirements for the degree of

DOCTOR OF PHILOSOPHY

Major: Organic Chemistry

Program of Study Committee:

Yan Zhao, Major Professor
Aaron D. Sadow
Javier Vela
Arthur Winter
Keith Woo

Iowa State University

Ames, Iowa

2015

DEDICATION

To my late Dad Mariko Awino,

It seems like yesterday when you passed away,

Although my world changed so much when you left,

The burning desire to succeed and show gratitude to you has always lived.

TABLE OF CONTENTS

Page

DEDICATION ii

ACKNOWLEDGEMENTS v

CHAPTER 1. GENERAL INTRODUCTION

Literature Review 1

References 5

CHAPTER 2. PROTEIN MIMETIC, MOLECULARLY IMPRINTED NANOPARTICLES FOR SELECTIVE BINDING OF BILE SALT DERIVATIVES IN WATER

Abstract 7

Introduction 8

Results and Discussion 9

Conclusion 18

Acknowledgement 18

Experimental Section 18

Notes and References 34

CHAPTER 3. MOLECULARLY IMPRINTED NANOPARTICLES AS TAILOR-MADE SENSORS FOR SMALL FLUORESCENT MOLECULES

Abstract 37

Introduction 38

Results and Discussion 39

Conclusion 45

Acknowledgement 46

Experimental Section 46

Notes and References 69

CHAPTER 4. WATER-SOLUBLE MOLECULARLY IMPRINTED NANOPARTICLES (MINPs) WITH TAILORED, FUNCTIONALIZED, MODIFIABLE BINDING POCKETS

Abstract 72

Introduction 73

Results and Discussion 74

Conclusion 87

Acknowledgement 87
Experimental Section 88
Notes and References 113

CHAPTER 5. POLYMERIC NANOPARTICLE RECEPTORS AS SYNTHETIC ANTIBODIES FOR NONSTEROIDAL ANTI-INFLAMMATORY DRUGS (NSAIDs)
Abstract 117
Introduction 118
Results and Discussion 120
Conclusion 129
Acknowledgement 129
Experimental Section 130
Notes and References 135

CHAPTER 6. RIGIDITY VERSUS AMPHIPHILICITY IN TRANSMEMBRANE NANOPORE FORMATION BY CHOLATE-BASED MACROCYCLES
Abstract 140
Introduction 141
Results and Discussion 144
Conclusion 157
Acknowledgement 158
Experimental Section 158
Notes and References 167

CHAPTER 7. CONCLUSIONS 172

ACKNOWLEDGEMENTS

I would like to start by extending my sincere gratitude to Dr. Yan Zhao, the committee chair and immediate advisor, who patiently guided me through my research work, with excellence and knowledge, while giving me the opportunity to explore ideas in my own way. Without him, this dissertation would not have been accomplished.

Dr. Aaron Sadow, Dr. Keith Woo, Dr. Arthur Winter, and Dr. Javier Vela deserve special thanks for their commitment to serve as my committee members and advisors. They generously devoted their time in providing me with ideas and direction during my studies, whenever necessary.

I am grateful to the chemistry department and the Henry Gilman Fellowship program for providing me with the financial support during my final year of study in order to devote my time and demonstrate my study skills in constructive research. Many thanks also go to the members of Yan Zhao group for healthy discussions, collaboration, and for providing a good working environment in the research laboratory.

Finally, I would like to acknowledge with gratitude, the support and love of my family–my Mom, Justine; my brothers, Johnson and Moses; my wife Valerie, and the rest of my family, relatives and friends. They all kept me going and continuously cheered me up.

CHAPTER 1

GENERAL INTRODUCTION

Dissertation Organization

Synthesis of molecularly imprinted polymeric nanoparticles with tailored hydrophobic binding pockets that function in water has not been achieved before. This dissertation presents an accumulated experimental investigation into the design and application of molecularly imprinted nanoparticles (MINPs) as antibody mimics.

The dissertation comprises of 7 chapters. Chapter 1 is a review on molecularly imprinted polymers (MIPs) and their application as synthetic antibodies. Chapter 2 was published in the *Journal of the American Chemical Society* in 2013. Molecularly imprinted nanoparticles (MINPs) were synthesized in the presence of bile salt derivative as templates. The MINPs were characterized and the activity of the hydrophobic binding pockets was studied using fluorescent spectroscopy and Isothermal Titration Calorimetry (ITC). The molecularly imprinted pocket showed high binding affinity and selectivity for its corresponding template. This phenomenon was attributed to highly selective hydrophobic binding sites created within the core of MINPs, with shape and size perfectly matching those of the corresponding substrates.

Chapter 3 was published in the *Chemical Communications* in 2014. Fluorescent dansyl groups were installed during naphthyl-templated synthesis of MINPs. Förster resonance energy transfer (FRET) within MINPs was studied in order to detect the presence of target analytes in water. Dansyl functionalized MINPs displayed remarkable sensing of the corresponding substrate in water, even in the presence of compounds closely related to the corresponding substrate in shape and structure. The radius of MINP, approximately 1.5

nm (excluding the surface ligands), ensured the right placement of the functional groups in the binding sites to generate dansyl-funtionalized MINPs with high affinity and excellent selectivity.

Chapter 4 was published in *Chemistry - A European Journal* in 2015. MINPs were core-functionalized with carboxylic acid in a process that involved covalent polymerization in the presence of an *o*-nitrobenzyl group. The property of the acid-functionalized hydrophobic pocket of MINPs was studied using an amine derivative and other analogues of the template at various pH values. The pocket displayed a strong interaction with the amine derivative at optimal pH. This phenomenon is typical to acid-base fluorescence titration as well as the highly functionalized hydrophobic pocket that discriminates against the structural analogues.

Chapter 5 had been submitted to the *ACS Biomaterials Science & Engineering*. The MINPs technique was used to create synthetic mimics of monoclonal antibodies for nonsteroidal anti-inflammatory drugs (NSAIDs). Selective binding and cross reactivity studies were performed using Isothermal Titration Calorimetry. The antibodies displayed strong binding for their corresponding drugs while exhibiting very low cross-reactivity ratios for drugs closely related to the analyte. The binding selectivity for the synthetic antibodies rivaled those of their natural counterparts usually prepared in much lengthier processes.

Chapter 6 was published in the *Supramolecular Chemistry* in 2014. Macrocyclic oligocholates were synthesized and their properties as transmembrane pore-forming agents studied. Assisted by the water molecules within the macrocycles, the rigid cyclic macrocycles formed nanopores across lipid membranes that helped to steadily transverse

glucose from the interior to the exterior of the lipid bilayer membranes. Chapter 7 contains general conclusions and future direction with the likelihood of widening the scope of MINPs.

Literature Review

Antibodies are natural receptor molecules that are produced when an immune system detects and responds to the presence of an antigen. They are able to recognize and bind to their antigens with high affinity and selectivity. For this reason, antibodies have good use in therapeutics for treatment and diagnosis of various medical conditions,[1-4] and in enzyme-linked immunosorbent assays (ELISA) [5]

Molecular imprinting is a technique that has been well documented for its use in creating synthetic antibodies that mimic these natural receptors. [6-9] The technique allows polymerization of functional monomers and cross-linkers around a template, in the presence of an initiator, to generate recognition sites with predetermined selectivity and specificity within the polymeric network. The beauty of molecular imprinting is that it can be used to create synthetic antibodies against virtually any molecule of interest, at least in theory. Binding affinities displayed by the recognition sites from molecular imprinting have been shown to rival, or even sometimes outperform their natural counterparts.[10]

The choice of the solvent in the synthesis of MIPs is important as it serves to bring together the monomers, template, cross-linker, and initiator into one phase during polymerization. The most common solvents used are toluene, chloroform, dichloromethane or acetonitrile. Greater template-monomer complexation is normally achieved using less polar solvents such as chloroform or toluene when polar interactions such as hydrogen bonds are involved in the process. More polar solvents like water are normally avoided because of

their ability to compete with intermolecular forces, thoroughly weakening the much needed template-monomer complexation. Characteristically, the MIPs generated are chemically inert, have long-term stability, contain a heterogeneous population of binding sites, and are insoluble in water and most organic solvents. With these features, MIPs have been widely studied for biomimetic applications such as molecular recognition,[11-13] molecular sensing,[14, 15] catalysis,[16-18] separation of compounds, [19-21] and therapeutics.[22-26]

To widen the application of molecular imprinting technique, some of the shortcomings arising from MIPs need to be addressed. For instance in pharmaceutical and biological applications, solubility of the molecules in water is extremely important. Most biomolecules tend to become insoluble or lose their activity in organic solvents. The heterogeneity of the binding sites acquired from MIPs that make them comparable to polyclonal antibodies is another issue to be addressed. [27, 28] In fact, molecular imprinting is currently generating an increasing biological interest with demand for commercially relevant applications, which in turn creates new challenges for researchers to come up with simple and practicable solutions.[8] Immediate need for a new design of molecularly imprinted materials that can generate a homogenous population of binding sites with complete functionality in water [29] is therefore paramount.

Membrane proteins possess hydrophilic and hydrophobic phases, yet it is a widely accepted fact that hydrophobic forces dominate protein-protein interactions,[30, 31] with van der Waals interactions and hydrogen bonds making only a small net contribution to the binding energy.[32] Exploiting these hydrophobic interactions is one way to strengthen the template-functional monomer complexation in water. Unfortunately, for molecular imprinting, the principle of hydrophobic interactions is not easy to explore since hydrophobic materials often

bind nonpolar molecules nonspecifically. In this dissertation I present an accumulated research work that has been accomplished using molecular imprinting technology to create molecularly imprinted nanoparticles (MINPs) as antibody mimics that are fully compatible with water, while bearing a hydrophobic binding pocket in the interior.

References

(1) Oldham, R. K.; Dillman, R. O. *J Clin Oncol* **2008**, *26*, 1774.

(2) Bebbington, C.; Yarranton, G. *Curr Opin Biotech* **2008**, *19*, 613.

(3) Catley, M. C.; Coote, J.; Bari, M.; Tomlinson, K. L. *Pharmacol Therapeut* **2011**, *132*, 333.

(4) Weisman, L. E. *Arch Pediatrie* **2007**, *14*, S31.

(5) Yarmush, M. L.; Weiss, A. M.; Antonsen, K. P.; Odde, D. J.; Yarmush, D. M. *Biotechnol Adv* **1992**, *10*, 413.

(6) Mosbach, K.; Ramstrom, O. *Bio-Technol* **1996**, *14*, 163.

(7) Haupt, K.; Mosbach, K. *Trends Biotechnol* **1998**, *16*, 468.

(8) Haupt, K. *Nat Mater* **2010**, *9*, 612.

(9) Wulff, G. *Angewandte Chemie-International Edition in English* **1995**, *34*, 1812.

(10) Schirhagl, R.; Latif, U.; Dickert, F. L. *J Mater Chem* **2011**, *21*, 14594.

(11) Bossi, A.; Bonini, F.; Turner, A. P. F.; Piletsky, S. A. *Biosens Bioelectron* **2007**, *22*, 1131.

(12) Lepisto, M.; Sellergren, B. *J Org Chem* **1989**, *54*, 6010.

(13) Vlatakis, G.; Andersson, L. I.; Muller, R.; Mosbach, K. *Nature* **1993**, *361*, 645.

(14) Haupt, K.; Mosbach, K. *Chem Rev* **2000**, *100*, 2495.

(15) Ansell, R. J.; Kriz, D.; Mosbach, K. *Curr Opin Biotech* **1996**, *7*, 89.

(16) Hilvert, D.; Hill, K. W.; Nared, K. D.; Auditor, M. T. M. *J Am Chem Soc* **1989**, *111*, 9261.

(17) Svenson, J.; Zheng, N.; Nicholls, I. A. *J Am Chem Soc* **2004**, *126*, 8554.

(18) Wulff, G. *Chem Rev* **2002**, *102*, 1.

(19) Kempe, M.; Mosbach, K. *J Chromatogr A* **1995**, *691*, 317.

(20) Fischer, L.; Muller, R.; Ekberg, B.; Mosbach, K. *J Am Chem Soc* **1991**, *113*, 9358.

(21) Hart, B. R.; Rush, D. J.; Shea, K. J. *J Am Chem Soc* **2000**, *122*, 460.

(22) Huval, C. C.; Bailey, M. J.; Braunlin, W. H.; Holmes-Farley, S. R.; Mandeville, W. H.; Petersen, J. S.; Polomoscanik, S. C.; Sacchiro, R. J.; Chen, X.; Dhal, P. K. *Macromolecules* **2001**, *34*, 1548.

(23) Whitcombe, M. J.; Rodriguez, M. E.; Villar, P.; Vulfson, E. N. *J Am Chem Soc* **1995**, *117*, 7105.

(26) Hoshino, Y.; Koide, H.; Urakami, T.; Kanazawa, H.; Kodama, T.; Oku, N.; Shea, K. J. *J Am Chem Soc* **2010**, *132*, 6644.

(27) Sellergren, B.; Allender, C. J. *Adv Drug Deliver Rev* **2005**, *57*, 1733.

(28) Ansell, R. J.; Ramstrom, O.; Mosbach, K. *Clin Chem* **1996**, *42*, 1506.

(29) Karlsson, B. C. G.; O'Mahony, J.; Karlsson, J. G.; Bengtsson, H.; Eriksson, L. A.; Nicholls, I. A. *J Am Chem Soc* **2009**, *131*, 13297.

(30) Wu, X. Y.; Carroll, W. R.; Shimizu, K. D. *Chem Mater* **2008**, *20*, 4335.

(31) Chadha, G.; Zhao, Y. *Chem Commun* **2014**, *50*, 2718.

(32) Tanford, C. *J Am Chem Soc* **1962**, *84*, 4240.

(33) Kellis, J. T.; Nyberg, K.; Sali, D.; Fersht, A. R. *Nature* **1988**, *333*, 784.

(34) Chandler, D. *Nature* **2005**, *437*, 640.

CHAPTER 2

PROTEIN MIMETIC, MOLECULARLY IMPRINTED NANOPARTICLES FOR SELECTIVE BINDING OF BILE SALT DERIVATIVES IN WATER

A paper published in *Journal of the American Chemical Society* **2013**, *135*, 12552-12555.

Joseph K. Awino and Yan Zhao

Abstract

A tripropargylammonium surfactant with a methacrylate-terminated hydrophobic tail was combined with a bile salt derivative, divinyl benzene (DVB), and a photocross-linker above its critical micelle concentration (CMC). Surface-cross-linking with a diazide, surface-functionalization with an azido sugar derivative, and free-radical-core-cross-linking under UV irradiation yielded molecular imprinted nanoparticles (MINPs) with template-specific binding pockets. The MINPs resemble protein receptors in size, complete water-solubility, and tailored binding sites in their hydrophobic cores. Strong and selective binding of bile salt derivatives was obtained, depending on the cross-linking density of the system.

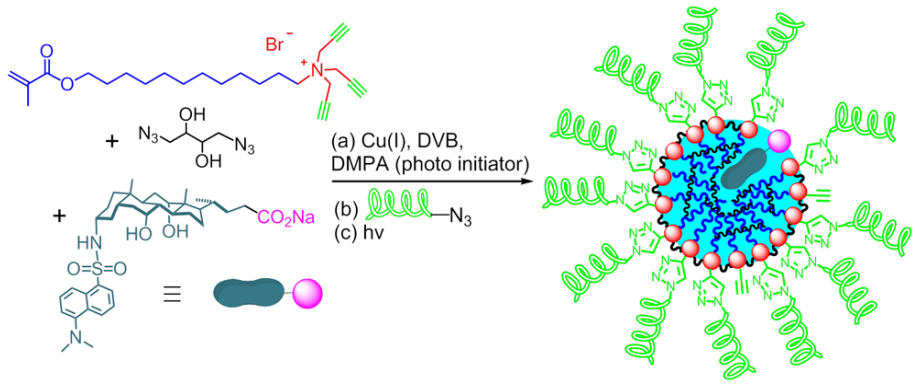

Scheme 1. General design for the synthesis of MINPs

Introduction

Molecularly imprinted polymers (MIPs) have binding sites potentially complementary to guests in size, shape, and distribution of functional groups.[1-3] They are usually prepared by co-polymerization of functional monomers and cross-linkers in the presence of a template. Tremendous progress has been made in the last decades in this technology, with imprinted materials generated for small and large guests,[1-3] in macroporous polymers and on surface,[4] for molecular recognition and catalysis,[5,6] and even unimolecularly within dendrimers.[7,8]

A difficult challenge in molecular imprinting remains the creation of protein-like, water-soluble nanoparticles with high binding affinity and selectivity for guests.[9-11] Part of the challenge comes from the general difficulty in constructing synthetic receptors that function in water.[12] Hydrogen bonds as directional intermolecular forces are the most popular tools used by chemists for molecular recognition but tend to become ineffective in aqueous solution due to competition from the solvent. The hydrophobicity of typical MIPs represents another hurdle, as hydrophobic materials often bind nonpolar molecules nonspecifically.

In this communication, we report a method to prepare molecularly imprinted nanoparticles (MINPs) for selective binding of bile salt derivatives in water. Although imprinted polymeric nanoparticles have been reported in the literature,[13-15] our MINP is characterized by its discrete binding sites and great resemblance to protein receptors in its nanodimension, complete water-solubility, functionalizable exterior, and easily accessible, tailor-made hydrophobic binding pocket. We chose bile salts as the template/guest molecules because of their important biological properties and water-solubility.[16,17]

Results and Discussion

Design and Synthesis of MINPs

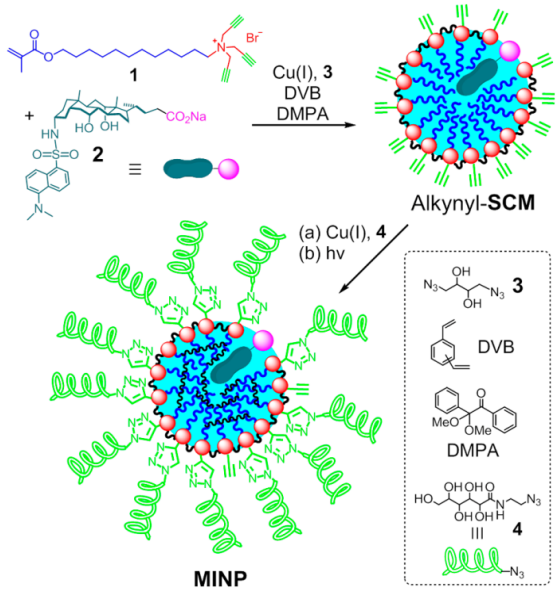

Scheme 2. Preparation of MINP.

The key design in our MINPs is the doubly cross-linkable surfactant **1**. The tripropargylated surfactant forms micelles in water with a high density of alkyne on the surface. Covalent fixation by a diazide cross-linker using Cu(I) catalysts yields surface-cross-linked micelles (SCMs) that could be easily functionalized through another round of click reaction.[18-21] Unlike previously synthesized tripropargylated surfactants, however, **1** has a polymerizable group (i.e., methacrylate) and thus can undergo free-radical polymerization orthogonal to the surface-cross-linking by the click reaction. Surfactant **1** has three alkyne groups and cross-linker **3** two azides. In the first stage of the reaction, we performed the surface-cross-linking of the micelles using [**3**]:[**1**] = 1.2/1, allowing good cross-linking while leaving sufficient alkyne groups on the SCM surface for further functionalization (Scheme 2).[18-21] The cross-linking was prepared with 10 mM of **1** in water, above its CMC of 0.55

mM (Figure 4 in Supporting Information). Our DLS study showed that each SCM contained ca. 50 surfactants (Figure 5). Thus, a ratio of [**1**]:[**2**] = 1:0.02 in theory placed one template (i.e., bile salt derivative **2**) within each SCM. The cross-linking chemistry and covalent structure of the SCMs have been previously characterized by mass spectrometry and TEM.[18]

After surface-cross-linking, sugar-derived ligand **4** was added to the reaction mixture. The surface functionalization, catalyzed also by Cu(I), made the final MINPs completely hydrophilic and easy to purify (vide infra). After surface functionalization, the sample was immediately subjected to UV irradiation to co-polymerize the methacrylate of **1** and DVB solubilized within the SCMs. The photopolymerization was initiated by DMPA (i.e., 2,2-dimethoxy-2-phenylacetophenone, a photoinitiator) added together with DVB at the beginning of the reaction. After 12 h of irradiation, ^{1}H NMR spectroscopy indicated complete disappearance of alkenic protons (Figure 6). DLS showed a narrow distribution of nanoparticles ca. 4.2 nm in diameter for alkynyl-SCM, 5.9 nm after surface functionalization, and 5.0 nm after core-cross-linking (Figure 7).

Preparation of the MINPs was remarkably simple. The entire synthesis was a one-pot reaction over 2 d at room temperature in water. Equally important was the extremely easy purification. The nanoparticles could be precipitated from acetone after the core-cross-linking, due to the sugar-derived surface ligand **4**. Repeated washing by methanol/acetic acid and methanol completely removed the template (as shown by fluorescence spectroscopy) and afforded the final MINPs in ca. 80% yield. The materials obtained were fully soluble in water and showed no change in size compared to as synthesized MINPs.

An important strategy in the MINP synthesis was the combination of a cationic cross-linkable surfactant and an anionic template. Their electrostatic interactions not only make it

easy to incorporate the template inside the micelle and ultimately inside MINP, but also orient the hydrophobic part of template within the hydrophobic core of the micelle and the carboxylate on the surface. The result is easy removal of the template, which vacates the binding site, and facile re-binding of the guest.

Binding Studies

The dansyl group of **2** allowed us to study its binding by fluorescence spectroscopy. As shown in Figure 1a, upon the addition of MINP(**2**)—i.e., MINP imprinted against **2**—to an aqueous solution of **2**, the dansyl emission at 550 nm immediately shifted to 475 nm. A large blue shift and enhanced emission suggest a more hydrophobic environment around dansyl[22] and are frequently observed when dansyl-labeled compounds are internalized by micelles.[23,24] The fluorescence intensity at 475 nm fitted nicely to a 1:1 binding isotherm to give an association constant (K_a) of 3.3 $\times 10^6$ M^{-1} (Figure 1b). The binding affinity was among the highest observed between synthetic hosts and steroid derivatives including bile salt derivatives.[17]

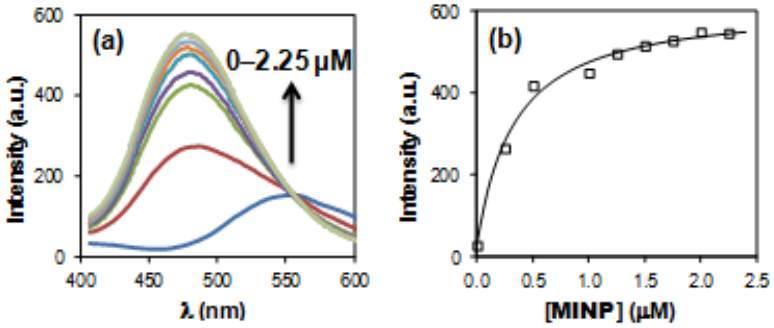

Figure 1. (a) Emission spectra of **2** upon the addition of different concentrations of MINP(**2**). [**2**] = 0.050 μM. The concentration of MINP was calculated based on a M.W. of 49800 g/mol determined by DLS (see Figure 9 for details). (b) Nonlinear least squares fitting of the emission intensity of **2** at 475 nm to a 1:1 binding isotherm.

After confirming effective binding of the template molecule, we studied the binding of several other bile salt derivatives (**5**–**9**) to understand the selectivity of the MINPs. After all, molecular imprinting is meant to create binding sites complementary to the template. Among these compounds, **5** and **6** have the acyl group on the amine gradually decrease in size and were designed to test the size/shape selectivity of the MINPs.

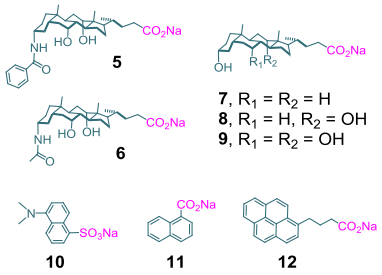

Substrates used

Table 1 summarizes the binding data of MINPs generated from **2** and **6** as the templates. For the majority of the bindings, we employed isothermal titration calorimetry (ITC) because most of the guests were not fluorescent. An important benefit of ITC is the simultaneous determination of the number of binding sites (*N*) on the MINP. Figure 3 shows three typical ITC titration curves between MINP(**2**) and bile salt derivatives. Note that, for the fluorescent guest (**2**), the binding constants obtained by the fluorescence titration and ITC showed excellent agreement (Table 1, compare entries 1 & 2 and 10 & 11).

Our first batch of MINPs was prepared with 0.5 equiv of DVB. ITC shows that MINP(**2**) synthesized under this condition bound its template with K_a = 3.5 $\times 10^6$ M^{-1} (Table 1, entry 2). As the acyl group decreased in size, the binding deteriorated, with K_a going down to 2.5 $\times 10^6$ for the benzoyl derivative (**5**) and to 0.05 $\times 10^6$ when the benzoyl was replaced by acetyl. In other words, the template itself fitted the binding pocket better than the other two (smaller) analogues, demonstrating the effectiveness of the imprinting. Among the naturally

occurring bile salts, **7** showed similar binding as **6** but none of the more hydrophilic compounds (**8** and **9**) gave any detectable binding.

Table 1. Binding data for MINPs (obtained by ITC unless indicated otherwise)[a]

Entry	MINP	DVB (equiv)	Guest	K_a ($\times 10^6$ M^{-1})	$-\Delta G$ (kcal/mol)	N
1	MINP(**2**)	0.5	**2**	3.3 ± 0.5[b]	8.9	-[b]
2	MINP(**2**)	0.5	**2**	3.5 ± 0.2	8.9	1.0
3	MINP(**2**)	0.5	**5**	2.5 ± 0.1	8.7	0.9
4	MINP(**2**)	0.5	**6**	0.05 ± 0.01	6.4	0.7
5	MINP(**2**)	0.5	**7**	0.03 ± 0.01	6.0	0.3[c]
6	MINP(**6**)	0.5	**2**	1.39 ± 0.02	8.4	0.5
7	MINP(**6**)	0.5	**5**	1.99 ± 0.03	8.6	0.7
8	MINP(**6**)	0.5	**6**	0.09 ± 0.01	6.8	0.8
9	MINP(**6**)	0.5	**7**	0.02 ± 0.01	5.9	0.2[c]
10	MINP(**2**)	1.0	**2**	3.7 ± 0.8[b]	8.9	-[b]
11	MINP(**2**)	1.0	**2**	3.5 ± 0.2	9.0	1.0
12	MINP(**2**)	1.0	**5**	0.46 ± 0.07	7.7	0.7
13	MINP(**2**)	1.0	**6**	0.28 ± 0.04	7.4	0.6
14	MINP(**2**)	1.0	**7**	-[d]	-[d]	-[d]
15	MINP(**2**)	1.0	**10**	0.07 ± 0.01	6.6	0.3[c]
16	MINP(**2**)	1.0	**11**	0.0045 ± 0.0002	5.0	0.2[c]
17	MINP(**2**)	1.0	**12**	0.28 ± 0.03	7.4	0.6
18	MINP(**2**)	1.0	**2**[e]	3.21 ± 0.02	8.9	1.0
19	MINP(**2**)	1.0	**2**[f]	3.28 ± 0.02	8.9	1.0
20	MINP(**6**)	1.0	**2**	0.27 ± 0.12	7.4	0.7
21	MINP(**6**)	1.0	**5**	0.58 ± 0.02	7.9	0.6
22	MINP(**6**)	1.0	**6**	1.1 ± 0.2	8.2	0.8
23	MINP(**6**)	1.0	**7**	-[d]	-[d]	-[d]
24	MINP(**2**)$_2$[g]	1.0	**2**	3.56 ± 0.01	8.9	1.2
				3.07 ± 0.04	8.8	1.2

[a] The titrations were generally performed in duplicates and the errors between the runs were <10%. Binding was measured in 50 mM Tris buffer (pH = 7.4) with 150 mM NaCl unless otherwise noted. Compounds **8** and **9** showed no detectable binding by ITC with any of the MINPs. [b] Binding data were obtained from fluorescence titration and thus N was not available. [c] The weak binding made the curve fitting not as accurate. [d] Binding (K_a <1000 M^{-1}) was not detectable by ITC. [e] Binding was measured in 50 mM Tris buffer (pH = 7.4) with 200 mM NaCl. [f] Binding was measured in 50 mM Tris buffer (pH = 7.4) without NaCl. [g] The MINPs were prepared with [**1**]:[**2**] = 1:0.04, i.e., twice as much of the template was employed as

compared to other examples. The two binding constants were for the two independent binding sites, respectively.

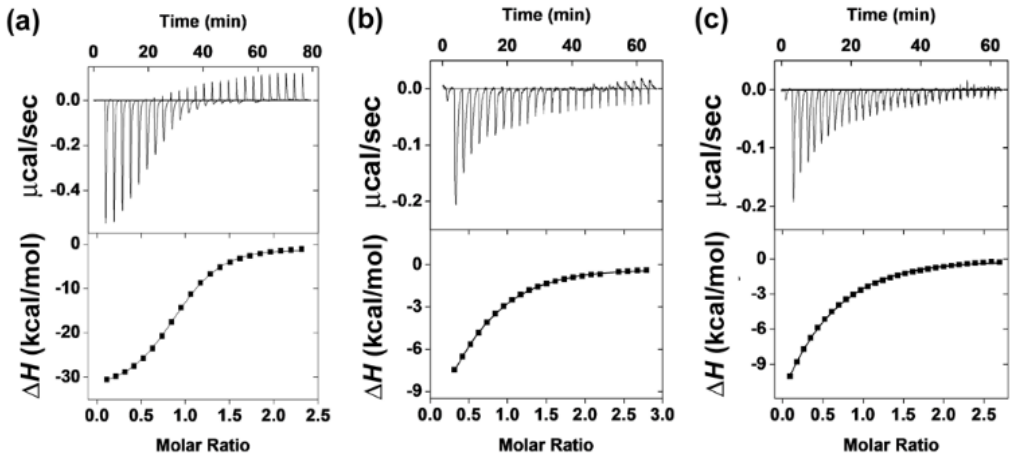

Figure 2. ITC titration curves obtained at 298 K for the binding of **2** (a), **5** (b), and **6** (c) by MINP(**2**) prepared with 1 equiv of DVB. The data correspond to entries 11–13 in Table 1. Additional ITC titration curves can be found in the Supporting Information (Figures 9–13). In general, an aqueous solution of an appropriate bile salt in Tris buffer (50 mM Tris, 150 mM NaCl, pH = 7.4) was injected in equal steps into 1.428 mL of the corresponding MINP solution (4.0 mg/mL) in the same buffer. The top panel shows the raw calorimetric data. The area under each peak represents the amount of heat generated at each ejection and is plotted against the molar ratio of the MINP to the bile salt. The smooth solid line is the best fit of the experimental data to the sequential binding of *N* equal and independent binding sites on the MINP. The heat of dilution for the bile salt, obtained by adding the bile salt to the buffer, was subtracted from the heat released during the binding. Binding parameters were auto-generated after curve fitting using Microcal Origin 7.

We then synthesized MINPs using the smaller bile salt derivative **6** as the template. The result was somewhat disappointing. On one hand, the largest bile salt (**2**) showed weaker

binding to MINP(**6**) than to MINP(**2**), as expected from the smaller size of the binding pocket in the former (Table 1, compare entries 2 and 6). On the other hand, although **2** bound to MINP(**6**) less strongly than **5**, both compounds bound much more strongly than **6** itself (K_a = 0.09 $\times 10^6$ M^{-1}). It appears that both hydrophobic effects and size/shape selectivity were playing roles in this MINP. Essentially, although the binding pocket of MINP(**6**) was smaller than that of MINP(**2**), the stronger hydrophobicity of **2** and **5** gave them a larger driving force to occupy the hydrophobic pocket than the somewhat hydrophilic **6**. Whereas **6** might fit the binding site of MINP(**6**) better than the larger bile salts, its weaker hydrophobicity lowers its tendency to enter the pocket.

Not satisfied with the above results, we decided to increase the amount of DVB to 1 equiv to **1** for the core-cross-linking. This was the highest amount of DVB that could be solubilized by the surfactant in water. To our delight, binding selectivity increased dramatically. Using this more highly cross-linked MINP(**2**), we were able to distinguish the size of the acyl group easily: the dansyl, benzoyl, and acetyl derivatives afforded K_a of 3.5, 0.46, and 0.28 $\times 10^6$ M^{-1}, respectively (Table 1, entries 11–13). Lithocholate **7** displayed no binding at all.

For the more highly cross-linked MINP(**2**), we also studied several non-steroid aromatic guests (**10**–**12**) to understand the binding selectivity. Dansyl sulfonate **10** in a sense was a "half-match" for the binding site generated from dansylated **2**. Its K_a (= 0.07 $\times 10^6$ M^{-1}) was reduced by ca. 50 times from that of **2**. A further decrease of the hydrophobic size made naphthalene-1-carboxylate (**11**) an even poorer guest, whose K_a was only 0.0045 $\times 10^6$ M^{-1} or about 800 times weaker than that of **2**. As soon as the guest size increased, binding resumed,

as pyrenebutyrate **12** displayed identical binding constant to that of **6** (K_a = 0.28 ×10^6 M^{-1}) or 1/13 of that of **2**.

All the bindings were measured in 50 mM Tris buffer with 150 mM NaCl. When the salt concentration was raised to 300 mM, the MINPs were found to precipitate out of the buffer. In 200 mM and 0 mM NaCl (Table 1, entries 18 and 19), similar binding constants were obtained for the MINP(**2**)–**2** complex and were essentially within the experimental error from that in 150 mM NaCl (entry 11). We attributed the insensitivity of binding to salt (at least over 0–200 mM NaCl) to the two opposing binding forces present in the system: whereas salt tends to strengthen hydrophobic interactions, it weakens the electrostatic interactions between the positively charged MINP and the negatively charged guest.

Importantly, when 1 equiv DVB was used in the core-cross-linking, selective binding pockets could be created for the smaller bile salt **6** as well. As the acyl group became smaller, the bile salts exhibited a consistent increase in their binding affinity toward the highly cross-linked MINP(**6**), with K_a increasing from 0.27 ×10^6 to 0.58 ×10^6 and further to 1.1 ×10^6 M^{-1} (entries 20–22). This trend was opposite to the hydrophobicity of the guest and different from what was observed for MINP(**6**) prepared with 0.5 equiv DVB. Clearly, the higher cross-linking density of the material significantly enhanced the rigidity of the binding pockets. Under this condition, even though the more hydrophobic guests (**2** and **5**) possess stronger thermodynamic “desires” to enter the hydrophobic pocket, they were excluded most likely because of their misfit to the less "forgiving" binding sites.

It should be pointed out that, unlike conventional MIPS and the reported molecularly imprinted nanoparticles,[13-15] our MINPs on average possessed approximately one guest-binding site per particle. Except when weak binding made the curve fitting less accurate, the

number of independent binding sites (*N*) obtained by ITC was close to 1 in most cases for the MINPs (Table 1). This feature comes directly from the stoichiometry of template used in the synthesis relative to the micelle aggregation number of **1**.

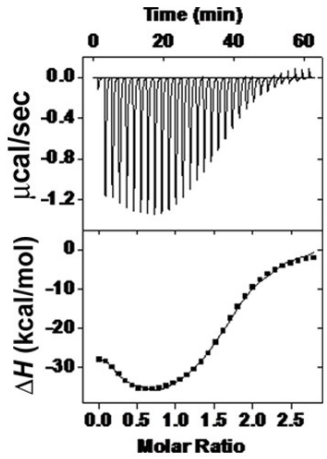

Figure 3. ITC titration curves obtained at 298 K for the binding of **2** by MINP(**2**)$_2$ prepared with 1 equiv of DVB. The data correspond to entry 20 in Table 1. The smooth solid line is the best fit of the experimental data to the sequential binding of 2 equal and independent binding sites on the MINP.

To demonstrate the tunability in binding stoichiometry, we prepared MINP(**2**)$_2$ with [**1**]:[**2**] = 1:0.04, i.e., doubling the amount of template employed during the imprinting. Figure 3 shows the ITC titration curve for the re-binding of **2**. The distinctively different curve as compared to those in Figure 2 fitted best to a binding model with two independent binding sites per nanoparticle. As shown by entry 20 in Table 1, the two binding sites had very similar binding constants (K_a = 3.56 and 3.07 $\times 10^6$ M^{-1}), which were essentially the same as that of the MINP(**2**)–**2** complex (K_a = 3.5 $\times 10^6$ M^{-1}). Thus, the same hydrophobic and electrostatic interactions were behind all these binding events, whether the MINP contained one or two binding sites.

Conclusion

To summarize, we have developed a facile method to create protein-like, water-soluble receptors for selective binding of bile salt derivatives in water. Unlike proteins, however, these nanoparticles are extremely robust and have outstanding tolerance for organic solvents and adverse temperature/pH conditions. The robustness comes directly from their highly cross-linked nature and was demonstrated by our washing conditions in the purification. Their nanodimension, readily modified structure,[18-21,25-27] and excellent properties of molecular recognition should make them highly useful materials for chemistry and biology.

Acknowledgement

We thank NSF (CHE-1303764) for partial support of the research.

Experimental Section

General Method

For spectroscopic purpose, methanol, hexanes, and ethyl acetate were of HPLC grade. All other reagents and solvents were of ACS-certified grade or higher, and were used as received from commercial suppliers. Routine ^{1}H and ^{13}C NMR spectra were recorded on a Bruker DRX-400 or on a Varian VXR-400 spectrometer. MALDI-TOF mass was recorded on a Thermobioanalysis Dynamo mass spectrometer. UV-vis spectra were recorded at ambient temperature on a Cary 100 Bio UV-visible spectrophotometer. Fluorescence spectra were recorded at ambient temperature on a Varian Cary Eclipse Fluorescence spectrophotometer. ITC was performed using a MicroCal VP-ITC Microcalorimeter with Origin 7 software and VPViewer2000 (GE Healthcare, Northampton, MA).

Syntheses

Syntheses of compounds **3**,[28] **4**,[29] **13**,[30] **15**,[31] and **2**[30] were previously reported.

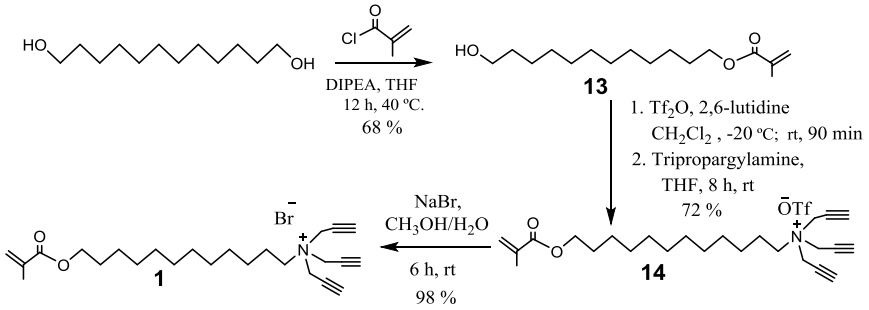

Scheme 3. Synthesis of compound **1**

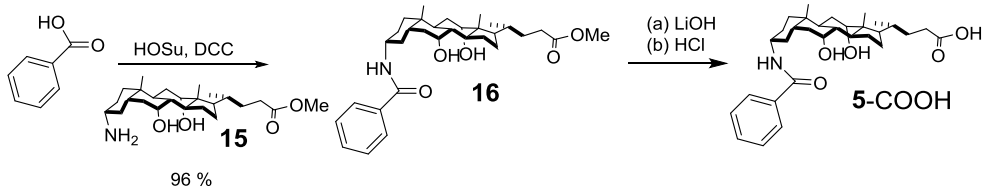

Scheme 4. Synthesis of compound **5**-COOH

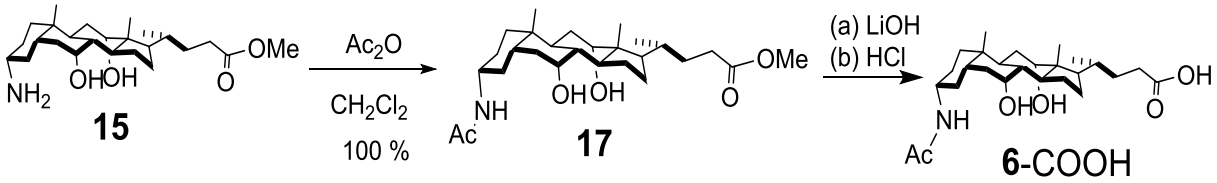

Scheme 5. Synthesis of compound **6**-COOH

General procedure (hydrolysis of methyl ester). The methyl ester of a cholate derivative (0.10 mmol) was dissolved in a mixture of THF (1 mL) and MeOH (1 mL). A solution of 2 M LiOH (0.5 mL, 1 mmol) was added. The reaction was monitored by TLC and was complete in 10–24 h. The organic solvents were removed by rotary evaporation. After

addition of a dilute HCl solution (0.05 M, 30 mL), the precipitate formed was collected by suction filtration or centrifugation, washed with water, and dried in vacuo.

Compound 1. Triflic anhydride (0.35 mL, 2.1 mmol) and 2,6-lutidine (0.24 mL, 2.1 mmol) were added to 5 mL of dry dichloromethane, which was cooled at -20 °C. The cooling bath was removed and compound **13** (430 mg, 1.6 mmol) in CH_2Cl_2 (2 mL) was added dropwise to the stirred solution. After being stirred at room temperature for 90 min, the reaction mixture was diluted with CH_2Cl_2 (5 mL). The organic layer was washed with 1 M HCl (10 mL) and water (2 × 10 mL), dried with magnesium sulfate, filtered, and concentrated by rotary evaporation to give the triflate as yellowish oil (600 mg, 93 %). The oil was dissolved in dry THF (10 mL) and tripropargylamine (0.3 mL, 2.1 mmol) added dropwise. After being stirred at room temperature overnight, the reaction mixture was concentrated by rotary evaporation and the residue was purified by column chromatography over silica gel using 1: 10 methanol/CH_2Cl_2 as eluent to afford colorless oil (575 mg, 72 %). This oil was dissolved in methanol (5 mL), followed by the addition of excess sodium bromide solution in 5 mL of water (3.86 g, 37.5 mmol). After being stirred for 6 h, the reaction mixture was diluted with CH_2Cl_2 (10 mL). The organic layer was washed with water (2 × 30 mL), dried with sodium sulfate, and concentrated by rotary evaporation. The process was repeated one more time to afford a colorless oil (430 mg, 100 %). ^{1}H NMR (400 MHz, $CDCl_3$, δ): 6.02 (d, J = 1.6 Hz, 1H), 5.47 (d, J = 1.6 Hz, 1H), 4.89 (d, J = 2.4 Hz, 6H), 4.06 (t, J = 1.6 Hz, 2H), 3.40 (t, J = 6.0 Hz, 2H), 2.8 (s, 3H), 1.87 (s, 3H), 1.53-1.43 (series of m, 8H), 1.26 (m, 12H). ^{13}C NMR (100 MHz, CDCl3, δ): 167.6, 136.5, 125.2, 82.5, 82.5, 82.5, 70.6, 70.6, 70.6, 64.5, 60.8, 50.5, 50.5, 50.5, 32.3, 29.3, 29.2, 29.2, 29.1, 29.1, 28.8, 28.2, 25.6, 25.4, 17.9. ESI-HRMS (*m/z*): $[M - Br]^+$ calcd for $C_{25}H_{38}NO_2$, 384.2897; found, 384.2903.

Compound 5-COOH. A solution of DCC (18.6 mg, 0.09 mmol) in THF (1 mL) was added to a stirred solution of benzoic acid (10 mg, 0.082 mmol) and N-hydroxysuccinimide (10.4 mg, 0.09 mmol) in THF (5 mL). After 10 h at room temperature, the white precipitate formed was removed by filtration. Compound **15** (50 mg, 0.12 mmol) in THF (1 mL) was added to the filtrate and the reaction mixture was stirred overnight. After THF was removed by rotary evaporation, the residue was purified by preparative TLC using 1:10 methanol/CH_2Cl_2=1/10) as developing solvent to give a white powder (30.3 mg, 96 %). ^{1}H NMR (400 MHz, $CDCl_3/CD_3OD$ = 2:1, δ): 7.67 (t, *J* = 2.0 Hz, 2H), 7.39 (m, 3H), 5.93 (d, *J* = 8.0 Hz, 1H), 3.94 (t, *J* = 6.8 Hz, 1H), 3.82 (m, 1H), 3.65 (s, 3H), 2.4 – 1.55 (series of m), 1.18 (s, 2H), 0.91 (t, *J* = 6.4 Hz, 3H), 0.87 (s, 3H), 0.64 (s, 3H). The methyl ester (**16**) was hydrolyzed according to the general procedure above to afford a white powder (30 mg, 100 %). ^{1}H NMR (400 MHz, $CDCl_3$, δ): 7.67 (t, *J* = 2.0 Hz, 2H), 7.39 (m, 3H), 5.93 (d, *J* = 8.0 Hz, 1H), 3.94 (t, *J* = 6.8 Hz, 1H), 3.82 (m, 1H), 3.40 (br, 1H), 2.4 – 1.55 (series of m), 1.18 (s, 2H), 0.91 (t, *J* = 6.4 Hz, 3H), 0.87 (s, 3H), 0.64 (s, 3H). ^{13}C NMR (100 MHz, $CDCl_3/CD_3OD$ = 1:1, δ): 175.4, 170.8, 134.9, 131.3, 128.2, 128.2, 126.9, 126.9, 72.8, 67.9, 51.2, 50.1, 48.6, 48.3, 48.1, 46.7, 46.2, 43.9, 43.6, 39.2, 35.3, 34.6, 34.4, 30.9, 30.8, 28.1, 26.4, 23.0, 22.3, 16.8, 12.3. ESI-HRMS (*m/z*): $[M - H]^-$ calcd for $C_{31}H_{44}NO_5$, 510.3225; found, 510.3227.

Compound 6-COOH. Acetic anhydride (25 μL, 0.26 mmol) was added to a solution of compound **15** (100 mg, 0.24 mmol) and pyridine (46 μL, 0.26 mmol) in CH_2Cl_2 (5 mL) under N_2. The reaction mixture was stirred at room temperature for 1 h and diluted with CH_2Cl_2 (5 mL). The resulting organic solution was washed with 1 M HCl (3 mL) and water (2 × 10 mL) and was concentrated by rotary evaporation to give a white powder (110 mg, 100 %). ^{1}H NMR (400 MHz, $CDCl_3/CD_3OD$ = 2:1, δ): 5.34 (br, 1H), 3.97 (t, *J* = 2.8 Hz, 1H),

3.85 (t, *J* = 2.4 Hz, 1H), 3.65 (s, 3H), 2.40 – 2.01 (series of m), 1.9 (s, 3H), 1.75 -1.19 (series of m), 1.18 (s, 2H), 0.91 (t, *J* = 6.4 Hz, 3H), 0.87 (s, 3H), 0.64 (s, 3H). The methyl ester (**17**) was hydrolyzed according to the general procedure above to afford a white powder (108 mg, 100%). ^{1}H NMR (400 MHz, CDCl3/CD3OD = 1:1, δ): 5.34 (br, 1H), 3.97 (t, *J* = 2.8 Hz, 1H), 4.85 (t, *J* = 2.4 Hz, 1H), 4.55 (br, 1H), 3.40 – 3.01 (series of m), 2.9 (s, 3H), 2.75 -2.19 (series of m), 2.18 (s, 2H), 1.91 (t, *J* = 6.4 Hz, 3H), 1.87 (s, 3H), 1.64 (s, 3H). ^{13}C NMR (100 MHz, CDCl3/CD3OD = 1:1, δ): 176.8, 170.5, 72.7, 67.8, 49.1, 48.6, 48.3, 48.1, 46.7, 46.2, 45.7, 43.9, 43.6, 39.2, 35.3, 34.6, 34.4, 30.9, 30.8, 30.7, 28.1, 26.4, 23.0, 22.3, 16.8, 12.3. ESI-HRMS (*m/z*): $[M + H]^+$ calcd for $C_{26}H_{44}NO_5$, 450.3219; found, 450.3215.

Determination of Critical Micelle Concentration (CMC) of Compound 1. The determination of CMC was carried out according to literature procedures.[32] Specifically, a stock solution was prepared by adding surfactant **1** (9.3 mg, 0.02 mmol) to 2.0 mL of an aqueous solution of pyrene (1.0×10^{-7} M). To 11 separate vials, 100, 90, 80, 70, 60, 50, 40, 30, 20, 10, and 5 μL of the above stock solution were added. Millipore water was added to each vial to make the total volume 2.0 mL. Fluorescence spectra were recorded with the excitation wavelength at 336 nm. The final results were based on duplicate experiments with separately prepared solutions.

Preparation of Molecularly Imprinted Nanoparticles (MINPs). To a micellar solution of compound **1** (9.3 mg, 0.02 mmol) in D_2O (2.0 mL), divinylbenzene (DVB, 2.8 μL, 0.02 mmol), compound **2**-COONa in D_2O (10 μL of a solution of 26.5 mg/mL, 0.0004 mmol), and 2,2-dimethoxy-2-phenylacetophenone (DMPA,10 μL of a 12.8 mg/mL solution in DMSO, 0.0005 mmol) were added. The mixture was subjected to ultrasonication for 10 min before compound **3** (4.1 mg, 0.024 mmol), $CuCl_2$ (10 μL of a 6.7 mg/mL solution in D_2O, 0.0005

mmol), and sodium ascorbate (10 μL of a 99 mg/mL solution in D_2O, 0.005 mmol) were added. After the reaction mixture was stirred slowly at room temperature for 12 h, compound **4** (10.6 mg, 0.04 mmol), $CuCl_2$ (10 μL of a 6.7 mg/mL solution in D_2O, 0.0005 mmol), and sodium ascorbate (10 μL of a 99 mg/mL solution in D_2O, 0.005 mmol) were added. After being stirred for another 6 h at room temperature, the reaction mixture was transferred to a glass vial, purged with nitrogen for 15 min, sealed with a rubber stopper, and irradiated in a Rayonet reactor for 12 h. ^1H NMR spectroscopy was used to monitor the progress of reaction. The reaction mixture was poured into acetone (8 mL). The precipitate was collected by centrifugation and washed with a mixture of acetone/water (5 mL/1 mL) three times. The crude produce was washed by methanol/acetic acid (5 mL/0.1 mL) three times until the emission peak at 480 nm (for the dansyl) disappeared and then with excess methanol. The off white powder was dried in air to afford the final MINPs (16 mg, 80%).

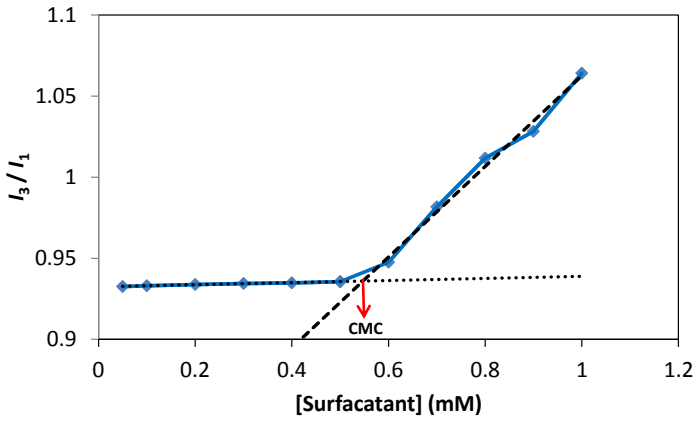

Figure 4. Pyrene I_3/I_1 ratio as a function of [**1**]. [pyrene] = 0.1 μM. The five vibronic bands of pyrene respond to environmental polarity differently. The intensity ratio between the third (~384 nm) and the first band (~372 nm) is particularly sensitive to environmental changes.

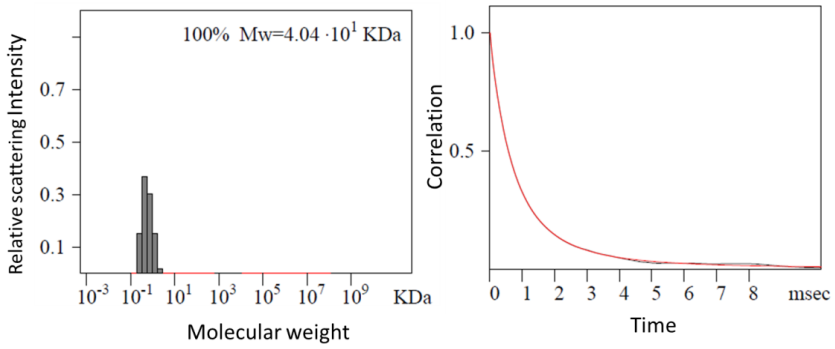

Figure 6. Distribution of the molecular weights of the alkynyl-SCMs and the correlation curve for DLS. The molecular weight distribution was calculated by the PRECISION DECONVOLVE program assuming the intensity of scattering is proportional to the mass of the particle squared. If each unit of building block for the alkynyl-SCM is assumed to contain one molecule of compound **1** (MW = 465 g/mol), 1.2 molecules of compound **3** (MW = 172 g/mol), and one molecule of DVB (MW = 130 g/mol), the molecular weight of the alkynyl-SCM translates to 50 [= 40400/(465+1.2×172+130)] of such units.

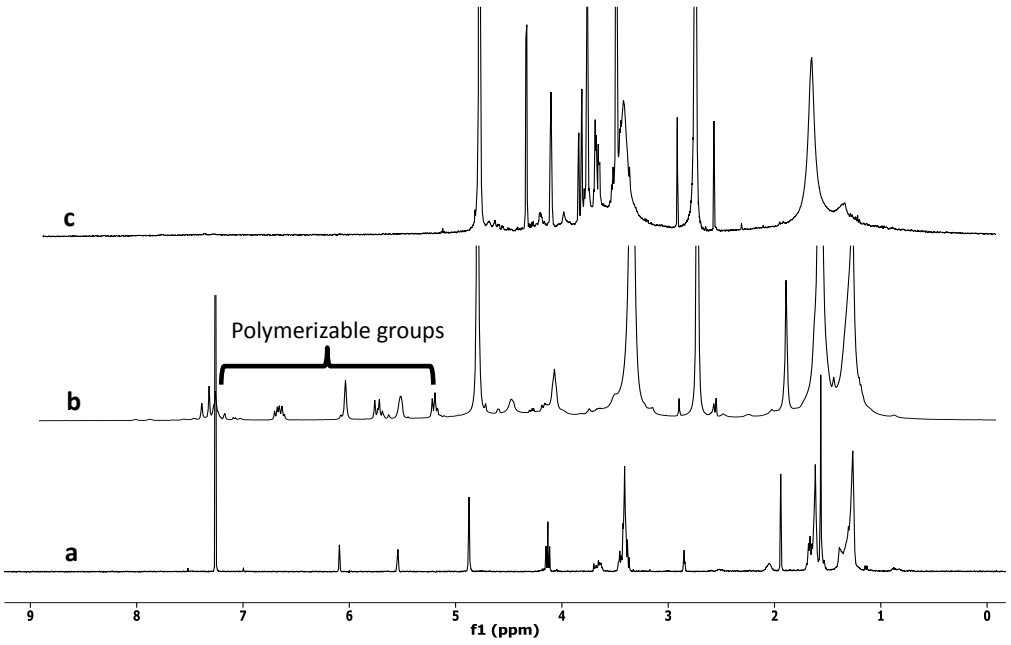

Figure 6. ^{1}H NMR spectra of (a) **1** in $CDCl_3$, (b) alkynyl-SCM in D_2O, (c) MINP(**2**) in D_2O.

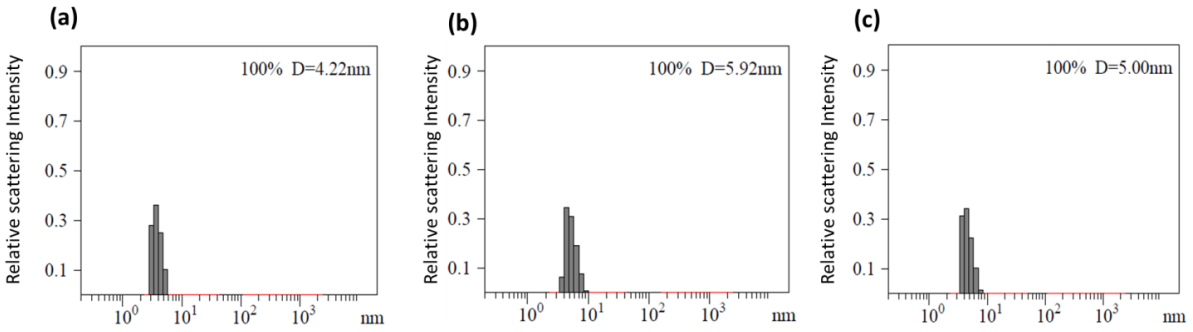

Figure 7. Distribution of the hydrodynamic diameters of the nanoparticles in water as determined by DLS for (a) alkynyl-SCM (b) surface-functionalized SCM, and (c) MINP(**2**) after purification.

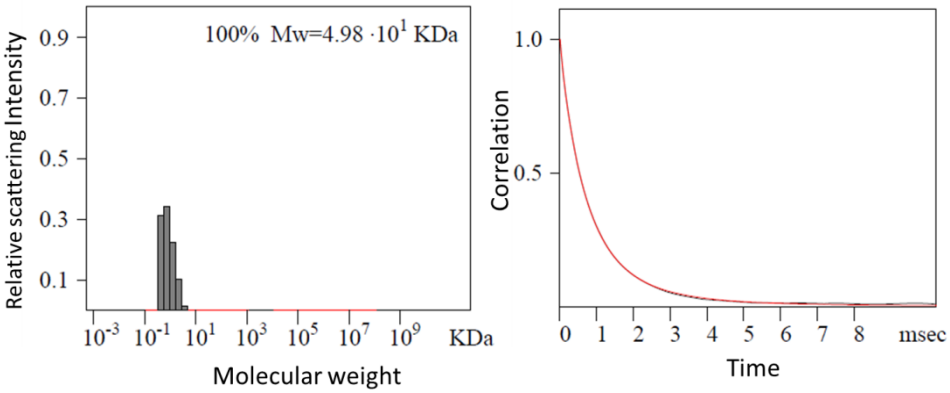

Figure 8. Distribution of the molecular weights of MINP(**2**) and the correlation curves for DLS. The molecular weight distribution was calculated by the PRECISION DECONVOLVE program assuming the intensity of scattering is proportional to the mass of the particle squared. If each unit of building block for the MINP(**2**) is assumed to contain one molecule of compound **1** (MW = 465 g/mol), 1.2 molecules of compound **3** (MW = 172 g/mol), one molecule of DVB (MW = 130 g/mol), and 0.8 molecules of compound **4** (MW = 264 g/mol), the molecular weight of MINP(**2**) translates to 49 [= 49800/(465+1.2×172+130+0.8×264)] of such units.

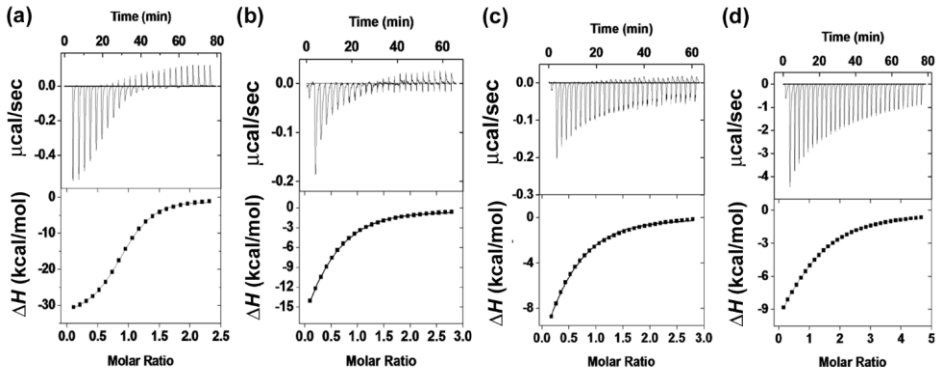

Figure 9. ITC titration curves obtained at 298 K for the binding of **2** (a), **5** (b), **6** (c), and **7** (d) by MINP(**2**) prepared with 0.5 equiv of DVB. The data correspond to entries 2–5 in Table 1. The top panel shows the raw calorimetric data. The area under each peak represents the amount of heat generated at each ejection and is plotted against the molar ratio of the MINP to the bile salt. The solid line is the best fit of the experimental data to the sequential binding of N equal and independent binding sites on the MINP. The heat of dilution for the bile salt, obtained by adding the bile salt to the buffer, was subtracted from the heat released during the binding. Binding parameters were auto-generated after curve fitting using Microcal Origin 7.

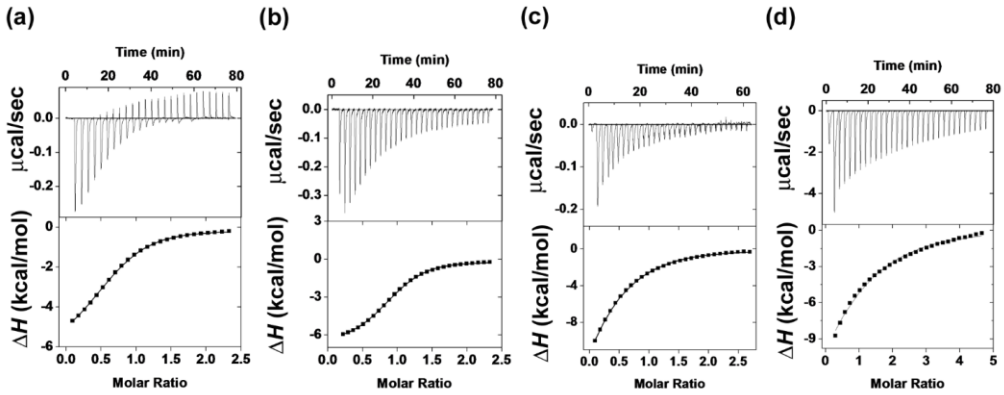

Figure 10. ITC titration curves obtained at 298 K for the binding of **2** (a), **5** (b), **6** (c), and **7** (d) by MINP(**6**) prepared with 0.5 equiv of DVB. The data correspond to entries 6–9 in Table 1. The top panel shows the raw calorimetric data. The area under each peak represents the

amount of heat generated at each ejection and is plotted against the molar ratio of the MINP to the bile salt. The solid line is the best fit of the experimental data to the sequential binding of N equal and independent binding sites on the MINP. The heat of dilution for the bile salt, obtained by adding the bile salt to the buffer, was subtracted from the heat released during the binding. Binding parameters were auto-generated after curve fitting using Microcal Origin 7.

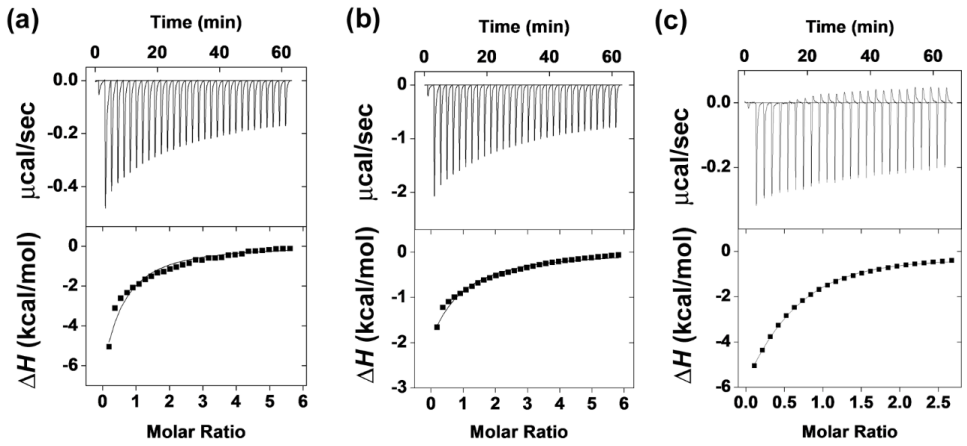

Figure 11. ITC titration curves obtained at 298 K for the binding of **10** (a), **11** (b), and **13** (c) by MINP(**2**) prepared with 1.0 equiv of DVB. The data correspond to entries 15–17 in Table 1. The top panel shows the raw calorimetric data. The area under each peak represents the amount of heat generated at each ejection and is plotted against the molar ratio of the MINP to the bile salt. The solid line is the best fit of the experimental data to the sequential binding of N equal and independent binding sites on the MINP. The heat of dilution for the bile salt, obtained by adding the bile salt to the buffer, was subtracted from the heat released during the binding. Binding parameters were auto-generated after curve fitting using Microcal Origin 7.

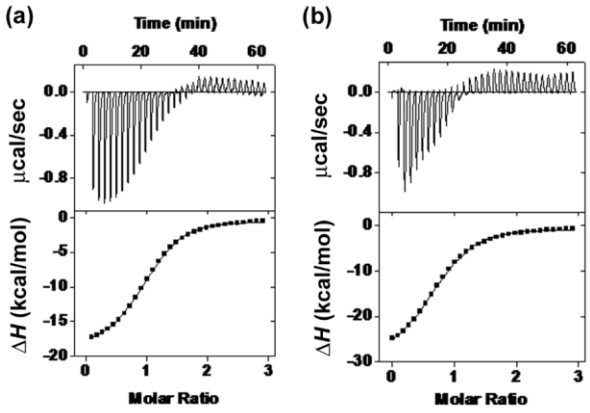

Figure 12. ITC titration curves obtained at 298 K for the binding of **2** by MINP(**2**) prepared with 1 equiv of DVB in 50 mM Tris buffer (pH = 7.4) with (a) 200 mM and (b) 0 mM NaCl. The data correspond to entries 18–19 in Table 1. The top panel shows the raw calorimetric data. The area under each peak represents the amount of heat generated at each ejection and is plotted against the molar ratio of the MINP to the bile salt. The solid line is the best fit of the experimental data to the sequential binding of N equal and independent binding sites on the MINP. The heat of dilution for the bile salt, obtained by adding the bile salt to the buffer, was subtracted from the heat released during the binding. Binding parameters were auto-generated after curve fitting using Microcal Origin 7.

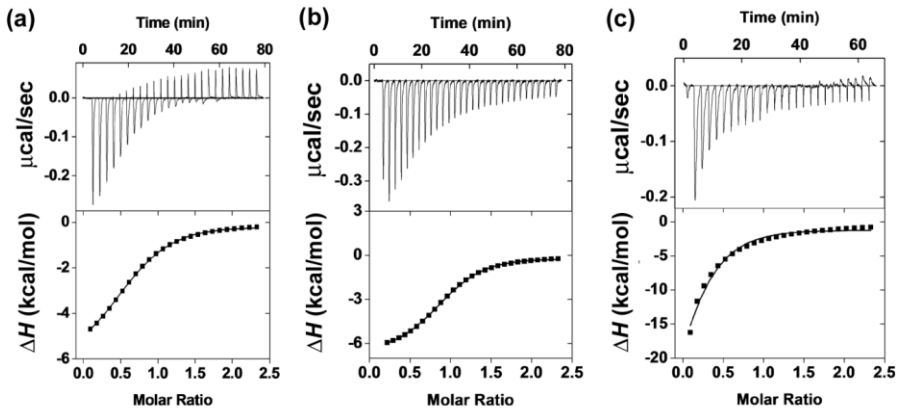

Figure 13. ITC titration curves obtained at 298 K for the binding of **2** (a) **5** (b), and **6** (c) by MINP(**6**) prepared with 1 equiv of DVB. The data correspond to entries 20–22 in Table 1. The top panel shows the raw calorimetric data. The area under each peak represents the amount of heat generated at each ejection and is plotted against the molar ratio of the MINP to the bile salt. The solid line is the best fit of the experimental data to the sequential binding of N equal and independent binding sites on the MINP. The heat of dilution for the bile salt, obtained by adding the bile salt to the buffer, was subtracted from the heat released during the binding. Binding parameters were auto-generated after curve fitting using Microcal Origin 7.

[1] H NMR of compound **1**

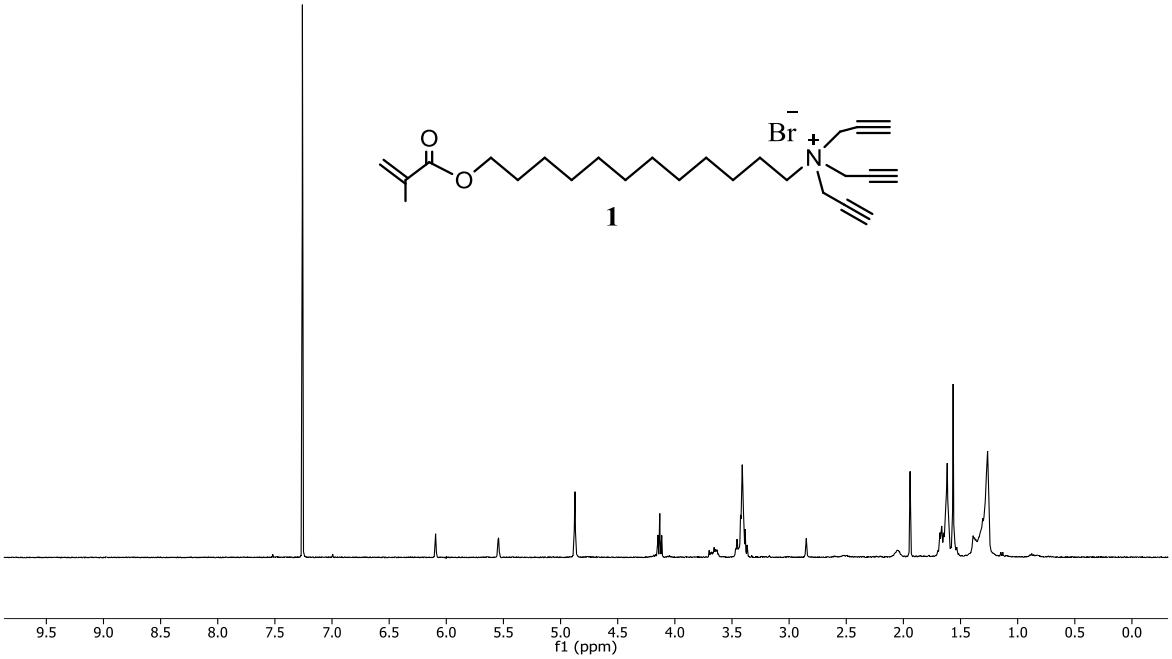

[13] C NMR of compound **1**

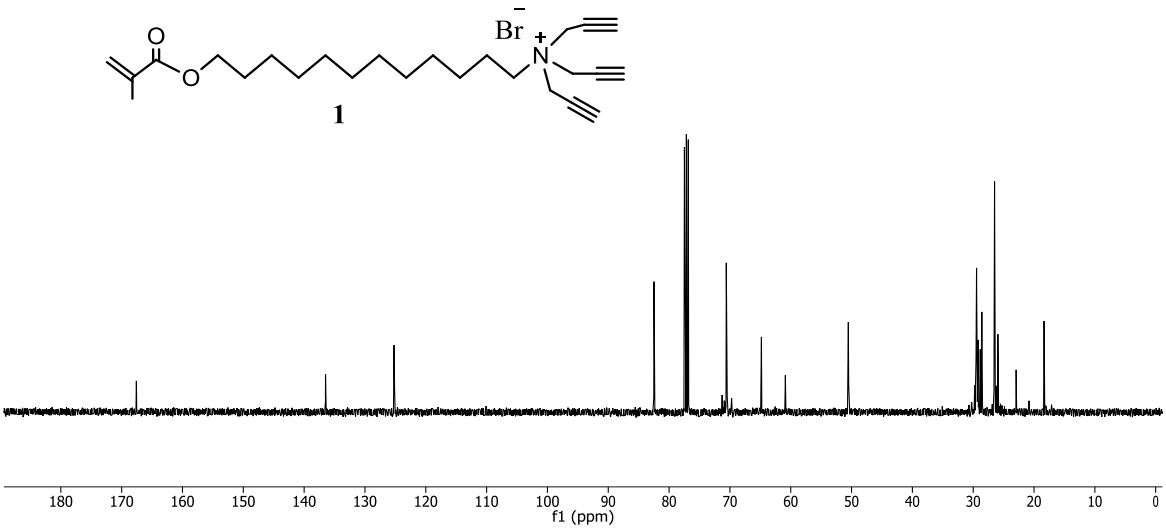

^{1}H NMR of compound **16**

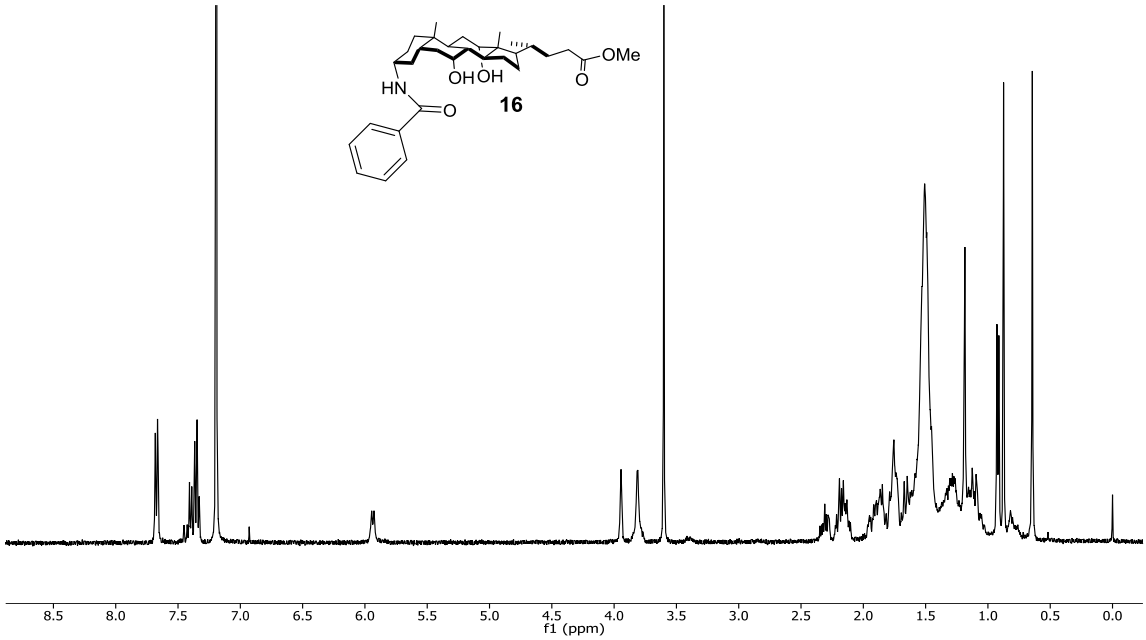

^{1}H NMR of compound **5-COOH**

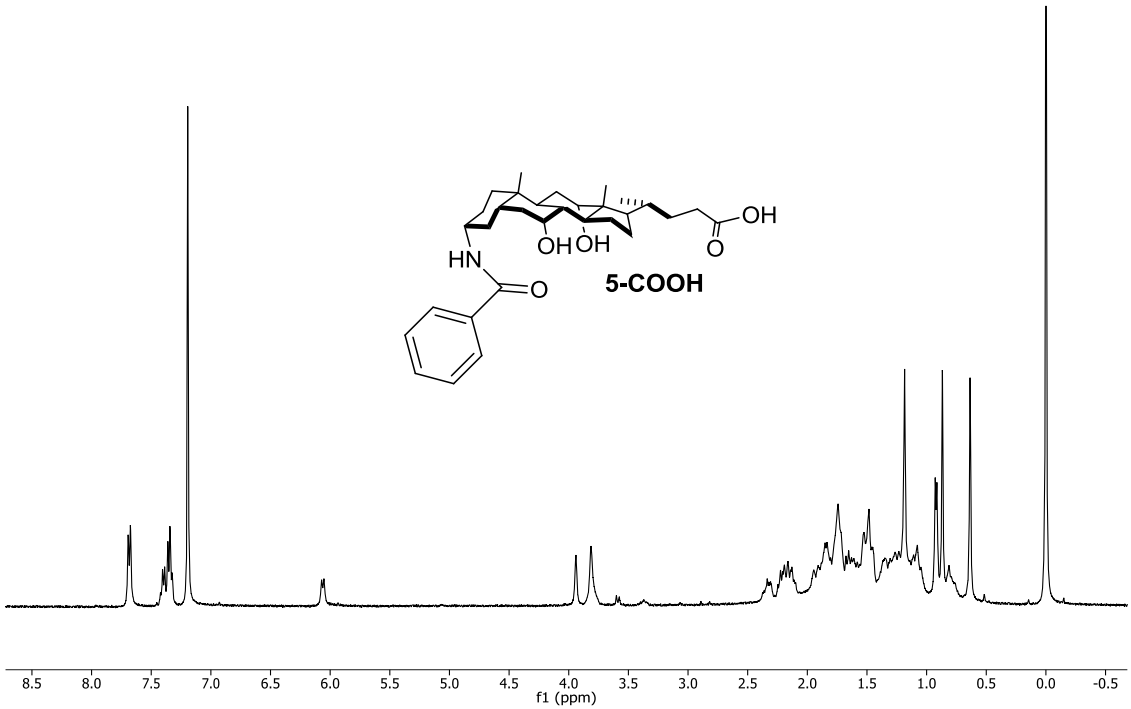

^{13}C NMR of compound **5-COOH**

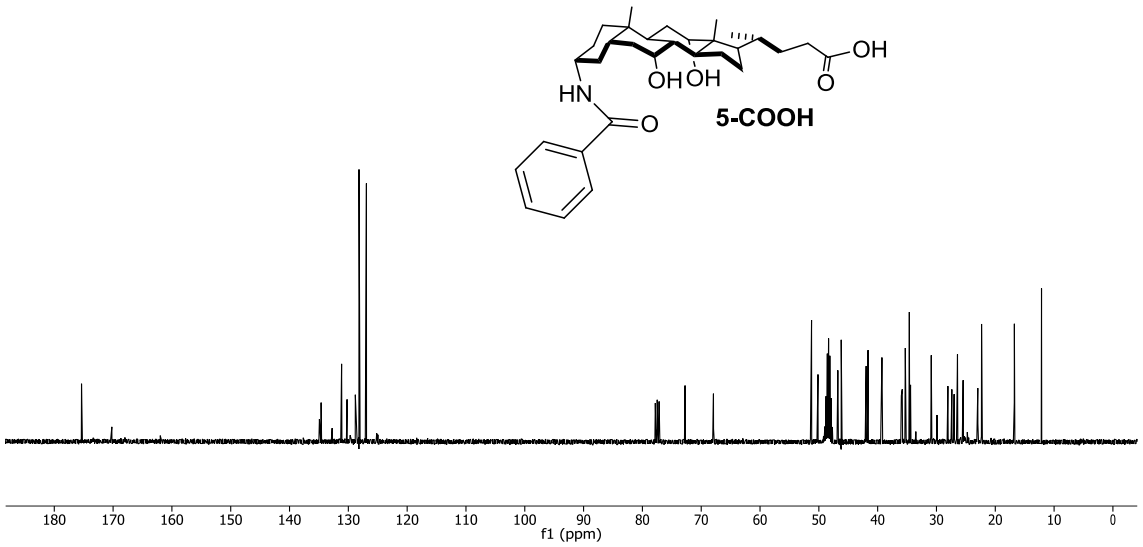

^{1}H NMR of compound **17**

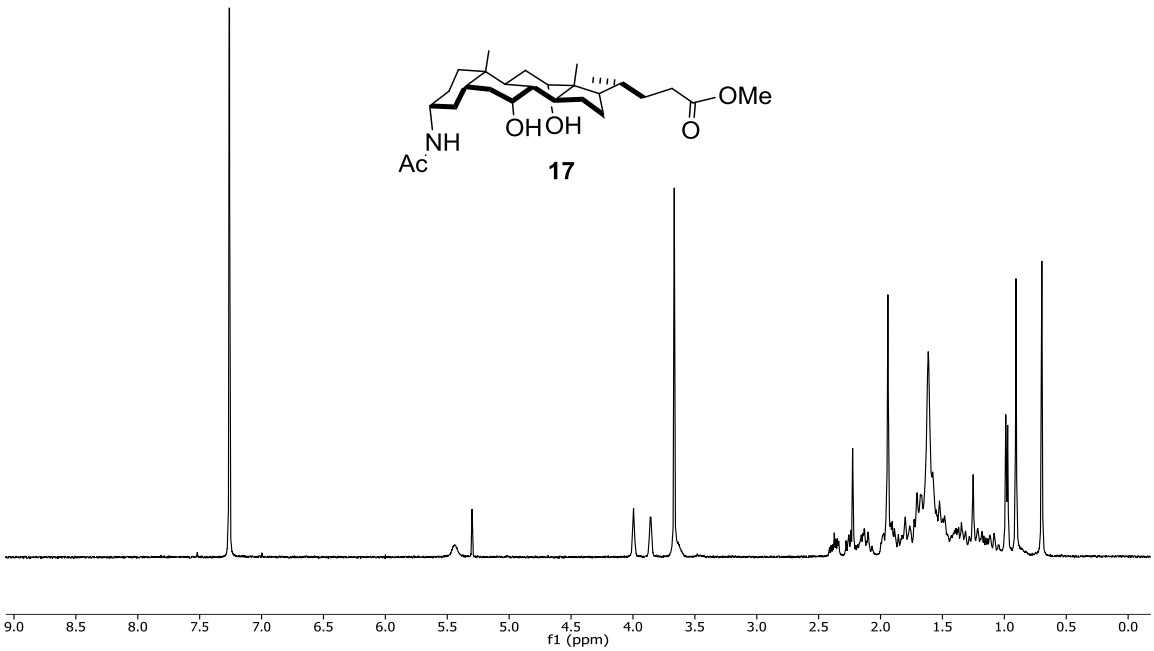

^{1}H NMR of compound **6-COOH**

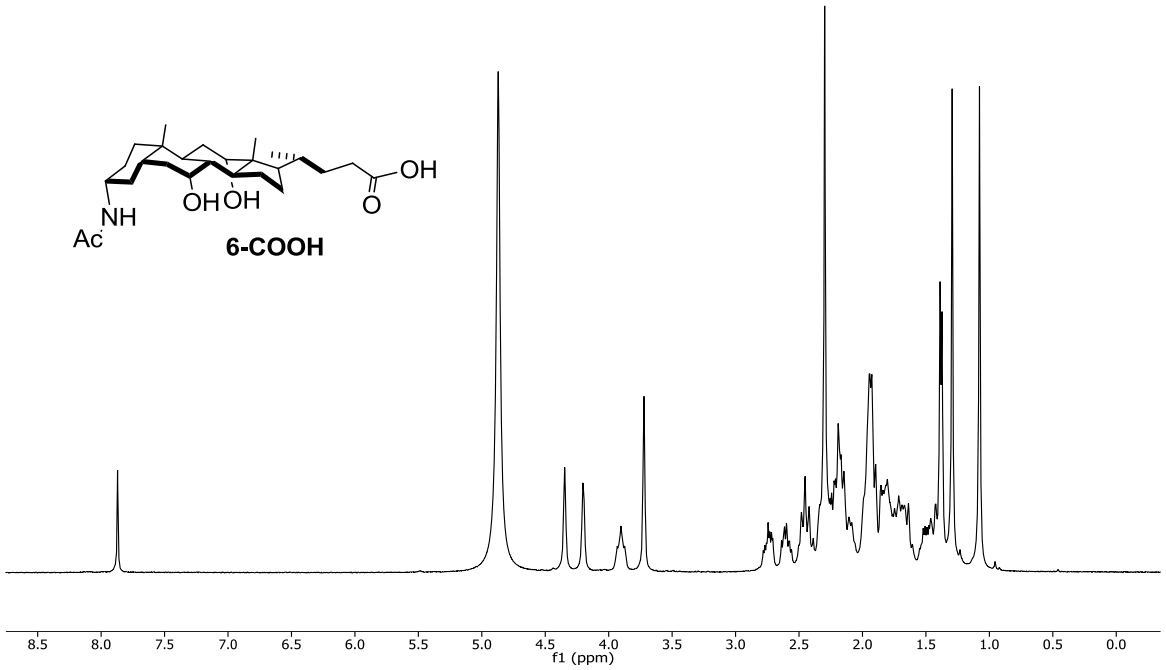

^{13}C NMR of compound **6-COOH**

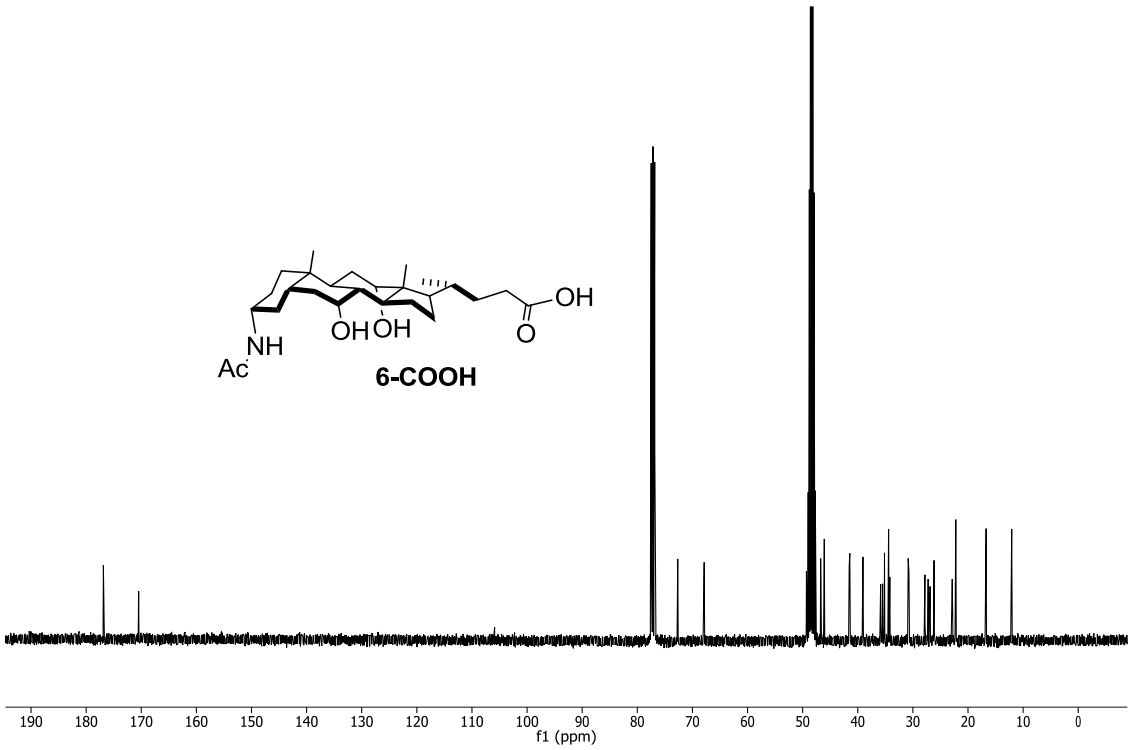

Notes and References

(1) Wulff, G. *Angew. Chem. Int. Ed. Engl.* **1995**, *34*, 1812-1832.

(2) Mosbach, K.; Ramström, O. *Nat. Biotechnol.* **1996**, *14*, 163-170.

(3) Haupt, K.; Mosbach, K. *Chem. Rev.* **2000**, *100*, 2495-2504.

(4) Sellergren, B. *Molecularly Imprinted Polymers: Man-Made Mimics of Antibodies and Their Applications in Analytical Chemistry*; Elsevier: Amsterdam, 2001.

(5) Wulff, G. *Chem. Rev.* **2001**, *102*, 1-28.

(6) Komiyama, M. *Molecular Imprinting: From Fundamentals to Applications*; Wiley-VCH: Weinheim, 2003.

(7) Zimmerman, S. C.; Wendland, M. S.; Rakow, N. A.; Zharov, I.; Suslick, K. S. *Nature* **2002**, *418*, 399-403.

(8) Zimmerman, S. C.; Zharov, I.; Wendland, M. S.; Rakow, N. A.; Suslick, K. S. *J. Am. Chem. Soc.* **2003**, *125*, 13504-13518.

(9) Dirion, B.; Cobb, Z.; Schillinger, E.; Andersson, L. I.; Sellergren, B. *J. Am. Chem. Soc.* **2003**, *125*, 15101-15109.

(10) Cutivet, A.; Schembri, C.; Kovensky, J.; Haupt, K. *J. Am. Chem. Soc.* **2009**, *131*, 14699-14702.

(11) Ma, Y.; Pan, G. Q.; Zhang, Y.; Guo, X. Z.; Zhang, H. Q. *Angew. Chem. Int. Ed.* **2013**, *52*, 1511-1514.

(12) Oshovsky, G. V.; Reinhoudt, D. N.; Verboom, W. *Angew. Chem. Int. Ed.* **2007**, *46*, 2366-2393.

(13) Hoshino, Y.; Kodama, T.; Okahata, Y.; Shea, K. J. *J. Am. Chem. Soc.* **2008**, *130*, 15242-15243.

(14) Yang, K. G.; Berg, M. M.; Zhao, C. S.; Ye, L. *Macromolecules* **2009**, *42*, 8739-8746.

(15) Zeng, Z. Y.; Patel, J.; Lee, S. H.; McCallum, M.; Tyagi, A.; Yan, M. D.; Shea, K. J. *J. Am. Chem. Soc.* **2012**, *134*, 2681-2690.

(16) Danielsson, H.; Sjövall, J. *Sterols and Bile Acids*; Elsevier: Amsterdam, 1985.

(17) Wallimann, P.; Marti, T.; Furer, A.; Diederich, F. *Chem. Rev.* **1997**, *97*, 1567-1608.

(18) Zhang, S.; Zhao, Y. *Macromolecules* **2010**, *43*, 4020-4022.

(19) Zhang, S.; Zhao, Y. *J. Am. Chem. Soc.* **2010**, *132*, 10642-10644.

(20) Li, X.; Zhao, Y. *Bioconjugate Chem.* **2012**, *23*, 1721-1725.

(21) Peng, H.-Q.; Chen, Y.-Z.; Zhao, Y.; Yang, Q.-Z.; Wu, L.-Z.; Tung, C.-H.; Zhang, L.-P.; Tong, Q.-X. *Angew. Chem. Int. Ed.* **2012**, *51*, 2088-2092.

(22) Li, Y. H.; Chan, L. M.; Tyer, L.; Moody, R. T.; Himel, C. M.; Hercules, D. M. *J. Am. Chem. Soc.* **1975**, *97*, 3118-3126.

(23) Zhong, Z.; Zhao, Y. *J. Org. Chem.* **2008**, *73*, 5498-5505.

(24) Zhao, Y. *J. Org. Chem.* **2009**, *74*, 834-843.

(25) Li, X.; Zhao, Y. *Langmuir* **2012**, *28*, 4152-4159.

(26) Zhang, S.; Zhao, Y. *Chem. Commun.* **2012**, *48*, 9998-10000.

(27) Chadha, G.; Zhao, Y. *J. Colloid Interface Sci.* **2013**, *390*, 151-157.

(28) Zhong, Z.; Zhao, Y. *Macromolecules* **2010**, *43*, 4020-4022.

(29) Ryu, E.-H.; Zhao, Y. *Org. Lett.* **2005**, *7*, 1035-1037.

(30) Seuring, J.; Reiss, P.; Koert, U.; Agarwal, S. *Chem. Phys. Lipids* **2010**, *163*, 367-372.

(31) Zhao, Y.; Zhong, Z. *J. Am. Chem. Soc.* **2005**, *127*, 17894-17901.

(32) Zhang, S.; Zhao, Y. *J. Am. Chem. Soc.* **2010**, *132*, 10642-10644.

CHAPTER 3

MOLECULARLY IMPRINTED NANOPARTICLES AS TAILOR-MADE SENSORS FOR SMALL FLUORESCENT MOLECULES

A paper published in *Chemical Communication*, **2014**, *50*, 5752-5755.

Joseph K. Awino and Yan Zhao

Abstract

Water-soluble nanoparticles molecularly imprinted against naphthyl derivatives could bind the templates with high affinity and excellent selectivity among structural analogues in aqueous solution. Fluorescent dansyl groups installed during template polymerization allowed these nanoparticles to detect the presence of the target analytes by Förster resonance energy transfer.

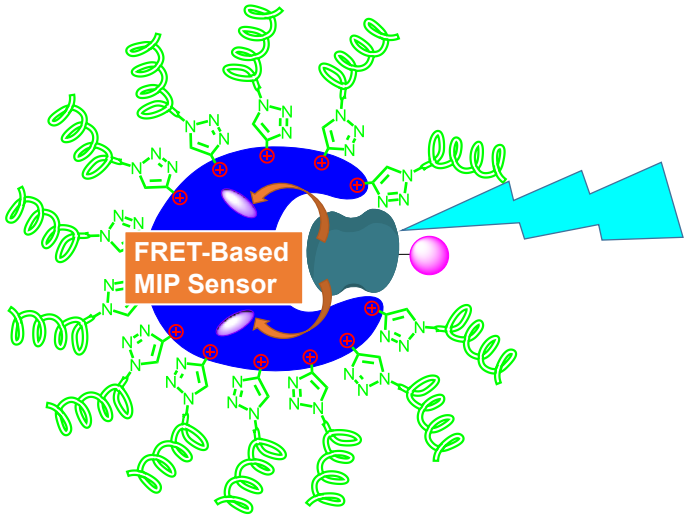

Scheme 1. General design

Introduction

Chemical sensors are important to a wide range of applications including clinical diagnostics, environmental remediation, drug analysis, and chemical detection. Sensors ideally should detect specific chemicals of interest with minimal interference from other chemicals present in the same sample. What is vital to the sensing specificity is typically a molecular-recognition unit in the sensor that binds the analyte with high affinity and selectivity.

Molecular imprinting is a technique to create guest-complementary binding sites, most often in a cross-linked polymer matrix.[1] It usually involves polymerization of a mixture of imprint molecules (i.e., the templates), functional monomers, and cross-linkers into a highly cross-linked material. Template-complementary binding sites are created upon the removal of the templates from the polymer matrix. Because molecularly imprinted polymers (MIPs) potentially can be prepared for any molecule that can form a suitable template–functional monomer complex, molecular imprinting is a powerful technique to prepare synthetic receptors.

A key benefit of MIP is its predetermined binding selectivity (for the template or its mimics). This feature is enormously useful to molecular sensing in which the molecules of interest are typically known.[1c] Indeed, when coupled with optical,[2] mass,[3] refractive index,[4] or other signal-transducing mechanisms, MIPs have been used as sensors for a variety of analytes.[5]

We recently reported a method to prepare molecularly imprinted nanoparticles (MINPs)[6] by surface–core-doubly cross-linking surfactant micelles in water.[7] The nanoparticles imprinted against a bile salt derivative were found to bind the template among

its structural analogues with excellent selectivity and affinity. Because of the radius of the MINP (ca. 1.5 nm for hydrophobic core and 2.5 nm including the surface ligands) is within the Förster distance (R_0) of many fluorophore pairs,[8] we reasoned that a MINP functionalized with an appropriate fluorophore should be able to detect analytes through Förster resonance energy transfer (FRET). As pointed out in a recent review, "ability to spectroscopically characterize binding sites" is a highly desirable feature for MIPs, especially if the materials can be made "either soluble or insoluble" and "readily processable".[9]

Results and Discussion

Design and Synthesis of MINPs

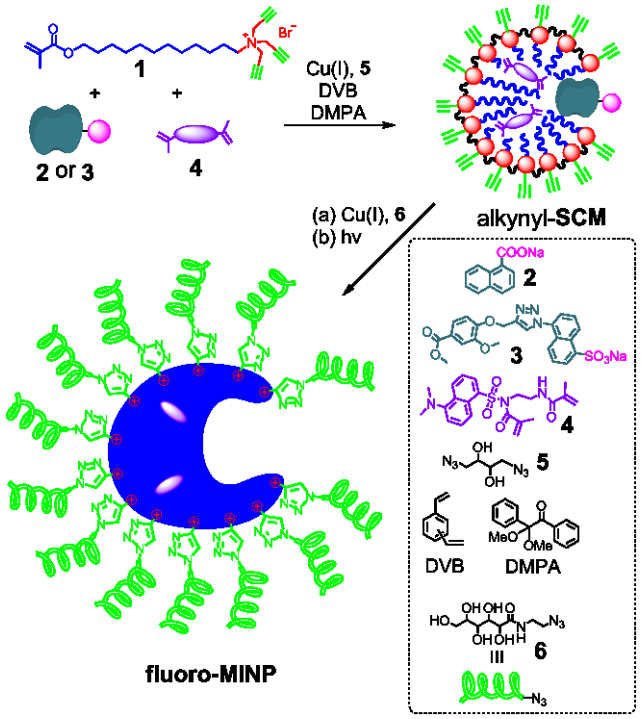

Scheme 2. Preparation of fluoro-MINP

To demonstrate the concept, we first prepared an aqueous solution of cross-linkable surfactant **1**, template **2** (or **3**), and fluorescent dansyl derivative **4** that has two polymerizable methacrylate groups (Scheme 2). Surfactant **1** has a critical micelle concentration (CMC) of 0.55 mM and aggregation number of 50 in water.[6] With [**1**] = 10 mM and [**1**]/[**2** or **3**] = 50/1, the resulting MINP was expected to contain on average one binding site per particle. To enable the resulting MINP to detect the template (the target analyte) by FRET, we chose to employ a naphthalene-containing template (**2** or **3**) that could serve as a FRET donor for the dansyl acceptor to be incorporated into the MINP through co-polymerization of **4**.

The details of the MINP synthesis and characterization are reported in the Experimental Section (Fig. 3–9, Experimental Section). As shown by Scheme 1, the micelles of **1** were first cross-linked via click chemistry on the surface by diazide **5** using Cu(I) catalysts. At this point, the organic additives including **4**, DVB (divinylbenzene), and DMPA (2,2-dimethoxy-2-phenylaceto-phenone, a photoinitiator) should simply be trapped within the SCM. Immediately after the surface-cross-linking, a sugar-derived azide (**6**) was added to the mixture to functionalize the surface of the alkynyl-SCM. The alkynyl-SCM had extra alkynes on the surface because the ratio of [**1**]/[**5**] was 1.2 in the reaction mixture while surfactant **1** had 3 alkynyl groups and cross-linker **5** only 2 azides. After surface-functionalization, UV irradiation triggered free radical polymerization of the methacrylate groups of **1** and **4**, as well as DVB solubilized within the SCM core. The micelles were able to solubilize one DVB per surfactant and this high level of DVB was found to enhance the rigidity of the core and the binding selectivity.[6] At the end of the core-cross-linking, the fluoro-MINPs were recovered by precipitation from acetone, followed by methanol washing (to remove the imprint molecules).

Molecular sensing

Fig. 1a,c shows normalized excitation spectra of fluoro-MINP(**2**) and fluoro-MINP(**3**) in the presence of different concentrations of **2** and **3** in Tris buffer (pH 7.4), when the dansyl emission at 500 nm was monitored. In the absence of binding, the donor fluorophore (**2** or **3**) would stay largely in solution, far from the dansyl acceptors imbedded within the fluoro-MINPs. Titration of the fluoro-MINP with **2** or **3** would not affect the excitation spectrum (of the dansyl) since all the emission would be caused by direct excitation of the dansyl in this scenario. In the event of a binding, the donor molecule bound by the MINP would absorb light, undergo excitation, and transfer the excited energy to the dansyl acceptor in the same nanoparticle. In the latter case, the donor would contribute to the acceptor emission and thus peaks corresponding to the donor absorption would appear in the excitation spectrum of the dansyl acceptor.

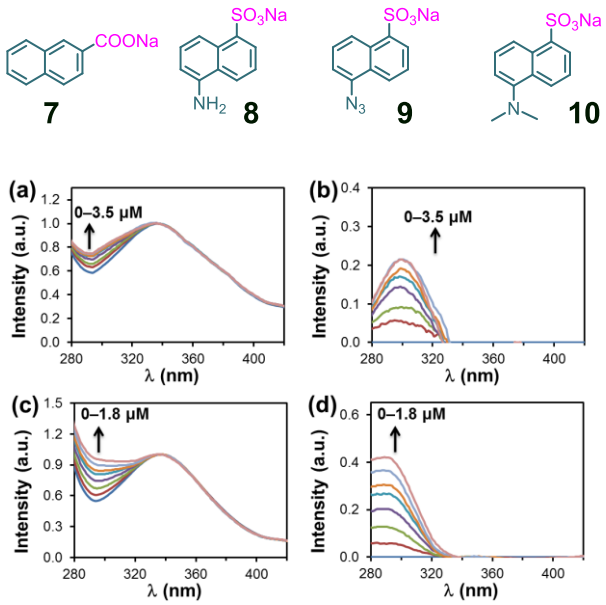

Figure 1. (a) Normalized excitation spectra of Fluoro-MINP(**2**) in the presence of different concentrations of **2** and (b) the excitation spectra with the contribution of Fluoro-MINP(**2**)

subtracted. (c) Normalized excitation spectra of Fluoro-MINP(**3**) in the presence of different concentrations of **3** and (d) the excitation spectra with the contribution of Fluoro-MINP(**3**) subtracted. The emission for the dansyl acceptor at 500 nm (λ_{em}) was monitored as the excitation wavelength (λ_{ex}) was scanned from 250 to 450 nm. [MINP] = 2.5 μM in 50 mM Tris buffer (pH = 7.4)

We chose to have a 2:1 ratio of dansyl derivative **4** to the template (**2** or **3**) so that each MINP had 2 dansyl groups on average and a good chance existed for the naphthyl template to be within the Förster distance (R_0 = 2.2 nm)[10] of the dansyl acceptor during rebinding. Indeed, the characteristic contribution from the donor absorption (@ 290–310 nm) appeared when the template molecule was added to the "correct" fluoro-MINP (Fig. 1a,c). When the contribution of the acceptor (i.e., the fluoro-MINP) was subtracted, a distinctive peak near 300–310 nm from the donor (**2** or **3**) appeared (Fig. 1b,d), indicative of increasing FRET with higher concentrations of the template added to the solution. When the "wrong" template was added, e.g., **3** to fluoro-MINP(**2**) or **2** to fluoro-MINP (**3**), as shown by Fig. 10 and 11, the FRET signal was either absent or much weaker. Similar observations were made when the MINPs were titrated with other structural analogues, including **7** that only differed from **2** by the position of the carboxylate (Fig. 12–19).

Isothermal Titration Calorimetry

The above results indicate that non-specific binding (from generic hydrophobic and electrostatic interactions) between the MINPs and the negatively charged template analogues could not trigger FRET, even those with very similar structures.[11] FRET was apparently a result of strong and specific binding, which was confirmed by isothermal titration

calorimetry (ITC) shown in Fig. 2a,b. With ITC, we could obtain the binding data even for those structural analogues that caused no change in the fluorescence excitation spectra. Additionally, the technique allowed us to determine the number of binding sites (*N*) on the MINP.

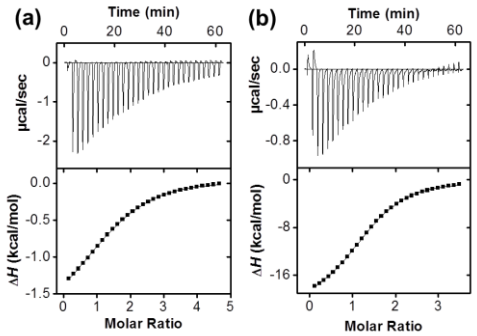

Figure 2. ITC titration curve obtained at 298 K for the bindings between (a) Fluoro-MINP(**2**) and **2** and (b) between Fluoro-MINP(**3**) and **3** in 50 mM Tris buffer (pH 7.4). Additional ITC curves (Fig. 20–21) are reported in the Experimental Section.

Table 1. Binding data for MINPs obtained by ITC[a]

Entry	MINP	Guest	K_a ($\times 10^6$ M^{-1})	$-\Delta G$ (kcal/mol)	*N*
1	MINP(**2**)	**2**	0.43 ± 0.01	7.7	1.1
2	MINP(**2**)	**3**	-[b]	-[b]	-[b]
3	MINP(**2**)	**7**	0.0023 ± 0.0004	4.6	0.8
4	MINP(**2**)	**8**	0.0015 ± 0.0001	4.3	1.1
5	MINP(**2**)	**9**	0.0033 ± 0.0003	4.8	1.0
6	MINP(**2**)	**10**	0.0011 ± 0.0001	4.1	0.8
7	MINP(**3**)	**2**	0.0070 ± 0.0002	5.2	1.2
8	MINP(**3**)	**3**	1.00 ± 0.04	8.2	1.2
9	MINP(**3**)	**7**	0.0015 ± 0.0002	4.3	1.0
10	MINP(**3**)	**8**	0.0095 ± 0.0002	5.4	0.7
11	MINP(**3**)	**9**	0.0082 ± 0.0010	5.3	1.1
12	MINP(**3**)	**10**	0.0095 ± 0.0003	5.4	0.5

[a] The titrations were generally performed in duplicates and the errors in K_a between the runs were generally < 20%. Binding was measured in 50 mM Tris buffer (pH = 7.4). [b] Binding was not detectable by ITC.

The ITC binding data in Table 1 shows that the MINPs were highly selective in their binding. For MINP(**2**), the template itself gave a binding constant of K_a = 0.43 × 10^6 M^{-1}, which translates to a binding free energy of $-\Delta G$ = 7.7 kcal/mol. The affinity was quite remarkable for a small molecule like **2** and should have resulted from the combination of hydrophobic interactions and electrostatic interactions between the oppositely charged MINP and the guest. None of the other anionic analogues, whether larger or smaller than **2**, showed any comparable binding; all the K_a values were at least two orders of magnitude lower that for the template itself (Table 1, entries 2–6).

Convinced of the highly selective binding, we examined the FRET signals in the presence of potentially interfering structural analogues. Because of the stronger FRET of MINP(**3**) with its template, we examined the FRET detection of **3** in the presence of various structural analogues as potential interfering species. When 2 μM of **3** was added to a solution of 0.50 μM MINP(**3**), FRET from the donor to the MINP acceptor was clearly visible in the excitation spectrum (Fig. 3a, compare the MINP spectra before and after the addition of compound **3**; the dotted spectrum in black was obtained by subtracting the MINP spectrum from that of the MINP plus **3**, showing λ_{max} = 310 nm from the donor).[14] Significantly, when 2–12 μM of compound **2** (Fig. 3a), **7** (Fig. 22), or **9** (Fig. 23) was added,[15] the excitation spectra showed essentially no change. Compound **8** did show some interference (Fig. 3b). Since **8** and **9** were bound by MINP(**3**) similarly, the interference from **8** should derive from its spectroscopic instead of binding properties. We also examined the interference of two additional analogues of **3**, with the methyl ester hydrolyzed (in **11**) and replaced with a longer, hexyl group (in **12**), respectively. As shown by Fig. 24 and 25, these analogues did not affect the FRET signal at all, despite their similarity to **3**.

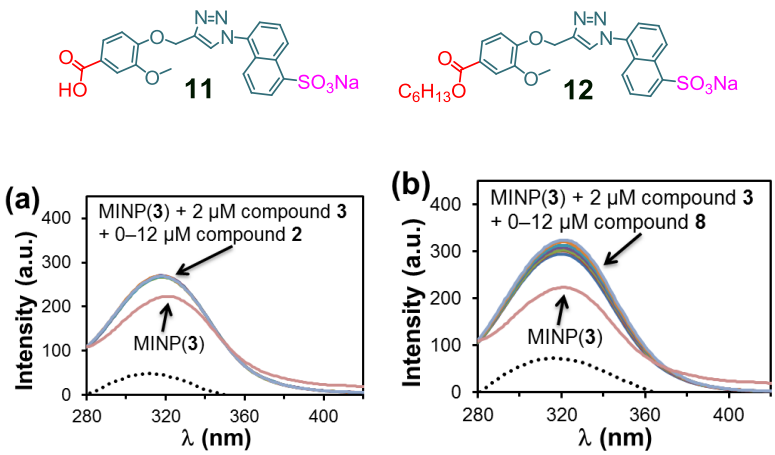

Figure 3. (a) Excitation spectra of MINP(**3**) with 2 μM of compound **3**, titrated with 0–12 μM of compound **2**. (b) Excitation spectra of MINP(**3**) with 2 μM of compound **3**, titrated with 0–12 μM of compound **8**. The dotted spectrum in black was obtained by subtracting the MINP spectrum from that of the MINP plus compound **3**. The emission for the dansyl acceptor at 520 nm (λ_{em}) was monitored as the excitation wavelength (λ_{ex}) was scanned from 250 to 450 nm. [MINP] =0.50 μM in 50 mM Tris buffer (pH = 7.4).

Conclusion

In summary, we have demonstrated that fluorescently-labelled MINPs can be generated against hydrophobic guests for highly specific binding among their structural analogues. The combination of predetermined binding properties from molecular imprinting and easy-to-perform FRET-based detection make these MINPs potentially very useful as sensors for small fluorescent molecules in water. Since the fluorophore was introduced independently from the molecular recognition-aspect of the imprinting, the FRET-detection and molecular imprinting in principle are orthogonal to each other.

Acknowledgement

We thank NSF for supporting the research.

Experimental Section

General Method

Methanol, methylene chloride, and ethyl acetate were of HPLC grade and were purchased from Fisher Scientific. All other reagents and solvents were of ACS-certified grade or higher, and were used as received from commercial suppliers. Routine ^{1}H and ^{13}C NMR spectra were recorded on a Bruker DRX-400 or on a Varian VXR-400 spectrometer. ESI-MS mass was recorded on Shimadzu LCMS-2010 mass spectrometer. Dynamic light scattering (DLS) was performed on a PD2000DLS+ dynamic light scattering detector. Fluorescence spectra were recorded at ambient temperature on a Varian Cary Eclipse Fluorescence spectrophotometer. Isothermal titration calorimetry (ITC) was performed using a MicroCal VP-ITC Microcalorimeter with Origin 7 software and VPViewer2000 (GE Healthcare, Northampton, MA).

Syntheses

Compounds **1**,[16] **5**,[17] **6**,[18] **9**,[19] **10**,[20] **13**,[21] and **14**[22] were previously reported.

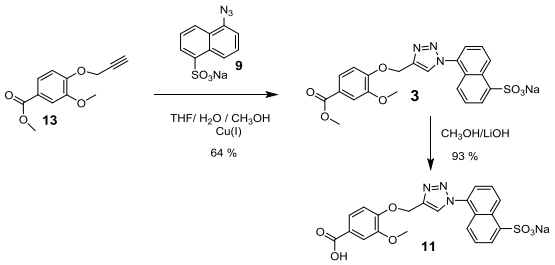

Scheme 3. Synthesis of compound **11**

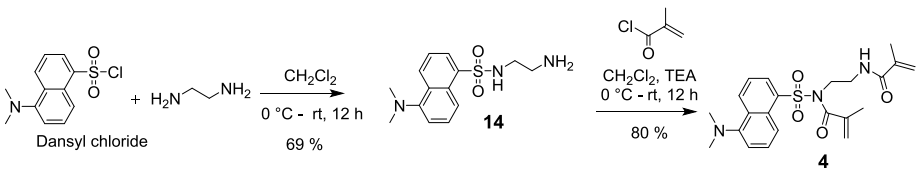

Scheme 4. Synthesis of compound **4**

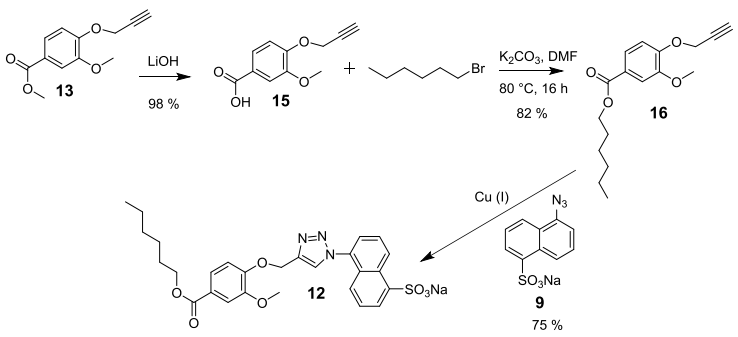

Scheme 5. Synthesis of compound **12**

Compound 3. To a solution of **9** (0.18 g, 0.66 mmol), copper sulfate hydrate (0.13 g, 0.66 mmol), and sodium ascorbate (0.33 g, 1.32 mmol) in a 2:1:1 THF/H_2O/CH_3OH mixture (20 mL), **13** (0.18 g, 0.80 mmol) in THF (1 mL) was added dropwise. After being stirred at 40 °C for 12 h, the reaction mixture was concentrated. The residue was diluted with THF (10 mL). The solid was filtered off and the filtrate was concentrated in vacuo. The residue was then purified by column chromatography over silica gel using 1:3 methanol/methylene chloride as the eluent to give an off-white powder (0.25 g, 64%). ^{1}H NMR (400 MHz, CD_3OD, δ): 9.16 (d, *J* = 8.4 Hz, 1H), 8.51 (s, 1H), 8.51 (d, *J* = 8.0 Hz, 1H), 8.28(d, *J* = 6.8 Hz, 1H), 7.80 - 7.51 (m, 4H), 7.29 (d, *J* = 8.4 Hz, 1H), 7.13(d, *J* = 8.4 Hz, 1H), 5.45(s, 2H), 3.90 (s, 6H). ^{13}C NMR (100 MHz, $CDCl_3$/CD_3OD = 1:1, δ): 167.7, 152.2, 149.7, 133.9, 130.4, 129.9, 129.8, 127.4, 127.3, 126.8, 126.2, 125.5, 124.5, 123.9, 123.9, 123.8, 113.5, 112.9, 62.8, 56.1, 52.3. ESI-HRMS (*m/z*): $[M-Na]^-$ calcd for $C_{22}H_{18}N_3O_7S$, 468.0860; found, 468.0865.

Compound 4. The compound was synthesized according to a modified literature procedure.[23] Compound **14** (110.0 mg, 0.38 mmol) and triethylamine (TEA, 56.7 mg, 0.56 mmol) were dissolved in dichloromethane (20 mL) and cooled on an ice bath. Methacryloyl chloride (58.8 mg, 0.56 mmol) in dichloromethane (5 mL) was added dropwise to the stirred solution. The ice bath was removed and the reaction mixture was stirred at room temperature for 3 h. The solution was carefully acidified with 1M hydrochloric acid to pH 4 and washed with water (3 × 20 mL). The organic solvent was dried over Na_2SO_4 and concentrated in vacuo. The residue was purified by column chromatography over silica gel using 1:20 methanol/methylene chloride as the eluent to give a yellow powder (102 mg, 63%). ^{1}H NMR (400 MHz, DMSO-d_6, δ): 8.56 (d, J = 8.4 Hz, 1H), 8.27 (d, J = 7.2 Hz, 1H), 8.16 (d, J = 7.2 Hz, 1H), 7.81 (d, J = 7.2 Hz, 1H), 7.70 –7.67 (m, 2H) , 7.28 (d, J = 5.6 Hz, 1H), 5.76 (s, 1H), 5.35 (d, J = 9.2 Hz, 2H), 5.19 (s, 1H), 4.03 (t, J = 6.4 Hz, 2H), 3.40 (t, J = 6.4 Hz, 2H), 2.83 (s, 6H), 1.86 (s, 3H), 1.63 (s, 3H). ^{13}C NMR (100 MHz, $CDCl_3$, δ): 172.3, 168.5, 139.5, 139.3, 132.8, 132.8, 131.9, 129.7, 129.5, 128.8, 123.1, 121.1, 120.5, 120.5, 117.8, 115.4, 46.2, 45.4, 39.5, 29.7, 19.1, 18.5. ESI-HRMS (*m/z*): $[M + H]^+$ calcd for $C_{22}H_{28}N_3O_4S$, 430.1795; found, 430.1803.

Compound 16. To compound **15** (0.20 g, 0.97 mmol) in anhydrous DMF (30 mL), potassium carbonate (0.34 g, 2.43 mmol) and 1-bromohexane (0.24 mg, 1.46 mmol) were added. After being stirred at 80 ˚C for 16 h, the reaction mixture was cooled to room temperature and the solid was removed by vacuum filtration. The DMF solution was combined with water (50 mL) and the resulting solution was extracted with ethyl acetate (3 × 15 mL). The combined organic layers were dried over sodium sulfate and concentrated in vacuo. The residue was purified by column chromatography over silica gel using 1:6 ethyl

acetate/hexane as the eluent to afford a colorless oil (0.23 g, 82%). ^{1}H NMR (400 MHz, $CDCl_3$), δ: 7.68 (m, 1H), 7.56 (s, 1H), 7.05 (d, *J* = 8.4 Hz, 1H), 4.82 (s, 2H), 4.30 (t, *J* = 6.8 Hz, 2H), 3.90 (s, 3H), 2.53 (s, 1H), 1.77 (m, 2H), 1.34–1.31 (m, 6H), 0.91 (t, *J* = 6.8 Hz, 3H). ^{13}C NMR (100 MHz, $CDCl_3$, δ): 166.3, 150.5, 149.1, 124.2, 123.0, 123.0, 112.5, 77.8, 76.3, 65.1, 56.5, 56.0, 31.5, 28.7, 25.7, 22.5, 14.0. ESI-HRMS (*m/z*): $[M + H]^+$ calcd for $C_{17}H_{23}O_4$, 291.1596; found, 291.1598.

Compound 12. To a solution of **9** (90 mg, 0.33 mmol), copper sulfate hydrate (66 mg, 0.33 mmol), and sodium ascorbate (165 mg, 0.66 mmol) in a 2:1:1 THF/H_2O/CH_3OH mixture (20 mL), **16** (116 mg, 0.4 mmol) in THF (1 mL) was added dropwise. After being stirred at 40 °C for 24 h, the reaction mixture was concentrated. The residue was diluted with THF (10 mL). The solid was filtered off and the filtrate was concentrated in vacuo. The residue was then purified by column chromatography over silica gel using 1:3 methanol/methylene chloride as the eluent to give an off-white powder (146 mg, 75%). ^{1}H NMR (400 MHz, CD_3OD /DMSO-d_6), δ: 8.04 (s, 1H), 7.65 (m, 2H), 7.63 (m, 2H), 7.13 (d, *J* = 8.4 Hz, 2H), 6.92 (s, 1H), 6.85 (t, *J* = 8.4 Hz, 1H), 6.60 (s, 1H), 4.83 (s, 2H), 4.30 (t, *J* = 8.4 Hz, 1H), 3.90 (s, 3H), 1.77 (m, 2H), 1.34–1.31 (m, 6H), 0.91 (t, *J* = 6.8 Hz, 3H). ^{13}C NMR (100 MHz, $CDCl_3$, δ): 166.3, 150.5, 149.9, 149.1, 146.1, 124.2, 124.0, 123.0, 123.0, 123.0, 123.0, 114.0, 112.5, 112.5, 112.5, 112.4, 112.4, 112.4, 111.7, 65.1, 56.5, 56.0, 31.5, 28.7, 25.7, 22.5, 14.0. ESI-HRMS (*m/z*): $[M-Na]^-$ calcd for $C_{27}H_{28}N_3O_7S$, 538.1653; found, 538.1648.

MINP(2). To a micellar solution of **1** (9.3 mg, 0.02 mmol) in D_2O (2.0 mL), divinylbenzene (DVB, 2.8 μL, 0.02 mmol), **2** in D_2O (10 μL of 7.8 mg/mL, 0.0004 mmol), **4** in dimethyl sulfoxide (DMSO, 10 μL 34.4 mg/mL, 0.0008 mmol), and 2,2-dimethoxy-2-phenylacetophenone (DMPA,10 μL of a 12.8 mg/mL solution in DMSO, 0.0005 mmol) were

added. The mixture was subjected to ultrasonication for 10 min before compound **5** (4.1 mg, 0.024 mmol), $CuCl_2$ (10 μL of a 6.7 mg/mL solution in D_2O, 0.0005 mmol), and sodium ascorbate (10 μL of a 99 mg/mL solution in D_2O, 0.005 mmol) were added. After the reaction mixture was stirred slowly at room temperature for 12 h, compound **6** (10.6 mg, 0.04 mmol), $CuCl_2$ (10 μL of a 6.7 mg/mL solution in D_2O, 0.0005 mmol), and sodium ascorbate (10 μL of a 99 mg/mL solution in D_2O, 0.005 mmol) were added. After being stirred for another 6 h at room temperature, the reaction mixture was transferred to a glass vial, purged with nitrogen for 15 min, sealed with a rubber stopper, and irradiated in a Rayonet reactor for 12 h. ^1H NMR spectroscopy was used to monitor the progress of reaction. The reaction mixture was poured into acetone (8 mL). The precipitate was collected by centrifugation and washed with a mixture of acetone/water (5 mL/1 mL) three times. The crude produce was washed by methanol/acetic acid (5 mL/0.1 mL) three times until no fluorescence could be observed in the residual wash, and then with excess acetone. The off white powder was dried in air to afford the final MINPs (17 mg, 85%).

MINP(3). To a micellar solution of **1** (9.3 mg, 0.02 mmol) in D_2O (2.0 mL), divinylbenzene (DVB, 2.8 μL, 0.02 mmol), **3** in D_2O (10 μL of 18 mg/mL in D_2O, 0.0004 mmol), **4** in dimethyl sulfoxide (DMSO, 10 μL 34.4 mg/mL, 0.0008 mmol), and 2,2-dimethoxy-2-phenylacetophenone (DMPA,10 μL of a 12.8 mg/mL solution in DMSO, 0.0005 mmol) were added. The mixture was subjected to ultrasonication for 10 min before compound **5** (4.1 mg, 0.024 mmol), $CuCl_2$ (10 μL of a 6.7 mg/mL solution in D_2O, 0.0005 mmol), and sodium ascorbate (10 μL of a 99 mg/mL solution in D_2O, 0.005 mmol) were added. After the reaction mixture was stirred slowly at room temperature for 12 h, compound **6** (10.6 mg, 0.04 mmol), $CuCl_2$ (10 μL of a 6.7 mg/mL solution in D_2O, 0.0005 mmol), and sodium ascorbate

(10 μL of a 99 mg/mL solution in D_2O, 0.005 mmol) were added. After being stirred for another 6 h at room temperature, the reaction mixture was transferred to a glass vial, purged with nitrogen for 15 min, sealed with a rubber stopper, and irradiated in a Rayonet reactor for 12 h. ^1H NMR spectroscopy was used to monitor the progress of reaction. The reaction mixture was poured into acetone (8 mL). The precipitate was collected by centrifugation and washed with a mixture of acetone/water (5 mL/1 mL) three times. The crude produce was washed by methanol/acetic acid (5 mL/0.1 mL) three times until no fluorescence could be observed in the residual wash, and then with excess acetone. The off white powder was dried in air to afford the final MINPs (17 mg, 85%).

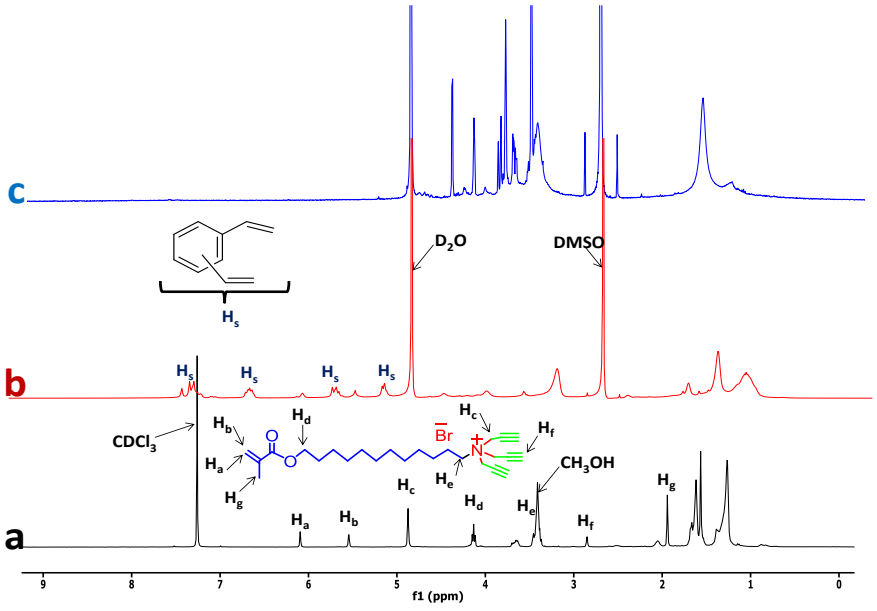

Figure 4. ^1H NMR spectra of **1** in $CDCl_3$ (black), alkynyl-SCM in D_2O (red), and fluoro-MINP(**2**) (blue) in D_2O

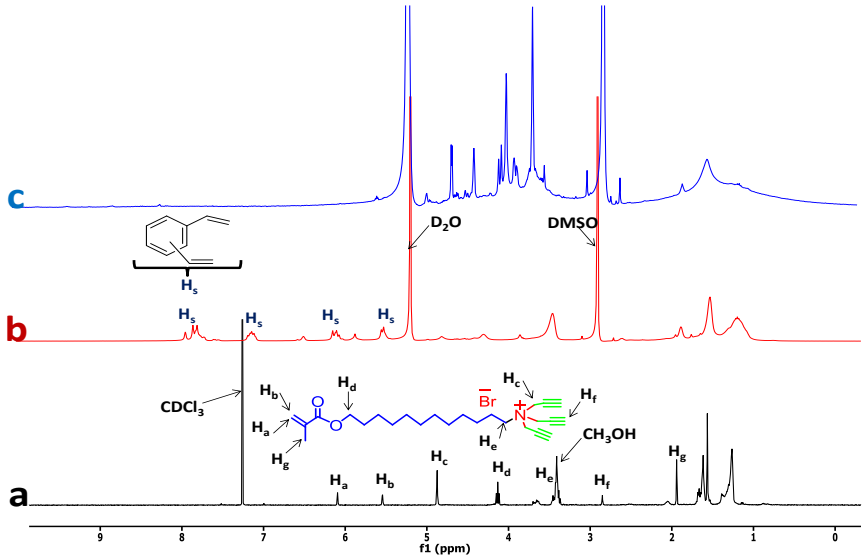

Figure 5. ^{1}H NMR spectra of **1** in $CDCl_3$ (black), alkynyl-SCM in D_2O (red), and fluoro-MINP(**3**) (blue) in D_2O

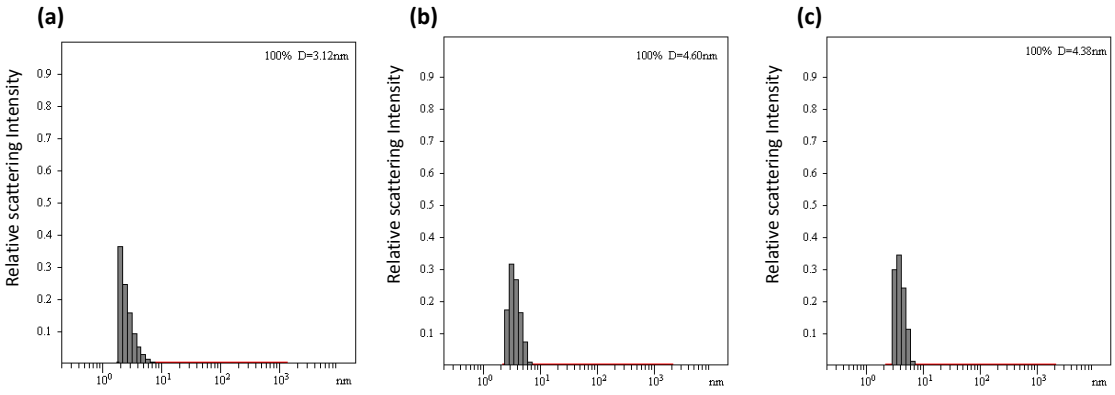

Figure 6. Distribution of the hydrodynamic diameters of the nanoparticles in water as determined by DLS for (a) alkynyl-SCM, (b) surface-functionalized SCM and (c) MINP(**2**) after purification.

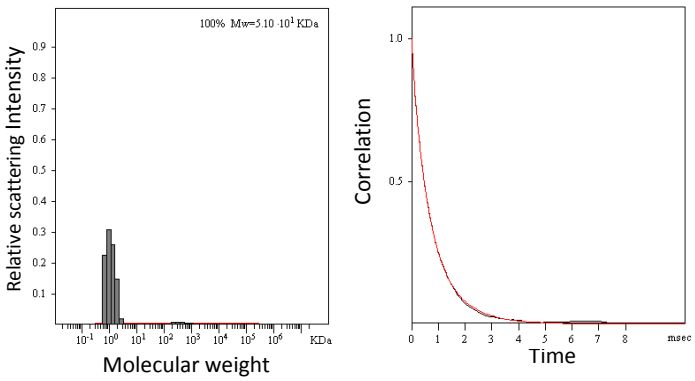

Figure 7. Distribution of the molecular weights of fluoro-MINP(**2**) and the correlation curves for DLS. The PRECISION DECONVOLVE program assumes the intensity of scattering is proportional to the mass of the particle squared. If each unit of building block for the fluoro-MINP(**2**) is assumed to contain one molecule of compound **1** (MW = 465 g/mol), 0.04 molecules of compound **4** (MW = 430 g/mol), 1.2 molecules of compound **5** (MW = 172 g/mol), one molecule of DVB (MW = 130 g/mol), and 0.8 molecules of compound **6** (MW = 264 g/mol), the molecular weight of fluoro-MINP(**3**) translates to 50 [= 51000/(465+0.04×430+1.2×172+130+0.8×264)] of such units.

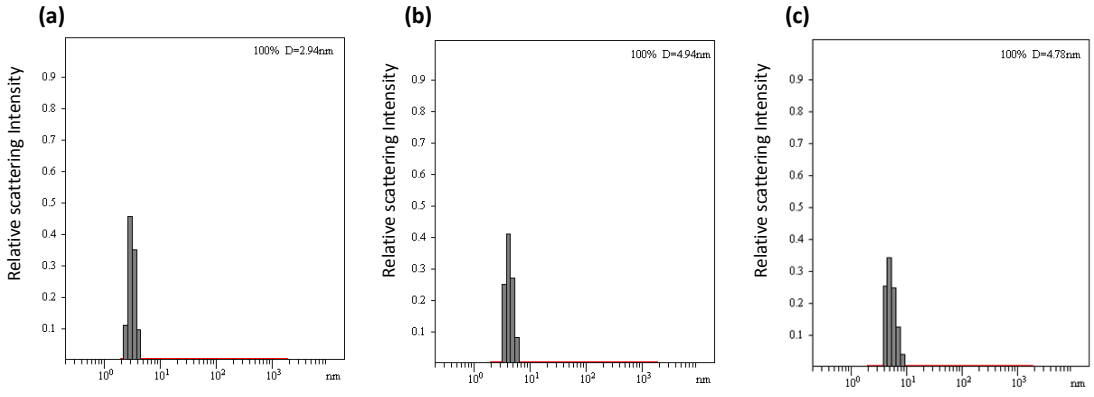

Figure 8. Distribution of the hydrodynamic diameters of the nanoparticles in water as determined by DLS for (a) alkynyl-SCM, (b) surface-functionalized SCM and (c) MINP(**3**) after purification.

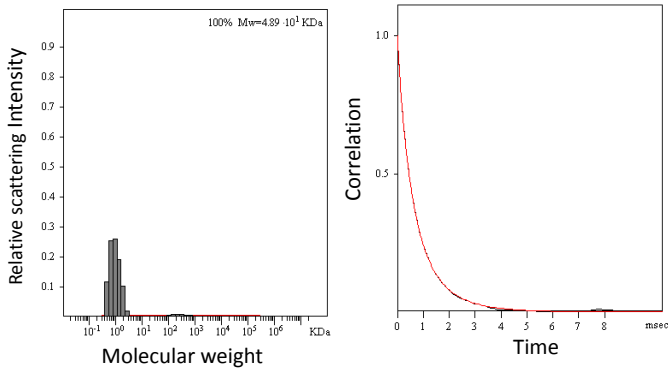

Figure 9. Distribution of the molecular weights of fluoro-MINP(**3**) and the correlation curves for DLS. The PRECISION DECONVOLVE program assumes the intensity of scattering is proportional to the mass of the particle squared. If each unit of building block for the fluoro-MINP(**3**) is assumed to contain one molecule of compound **1** (MW = 465 g/mol), 0.04 molecules of compound **4** (MW = 430 g/mol), 1.2 molecules of compound **5** (MW = 172 g/mol), one molecule of DVB (MW = 130 g/mol), and 0.8 molecules of compound **6** (MW = 264 g/mol), the molecular weight of fluoro-MINP(**3**) translates to 47 [= 48900/(465+0.04×430+1.2×172+130+0.8×264)] of such units.

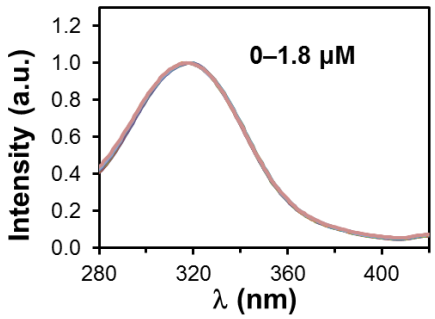

Figure 10. Normalized excitation spectra of Fluoro-MINP(**2**) in the presence of different concentrations of **3**. The emission for the dansyl acceptor at 500 nm (λ_{em}) was monitored as the excitation wavelength (λ_{ex}) was scanned from 250 to 450 nm was scanned. [MINP] = 0.25 μM in 50 mM Tris buffer (pH 7.4).

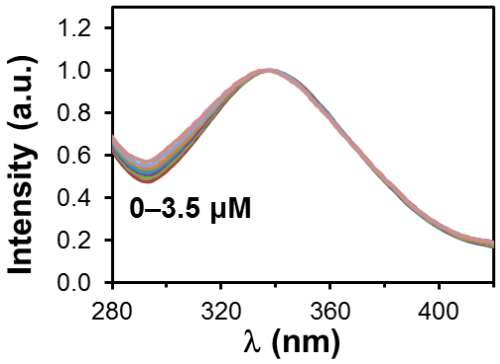

Figure 11. Normalized excitation spectra of Fluoro-MINP(**3**) in the presence of different concentrations of **2**. The emission for the dansyl acceptor at 500 nm (λ_{em}) was monitored as the excitation wavelength (λ_{ex}) was scanned from 250 to 450 nm was scanned. [MINP] = 0.25 μM in 50 mM Tris buffer (pH 7.4). *Weak FRET was observed.*

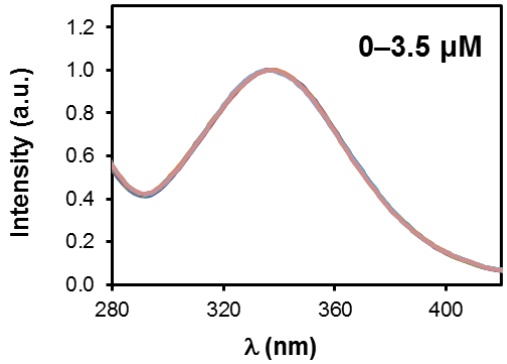

Figure 12. Normalized excitation spectra of Fluoro-MINP(**2**) in the presence of different concentrations of **7**. The emission for the dansyl acceptor at 500 nm (λ_{em}) was monitored as the excitation wavelength (λ_{ex}) was scanned from 250 to 450 nm was scanned. [MINP] = 0.25 μM in 50 mM Tris buffer (pH 7.4).

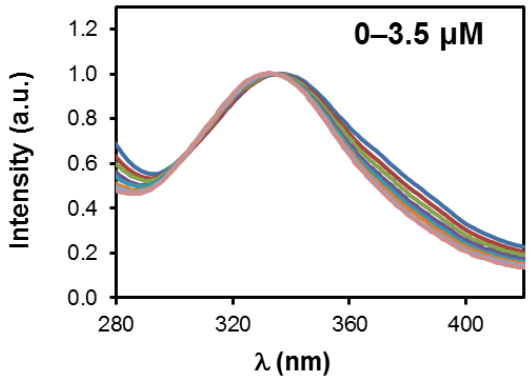

Figure 13. Normalized excitation spectra of Fluoro-MINP(**2**) in the presence of different concentrations of **8**. The emission for the dansyl acceptor at 500 nm (λ_{em}) was monitored as the excitation wavelength (λ_{ex}) was scanned from 250 to 450 nm was scanned. [MINP] = 0.25 μM in 50 mM Tris buffer (pH 7.4). *The emission had a gradual shift to the red upon titration with **8**. The intensity near 300–310 nm decreased rather than increased as in the case of FRET.*

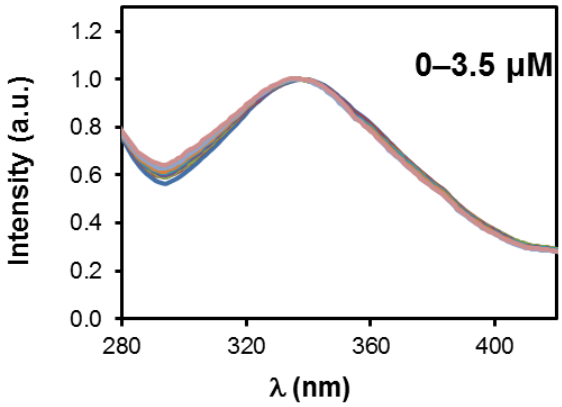

Figure 14. Normalized excitation spectra of Fluoro-MINP(**2**) in the presence of different concentrations of **9**. The emission for the dansyl acceptor at 500 nm (λ_{em}) was monitored as the excitation wavelength (λ_{ex}) was scanned from 250 to 450 nm was scanned. [MINP] = 0.25 μM in 50 mM Tris buffer (pH 7.4). *Weak FRET was observed.*

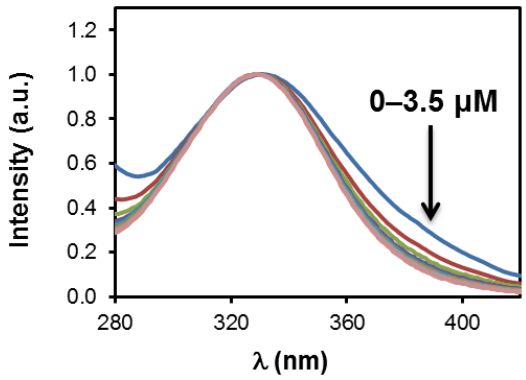

Figure 15. Normalized excitation spectra of Fluoro-MINP(**2**) in the presence of different concentrations of **10**. The emission for the dansyl acceptor at 500 nm (λ_{em}) was monitored as the excitation wavelength (λ_{ex}) was scanned from 250 to 450 nm was scanned. [MINP] = 0.25 μM in 50 mM Tris buffer (pH 7.4). *Compound **10** had the same dansyl as the acceptors on the MINP and thus the excitation spectrum toward higher concentration of **10** mainly was from compound **10** itself.*

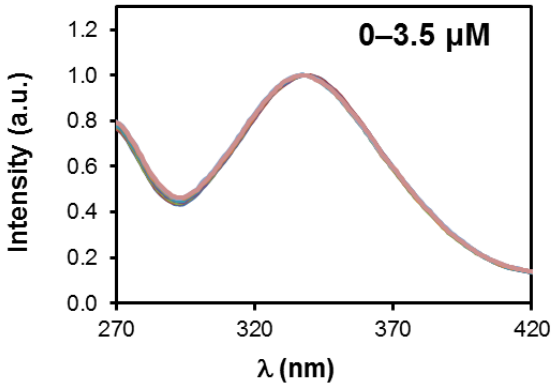

Figure 16. Normalized excitation spectra of Fluoro-MINP(**3**) in the presence of different concentrations of **7**. The emission for the dansyl acceptor at 500 nm (λ_{em}) was monitored as the excitation wavelength (λ_{ex}) was scanned from 250 to 450 nm was scanned. [MINP] = 0.25 μM in 50 mM Tris buffer (pH 7.4).

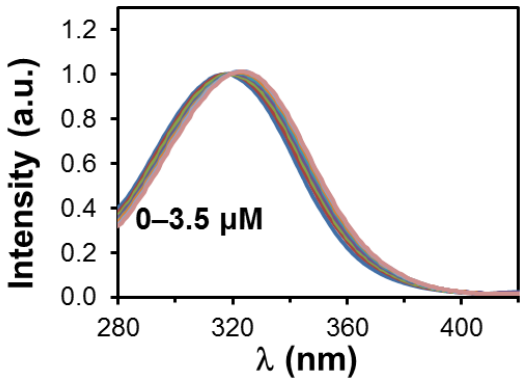

Figure 17. Normalized excitation spectra of Fluoro-MINP(**3**) in the presence of different concentrations of **8**. The emission for the dansyl acceptor at 500 nm (λ_{em}) was monitored as the excitation wavelength (λ_{ex}) was scanned from 250 to 450 nm was scanned. [MINP] = 0.25 μM in 50 mM Tris buffer (pH 7.4).

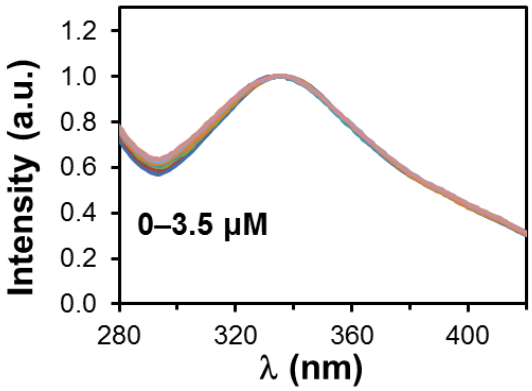

Figure 18. Normalized excitation spectra of Fluoro-MINP(**3**) in the presence of different concentrations of **9**. The emission for the dansyl acceptor at 500 nm (λ_{em}) was monitored as the excitation wavelength (λ_{ex}) was scanned from 250 to 450 nm was scanned. [MINP] = 0.25 μM in 50 mM Tris buffer (pH 7.4). *Very weak FRET was observed.*

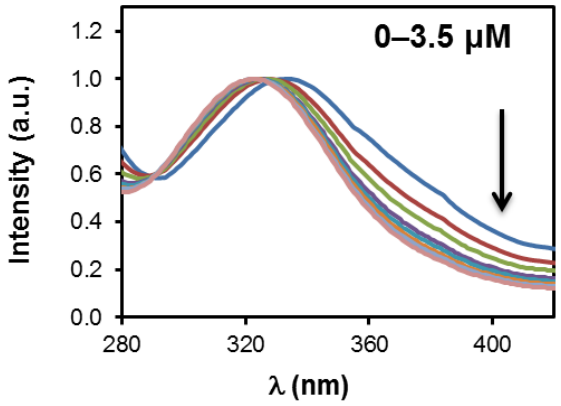

Figure 19. Normalized excitation spectra of Fluoro-MINP(**3**) in the presence of different concentrations of **10**. The emission for the dansyl acceptor at 500 nm (λ_{em}) was monitored as the excitation wavelength (λ_{ex}) was scanned from 250 to 450 nm was scanned. [MINP] = 0.25 μM in 50 mM Tris buffer (pH 7.4). *The emission had a gradual shift to the blue upon titration with **10**. Compound **10** had the same dansyl as the acceptors on the MINP and thus the excitation spectrum toward higher concentration of **10** mainly was from compound **10** itself.*

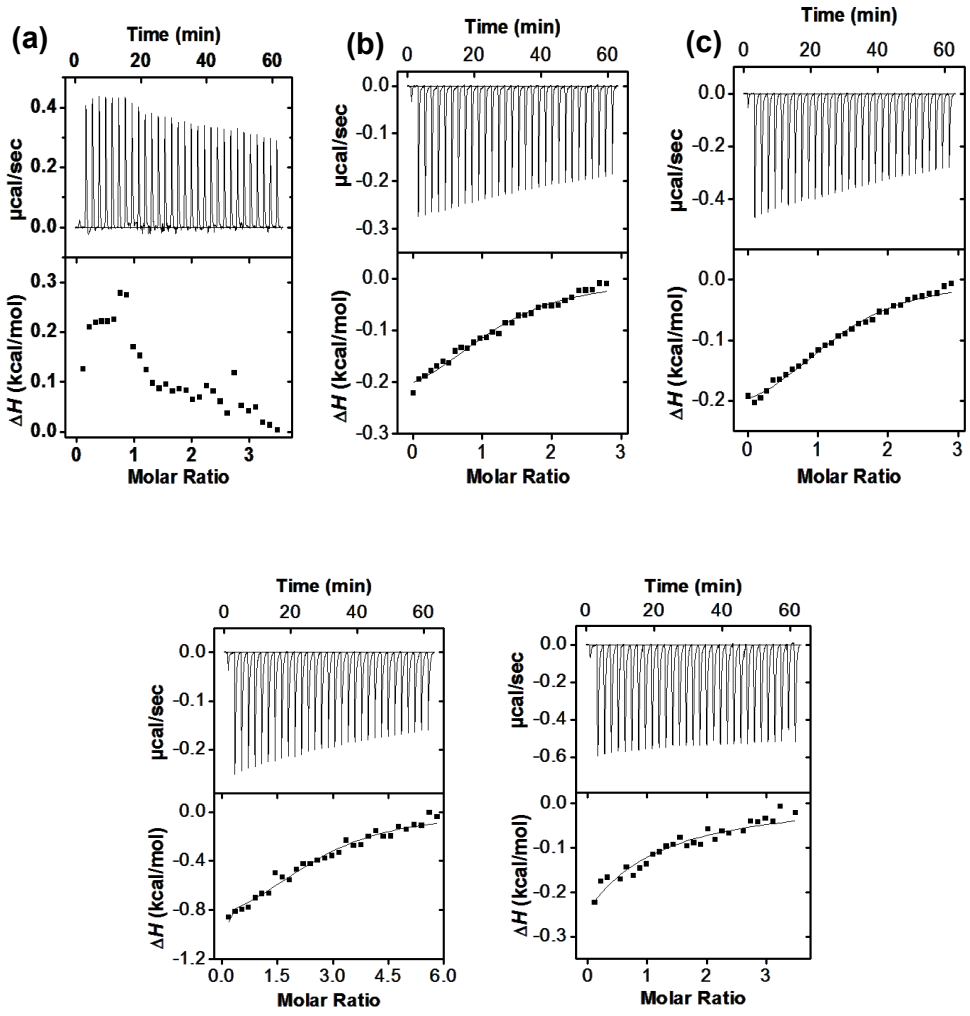

Figure 20. ITC titration curves obtained at 298 K for the titration of fluoro-MINP(**2**) with **3** (a), **7** (b), **8** (c), **9** (d), and **10** (e) in 50 mM Tris buffer (pH 7.4). The data correspond to entries 2–6, respectively, in Table 1. The top panel shows the raw calorimetric data. The area under each peak represents the amount of heat generated at each ejection and is plotted against the molar ratio of MINP to the substrate. The solid line is the best fit of the experimental data to the sequential binding of N equal and independent binding sites on the MINP. The heat of dilution for the substrate, obtained by adding the substrate to the buffer, was subtracted from the heat released during the binding. Binding parameters were auto-generated after curve fitting using Microcal Origin 7.

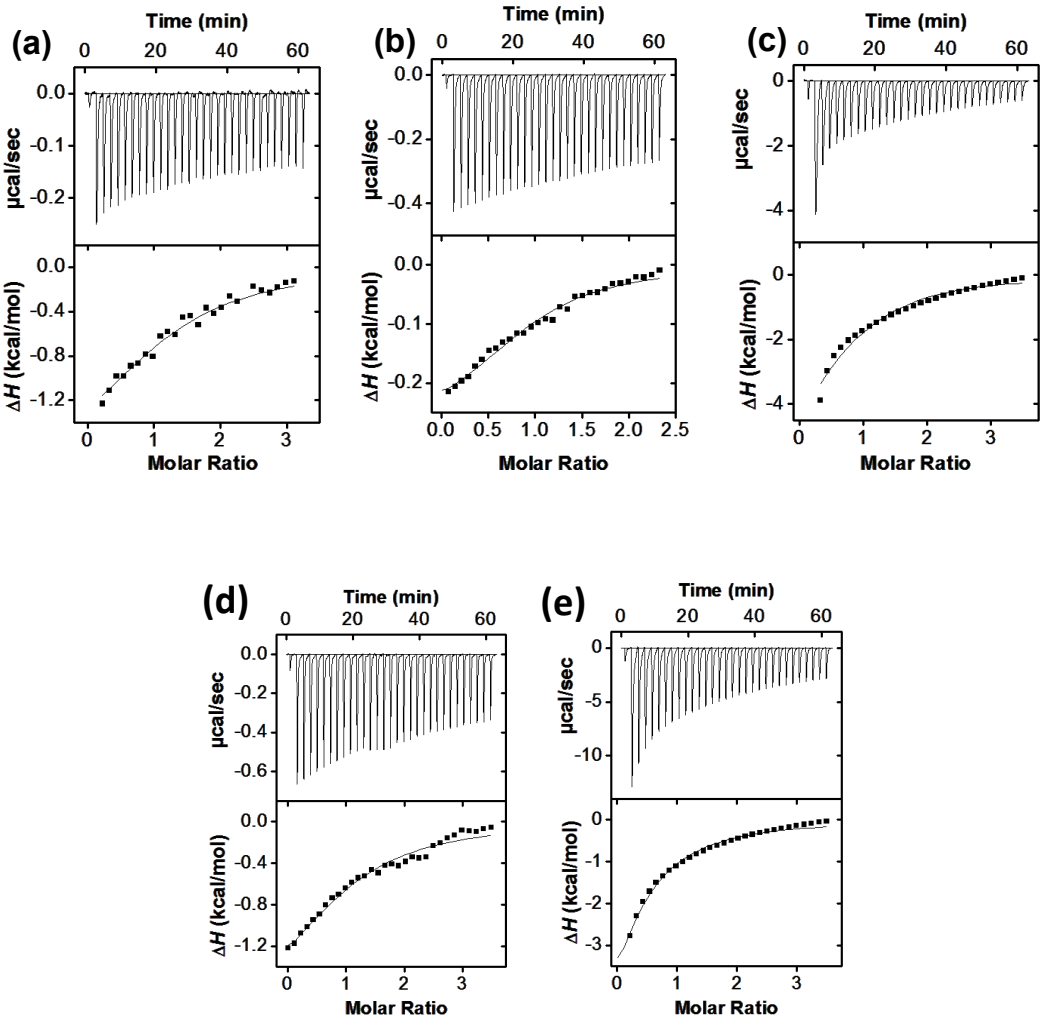

Figure 21. ITC titration curves obtained at 298 K for the titration of fluoro-MINP(**3**) with **2** (a), **7** (b), **8** (c), **9** (d), and **10** (e) in 50 mM Tris buffer (pH 7.4). The data correspond to entries 7 and 9–12, respectively, in Table 1. The top panel shows the raw calorimetric data. The area under each peak represents the amount of heat generated at each ejection and is plotted against the molar ratio of MINP to the substrate. The solid line is the best fit of the experimental data to the sequential binding of N equal and independent binding sites on the MINP. The heat of dilution for the substrate, obtained by adding the substrate to the buffer, was subtracted from the heat released during the binding. Binding parameters were auto-generated after curve fitting using Microcal's Origin 7 software.

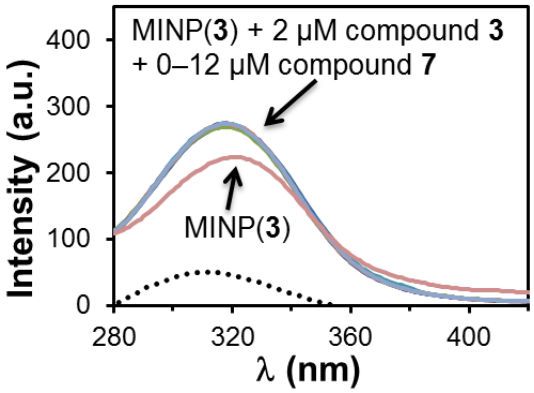

Figure 22. Excitation spectra of MINP(**3**) with 2 μM of compound **3**, titrated with 0–12 μM of compound **7**. The dotted spectrum in black was obtained by subtracting the MINP spectrum from that of the MINP plus compound **3**. The emission for the dansyl acceptor at 520 nm (λ_{em}) was monitored as the excitation wavelength (λ_{ex}) was scanned from 250 to 450 nm was scanned. [MINP] = 0.50 μM in 50 mM Tris buffer (pH 7.4).

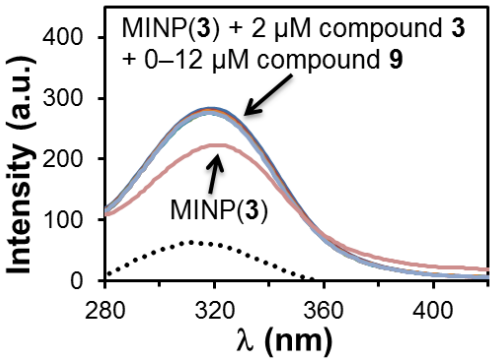

Figure 23. Excitation spectra of MINP(**3**) with 2 μM of compound **3**, titrated with 0–12 μM of compound **9**. The dotted spectrum in black was obtained by subtracting the MINP spectrum from that of the MINP plus compound **3**. The emission for the dansyl acceptor at 520 nm (λ_{em}) was monitored as the excitation wavelength (λ_{ex}) was scanned from 250 to 450 nm was scanned. [MINP] = 0.50 μM in 50 mM Tris buffer (pH 7.4).

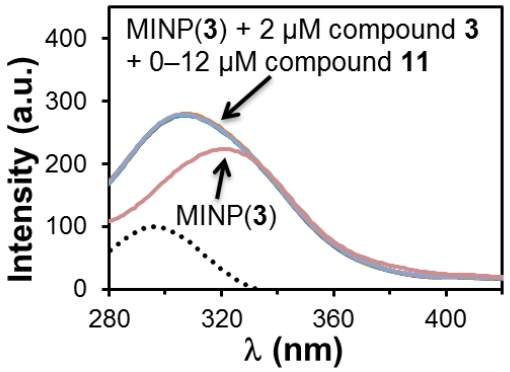

Figure 24. Excitation spectra of MINP(**3**) with 2 μM of compound **3**, titrated with 0–12 μM of compound **11**. The dotted spectrum in black was obtained by subtracting the MINP spectrum from that of the MINP plus compound **3**. The emission for the dansyl acceptor at 520 nm (λ_{em}) was monitored as the excitation wavelength (λ_{ex}) was scanned from 250 to 450 nm was scanned. [MINP] = 0.50 μM in 50 mM Tris buffer (pH 7.4).

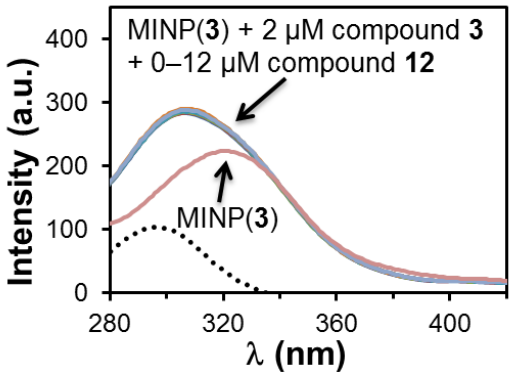

Figure 25. Excitation spectra of MINP(**3**) with 2 μM of compound **3**, titrated with 0–12 μM of compound **12**. The dotted spectrum in black was obtained by subtracting the MINP spectrum from that of the MINP plus compound **3**. The emission for the dansyl acceptor at 520 nm (λ_{em}) was monitored as the excitation wavelength (λ_{ex}) was scanned from 250 to 450 nm was scanned. [MINP] = 0.50 μM in 50 mM Tris buffer (pH 7.4).

^{1}H NMR of compound **3**

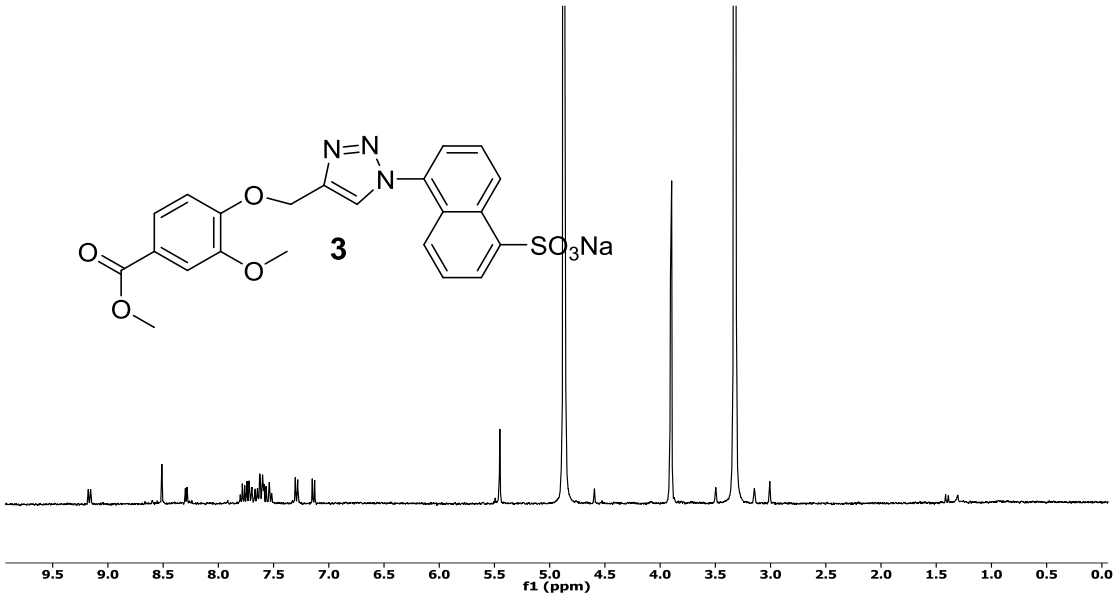

^{13}C NMR of compound **3**

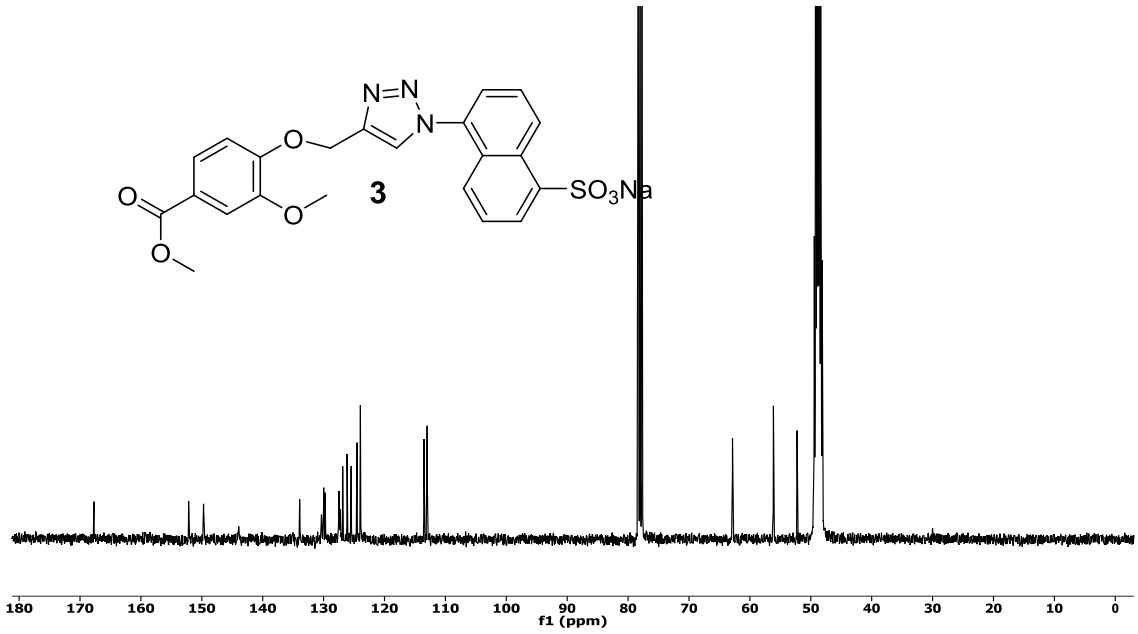

^{1}H NMR of compound **4**

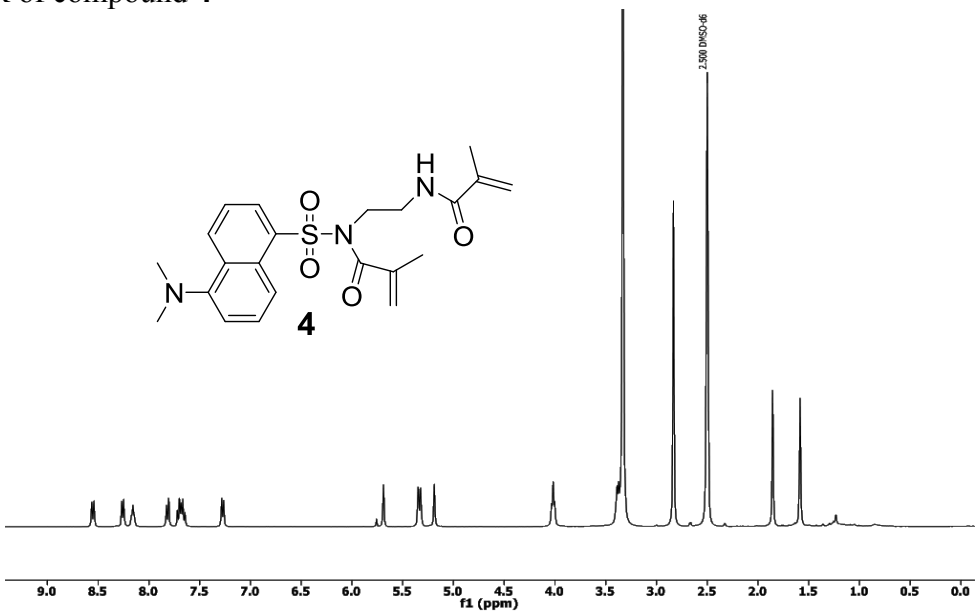

^{13}C NMR of compound **4**

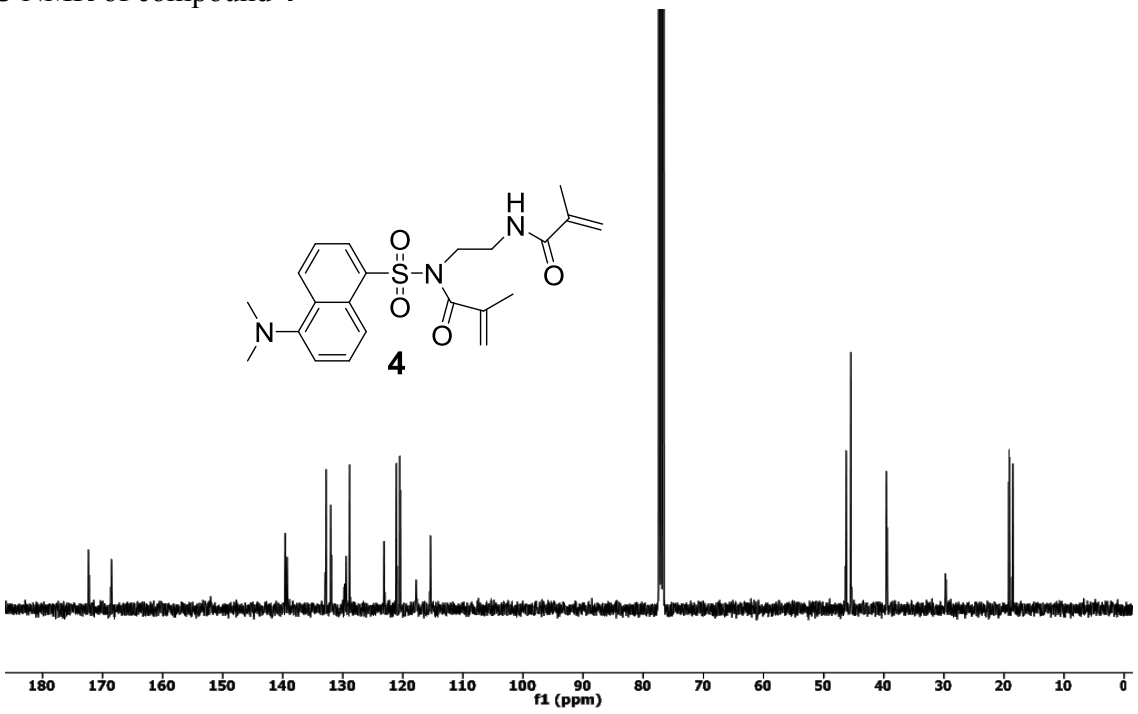

^{1}H NMR of compound **11**

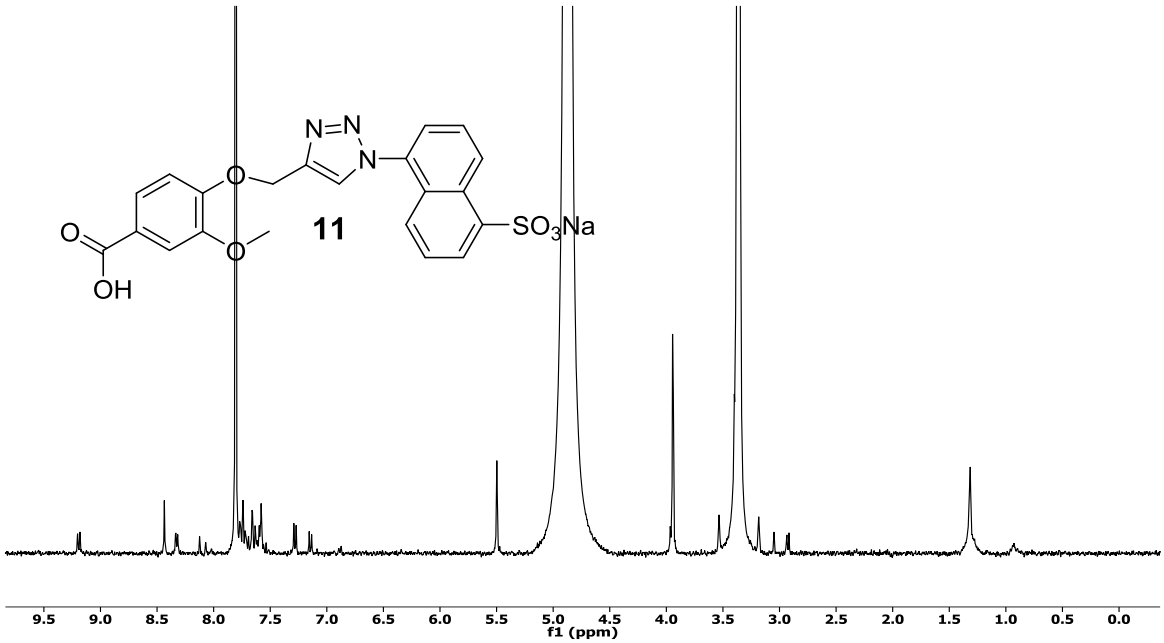

^{13}C NMR of compound **11**

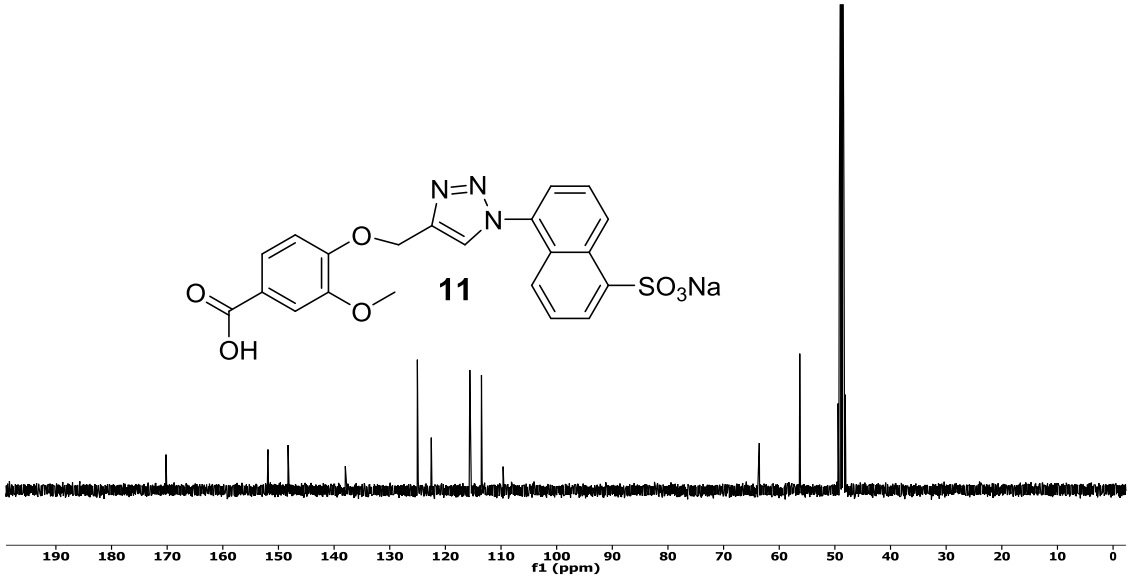

^{1}H NMR of compound **16**

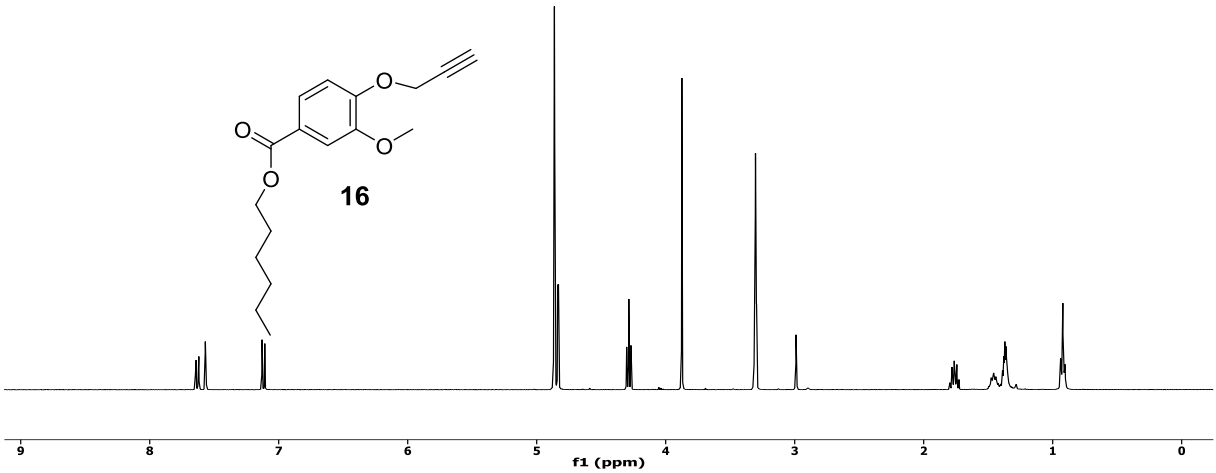

^{13}C NMR of compound **16**

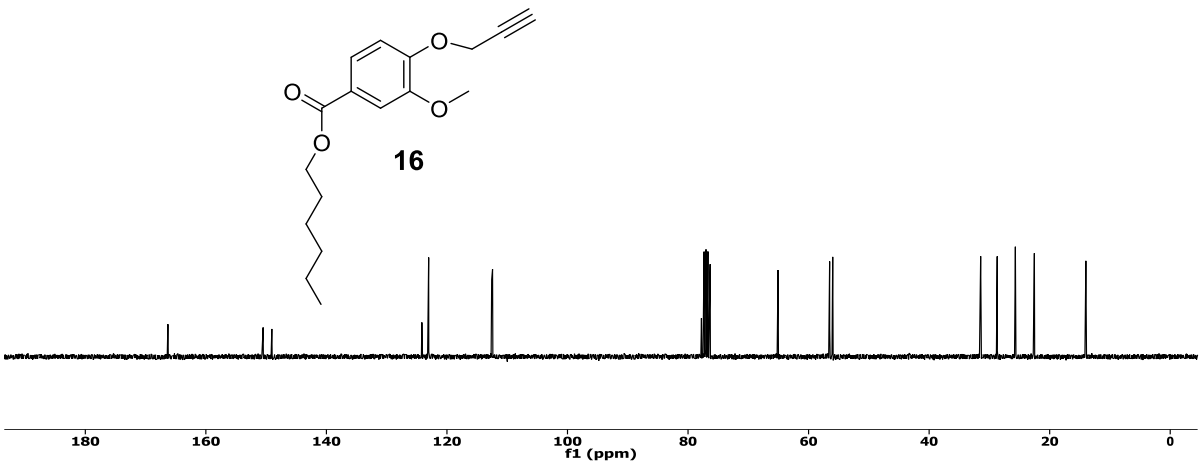

^{1}H NMR of compound **12**

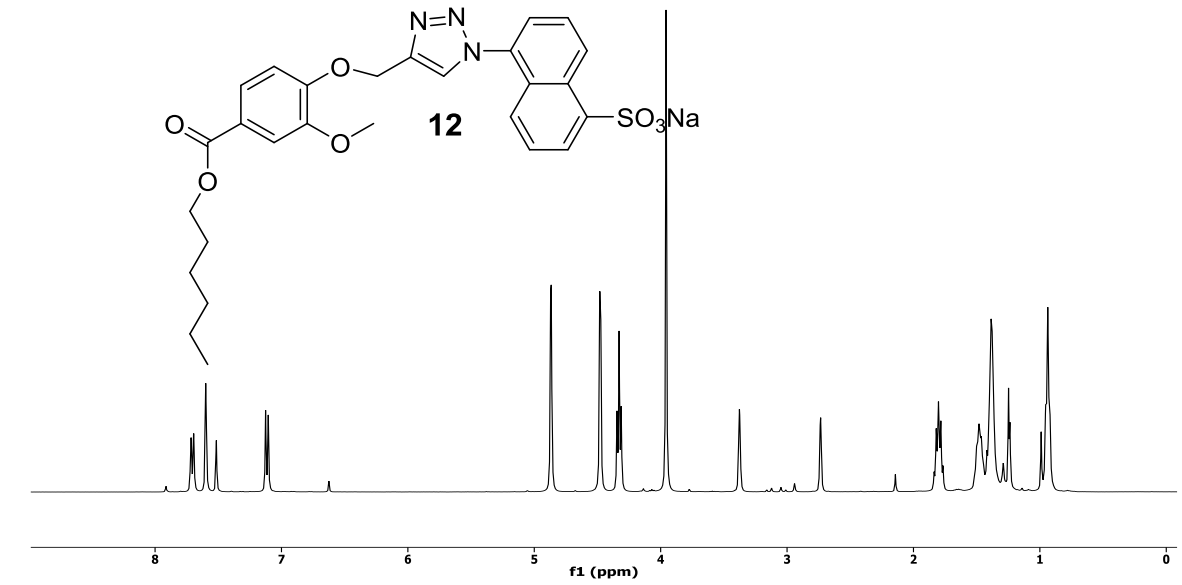

^{13}C NMR of compound **12**

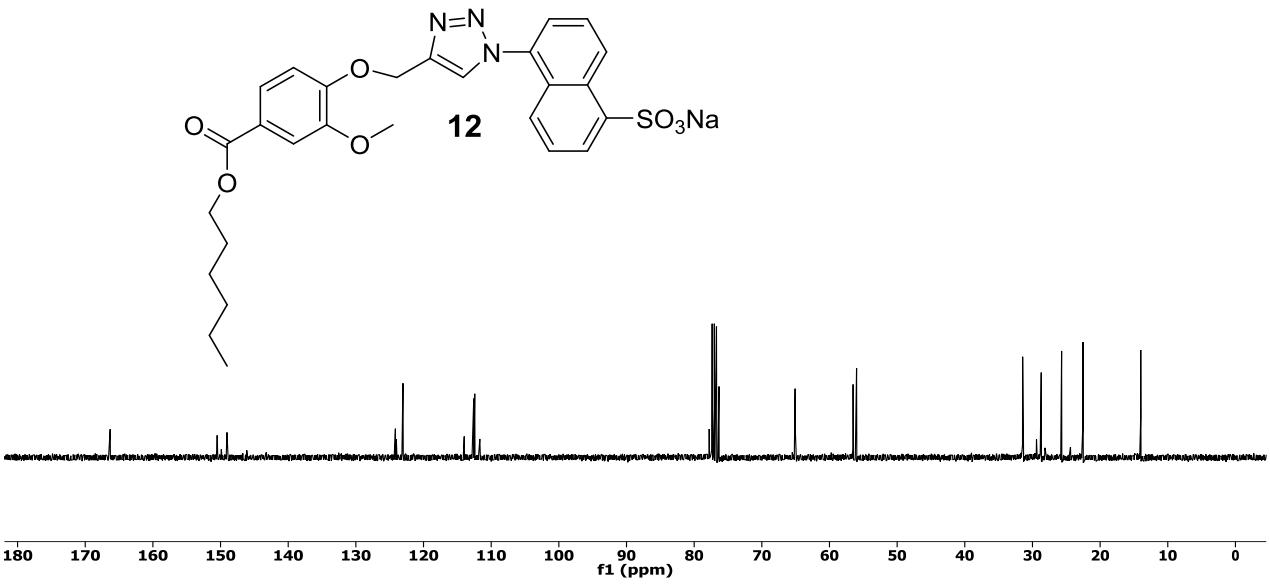

Notes and References

(1) (a) G. Wulff, *Angew. Chem. Int. Ed. Engl.*, 1995, **34**, 1812; (b) G. Wulff, *Chem. Rev.*, 2001, **102**, 1; (c) K. Haupt and K. Mosbach, *Chem. Rev.*, 2000, **100**, 2495; (d) K. J. Shea, *Trends Polym. Sci.*, 1994, **2**, 166; (e) B. Sellergren, *Molecularly Imprinted Polymers: Man-Made Mimics of Antibodies and Their Applications in Analytical Chemistry*, Elsevier, Amsterdam, 2001; (f) B. Sellergren, *Angew. Chem. Int. Ed.*, 2000, **39**, 1031; (g) M. Komiyama, *Molecular Imprinting: From Fundamentals to Applications*, Wiley-VCH, Weinheim, 2003; (h) M. Yan and O. Ramström, *Molecularly Imprinted Materials: Science and Technology*, Marcel Dekker, New York, 2005; (i) C. Alexander, H. S. Andersson, L. I. Andersson, R. J. Ansell, N. Kirsch, I. A. Nicholls, J. O'Mahony and M. J. Whitcombe, *J. Mol. Recognit.*, 2006, **19**, 106.

(2) (a) A. L. Jenkins, O. Manuel Uy and G. M. Murray, *Anal. Commun.*, 1997, **34**, 221; (b) P. Turkewitsch, B. Wandelt, G. D. Darling and W. S. Powell, *Anal. Chem.*, 1998, **70**, 2025; (c) S. A. Piletsky, E. Terpetschnig, H. S. Andersson, I. A. Nicholls and O. S. Wolfbeis, *Fresenius J. Anal. Chem.*, 1999, **364**, 512; (d) J. Matsui, M. Higashi and T. Takeuchi, *J. Am. Chem. Soc.*, 2000, **122**, 5218; (e) T. Takeuchi, T. Mukawa, J. Matsui, M. Higashi and K. D. Shimizu, *Anal. Chem.*, 2001, **73**, 3869; (f) A. Tong, H. Dong and L. Li, *Anal. Chim. Acta*, 2002, **466**, 31; (g) E. Mertz and S. C. Zimmerman, *J. Am. Chem. Soc.*, 2003, **125**, 3424; (h) N. T. Greene and K. D. Shimizu, *J. Am. Chem. Soc.*, 2005, **127**, 5695.

(3) (a) F. L. Dickert, O. Hayden and K. P. Halikias, *Analyst*, 2001, **126**, 766; (b) M. Zayats, M. Lahav, A. B. Kharitonov and I. Willner, *Tetrahedron*, 2002, **58**, 815; (c) K. Das, J. Penelle and V. M. Rotello, *Langmuir*, 2003, **19**, 3921.

(4) A. Kugimiya and T. Takeuchi, *Biosens. Bioelectron.*, 2001, **16**, 1059.

(5) (a) K. J. Shea, M. Yan and M. J. Roberts, eds., *Molecularly Imprinted Materials--Sensors and Other Devices*, Materials Research Society, Warrendale, PA, 2002; (b) L. Ye and K. Haupt, *Anal. Bioanal. Chem.*, 2004, **378**, 1887; (c) M. J. Whitcombe, I. Chianella, L. Larcombe, S. A. Piletsky, J. Noble, R. Porter and A. Horgan, *Chem. Soc. Rev.*, 2011, **40**, 1547.

(6) J. K. Awino and Y. Zhao, *J. Am. Chem. Soc.*, 2013, **135**, 12552.

(7) (a) S. Zhang and Y. Zhao, *Macromolecules*, 2010, **43**, 4020; (b) S. Zhang and Y. Zhao, *J. Am. Chem. Soc.*, 2010, **132**, 10642; (c) X. Li and Y. Zhao, *Langmuir*, 2012, **28**, 4152; (d) S. Zhang and Y. Zhao, *Chem. Commun.*, 2012, **48**, 9998; (e) G. Chadha and Y. Zhao, *Chem. Commun.*, 2014, **50**, 2718.

(8) B. W. v. d. Meer, G. Coker and S. Y. S. Chen, *Resonance Energy Transfer: Theory and Data*, VCH, New York, 1994.

(9) S. C. Zimmerman and N. G. Lemcoff, *Chem. Commun.*, 2004, 5.

(10) L. Stryer, *Annu. Rev. Biochem.*, 1978, **47**, 819.

(11) We also tried 1-, and 2-naphthaleneamine as the guests and observed no FRET either. They were not studied further because their water-insolubility did not allow us to determine their binding by ITC.

(12) Although compound **3** was significantly larger than **2**, the former had quite a number of oxygen and nitrogen atoms that might be hydrated when the molecule is in solution. The substantial desolvation during binding might be the reason why the binding for **3** was only marginally larger than that for **2** by their corresponding MINP.

(13) C. Tanford, *The Hydrophobic Effect: Formation of Micelles and Biological Membranes*, 2nd edn., Krieger, Malabar, Fla., 1991.

(14) The λmax of the donor (310 nm) was quite close to that of the acceptor (340 nm). An ideal FRET sensor should have very little overlap between the donor and the acceptor absorptions.

(15) Compound **10** contained the same dansyl as the MINP(**3**) itself and thus was not compared in this study.

(16) Awino, J. K.; Zhao, Y. *J Am Chem Soc* **2013**, *135*, 12552-12555

(17) Zhang, S. Y.; Zhao, Y. *J Am Chem Soc* **2010**, *132*, 10642-10644.

(18) Li, X.; Zhao, Y. *Bioconjugate Chem* **2012**, *23*, 1721-1725.

(19) Sato, S.; Aoyama, H.; Miyachi, H.; Naito, M.; Hashimoto, Y. *Bioorg Med Chem Lett* **2008**, *18*, 3354-3358.

(20) Oropeza, C.; Alpizar, L.; Loyolavargas, V. M.; Quiroz, J.; Scorer, K. N. *J Chromatogr* **1988**, *456*, 405-409.

(21) Pham, H. T.; Hanson, R. N.; Olmsted, S. L.; Kozhushnyan, A.; Visentin, A.; Weglinsky, P. J.; Massero, C.; Bailey, K. *Tetrahedron Lett* **2011**, *52*, 1053-1056.

(22) 7Doyle, E. L.; Hunter, C. A.; Phillips, H. C.; Webb, S. J.; Williams, N. H. *J Am Chem Soc* **2003**, *125*, 4593-4599.

(23) Koch, S. J.; Renner, C.; Xie, X. L.; Schrader, T. *Angew Chem Int Edit* **2006**, *45*, 6352-6355.

CHAPTER 4

WATER-SOLUBLE MOLECULARLY IMPRINTED NANOPARTICLES (MINPs) WITH TAILORED, FUNCTIONALIZED, MODIFIABLE BINDING POCKETS

A paper published in *Chemistry - A European Journal,* **2015***, 21,* 655-661

Joseph K. Awino and Yan Zhao

Abstract

Construction of receptors with binding sites of specific size, shape, and functional groups is important to both chemistry and biology. Covalent imprinting of a photocleavable template within surface–core-doubly cross-linked micelles yielded carboxylic acid-containing hydrophobic pockets within the water-soluble molecularly imprinted nanoparticles. The functionalized binding pockets were characterized by their binding of amine- and acid-functionalized guests under different pHs. The nanoparticles on average contained one binding site per particle and displayed highly selective binding among structural analogues. The binding sites could be modified further by covalent chemistry to modulate their binding properties.

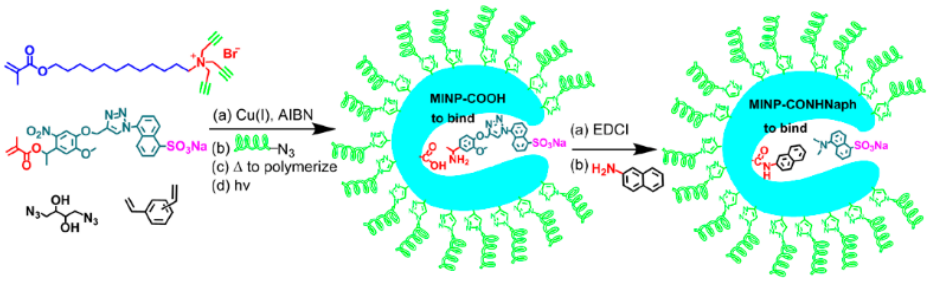

Scheme 1. General design

Introduction

The active (binding, transport, or catalytic) sites of proteins are key to their intended functions. Supramolecular chemists over the last decades have synthesized a great many synthetic receptors to mimic one or more aspects of these active sites, with the majority of them prepared through molecular synthesis.[1] Although molecular synthesis ensures synthetically pure and discrete functional molecules, the significant synthetic efforts required often become impediments to scale-up and practical applications of the materials.

Molecular imprinting is a conceptually different approach to synthetic receptors. [2] Instead of building the receptors first and then trying to fit their guests into the structures, one simply co-polymerizes appropriate functional monomers (FMs) and cross-linkers around molecular templates. Removal of the templates generates guest-complementary binding pockets within the polymer matrix. Much progress has been made in molecularly imprinted polymers (MIPs) since Wulff [3] and Mosbach [4] respectively pioneered the covalent and noncovalent imprinting (referring to the binding interactions between FMs and the template). The concept has also been extended beyond traditional macroporous polymers to imprinted surface[2] and even unimolecularly within dendrimers. [5]

Although molecular imprinting can create binding sites more efficiently than molecular synthesis, it is generally accepted that the binding sites obtained through imprinting are heterogeneous and less structurally defined. [2, 6] According to a representative review, [7] MIPs ideally are "preparable in one (or few) high yielding synthetic step(s)", "able to be post-synthetically functionalized," and possess "homogeneous imprinted sites of high stability" with "high (binding) affinity with possibility to tune." Although highly desirable

and important to many applications of MIPs, many of these features are yet to be realized with traditional imprinting techniques.

Herein, we report a method to construct tailor-made, hydrophobic binding pockets possessing specific binding functional groups in water-soluble nanoparticles. These molecularly-imprinted nanoparticles (MINPs) were shown to distinguish guests based on their size, shape, and functional groups. Most interestingly, the binding pockets could be modified through standard chemistry to alter their molecular-recognition properties.[8] Different from traditional MIPs [2] or other reported imprinted nanoparticles, [9] our MINPs on average contained one binding pocket per particle, thus bridging the gap between the discrete receptors made through molecular synthesis and those less well-defined receptors made through traditional imprinting.

Results and Discussion

Materials Design and Synthesis

The method was a development from on our recently reported molecular imprinting using surface-cross-linked micelles (SCMs) [10] prepared from **1** (Scheme 2). [11] This surfactant has a tripropargylammonium headgroup cross-linkable on the surface by the click reaction. Its methacrylate at the hydrophobic tail enables core-cross-linking around a hydrophobic template solubilized by the micelle in water. In the previous work, we demonstrated that selective binding pockets could be created within the SCM for bile salts. The limitation of the previous method lies in the fact that only hydrophobic pockets with prescribed shapes could be created within the MINPs. Without specific binding groups, the pockets recognize guests primarily based on their size and/or shape.

To install a functional group within a molecularly imprinted binding pocket, one normally has to employ FMs that bind the template through specific noncovalent interactions. Although such a method works well for conventional MIPs in organic media, it is completely unsuitable in our case because the entire imprinting takes place in aqueous solution. Not only do FMs with polar binding groups (e.g., methacrylic acid) tend to stay in water instead of within hydrophobic core of the micelle, the intended noncovalent template–FM complex is also unlikely to be stable when a large amount of water is present that competes in hydrogen-bonding. [12] Even if the template–FM complex is somehow made stable inside the micelle, the polar FM most likely would stay at the surfactant/water interface instead of in the hydrophobic core of the micelle. As a result, even if such imprinting is made to work, it will be difficult to have the polar functional group deep within the hydrophobic core of the resulting MINP. Needless to say, for molecular recognition in water, polar binding interactions typically are stronger in a more deeply imbedded hydrophobic microenvironment.

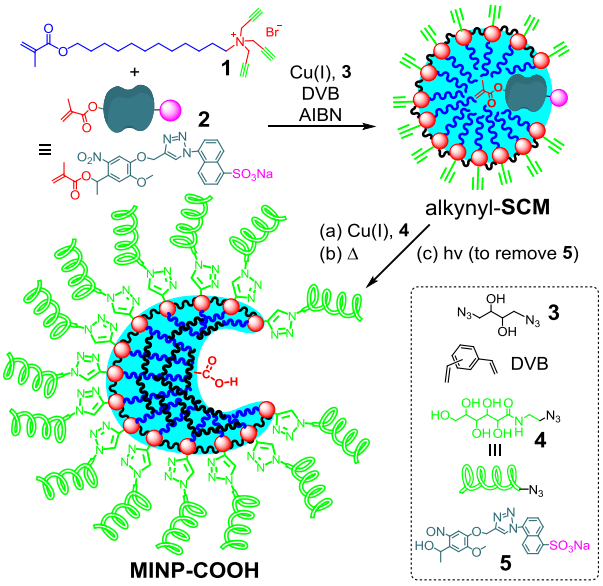

Scheme 2. Preparation of MINP-COOH

To overcome these challenging problems, we designed a photocleavable template (**2**) containing an *o*-nitrobenzyl linkage (Scheme 2). Its overall hydrophobicity allowed it to be easily incorporated into the micelle of **1**. The sulfonate group of the template had strategic purposes in our design: in addition to strengthening the binding with the cationic micelle of **1** through electrostatic interactions, it orients the template to make its methacrylate point inward. Because the methacrylate is nearly at the opposite end of molecule from the sulfate that is anchored at the micelle surface, the methacrylate (after polymerization and photo-deprotection) is expected to position the carboxylic acid deep inside the hydrophobic pocket of the final MINP-COOH (Scheme 2).

MINP-COOH synthesis was adapted from our earlier procedures. [11a] Click-cross-linking of the template-containing micelles by the water-soluble diazide **3** in the presence of Cu(I) catalysts created alkynyl-SCMs, which were surface-functionalized through another round of click reaction with sugar-derived **4**. The reactions were perfomed at 10 mM of **1** in water, above its CMC of 0.55 mM. Each SCM, according to our DLS study, contained ca. 50 surfactants. Thus, a ratio of [**1**]:[**2**] = 1:0.02 in theory placed one template within each SCM, a feature verified in our previous bile salt-binding MINPs. [11a]

In the previous procedure, we employed photo-polymerization to cross-link the methacrylate of **1** with DVB solubilized in the core. The method was clearly unsuitable with **2** having the photocleavable *o*-nitrobenzyl ether. We thus decided to solubilize a small amount of AIBN (i.e azobisisobutyronitrile, a thermal initiator) at the beginning of the procedure and carried out thermal polymerization of the methacrylate and DVB at 75 °C for 16 h after the "surface-clicking". Fortunately, since hydrophobic interactions generally remain effective at high temperatures (and generally change from entropically driven to

enthalpically driven with increasing temperatures), [13] template **2** was successfully cross-linked with the rest of the structure. Alkenic protons disappeared completely at the end of the thermal polymerization as shown by ^{1}H NMR spectroscopy (Figure 6, Experiemental Section).

Our last step in the materials synthesis was the photolytic cleavage of the *o*-nitrobenzyl linkage to remove nitroso derivative **5** and vacate the binding site. The reaction progress could be monitored easily by fluorescence spectroscopy (Figure7) because of the fluorescent naphthalene group of **5** (and **2**). [14]

According to DLS, the SCM, surface-functionalized SCM, and the final MINP-COOH averaged 3.5, 6.3, and 4.7 nm in diameter (Figure 8). The size of MINP-COOH translated to ca. 50,000 daltons in molecular weight (Figure 9), comparable to many proteins in this regard. Overall, the MINP-COOH bears much resemblance to a water-soluble protein receptor with a hydrophilic exterior, a hydrophobic core, a specifically shaped hydrophobic binding site, and an internal functional group. It is worth mentioning that the sugar-derived surface ligand **4** was installed not just to make the MINP mimic a water-soluble protein in the surface hydrophilicity; its high crystallinity allowed the MINPs to be easily precipitated from solvents such as acetone while maintaining complete solubility in water and polar solvents such as DMF. As will be shown later, solubility in selected organic solvents was highly beneficial in covalent modification of the MINPs.

Characterization of the Carboxylic Acid-Containing Binding Pockets

To characterize the carboxyl-functionalized MINP receptors, we first studied the binding of a template analogue **6**, which contained an amino group where methacrylate was

in template **2**. Since the carboxyl group in the MINP binding pocket was generated from the polymerized methacrylate of **2**, compound **6** upon binding should have its amino group in close proximity to the MINP carboxyl. The host–guest binding thus should be driven by a combination of hydrophobic interactions (between the hydrophobic portion of **6** and the MINP) and an ammonium–carboxylate salt bridge. Being located in a hydrophobic microenvironment, the salt bridge should be particularly strong. [15] As in our bile salt-binding MINPs, electrostatic interactions between the positively charged cross-linked micelle and the sulfonate group should contribute as well.

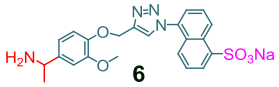

6

The water-solubility of our MINPs allowed us to study their binding properties using standard titration methods. [1c] As shown by Figure 1a, upon titration of **6** by MINP-COOH in Tris buffer at pH 7.4, its emission at 410 nm decreased and a weaker peak at 470 nm appeared gradually. Although we could not be certain why the MINP-bound **6** emitted at a longer wavelength, it is possible that the binding slowed down the rotation around the σ-bond between the triazole and the naphthyl ring and enhanced the conjugation between the two aromatic groups. For the same reason, although environmentally sensitive dansyl fluorophores are often used to probe the local polarity of the binding pocket, we could not do so with **6**, as its emission depends on multiple factors. Nonetheless, the fluorescence data fit nicely to a 1:1 binding isotherm to afford a binding constant of $K_a = (1.5 \pm 0.3) \times 10^6\ M^{-1}$ (Figure 1b).

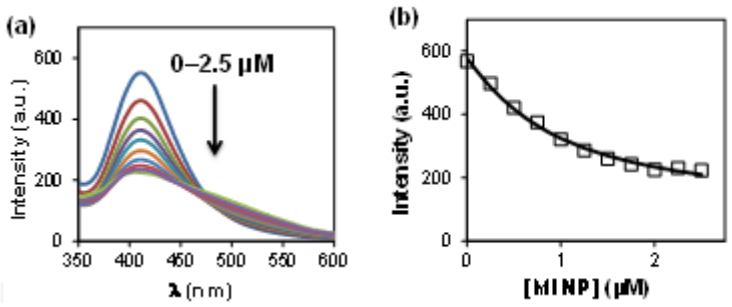

Figure 1. (a) Emission spectra of **6** (λ_{ex} = 300 nm) upon addition of different concentrations of MINP-COOH in 50 mM Tris buffer (pH 7.4). [**6**] = 0.5 μM. (b) Nonlinear least squares fitting of the emission intensity of **6** at 415 nm to a 1:1 binding isotherm.

To further understand the role of the MINP carboxyl in the binding, we performed similar fluorescence titrations of amine **6** at different pHs (2.2–9.5) in citrate–phosphate and Tris buffers. The concentration (10–50 mM) of the buffers showed negligible effect on the obtained binding constants. Such results generally suggest that ionic strength did not play any significant roles in the binding. [16] In the bile salt-binding MINPs, the negligible effect of ionic strength seemed to come from two opposing effects of salts on the hydrophobic interactions and electrostatic forces involved in the binding, respectively. [11a]

Because both the host and the guests contain removable protons, we have to consider the acid/base properties of all the reactants in the binding. [17] Scheme 3 shows the acid–base equilibria involved and the binding of amine **6** by MINP-COOH. The acidity constant of (protonated) amine **6** (pK_{NH3}) in solution is probably similar to that for 1-phentylethylamine (pK_a = 9.4). [18] Assuming MINP-COOH deprotonates more easily than protonated **6**, we anticipate that the strongest binding between MINP-COOH and **6** would occur in between pK_{MINP} and pK_{NH3}. Below pK_{MINP}, the dominant forms of the reactants are MINP-COOH and

RNH_3^+ (i.e., protonated **6**). These two species cannot form the ammonium–carboxylate salt bridge directly. Instead, MINP-COOH needs to undergo an unfavorable deprotonation (in the acidic medium) in order for the binding to occur. The binding thus would be compromised by the deprotonation of the MINP carboxyl. Above pK_{NH3}, MINP-COO^- and RNH_2 (i.e., **6** itself) will dominate on the other hand. In order to form the ammonium–carboxylate salt bridge, **6** has to undergo an unfavorable protonation under the now basic condition and thus would also weaken the binding.

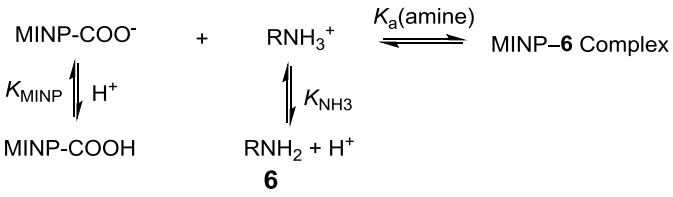

Scheme 3. The acid–base equilibria and the binding of amine **6** by MINP-COOH.

Our titration confirmed the predictions. As shown by Figure 2, the binding was undetectable by fluorescence spectroscopy at ≤pH 5, became stronger with increasing pH, and weakened again above pH 7.4. According to Scheme 2, the maximum K_a (= 1.5×10^6 M^{-1}) should reflect the binding when MINP-COO^- and RNH_3^+ predominate in the solution. If we take the midpoint between pH 5 (where the binding was still zero but began to rise) and pH 7.4 (where the binding was the strongest) as pK_{MINP}, the acidity constant of the MINP carboxyl is estimated to be ~6.2. This value is significantly higher than acetic acid (pK_a = 4.76) or benzoic acid (pK_a = 4.20) in water. The larger pK_a for MINP-COOH is very reasonable and strongly supports the location of the acidic group in a hydrophobic microenvironment. It is well known from protein chemistry that a carboxyl group located in a hydrophobic pocket is more difficult to deprotonate than in aqueous solution, as the resulting carboxylate could not be solvated properly in a hydrophobic microenvironment. [19]

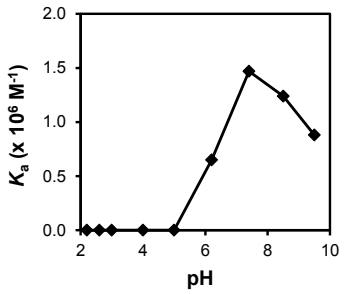

Figure 2. The apparent binding constants of MINP-COOH for **6** in citrate–phosphate buffer (pH 2.2–6.2) and Tris buffer (pH 7.4–9.5) obtained by fluorescence titration.

The presence of the carboxylic acid in the hydrophobic binding pocket of MINP-COOH was verified additionally by its binding of the carboxylic acid guest **7**. Scheme 4 shows the various acid–base equilibria involved in the binding. Because the carboxyl group of **7** is exposed to solvent, its pK_a is expected to be similar to that of 3,4-dimethoxybenzoic acid (pK_a = 4.43). [20] Since the binding between two carboxylic acids occurs through the hydrogen-bonded carboxylic acid dimer, both MINP-COOH and **7** need to be in the protonated form to achieve the strongest binding.

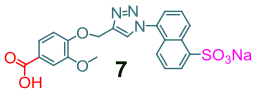

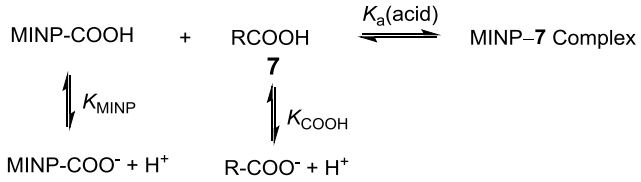

Scheme 4. The acid–base equilibria and the binding of acid **7** by MINP-COOH.

Indeed, as shown by Figure 3, the pH profile for the binding of **7** was nearly opposite to that of **6**: the strongest binding occurred at low pHs (2.2–2.6) and showed a sharp decrease

as the solution became less acidic. The binding weakened significantly at pH 3 and became completely undetectable by fluorescence at ≥pH 6.2. If we take the midpoint between pH 2.6 (where the binding was the maximum) and pH 6.2 (where the binding first became zero) as the acidity constant of **7**, a value of 4.4 was obtained, exactly as predicted from the pK_a of 3,4-dimethoxybenzoic acid.

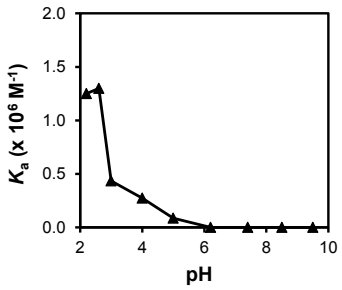

Figure 3. The apparent binding constants of MINP-COOH for **7** in citrate–phosphate buffer (pH 2.2–6.2) and Tris buffer (pH 7.4–9.5) obtained by fluorescence titration.

Because the maximum binding constants for **6** and **7** were quite similar (1.5 and 1.3 × 10^6 M^{-1}, respectively), it seems the ammonium–carboxylate salt bridge and the carboxylic acid dimer make similar contributions to the overall binding. This is a useful piece of information for molecular recognition in water. A recent work of ours shows that, although a (guanidinium–carboxylate) salt bridge could be strong, for molecular recognition in self-assembled hydrophobic entities such as micelles or lipid bilayers, a carboxylic acid dimer could be more useful. This is because the uncharged nature of a carboxylic acid dimer makes it more easily migrate into a hydrophobic microenvironment. [21] Charged functional groups (e.g., ammonium, guanidinium, or carboxylate) often have a strong tendency to stay within or at least close to water to satisfy their solvation needs. [22]

Binding Selectivity of MINP-COOH: An important property of molecularly imprinted materials is their binding selectivity. The above study demonstrated binding selectivity for acid- and base-functionalized template analogues in a pH-dependent manner. For example, at pH 7.4, the MINP receptor bound **6** with micromolar affinity but did not bind **7** at all. Under acidic conditions (pH 2.2–2.6), the exact opposite selectivity was achieved.

To understand the binding selectivity of the MINP receptor for other non-acidic/basic analogues (**8**–**11**), we switched to isothermal titration calorimetry (ITC) to determine the binding constants. One reason for the change was that fluoresence titration was unsuitable for bindings with lower binding affinities. Additionally, ITC could easily afford other useful information including binding enthalpy, entropy, and the number of binding sites per particle (*N*). Because these guests do not contain acid/base groups, we performed ITC titrations under neutral conditions in 50 mM Tris buffer.

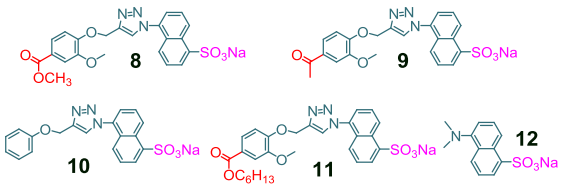

ITC confirmed both the 1:1 binding stoichiometry and the binding affinity for **6** and yielded a K_a value very similar to that obtained by fluorescence titration (i.e., 1.5×10^6 M^{-1}, see Table 1, entry 1). The titration curve and the fitting of the experimental data are shown in Figure 4. ITC was able to detect the binding of **7** (which could not be obtained by fluorescence titration) at pH 7.4 and, as expected, gave a much weaker K_a, ca. 1/17 of that for **6**. Ketone **8** and ester **9** were bound similarly as expected (entries 3 and 4) and were bound more strongly than acid **7**.[23] We were delighted to see the moderate selectivity for **6** over **8** or **9**. After all, these compounds were very similar guests in many regards.

Table 1. Binding data for MINP-COOH obtained by ITC[a]

Entry	Guest	K_a (10^4 M^{-1})	ΔG (kcal/mol)	ΔH (kcal/mol)	$-T\Delta S$ (kcal/mol)	N
1	**6**	152 ± 6	-8.4	-70.2	61.8	1.0 ± 0.1
2	**7**	8.8 ± 0.5	-6.7	-15.3	8.6	0.6 ± 0.1
3	**8**	76 ± 3	-8.0	-29.8	21.8	0.7 ± 0.1
4	**9**	73 ± 6	-8.0	-32.1	24.1	0.6 ± 0.1
5	**10**	0.6 ± 0.5	-5.2	-7.2	2.0	0.4 ± 0.1
6	**11**	5.2 ± 0.7	-6.4	-8.2	2.8	0.4 ± 0.1
7	**12**	0.27 ± 0.06	-4.7	-3.5	-1.1	1.2 ± 0.1
8	**6**[b]	3.1 ± 0.5	-6.1	-5.0	-1.1	0.6 ± 0.1
9	**12**[b]	25 ± 2	-7.4	-9.6	2.2	0.7 ± 0.1

[a] The titrations were generally performed in duplicates in 50 mM Tris buffer (pH 7.4) and the errors between the runs were <20% except in very weak bindings. [b] The host was MINP-CONHNaph.

It is interesting to consider the ionic state of the carboxyl group on MINP-COOH during binding. The binding study for amine **6** yields a pK_a of 6.2 for the MINP carboxyl. Upon "plugging" the binding pocket with a hydrophobic guest such as **8** or **9**, the immediate environment around the MINP carboxyl becomes more hydrophobic upon the expulsion of water from the binding pocket. We would not be surprised that the binding should further increase its pK_a so that the carboxyl stay "comfortably" protonated even when the bulk aqueous phase has a pH of 7.4. In other words, for an acidic (or basic) group relatively deep inside in a hydrophobic pocket in water, its acid or base property is not a fixed constant as in solution but is an intimate function of the guest present in the binding pocket. These properties apparently are critical to the binding and catalytic properties of proteins. [19]

Compound **10** is overall quite similar to **8** and **9** but misses a methoxy and a methyl ester or acetyl. It binding was two-orders-of-magnitude weaker, testifying to the excellent shape/size selectivity of the MINP (Table 1, entry 5). Ester **11** had a hexyl instead of methyl as in **8**. Although its binding was stronger than that of **10**, the one-order-of-magnitude

reduction in K_a from methyl ester **8** indicated that the binding pocket was quite discriminating.

Table 1 shows that all the bindings studied by ITC were largely enthalpically driven, with generally unfavorable entropic terms. We do not believe the results imply that the contribution of hydrophobic interactions were insignificant. Although classical hydrophobic effect is considered entropically driven, [24] the effect is multifaceted and the energetic characteristics may be different depending on the (aliphatic/aromatic) nature of the guests and the size/shape of the hydrophobic surfaces. [25]

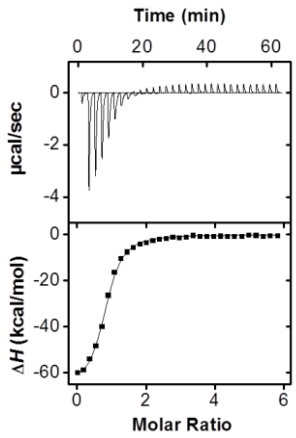

Figure 4. ITC titration curve obtained at 298 K for the binding of **6** in 50 mM Tris buffer (pH 7.4).

Notably, MINP-COOH contained one binding pocket per nanoparticle, evident from the binding studies for those guests with strong bindings (in which the ITC curve fitting would be more reliable). This feature came directly from the surfactant aggregation number and the ratio of surfactant to template during the imprinting. As demonstrated in the bile salt-binding MINPs, if needed, the binding stoichiometry could be tuned by the surfactant/template ratio quite easily. [11a]

Covalent Modification of the Binding Pockets: Similar to an active site of a protein, the binding pocket of MINP-COOH could be modified through covalent chemistry. This could be a great way to tune the binding properties of the MINP receptor. To demonstrate this feature, we dissolved the nanoparticles in DMF and activated the MINP carboxyl with 1-ethyl-3-(3-dimethylamino-propyl)carbodiimide hydrochloride or EDCI, a standard amide-coupling reagent. After treatment with 2-aminonaphthalene, the resulting MINP-CONHNaph displayed characteristic naphthalene emission at 410 nm (Figure 10).

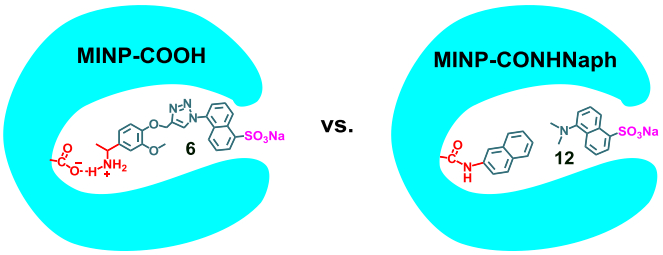

Figure 5. Binding of amine **6** by MINP-COOH versus binding of dansyl sulfonate **12** by MINP-CONHNaph.

Most interestingly, MINP-COOH and MINP-CONHNaph displayed (anticipated) highly different molecular-recognition properties. As described earlier, amine **6** was the best guest for MINP-COOH at pH 7.4, as everything including size, shape, and functional groups matched perfectly between the host and the guest. Not surprisingly, dansyl sulfate **12**, which at most represented a "half-matched" guest, was too small to bind strongly to MINP-COOH (Table 1, entry 7, K_a = 0.27 × 10^4 M^{-1} or 560 times weaker than that of **6**). Once naphthylated, however, the binding pocket was expected to bind dansyl sulfonate much better, as the 2-aminonaphthalene group was chosen to make up for what was missing in dansyl sulfate **12** from **6** (i.e., the phenyl–triazole spacer between the amino and the naphthyl group, compare the two structures in Figure 5). As shown by the data in Table 1 (entries 8

and 9), MINP-CONHNaph showed a remarkable reversal of binding selectivity for **6** and **12**: whereas the bigger guest was preferred by MINP-COOH by 560 times, the smaller guest was bound more strongly by the naphthylated receptor than the larger one by eight times.

Conclusion

Molecular imprinting in surfactant micelles is a powerful method to create nanoparticle receptors that resemble water-soluble proteins. Their hydrophilic exterior, [10a, c, d, g] hydrophobic core, [26] and internal tailor-made binding sites[11] all could be tuned easily with the surface-cross-linked-micelle platform. The previous noncovalent imprinting in the micelles only yielded hydrophobic pockets with predefined shape and size. [11] By combining covalent imprinting with a photoprotection strategy, we now can install specific functional groups within the binding pockets. Despite the many protein-like features, the MINP receptors are highly cross-linked materials with robust properties and long-term stability. Importantly, the entire preparation and purification of MINPs could be done in 2–3 days without special techniques. With their excellent molecular-recognition properties and facile preparation, we anticipate MINPs to become very useful in many applications where custom-made, specific binding sites are needed.

Acknowledgement

We thank NSF (CHE-1303764) for supporting the research.

Experimental Section

General Method

Methanol, methylene chloride, and ethyl acetate were of HPLC grade and were purchased from Fisher Scientific. All other reagents and solvents were of ACS-certified grade or higher, and were used as received from commercial suppliers. Routine 1H and 13C NMR spectra were recorded on a Bruker DRX-400 or on a Varian VXR-400 spectrometer. ESI-MS mass was recorded on Shimadzu LCMS-2010 mass spectrometer. UV-vis spectra were recorded at ambient temperature on a Cary 100 Bio UV-visible spectrophotometer. Fluorescence spectra were recorded at ambient temperature on a Varian Cary Eclipse Fluorescence spectrophotometer. ITC was performed using a MicroCal VP-ITC Microcalorimeter with Origin 7 software and VPViewer2000 (GE Healthcare, Northampton, MA). Syntheses of the compounds are reported in the Supporting Information.

Syntheses

Syntheses of compounds **1**,[27] **3**,[28] **4**,[29] **7**,[30] **11**,[30] **12**,[31] **13**,[32] **14**,[33] **15**,[34] **16**,[35] **17**,[36] **18**,[37] and **19**,[38] were previously reported.

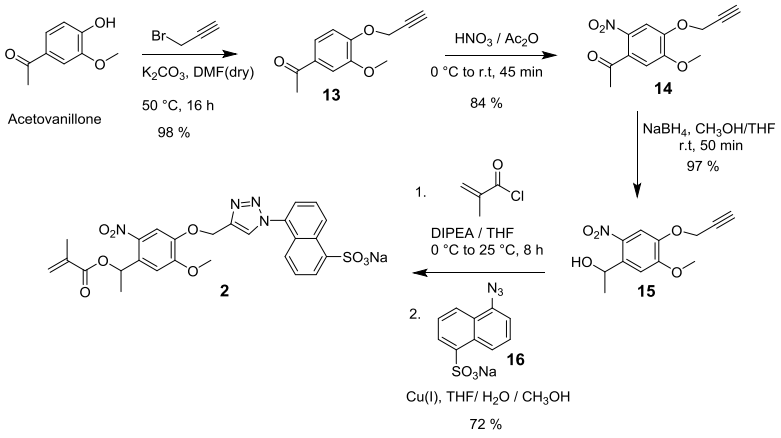

Scheme 5. Synthesis of compound **2**

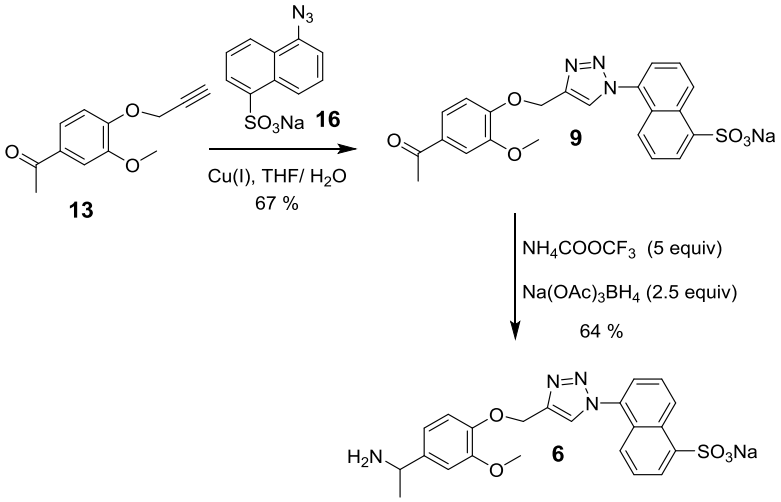

Scheme 6. Synthesis of compound **6**

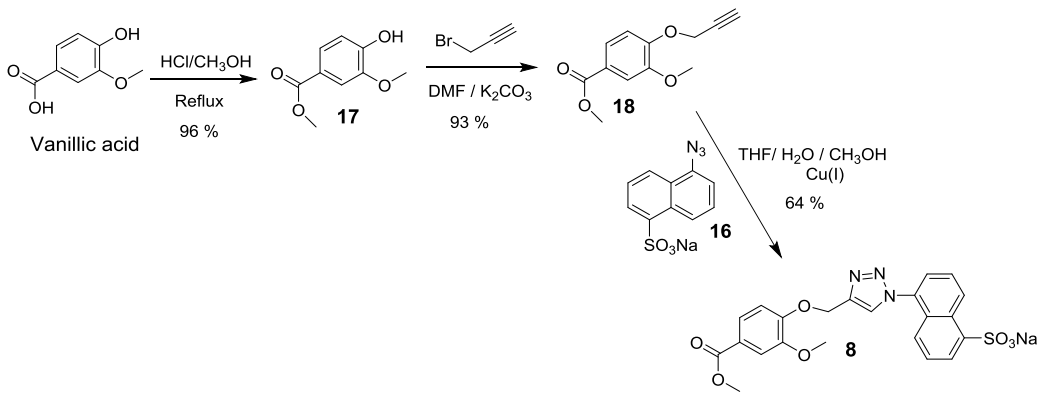

Scheme 7. Synthesis of compound **8**

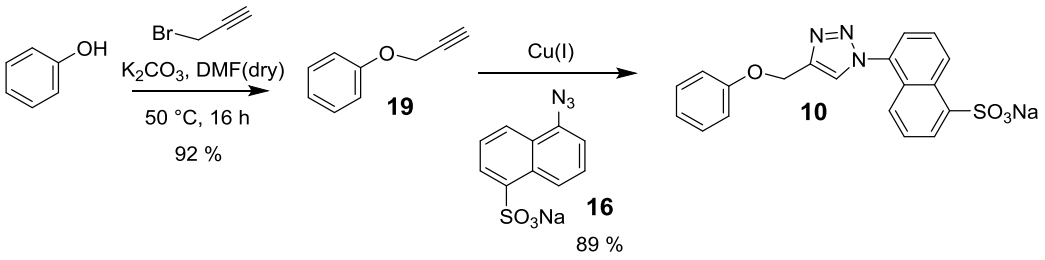

Scheme 8. Synthesis of compound **10**

Compound 2. To an ice-cold solution of **15** (1.00 g, 3.98 mmol) and DIPEA (1.10 mL, 5.95 mmol) in anhydrous THF (20 mL), methacryloyl chloride (0.50 mL, 5.15 mmol) was added dropwise under nitrogen. The mixture was brought to room temperature and stirred overnight. The resulting solution was diluted with water and extracted with ethyl acetate (2 × 10 mL). The organic solution was washed with 1 M HCl to pH 6.0 and then with water (2 × 10 mL), dried over sodium sulfate, and concentrated in vacuo to give clear oil. The oil obtained (1.27 g) was added to **16** (1.00 g, 3.69 mmol) in a 2:1 THF/water mixture (20 mL). Sodium ascorbate (0.93 g, 4.70 mmol) and copper sulfate hydrate (1.00 g, 4.00 mmol) were added and the mixture was stirred at 40 °C in the dark for 12 h. The organic solvent was removed in vacuo and sodium chloride (10 g) was added to the aqueous solution. The

precipitate formed was rinsed with dichloromethane (10 mL) and then dissolved in 5:3 dichloromethane/methanol. After removal of the solid by filtration, the filtrate was concentrated in vacuo and the residue was purified by column chromatography over silica gel using 5:1 methylene chloride: methanol as the eluent to afford an off-white powder (1.56 g, 72 %). ^{1}H NMR (400 MHz, CD_3OD, δ): 9.13 (d, *J* = 8.4 Hz, 1H), 8.50 (s, 1H), 8.30 (d, *J* = 7.2 Hz, 1H), 7.73 (m, 2H), 7.56 (m, 3H), 7.19 (s, 1H), 6.44 (d, *J* = 6.8 Hz, 1H), 6.20 (s, 1H), 5.67 (m, 1H), 5.43 (s, 2H), 3.94 (s, 3H), 1.94 (d, *J* = 6.8 Hz, 3H), 1.68 (m, 3H). ^{13}C NMR (100 MHz, CD_3OD, δ): 170.3, 138.4, 128.5, 125.8, 125.8, 125.8, 123.0, 123.0, 123.0, 123.0, 120.4, 120.4, 120.4, 120.4, 119.3, 119.3, 119.3, 112.8, 112.8, 112.8, 108.0, 80.0, 72.9, 55.2, 28.9, 27.9. ESI-HRMS (*m/z*): $[M-Na]^-$ calcd for $C_{26}H_{23}N_4O_9S$, 567.1180; found, 567.1186

Compound 9. To a solution of **16** (54.0 mg, 0.2 mmol), copper sulfate hydrate (50.0 mg, 0.2 mmol), and sodium ascorbate (80.0 mg, 0.4 mmol) in a 2:1:1 $THF/H_2O/CH_3OH$ mixture (20 mL), **15** (82.0 mg, 0.4 mmol) in THF (1 mL) was added dropwise. After being stirred at 40 °C for 12 h, the reaction mixture was concentrated. The residue was diluted with THF (10 mL). The solid was filtered off and the filtrate was concentrated in vacuo. The residue was then purified by column chromatography over silica gel using 1:3 methanol/methylene chloride as the eluent to give an off-white powder (63.7 mg, 67%). ^{1}H NMR (400 MHz, $CDCl_3/CD_3OD$ = 1:1, δ): 9.17 (d, *J* = 8.8 Hz, 1H), 8.52 (s, 1H), 8.30 (d, *J* = 6.8 Hz, 1H), 7.78 –7.71 (m, 2H), 7.60 –7.55 (m, 2H), 7.32 (d, *J* = 8.4 Hz, 1H), 7.16 (d, *J* = 8.4 Hz, 1H), 5.46 (s, 2H), 3.90 (s, 3H), 2.60 (s, 3H). ^{13}C NMR (100 MHz, CD_3OD, δ): 199.6, 153.1, 151.1, 140.2, 134.4, 132.6, 129.0, 128.1, 127.8, 127.0, 125.6, 124.8, 124.6, 124.5, 124.5, 114.3, 114.3, 112.2, 112.2, 77.7, 56.7, 26.6. ESI-HRMS (*m/z*): $[M-Na]^-$ calcd for $C_{22}H_{18}N_3O_6S$, 452.0916; found, 452.0911.

Compound 6. To a solution of **9** (0.15 g, 0.32 mmol) in anhydrous THF (10 mL), ammonium trifluoroacetate (0.21 g, 1.60 mmol) and sodium triacetoborohydrate (017 g, 0.80 mmol) were added. After being stirred at room temperature for 72 h, the mixture was concentrated in vacuo and purified by column chromatography over silica gel using 1:10 methanol/dichloromethane as the eluent to give the amine–trifluoroacetate salt as product. The amine–trifluoroacetate salt was dissolved in a saturated aqueous solution of sodium bicarbonate (~1.0 mL) to pH 6–7 and sodium chloride (0.20 g) was added. The precipitate formed was transferred into a filtration funnel, rinsed with water (2 × 2 mL), and dried for 30 min, rinsed again with ethyl acetate (3 × 15 mL), and dried under vacuum to afford the product as a white powder (97 mg, 64 %). ^{1}H NMR (400 MHz, D_2O, δ): 8.56 (d, J = 8.8 Hz, 1H), 8.29 (m, 2H), 7.77–7.66 (m, 4H), 7.50 (d, J = 3.6 Hz, 1H), 7.25 (m, 1H), 7.04 (m, 1H), 4.97(s, 2H), 3.97 (s, 4H), 2.66 (d, J = 2.4 Hz, 3H) . ^{13}C NMR (100 MHz, CD_3OD, δ): 154.1, 151.4, 135.4, 132.7, 131.5, 131.4, 131.2, 128.3, 127.9, 127.2, 126.5, 125.8, 124.9, 124.9, 124.7, 124.7, 114.5, 112.4, 77.9, 68.7, 56.8, 26.8. ESI-HRMS (*m/z*): [M-Na] $^-$ calcd for $C_{24}H_{22}F_3N_4O_7S$, 567.1167; found, 567.1175.

Compound 8. To a solution of **16** (0.18 g, 0.66 mmol), copper sulfate hydrate (0.13 g, 0.66 mmol), and sodium ascorbate (0.33 g, 1.32 mmol) in a 2:1:1 THF/H_2O/CH_3OH mixture (20 mL), **18** (0.18 g, 0.80 mmol) in THF (1 mL) was added dropwise. After being stirred at 40 °C for 12 h, the reaction mixture was concentrated. The residue was diluted with THF (10 mL). The solid was filtered off and the filtrate was concentrated in vacuo. The residue was then purified by column chromatography over silica gel using 1:3 methanol/methylene chloride as the eluent to give an off-white powder (0.25 g, 64%). ^{1}H NMR (400 MHz, CD_3OD, δ): 9.18 (d, J = 8.4 Hz, 1H), 8.51 (s, 1H), 8.30(d, J = 6.8 Hz, 1H), 7.80 - 7.51 (m, 5H), 7.30 (d, J = 8.4

Hz, 1H), 7.15(m, 1H), 5.45(s, 2H), 3.90 (s, 6H). ^{13}C NMR (100 MHz, $CDCl_3/CD_3OD$ = 1:1, δ): 167.7, 152.2, 149.7, 133.9, 130.4, 129.9, 129.8, 127.4, 127.3, 126.8, 126.2, 125.5, 124.5, 123.9, 123.9, 123.8, 113.5, 112.9, 62.8, 56.1, 52.3. ESI-HRMS (*m/z*): [M-Na] ⁻ calcd for $C_{22}H_{18}N_3O_7S$, 468.0860; found, 468.0865.

Compound 10. To a solution of **16** (0.18 g, 0.66 mmol), copper sulfate hydrate (0.13 g, 0.66 mmol), and sodium ascorbate (0.33 g, 1.32 mmol) in a 2:1:1 $THF/H_2O/CH_3OH$ mixture (20 mL), **19** (0.11 g, 0.80 mmol) in THF (1 mL) was added dropwise. After being stirred at 40 °C for 12 h, the reaction mixture was concentrated. The residue was rinsed with dichloromethane (2 × 15 mL) and combined with methanol (20 mL). The solid was filtered off and the filtrate was concentrated in vacuo. The residue was then purified by column chromatography over silica gel using 1:4 methanol/methylene chloride as the eluent to give an off-white powder (0.24 g, 89%).^{1}H NMR (400 MHz, $CDCl_3$), δ: 9.14 (d, *J* = 4.4 Hz, 1H), 8.47 (s, 1H), 8.27 (d, *J* = 6.8 Hz, 1H), 7.76 (m, 2H), 7.56 (m, 2H), 7.30 (m, 2H), 7.08 (d, *J* = 8.8 Hz, 2H), 6.97 (d, *J* = 7.2 Hz, 1H), 5.32 (s, 2H). ^{13}C NMR (100 MHz, $CDCl_3$, δ): 131.3, 131.2, 131.2, 131.2, 129.4, 128.3, 128.0, 127.4, 127.4, 126.0, 126.0, 123.6, 123.0, 116.7, 116.7, 116.7, 116.7, 116.7, 63.0. ESI-HRMS (*m/z*): [M-Na] ⁻ calcd for $C_{19}H_{14}N_3O_4S$, 380.0711; found, 380.0701.

MINP-COOH: To a 2.0 mL micellar solution of surfactant **1** (9.3 mg, 0.02 mmol) in D_2O, DVB (2.8 μL, 0.02 mmol), AIBN in DMSO (10 μL of 8.2 mg/mL, 0.0005 mmol), **2** in D_2O (10 μL, 0.0004 mmol) were added. The mixture was ultrasonicated for 10 min. Compound **3** (4.13 mg, 0.024 mmol), $CuCl_2$ in D_2O (10 μL of 6.7 mg/mL, 0.0005 mmol), and sodium ascorbate in D_2O (10 μL of 99 mg/mL, 0.005 mmol) were then added and the reaction mixture was stirred slowly at room temperature. After 12 h, compound **4** (10.6 mg, 0.04

mmol), $CuCl_2$ in D_2O (10 μL of 6.7 mg/mL, 0.0005 mmol), and sodium ascorbate in D_2O (10 μL of 99 mg/mL, 0.005 mmol) were added and the mixture was stirred for another 6 h. The reaction vial was sealed with a rubber stopper and the reaction mixture was purged with nitrogen for 15 min before it was stirred at 75 °C for 16 h. The resultant solution (2.0 mL) was cooled to room temperature and poured into acetone (8.0 mL). The precipitate formed was washed five times with 1:4 water/acetone mixture and dried overnight in the dark to give an off-white powder. The power was dissolved in Millipore water (1 mL) and irradiated in a Rayonet reactor for 12 h. Water was removed under reduced pressure and the residual sample was washed five times with 1:4 water/acetone mixture in a centrifuge tube and dried to give the product as a white powder (15 mg, 75 %).

MINP-CONHNaph: 1-Ethyl-3-(3-dimethylaminopropyl)carbodiimide (EDCI, 10 μL of 61.0 mg/mL in dry DMF, 0.004 mmol) was added to a stirred solution of MINP-COOH (20.0 mg, 0.0004 mmol) in dry DMF (1 mL) at 0˚C under nitrogen. After 2 h, 2-aminonaphthalene (10 μL of 56.2 mg/mL in DMF, 0.004 mmol) was added and the mixture was stirred for 24 h at room temperature. The mixture was concentrated in vacuo and poured into 2 mL of acetone. The precipitate was collected by centrifugation and rinsed several times with 2 mL of acetone to afford the product as an off-white powder (16 mg, 80 %).

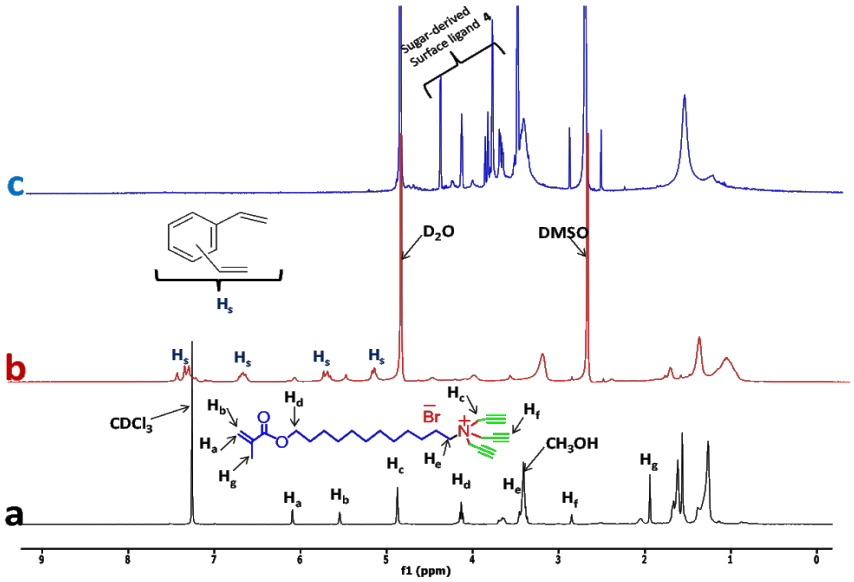

Figure 6. ^{1}H NMR spectra of **1** in $CDCl_3$ (black), alkynyl-SCM in D_2O (red), and MINP-COOH (blue) in D_2O

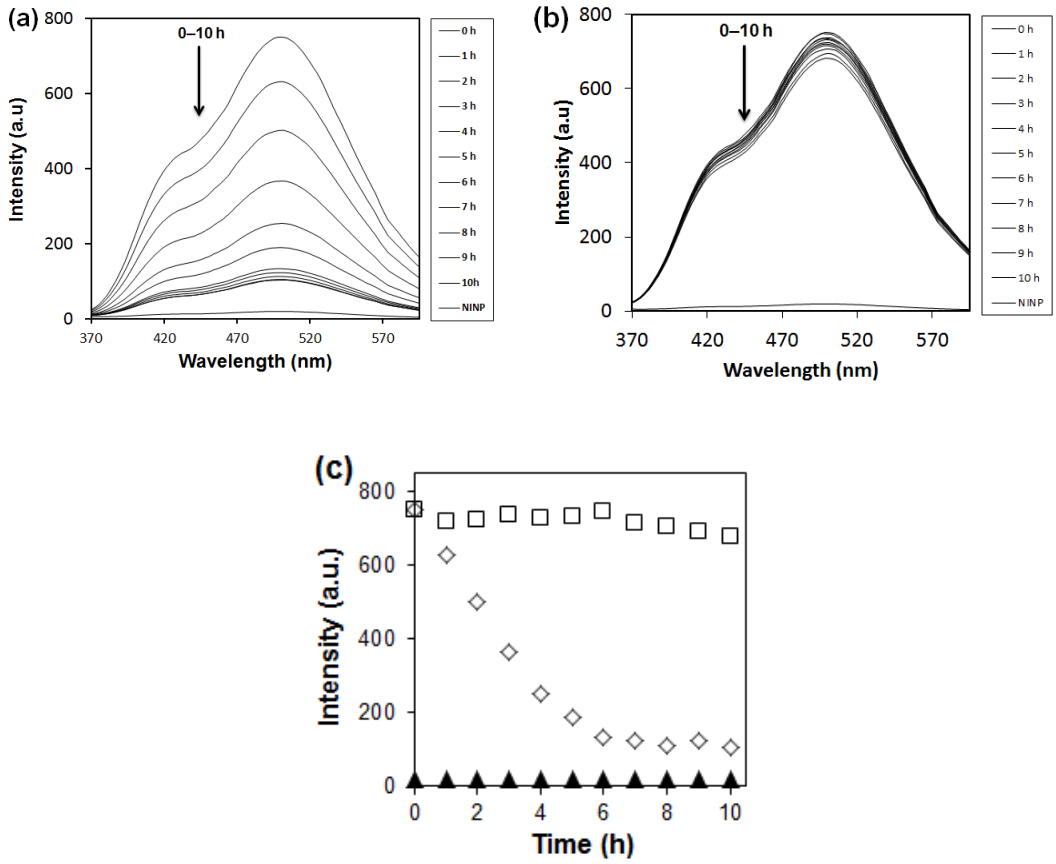

Figure 7. (a) Emission spectra of MINPs after different periods of time of UV irradiation, showing the release of nitroso derivative **5** to vacate the binding site of MINP. λ_{ex}= 295 nm, [MINPs] = 3 μM. (b) Emission spectra of MINPs without UV irradiation. λ_{ex}= 295 nm, [MINPs] = 3 μM. (c) Emission intensity at 497 nm of MINPs under irradiation (◇), MINPs without irradiation (□), and non-imprinted nanoparticles (i.e., nanoparticles prepared without template **2** or NINP) under irradiation (△) for comparison.

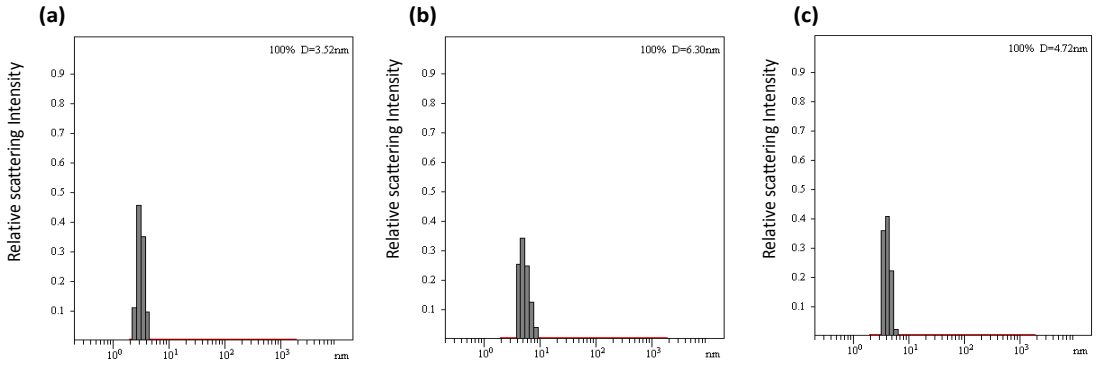

Figure 8. Distribution of the hydrodynamic diameters of the nanoparticles in water as determined by DLS for (a) alkynyl-SCM, (b) surface-functionalized SCM and (c) MINP-COOH after purification.

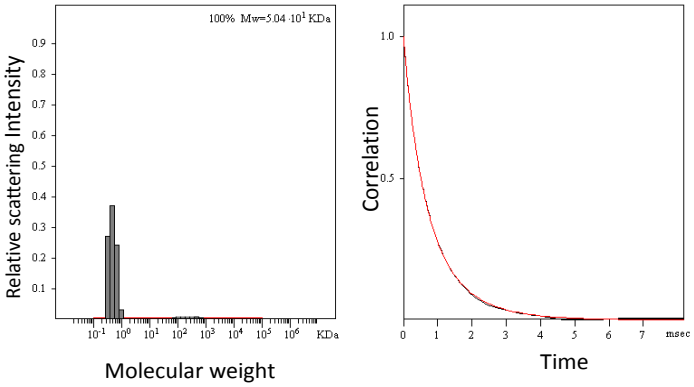

Figure 9. Distribution of the molecular weights of MINP-COOH and the correlation curves for DLS. The PRECISION DECONVOLVE program assumes the intensity of scattering is proportional to the mass of the particle squared. If each unit of building block for the MINP-COOH is assumed to contain one molecule of compound **1** (MW = 465 g/mol), 1.2 molecules of compound **3** (MW = 172 g/mol), one molecule of DVB (MW = 130 g/mol), 0.8 molecules of compound **4** (MW = 264 g/mol), and 0.02 molecules of methacrylic acid (MW = 86 g/mol), the molecular weight of MINP-COOH translates to 50 [= 50400/(465+1.2×172+130+0.8×264+0.02×86)] of such units.

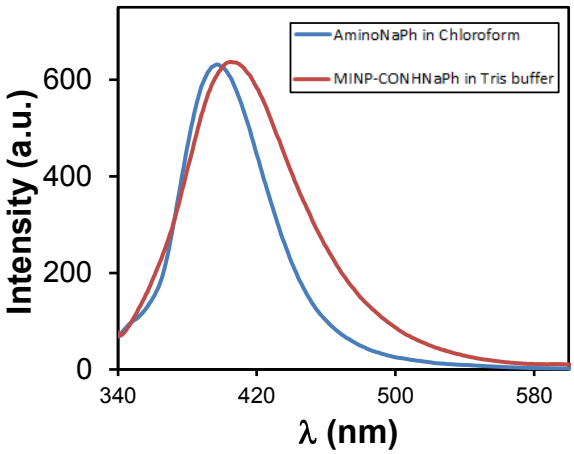

Figure 10. Fluorescence emission spectra of 2-aminonaphthalene in chloroform (red) and MINP-CONHNaph in 50 mM Tris buffer, pH 7.4 (blue). The excitation wavelength (λ_{ex}) was set at 300 nm. [naphthyl] = 2.5 μM.

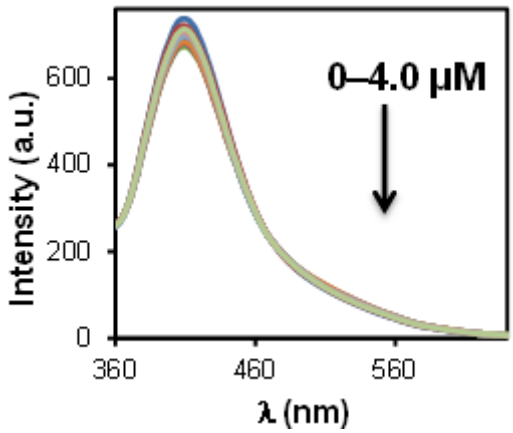

Figure 11. Fluorescence emission spectra of **6** (λ_{ex} = 300 nm) upon addition of different concentrations of MINP-COOH in citrate-phosphate buffer (pH 5.0), [**6**] = 0.50 μM.

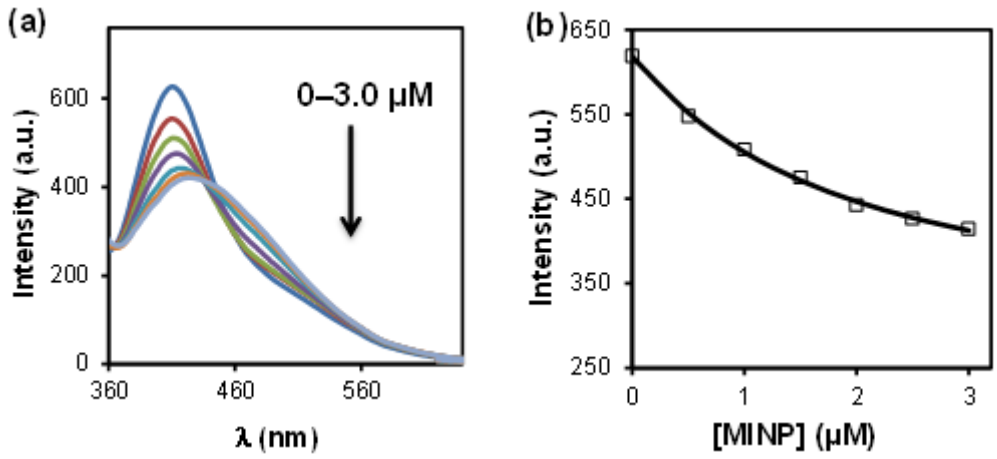

Figure 12. (a) Fluorescence emission spectra of **6** (λ_{ex} = 300 nm) upon addition of different concentrations of MINP-COOH in 10 mM citrate-phosphate buffer (pH 6.2). [**6**] = 0.50 μM. (b) Nonlinear least squares fitting of the emission intensity of **6** at 415 nm to a 1:1 binding isotherm; $K_a = 6.5 \pm 0.1 \times 10^5$ M^{-1}.

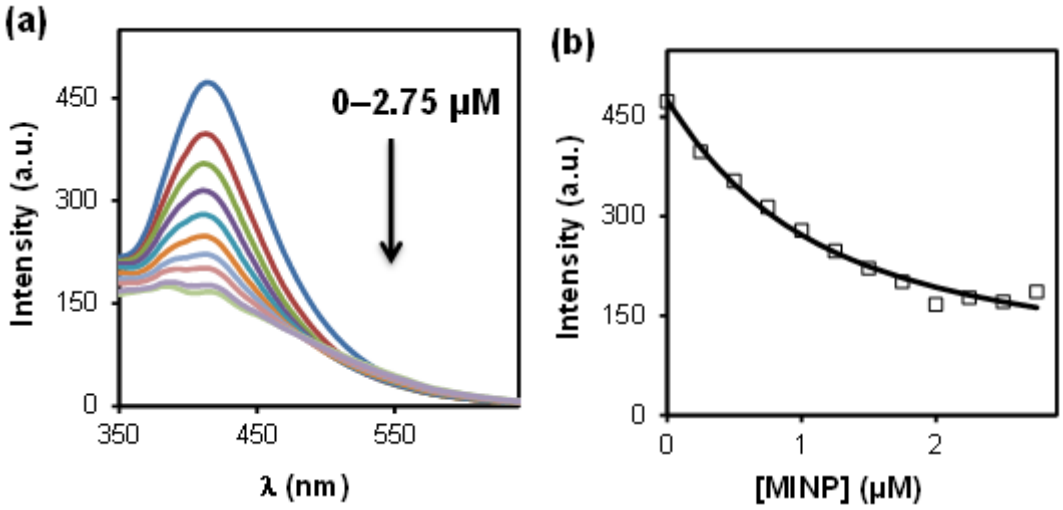

Figure 13. (a) Fluorescence emission spectra of **6** (λ_{ex} = 300 nm) upon addition of different concentrations of MINP-COOH in 50 mM Tris buffer (pH 8.5). [**6**] = 0.50 μM. (b) Nonlinear least squares fitting of the emission intensity of **6** at 415 nm to a 1:1 binding isotherm; $K_a = 1.2 \pm 0.3 \times 10^6$ M^{-1}.

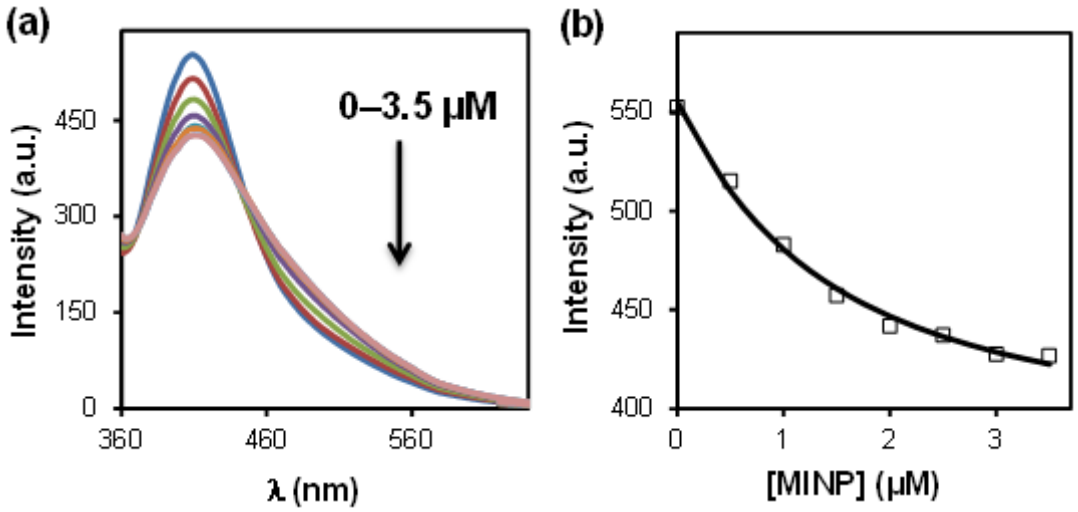

Figure 14. (a) Fluorescence emission spectra of **6** (λ_{ex} = 300 nm) upon addition of different concentrations of MINP-COOH in 50 mM Tris buffer (pH 9.5). [**6**] = 0.50 μM. (b) Nonlinear least squares fitting of the emission intensity of **6** at 415 nm to a 1:1 binding isotherm; K_a = $8.8 \pm 0.2 \times 10^5$ M^{-1}.

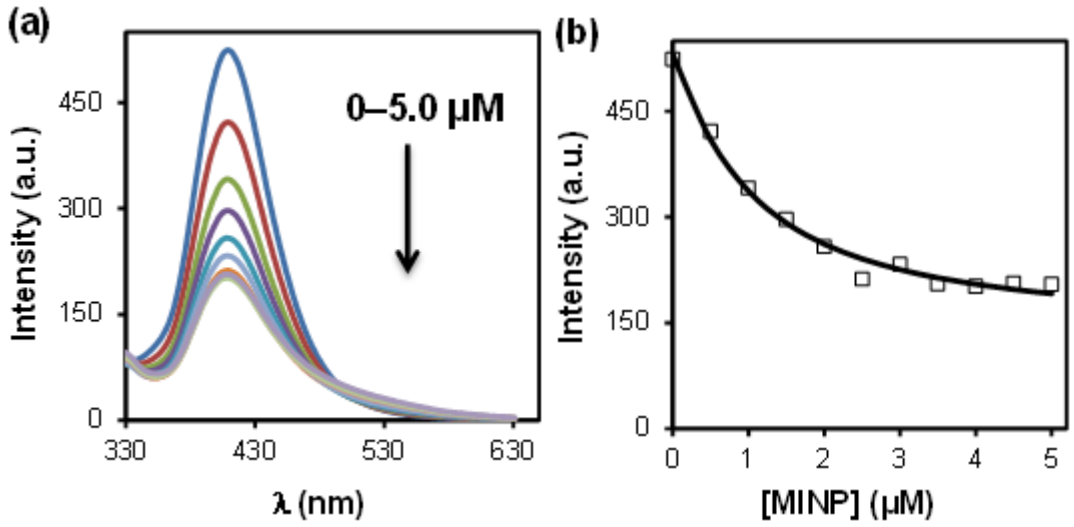

Figure 15. (a) Fluorescence emission spectra of **7** (λ_{ex} = 300 nm) upon addition of different concentrations of MINP-COOH in 10 mM citrate-phosphate buffer (pH 2.2). [**7**] = 0.50 μM. (b) Nonlinear least squares fitting of the emission intensity of **7** at 410 nm to a 1:1 binding isotherm; $K_a = 1.3 \pm 0.3 \times 10^6$ M^{-1}.

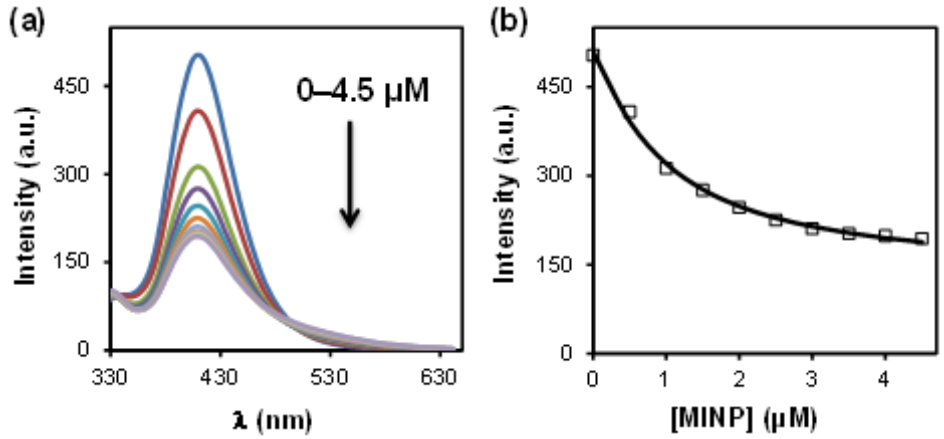

Figure 16. (a) Fluorescence emission spectra of **7** (λ_{ex} = 300 nm) upon addition of different concentrations of MINP-COOH in 10 mM citrate-phosphate buffer (pH 2.6). [**7**] = 0.50 μM. (b) Nonlinear least squares fitting of the emission intensity of **7** at 410 nm to a 1:1 binding isotherm; $K_a = 1.3 \pm 0.2 \times 10^6$ M^{-1}.

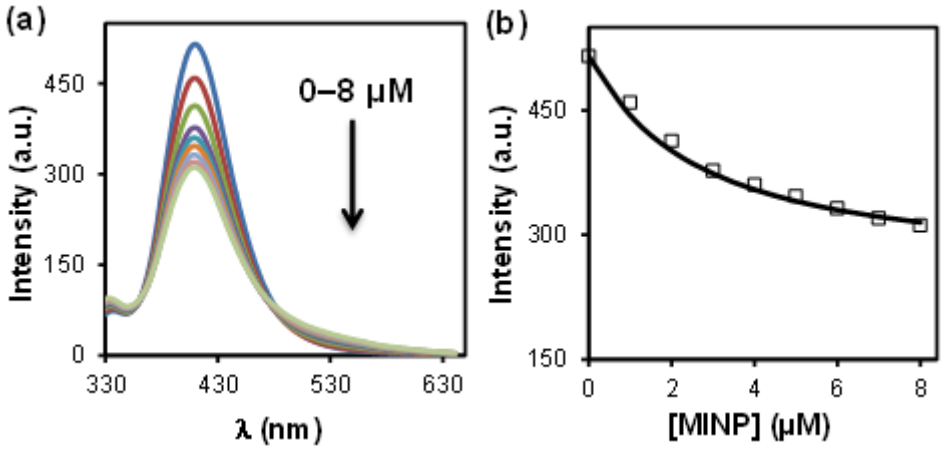

Figure 17. (a) Fluorescence emission spectra of **7** (λ_{ex} = 300 nm) upon addition of different concentrations of MINP-COOH in 10 mM citrate-phosphate buffer (pH 3.0). [**7**] = 0.50 μM. (b) Nonlinear least squares fitting of the emission intensity of **7** at 410 nm to a 1:1 binding isotherm; $K_a = 4.3 \pm 0.1 \times 10^5$ M^{-1}.

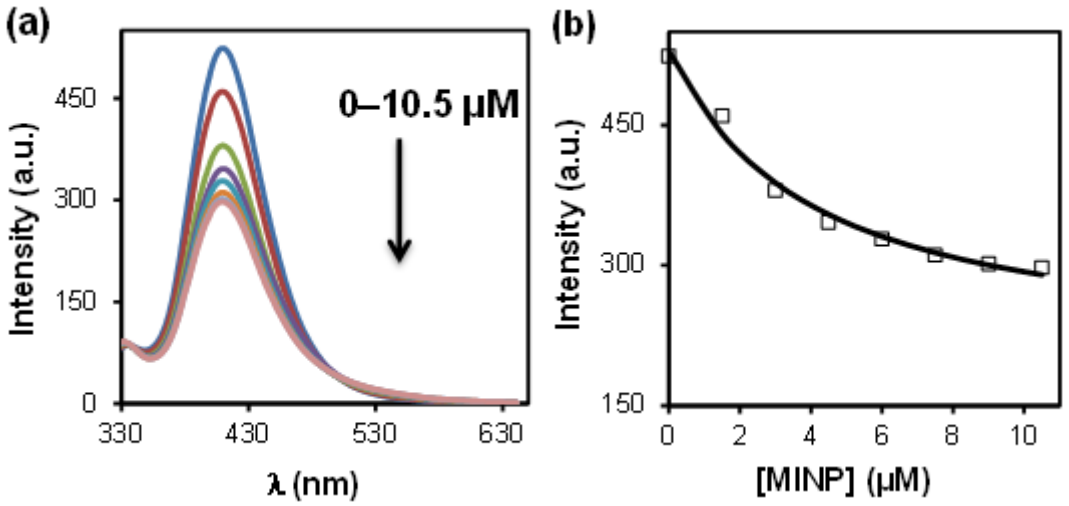

Figure 18. (a) Fluorescence emission spectra of **7** (λ_{ex} = 300 nm) upon addition of different concentrations of MINP-COOH in 10 mM citrate-phosphate buffer (pH 4.0). [**7**] = 0.50 μM. (b) Nonlinear least squares fitting of the emission intensity of **7** at 410 nm to a 1:1 binding isotherm; $K_a = 2.7 \pm 0.7 \times 10^5$ M^{-1}.

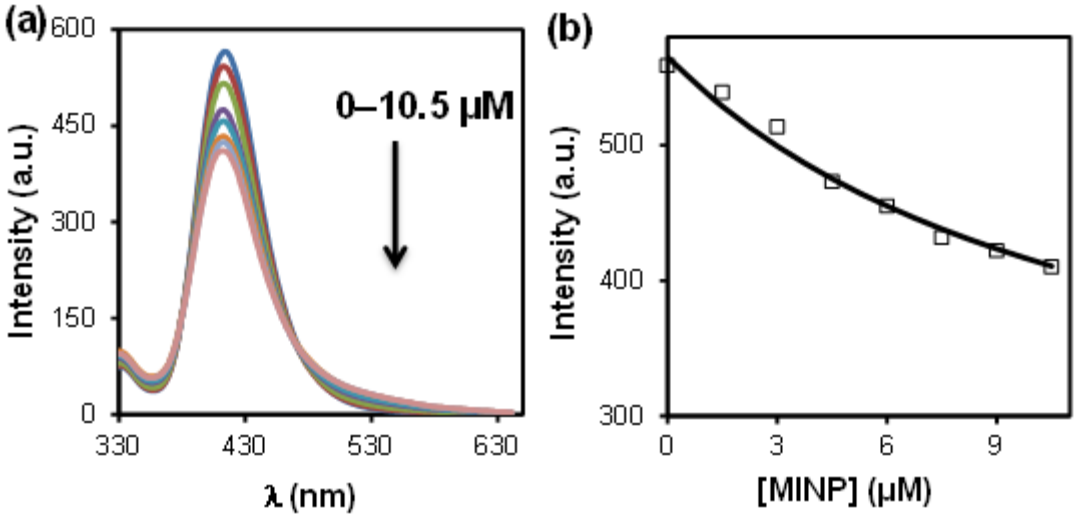

Figure 19. (a) Fluorescence emission spectra of **7** (λ_{ex} = 300 nm) upon addition of different concentrations of MINP-COOH in 10 mM citrate-phosphate buffer (pH 5.0). [**7**] = 0.50 μM. (b) Nonlinear least squares fitting of the emission intensity of **7** at 410 nm to a 1:1 binding isotherm; $K_a = 8.6 \pm 0.4 \times 10^4$ M^{-1}.

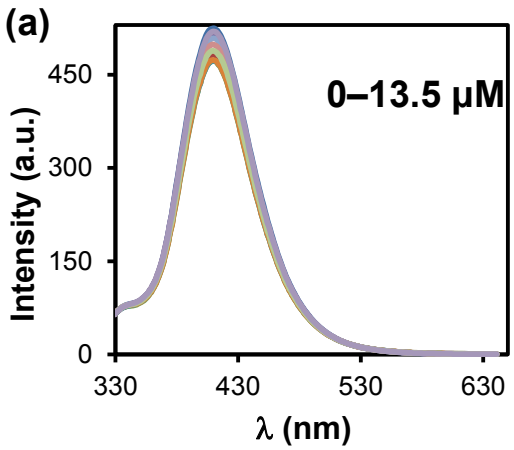

Figure 20. (a) Fluorescence emission spectra of **7** (λ_{ex} = 300 nm) upon addition of different concentrations of MINP-COOH in 10 mM citrate-phosphate buffer (pH 6.2). [**7**] = 0.50 μM.

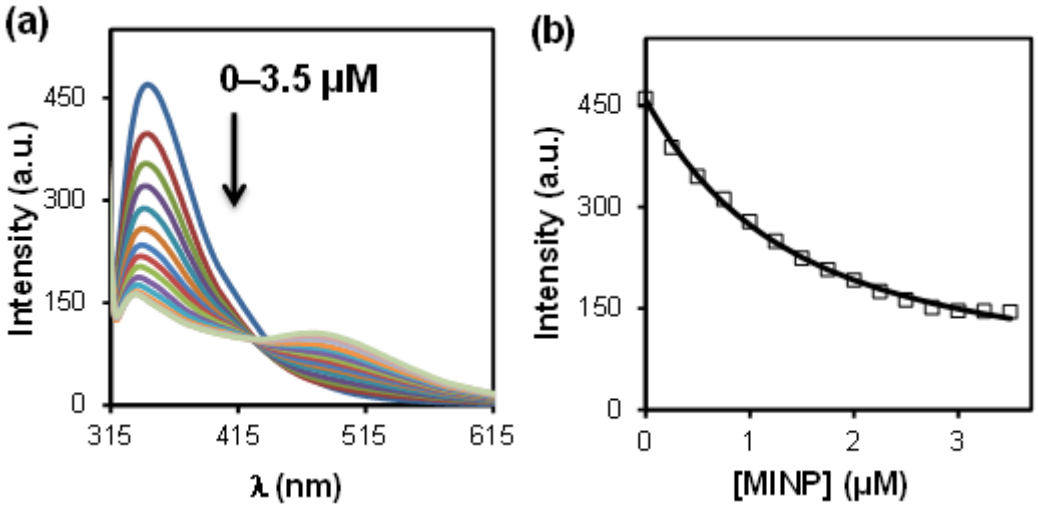

Figure 21. (a) Fluorescence emission spectra of **8** (λ_{ex} = 300 nm) upon addition of different concentrations of MINP-COOH in 10 mM sodium citrate buffer (pH 3.0). [**8**] = 0.50 μM. (b) Nonlinear least squares fitting of the emission intensity of **8** at 350 nm to a 1:1 binding isotherm; $K_a = 9.5 \pm 0.8 \times 10^5\ M^{-1}$.

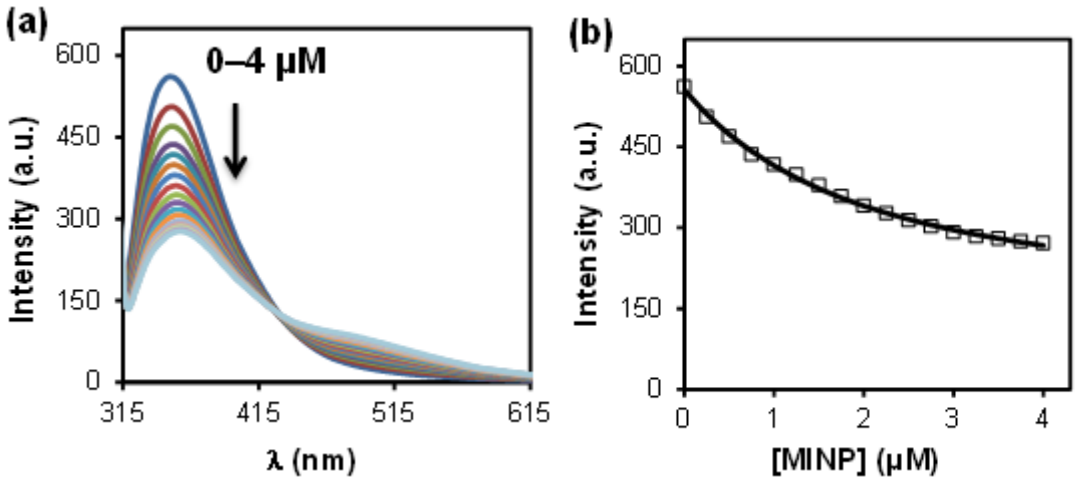

Figure 22. (a) Fluorescence emission spectra of **8** (λ_{ex} = 300 nm) upon addition of different concentrations of MINP-COOH in 50 mM Tris buffer (pH 7.4). [**8**] = 0.50 μM. (b) Nonlinear least squares fitting of the emission intensity of **8** at 350 nm to a 1:1 binding isotherm; K_a = 6.3 ± 0.6 × 10^5 M^{-1}.

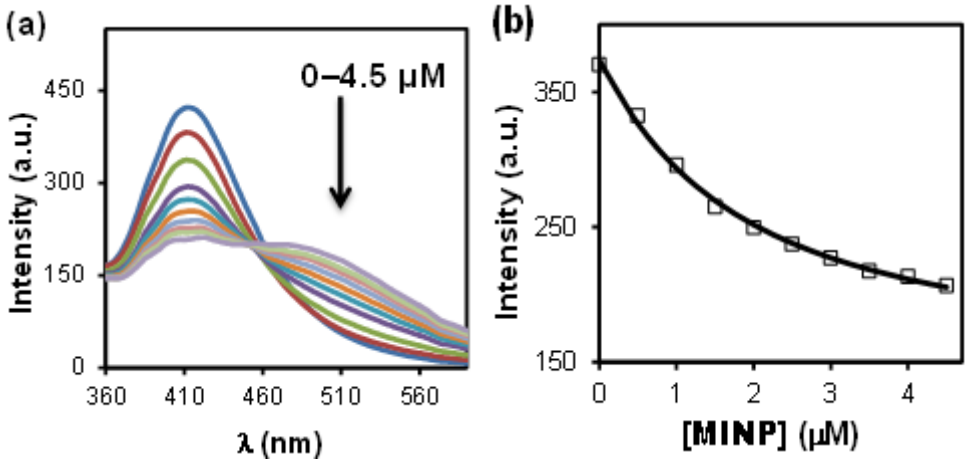

Figure 23. (a) Fluorescence emission spectra of **9** (λ_{ex} = 300 nm) upon addition of different concentrations of MINP-COOH in 10 mM sodium citrate buffer (pH 3.0). [**9**] = 0.50 μM. (b) Nonlinear least squares fitting of the emission intensity of **9** at 350 nm to a 1:1 binding isotherm; K_a = 6.4 ± 0.8 × 10^5 M^{-1}.

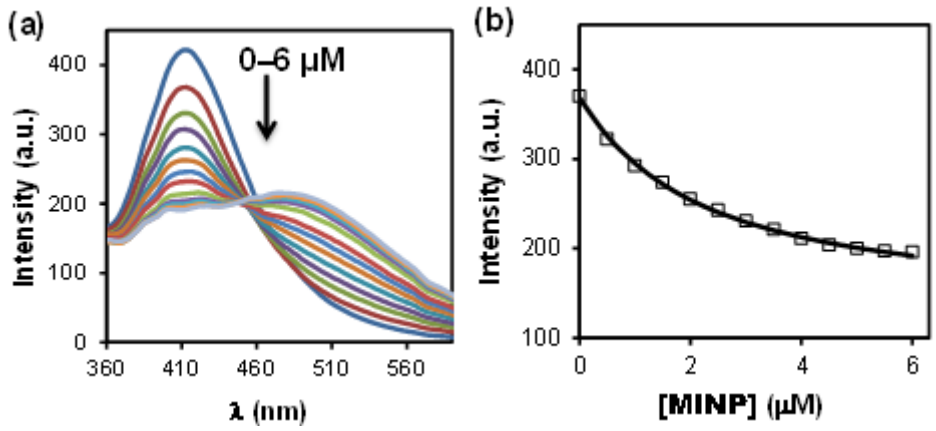

Figure 24. (a) Fluorescence emission spectra of **9** (λ_{ex} = 300 nm) upon addition of different concentrations of MINP-COOH in 50 mM Tris buffer (pH 7.4). [**9**] = 0.50 μM. (b) Nonlinear least squares fitting of the emission intensity of **9** at 350 nm to a 1:1 binding isotherm; K_a = $5.4 \pm 0.4 \times 10^5$ M^{-1}.

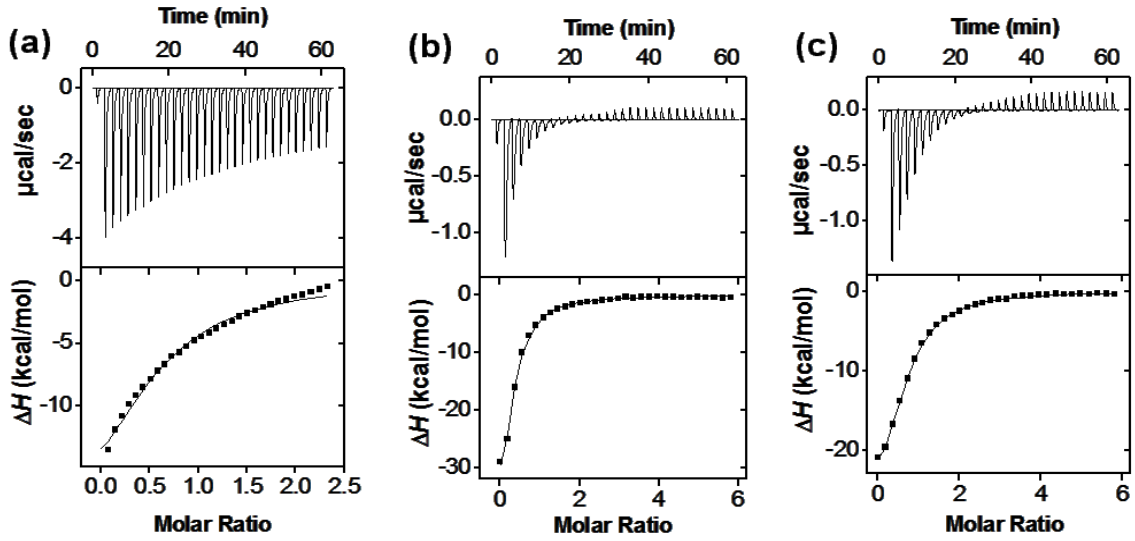

Figure 25. ITC titration curves obtained at 298 K for the binding of (a) **7** (0.5 mM) by MINP-COOH (50 μM); (b) **8** (0.2 mM) by MINP-COOH (8 μM); and (c) **9** (0.2 mM) by MINP-COOH (8 μM) in 50 mM Tris buffer (pH 7.4). The data correspond to entries 2, 3, and 4 respectively, in Table 1. The top panel shows the raw calorimetric data. The area under each

peak represents the amount of heat generated at each ejection and is plotted against the molar ratio of MINP to the substrate. The solid line is the best fit of the experimental data to the sequential binding of N equal and independent binding sites on the MINP. The heat of dilution for the substrate, obtained by adding the substrate to the buffer, was subtracted from the heat released during the binding. Binding parameters were auto-generated after curve fitting using Microcal Origin 7.

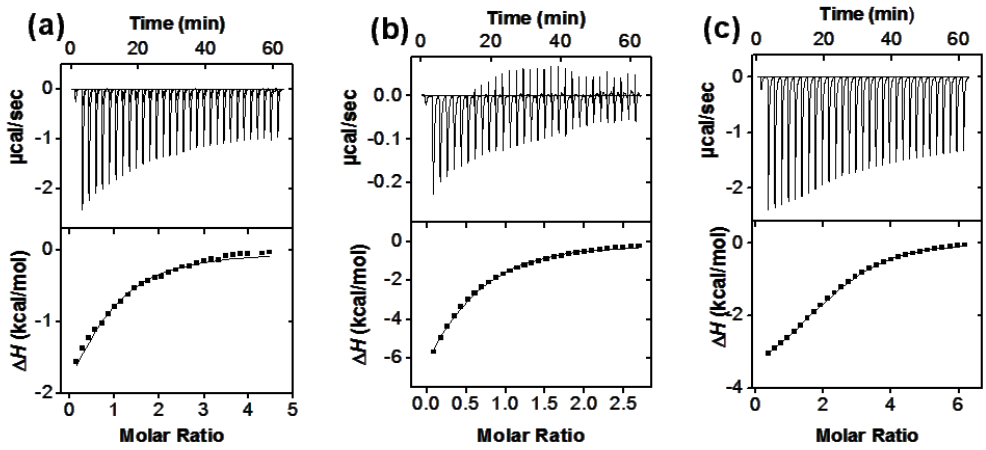

Figure 26. ITC titration curves obtained at 298 K for the binding of (a) **10** (2 mM) by MINP-COOH (0.1 mM); (b) **11** (10 µM) by MINP-COOH (10 µM); and (c) **12** (0.8 mM) by MINP-COOH (30 µM) in 50 mM Tris buffer (pH 7.4). The data correspond to entries 5, 6, and 7 respectively, in Table 1. The top panel shows the raw calorimetric data. The area under each peak represents the amount of heat generated at each ejection and is plotted against the molar ratio of MINP to the substrate. The solid line is the best fit of the experimental data to the sequential binding of N equal and independent binding sites on the MINP. The heat of dilution for the substrate, obtained by adding the substrate to the buffer, was subtracted from the heat released during the binding. Binding parameters were auto-generated after curve fitting using Microcal Origin 7.

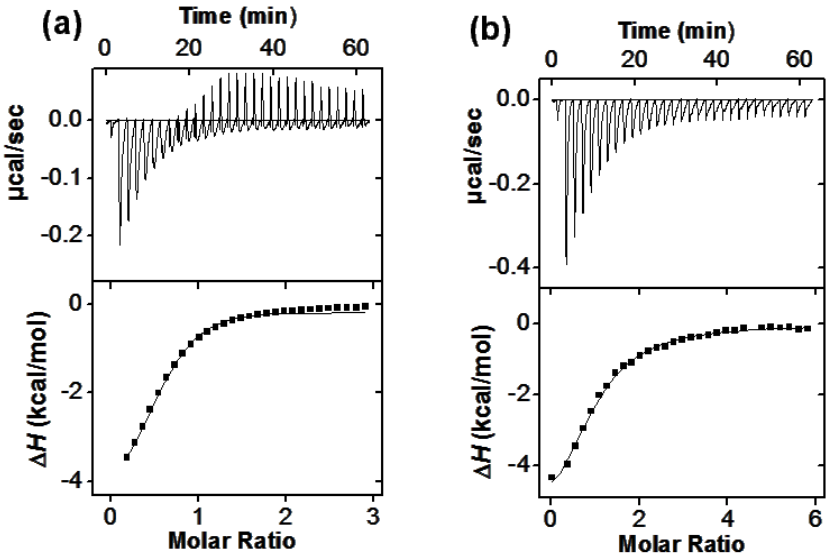

Figure 27. ITC titration curves obtained at 298 K for the binding of (a) **6** (0.25 mM) by MINP-CONHNaph (20 µM); and (b) **12** (0.25 mM) by MINP-CONHNaph (10 µM) in 50 mM Tris buffer (pH 7.4). The data correspond to entries 8 and 9, respectively, in Table 1. The top panel shows the raw calorimetric data. The area under each peak represents the amount of heat generated at each ejection and is plotted against the molar ratio of MINP to the substrate. The solid line is the best fit of the experimental data to the sequential binding of N equal and independent binding sites on the MINP. The heat of dilution for the substrate, obtained by adding the substrate to the buffer, was subtracted from the heat released during the binding. Binding parameters were auto-generated after curve fitting using Microcal Origin 7.

^{1}H NMR of compound **2**

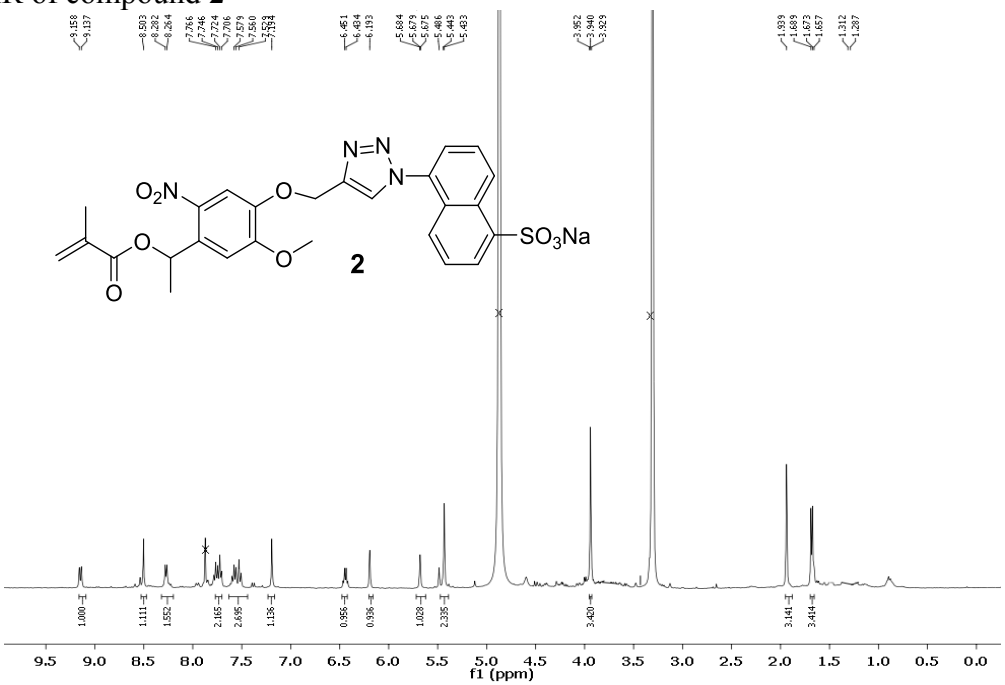

^{13}C NMR of compound **2**

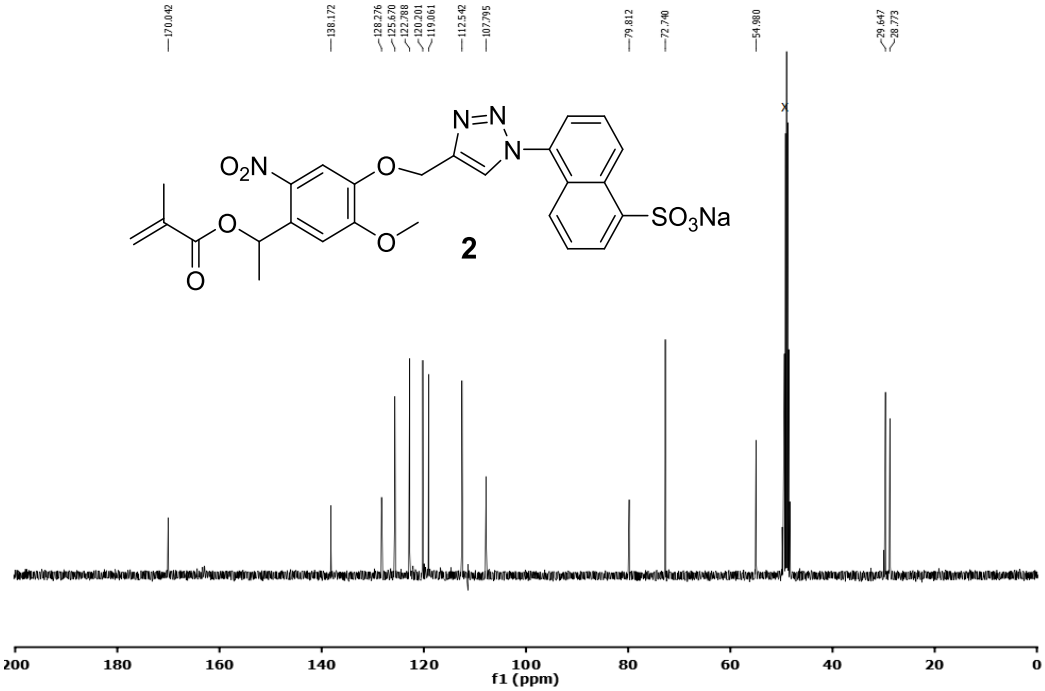

[1] H NMR of compound **6**

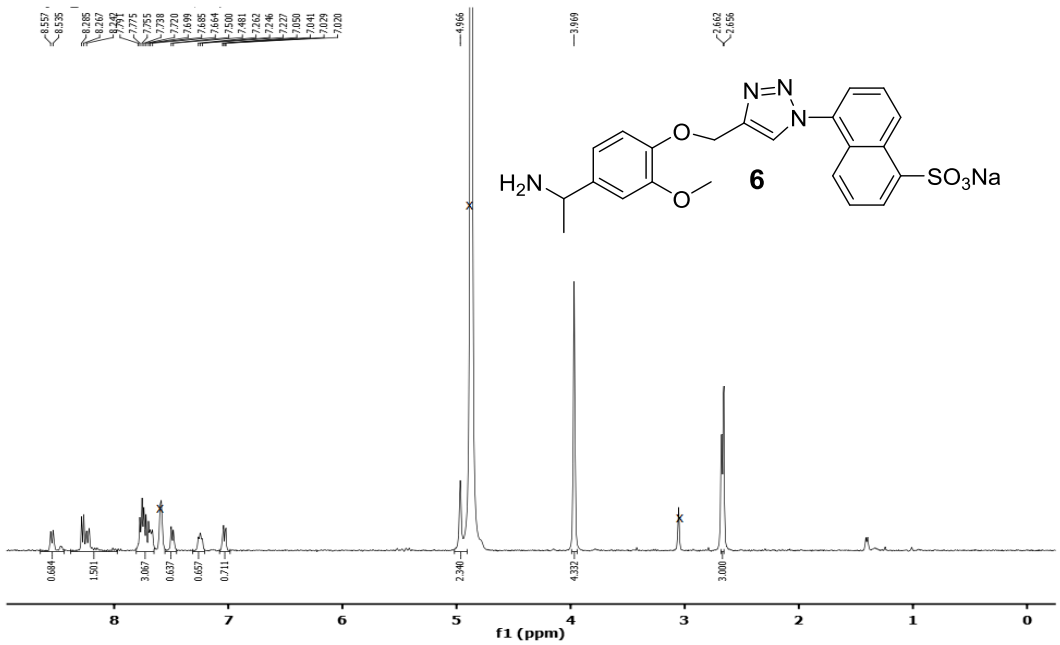

[13] C NMR of compound **6**

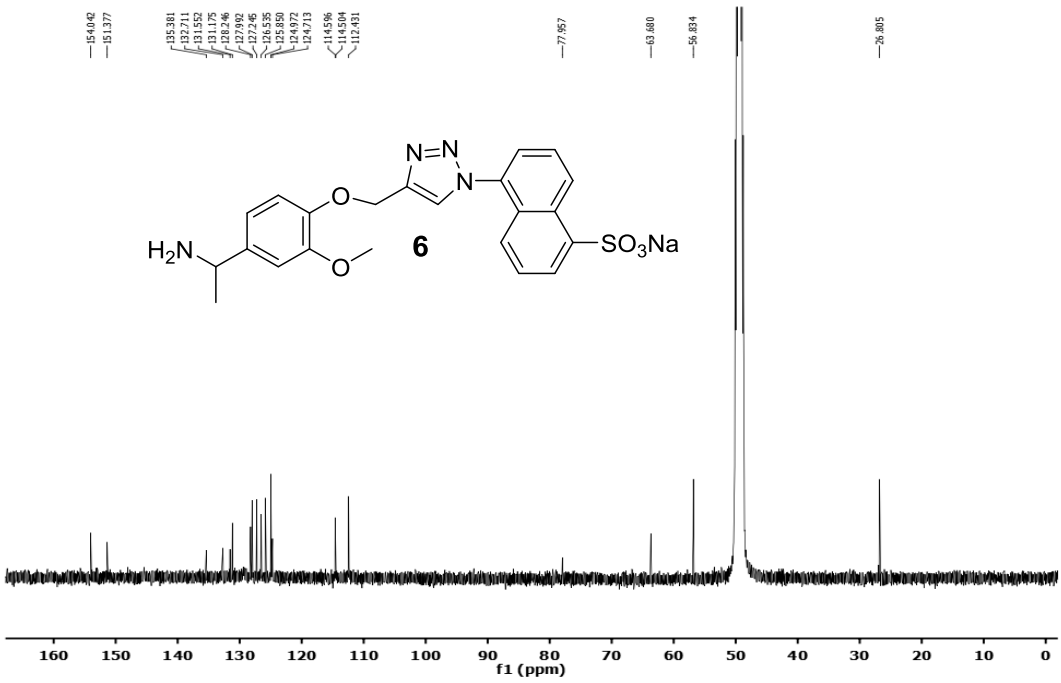

^{1}H NMR of compound **8**

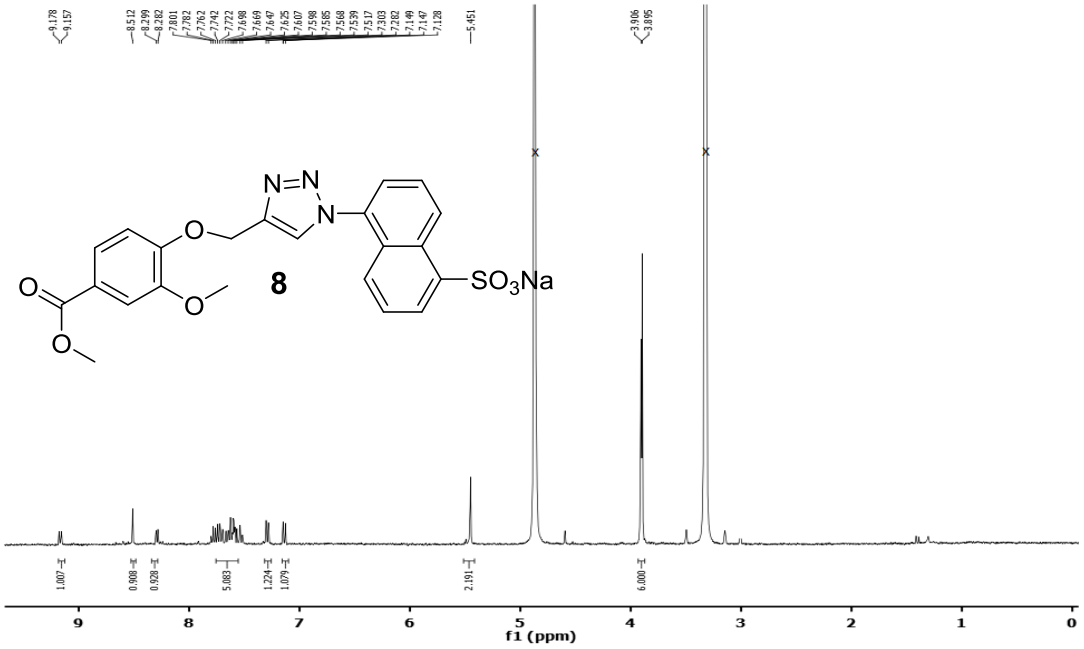

^{13}C NMR of compound **8**

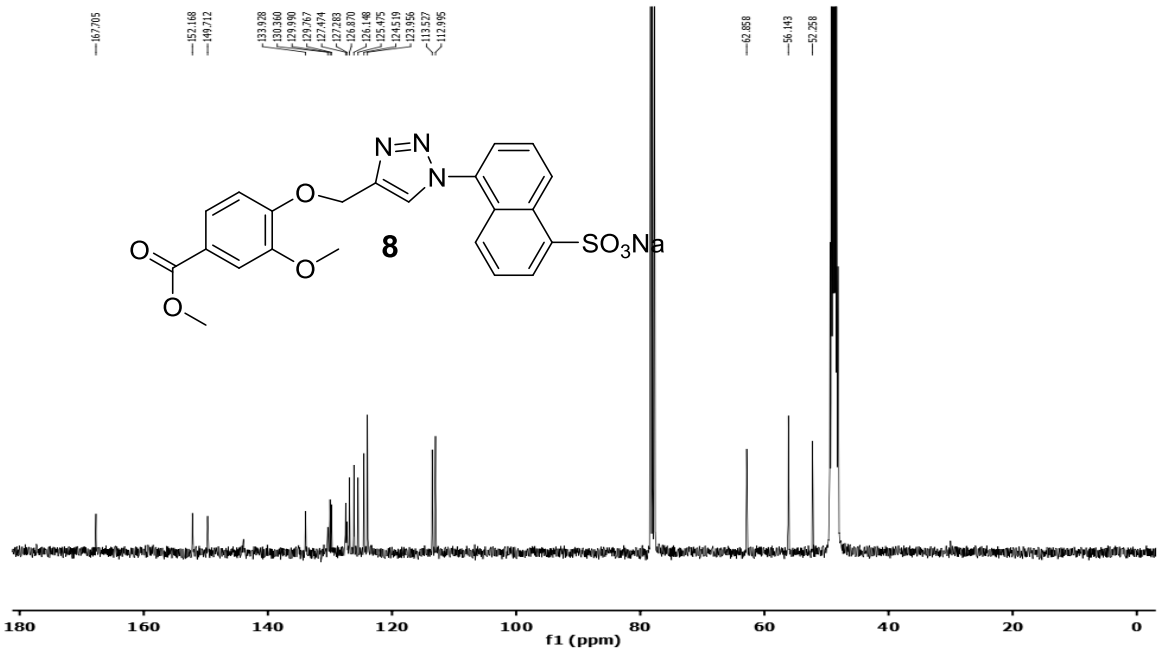

[1] H NMR of compound **9**

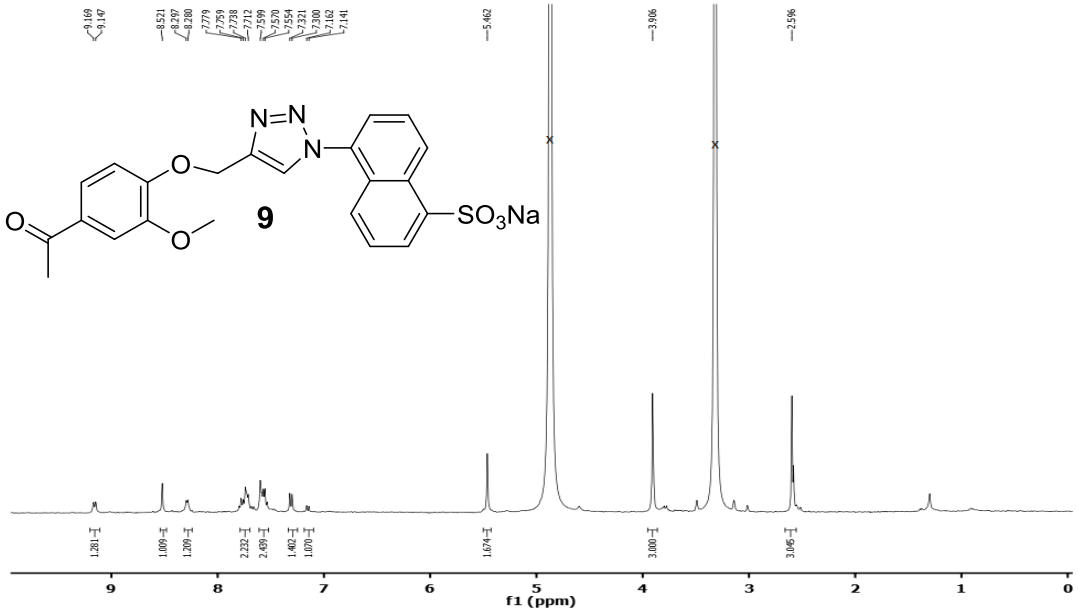

[13] C NMR of compound **9**

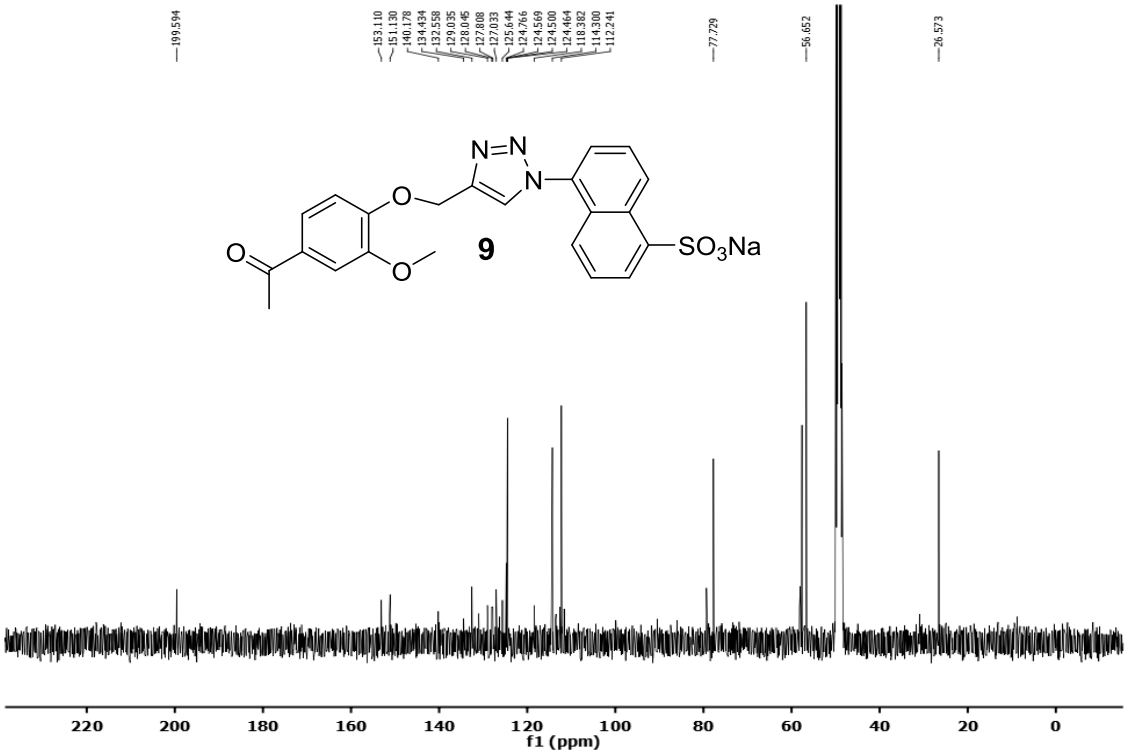

^{1}H NMR of compound **10**

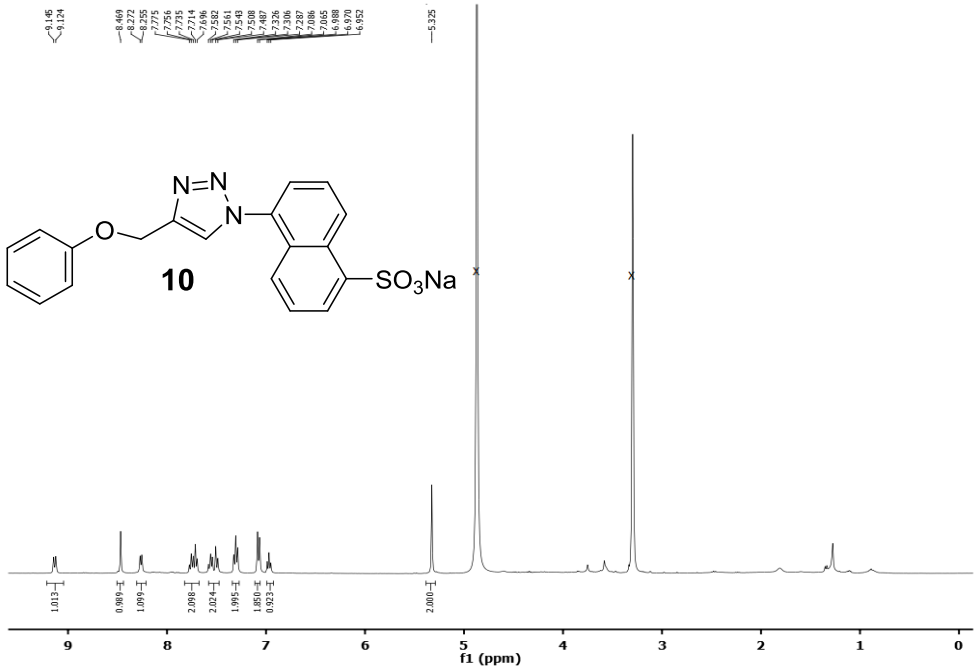

^{13}C NMR of compound **10**

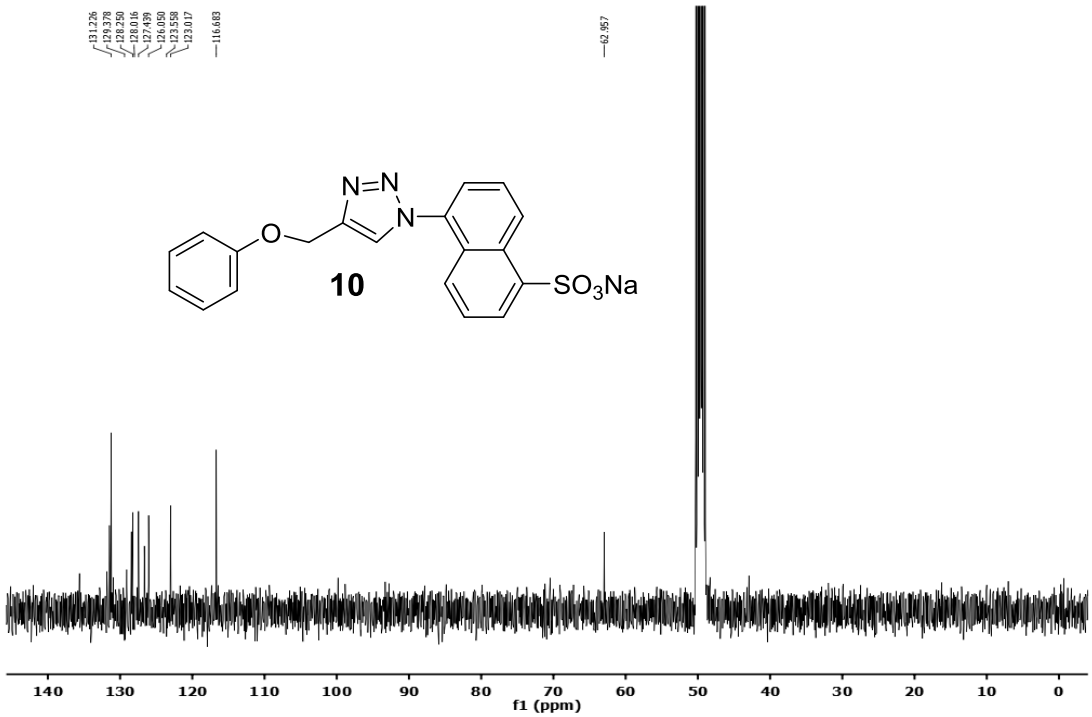

Notes and References

(1) (a) J. L. Atwood, J. M. Lehn, *Comprehensive Supramolecular Chemistry*, Pergamon, New York, **1996**, p; b) J. W. Steed, P. A. Gale, *Supramolecular Chemistry: From Molecules to Nanomaterials*, Wiley, Weinheim, **2012**, p; c) H.-J. Schneider, A. K. Yatsimirsky, *Principles and methods in supramolecular chemistry*, Wiley, New York, **2000**, p.

(2) (a) G. Wulff, *Angew. Chem. Int. Ed. Engl.* **1995**, *34*, 1812-1832; b) G. Wulff, *Chem. Rev.* **2001**, *102*, 1-28; c) K. Haupt, K. Mosbach, *Chem. Rev.* **2000**, *100*, 2495-2504; d) K. J. Shea, *Trends Polym. Sci.* **1994**, *2*, 166-173; e) B. Sellergren, *Molecularly imprinted polymers: man-made mimics of antibodies and their applications in analytical chemistry*, Elsevier, Amsterdam, **2001**, p; f) B. Sellergren, *Angew. Chem. Int. Ed.* **2000**, *39*, 1031-1037; g) M. Komiyama, *Molecular imprinting: from fundamentals to applications*, Wiley-VCH, Weinheim, **2003**, p; h) M. Yan, O. Ramström, *Molecularly imprinted materials: science and technology*, Marcel Dekker, New York, **2005**, p; i) C. Alexander, H. S. Andersson, L. I. Andersson, R. J. Ansell, N. Kirsch, I. A. Nicholls, J. O'Mahony, M. J. Whitcombe, *J. Mol. Recognit.* **2006**, *19*, 106-180.

(3) G. Wulff, A. Sarhan, K. Zabrocki, *Tetrahedron Lett.* **1973**, *14*, 4329-4332.

(4) B. Sellergren, M. Lepistoe, K. Mosbach, *J. Am. Chem. Soc.* **1988**, *110*, 5853-5860.

(5) (a) S. C. Zimmerman, M. S. Wendland, N. A. Rakow, I. Zharov, K. S. Suslick, *Nature* **2002**, *418*, 399-403; b) S. C. Zimmerman, I. Zharov, M. S. Wendland, N. A. Rakow, K. S. Suslick, *J. Am. Chem. Soc.* **2003**, *125*, 13504-13518.

(6) X. Wu, W. R. Carroll, K. D. Shimizu, *Chem. Mater.* **2008**, *20*, 4335-4346.

(7) S. C. Zimmerman, N. G. Lemcoff, *Chem. Commun.* **2004**, 5-14.

(8) (a) S. McNiven, Y. Yokobayashi, S. H. Cheong, I. Karube, *Chem. Lett.* **1997**, *26*, 1297-1298; b) N. Kirsch, C. Alexander, M. Lübke, M. J. Whitcombe, E. N. Vulfson, *Polymer* **2000**, *41*, 5583-5590; c) R. J. Umpleby, G. T. Rushton, R. N. Shah, A. M. Rampey, J. C. Bradshaw, J. K. Berch, K. D. Shimizu, *Macromolecules* **2001**, *34*, 8446-8452; d) B. Sellergren, *Macromolecules* **2006**, *39*, 6306-6309; e) T. Takeuchi, N. Murase, H. Maki, T. Mukawa, H. Shinmori, *Org. Biomol. Chem.* **2006**, *4*, 565-568.

(9) (a) Y. Hoshino, T. Kodama, Y. Okahata, K. J. Shea, *J. Am. Chem. Soc.* **2008**, *130*, 15242-15243; b) A. Cutivet, C. Schembri, J. Kovensky, K. Haupt, *J. Am. Chem. Soc.* **2009**, *131*, 14699-14702; c) K. G. Yang, M. M. Berg, C. S. Zhao, L. Ye, *Macromolecules* **2009**, *42*, 8739-8746; d) Z. Y. Zeng, J. Patel, S. H. Lee, M. McCallum, A. Tyagi, M. D. Yan, K. J. Shea, *J. Am. Chem. Soc.* **2012**, *134*, 2681-2690; e) Y. Ma, G. Q. Pan, Y. Zhang, X. Z. Guo, H. Q. Zhang, *Angew. Chem. Int. Ed.* **2013**, *52*, 1511-1514.

(10) a) S. Zhang, Y. Zhao, *Macromolecules* **2010**, *43*, 4020-4022; b) S. Zhang, Y. Zhao, *J. Am. Chem. Soc.* **2010**, *132*, 10642-10644; c) X. Li, Y. Zhao, *Bioconjugate Chem.* **2012**, *23*, 1721-1725; d) H.-Q. Peng, Y.-Z. Chen, Y. Zhao, Q.-Z. Yang, L.-Z. Wu, C.-H. Tung, L.-P. Zhang, Q.-X. Tong, *Angew. Chem. Int. Ed.* **2012**, *51*, 2088-2092; e) S. Zhang, Y. Zhao, *Chem. Commun.* **2012**, *48*, 9998-10000; f) Y.-Z. Chen, P.-Z. Chen, H.-Q. Peng, Y. Zhao, H.-Y. Ding, L.-Z. Wu, C.-H. Tung, Q.-Z. Yang, *Chem. Commun.* **2013**, *49*, 5877-5879; g) G. Chadha, Y. Zhao, *Org. Biomol. Chem.* **2013**, *11*, 6849-6855.

(11) (a) J. K. Awino, Y. Zhao, *J. Am. Chem. Soc.* **2013**, *135*, 12552-12555; b) J. K. Awino, Y. Zhao, *Chem. Commun.* **2014**, *50*, 5752-5755.

(12) G. V. Oshovsky, D. N. Reinhoudt, W. Verboom, *Angew. Chem. Int. Ed.* **2007**, *46*, 2366-2393.

(13) (a) A. Ben-Naim, *Hydrophobic interactions*, Plenum Press, New York, **1980**, p. xiii, 311 p; b) C. Tanford, *The Hydrophobic Effect: Formation of Micelles and Biological Membranes*, Krieger, Malabar, Fla., **1991**, p. ix, 233 p; c) W. Blokzijl, J. B. F. N. Engberts, *Angew. Chem. Int. Ed. Engl.* **1993**, *32*, 1545-1579.

(14) The cross-linking chemistry and covalent structure of the SCMs have been previously characterized by mass spectrometry and TEM, see ref 11a for details.

(15) I. Gitlin, J. D. Carbeck, G. M. Whitesides, *Angew. Chem. Int. Ed.* **2006**, *45*, 3022-3060.

(16) S.-J. Moon, J. W. Jeon, H. Kim, M. P. Suh, J. Suh, *J. Am. Chem. Soc.* **2000**, *122*, 7742-7749.

(17) B. Sellergren, K. J. Shea, *J. Chromatogr. A* **1993**, *654*, 17-28.

(18) D. D. Perrin, *Dissociation constants of organic bases in aqueous solution*, Butterworths, London, **1965**, p.

(19) F. H. Westheimer, *Tetrahedron* **1995**, *51*, 3-20.

(20) M. M. Byrne, N. H. P. Smith, *J. Chem. Soc. B* **1968**, 809-812.

(21) L. Widanapathirana, X. Li, Y. Zhao, *Org. Biomol. Chem.* **2012**, *10*, 5077-5083.

(22) Y. Zhao, H. Cho, L. Widanapathirana, S. Zhang, *Acc. Chem. Res.* **2013**, *46*, 2763-2772.

(23) As discussed in the previous section, the weak binding for 7 under pH 7.4 was caused by the deprotonation of both MINP-COOH and 7 at this pH. In order to bind, both have to undergo an unfavorable protonation under this condition.

(24) M. H. Abraham, *J. Am. Chem. Soc.* **1982**, *104*, 2085-2094.

(25) D. Chandler, *Nature* **2005**, *437*, 640-647.

(26) a) X. Li, Y. Zhao, *Langmuir* **2012**, *28*, 4152-4159; b) G. Chadha, Y. Zhao, *Chem. Commun.* **2014**, *50*, 2718-2720.

(27) Awino, J. K.; Zhao, Y. *J Am Chem Soc* **2013**, *135*, 12552.

(28) Zhang, S. Y.; Zhao, Y. *J Am Chem Soc* **2010**, *132*, 10642.

(29) Li, X.; Zhao, Y. *Bioconjugate Chem* **2012**, *23*, 1721.

(30) Awino, J. K.; Zhao, Y. *Chem Commun* **2014**, *50*, 5752.

(31) Oropeza, C.; Alpizar, L.; Loyolavargas, V. M.; Quiroz, J.; Scorer, K. N. *J Chromatogr* **1988**, *456*, 405.

(32) Hans, R. H.; Guantai, E. M.; Lategan, C.; Smith, P. J.; Wan, B. J.; Franzblau, S. G.; Gut, J.; Rosenthal, P. J.; Chibale, K. *Bioorg Med Chem Lett* **2010**, *20*, 942.

(33) Umeda, N.; Ueno, T.; Pohlmeyer, C.; Nagano, T.; Inoue, T. *J Am Chem Soc* **2011**, *133*, 12.

(34) Kaneko, S.; Nakayama, H.; Yoshino, Y.; Fushimi, D.; Yamaguchi, K.; Horiike, Y.; Nakanishi, J. *Phys Chem Chem Phys* **2011**, *13*, 4051.

(35) Sato, S.; Aoyama, H.; Miyachi, H.; Naito, M.; Hashimoto, Y. *Bioorg Med Chem Lett* **2008**, *18*, 3354.

(36) Sivakumar, S.; Reddy, M. L. P.; Cowley, A. H.; Vasudevan, K. V. *Dalton T* **2010**, *39*, 776.

(37) Pham, H. T.; Hanson, R. N.; Olmsted, S. L.; Kozhushnyan, A.; Visentin, A.; Weglinsky, P. J.; Massero, C.; Bailey, K. *Tetrahedron Lett* **2011**, *52*, 1053.

(38) Orbisaglia, S.; Jacques, B.; Braunstein, P.; Hueber, D.; Pale, P.; Blanc, A.; de Fremont, P. *Organometallics* **2013**, *32*, 4153.

CHAPTER 5

POLYMERIC NANOPARTICLE RECEPTORS AS SYNTHETIC ANTIBODIES FOR NONSTEROIDAL ANTI-INFLAMMATORY DRUGS (NSAIDs)

A manuscript submitted to the *ACS Biomaterials Science & Engineering,* **2015**.

Joseph K. Awino and Yan Zhao

Abstract

The wide usage and subsequent leakage of nonsteroidal anti-inflammatory drugs (NSAIDs) into the environment present an urgent need to create materials for selective binding of NSAID drugs, which are highly similar to one another in structure and functionality. Surface–core double-cross-linking of cationic micelles containing Naproxen or Indomethacin as the template yielded molecularly imprinted nanoparticles (MINPs) for these drugs. The nanoparticle receptors resembled water-soluble proteins in their hydrophilic exterior and hydrophobic core with guest-tailored binding pockets. Their binding selectivity for their templates over other NSAID analogues rivaled that of antibodies prepared though much lengthier procedures.

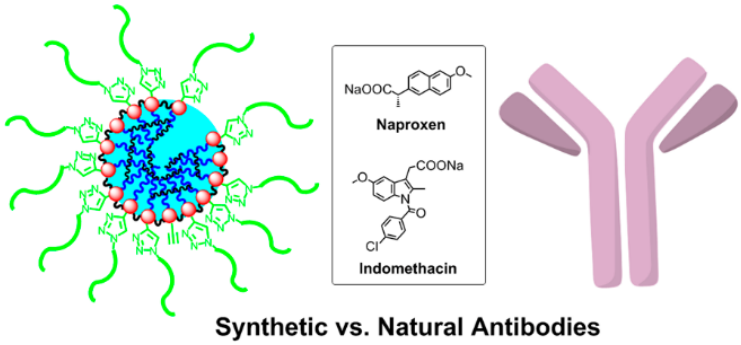

Figure1. Representation for the general design

Introduction

The immune system has remarkable abilities to generate antibodies for virtually any molecule of biological interest. The strong and specific recognition of antigens by their antibodies is at the heart of immune response and vital to the biological host's survival. Their extraordinary molecular recognition also makes antibodies powerful tools in diagnostics, therapeutics, imaging, analysis, and elucidation of biological mechanisms.[1]

However, antibodies are expensive biomolecules requiring lengthy procedures to produce. Immunization of animals itself often takes weeks of time, even if the molecules readily elicit immune responses. The (polyclonal) antibodies generated then need to be isolated and purified. Monoclonal antibodies are even more cumbersome to prepare, as they need to come from a single cell line. Just like any proteins, antibodies are subject to denaturation, whether by adverse temperatures, adsorption to surfaces, exposure to organic solvents, surfactants, or other chemical entities.

Chemists for decades have tried to create receptors for molecules of interest,[2,3] in a way similar to what nature does with antibodies. Although remarkable receptors have been made, sometimes with biological affinity and specificity,[4-6] synthetic receptors tend to be limited to specific classes of molecules or ions and a general method to create strong and specific antibody-resembling receptors remains an elusive goal.

Nonsteroidal anti-inflammatory drugs (NSAIDs, e.g., **1**–**5**) are one of the most used over-the-counter drugs.[7] Because of their wide usage and subsequent leakage into the environment, there is high interest in monitoring and detecting them in nature.[8] In addition to chemical methods, enzyme-linked immunosorbent assays (ELISA), which rely on NSAID-specific antibodies for operation, have been used for NSAID drug analysis.[9,10] The challenge

to design antibody-like receptors for these drugs (**1**–**5**) lies in their structual similarity: all have a carboxylate and a hydrophobic aromatic moeity. Naproxen and Ibuprofen (or Ketoprofen) in particular are closely related to one another in size and shape of the aromatic group. Needless to say, to recognize these drugs selectively, the receptor needs to have remarkable precision in its binding. Ideally, one also needs the receptors to function in water for drug monitoring or analysis.

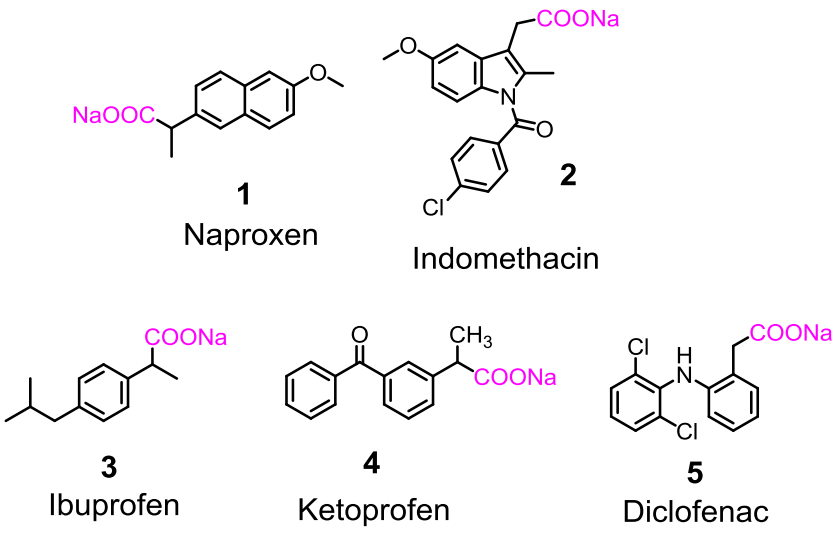

Herein, we report that antibody-like polymeric nanoparticle receptors can be created for NSAIDs through molecular imprinting in cross-linked micelles. The binding selectivity displayed by our "synthetic antibodies" was comparable to that found in biologically generated antibodies. Our materials, however, can be produced in 2–3 days rather than weeks without special techniques, provided that the building blocks (the polymerizable surfactants and cross-linkers) are available.

Results and Discussion

Materials Design and Synthesis

The synthesis of our nanoparticle receptors starts with micellization of cationic surfactant **6** above its 0.55 mM of critical micelle concentration (CMC) in water (Scheme **1**). Since the headgroup of this surfactant is a tripropargylammonium cation, its micellization places a layer of terminal alkynes on the surface of the micelle. In the presence of a diazide cross-linker (**7**) and Cu(I) catalysts, the highly efficient copper-catalyzed alkyne–azide cycloaddition[11] quickly cross-links the surface of the micelles to afford alkynyl-surface crosslinked micelles (alkynyl-SCMs) as water-soluble nanoparticles.

In our previous work, we have shown that water- or organic-soluble azide-functionalized ligands could be easily installed on the SCM surface if a sufficient number of alkyne groups are left on the surface of the cross-linked micelles.[12-15] This feature was achieved by using a ratio of [**6**]/[**7**] = 1:1.2 during the SCM preparation, as an excess of alkynes will be left after cross-linking. The alkynyl-SCMs were functionalized with sugar-derived ligand **8** so that the resulting nanoparticles were highly hydrophilic on the surface and completely soluble in water.

The details of the molecular imprinting procedure has been reported previously.[16] Briefly, the anionic and hydrophobic nature of the NSAID (e.g., **1** or **2**) allowed it to be readily incorporated into the cationic micelle and the resulting SCM. After the surface cross-linking and functionalization, we initiated core cross-linking of the methacrylate of **6** around the template. This step is the key to the molecular imprinting to form the final binding pocket. To facilitate this process, we solubilized 1 equiv of divinylbenzene (DVB) and 5 mol % of 2,2-dimethoxy-2-phenylacetophenone (DMPA, a photolytic radical initiator) in the very

beginning of the preparation and irradiated the surface-functionalized SCMs with UV light. UV irradiation initiated free radical polymerization between the methacrylate and DVB. Because the template molecule (**1** or **2**) had neither alkyne nor methacrylate to participate in any cross-linking, it acted as a place holder throughout the preparation while surface- and core cross-linking took place around the template to afford the binding pocket.

Molecularly imprinted polymers (MIPs)[17-25] have been reported in the literature for NSAID drugs.[26-29] They are typically prepared by polymerization of a functionalized monomer such as 4-vinylpyridine that binds the carboxylic acid of the NSAID and a large amount of a vinyl cross-linker. The bulk polymerization normally yields insoluble cross-linked polymers that need to be ground into smaller particles, sieved, and washed. In contrast, since the core-cross-linking was confined with each SCM in our case, the final molecularly imprinted nanoparticles (MINPs) were water-soluble nanoparticles similar to a water-soluble protein in size, hydrophilic exterior, hydrophobic interior, and a specific binding pocket in the hydrophobic core.

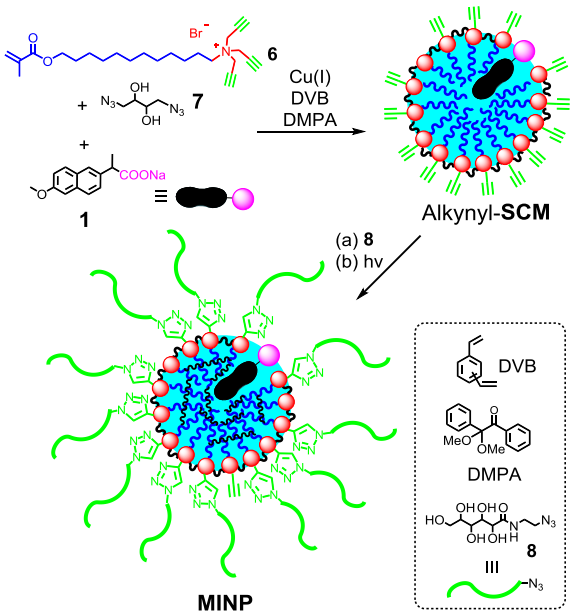

Scheme 1. Preparation of MINP with Naproxen as the template.

The MINP synthesis was monitored by ^{1}H NMR spectroscopy and dynamic light scattering (DLS). The SCMs had been characterized earlier additionally by mass spectrometry (after cleaving the 1,2-diol cross-linkages) and TEM.[12] Upon surface-cross-linking, all the ^{1}H NMR signals of surfactant **6** showed characteristic broadening (Experimental Section, Figure 3). The alkenic and aromatic protons of both **6** and DVB remained clearly visible in the SCMs but disappeared after the core-cross-linking. Disappearance of the alkenic protons should be caused by their consumption by the polymerization. The aromatic protons disappeared most likely because the high cross-linking density of the core restrained their movements in the core. DLS showed that the alkynyl-SCM, the surface-functionalized SCM, and the final MINP-**1** (i.e., MINP prepared with **1** as the template) had an average size of 4.0, 6.3, and 5.0 nm, respectively (Figure 5). The size change was consistent with our previous results,[16] suggesting that the nanoparticles became larger upon surface decoration and shrank during core-cross-linking.

The MINPs were purified by precipitation from acetone and repeated washing with water/acetone and methanol/acetic acid. The yield of the final MINPs was typically >80%. The fluorescence of Naproxen allowed us to monitor its removal from MINP-**1** by the disappearance of its characteristic emission peak at 360 nm. According to DLS, the final MINP-**1** averaged 5.0 nm in diameter, which translated to a molecular weight of 51,000 Daltons (Figure 6). Following the same procedures, we also prepared MINP-**2** against Indomethacin and characterized the materials similarly (Figures 7–9).

Binding Studies

In traditional MIPs, the insolubility of the receptors means that binding needs to be determined indirectly, often by measuring the amounts of guest absorbed by different amounts of polymer beads.[17-25] Neither the number of binding sites on a polymer bead nor their binding affinity can be controlled, as the polymer beads are obtained by grinding and sieving of insoluble macroporous polymers. A heterogeneous population of binding sites is typically obtained from such imprinting.

The water-solubility of MINP-**1** and the fluorescence of Naproxen enabled us to directly study the binding of MINP-**1** as a receptor by fluorescence titration. As shown by Figure 2, upon titration of Naproxen by different concentrations of MINP-**1** in an aqueous Tris buffer (50 mM Tris, pH = 7.4), the emission peak of the guest at 360 nm gradually decreased and a new peak at 430 nm emerged. The data fit nearly perfectly to a 1:1 binding isotherm to afford a binding constant (K_a) of (1.1 ± 0.2) × 10^6 M^{-1}. The binding constant translates to a binding free energy of -ΔG = 8.2 kcal/mol.

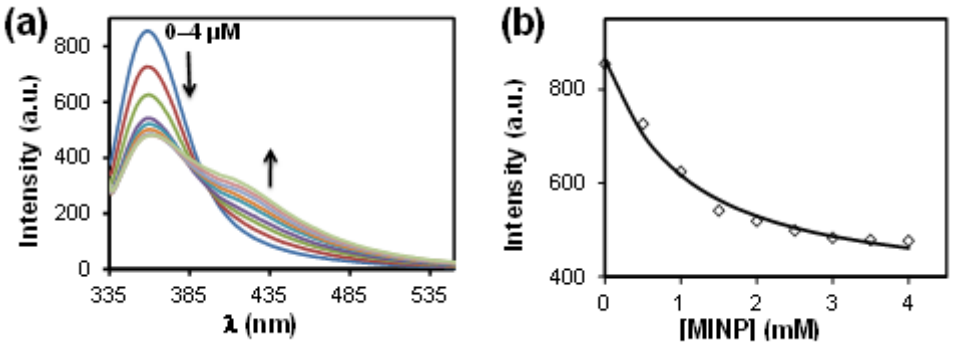

Figure 2. (a) Fluorescence emission spectra of **1** (λ_{ex} = 310 nm) upon addition of different concentrations of MINP-**1**. (b) Nonlinear least squares curving fitting of the emission intensity of **1** at λ = 358 nm as a function of MINP-**1** concentration. [**2**] = 0.25 μM.

As mentioned earlier, a successful receptor for a NSAID not only needs to have strong binding but also low cross-reactivity with its structural analogues. Since Naproxen is the only fluorescent molecule among the NSAIDs chosen, we turned to isothermal titration calorimetry (ITC) to study the binding of the other drugs by MINP-**1**. As shown by Figure 3a, the titration data for Naproxen and MINP-**1** yielded a K_a value of $(0.91 \pm 0.04) \times 10^6$ M^{-1}, experimentally the same as the value obtained from the fluorescence titration.

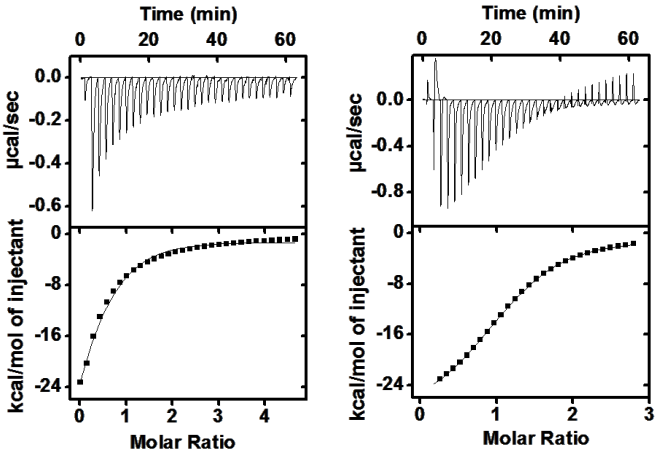

Figure 3. ITC titration curves obtained at 298 K for the binding of (a) **1** by MINP-**1** and (b) (a) **2** by MINP-**2**. The data correspond to entries 1 and 7 in Table 1. Additional ITC titration curves can be found in the Experimental Section (Figures 10–11). In general, an aqueous solution of an appropriate guest in Tris buffer (50 mM Tris, pH = 7.4) was injected in equal steps into 1.43 mL of the corresponding MINP solution in the same buffer. The top panel shows the raw calorimetric data. The area under each peak represents the amount of heat generated at each ejection and is plotted against the molar ratio of the MINP to the guest. The smooth solid line is the best fit of the experimental data to the sequential binding of N binding site on the MINP. The heat of dilution for the guest, obtained by adding the guest to the buffer, was subtracted from the heat released during the binding. Binding parameters were auto-generated after curve fitting using Microcal Origin 7.

Having confirmed the good agreement between the fluorescence and ITC binding data, we proceeded with the ITC binding studies of the other NSAIDs (**2**–**5**) by MINP-**1**. Recognizing the structural and functional-group similarity between the template (Naproxen) and Ibuprofen or Ketoprofen, we were apprehensive whether the MINP was able to distinguish these structural analogues.

Table 1. Binding data for MINPs obtained by ITC.[a]

Entry	Guest	Host	K_a (10^4 M^{-1})	-Δ*G* (kcal/mol)	CRR[b]	*N*
1	**1**	MINP-**1**	112 ± 20	8.2	--[c]	--[c]
2	**1**	MINP-**1**	91 ± 4	8.1	1	0.6 ± 0.1
3	**2**	MINP-**1**	0.8 ± 0.1	5.6	0.01	1.1 ± 0.1
4	**3**	MINP-**1**	8.7 ± 0.5	6.7	0.1	1.0 ± 0.1
5	**4**	MINP-**1**	2.9 ± 0.4	6.1	0.03	0.9 ± 0.1
6	**5**	MINP-**1**	3.7 ± 0.2	6.2	0.04	1.1 ± 0.1
7	**2**	MINP-**2**	98 ± 5	8.2	1	1.1 ± 0.1
8	**1**	MINP-**2**	5.2 ± 1.2	-6.4	0.05	0.7 ± 0.1
9	**3**	MINP-**2**	8.0 ± 0.1	-6.7	0.08	0.6 ± 0.1
10	**4**	MINP-**2**	0.8 ± 0.1	-5.3	0.01	0.4 ± 0.1
11	**5**	MINP-**2**	9.4 ± 1.0	-6.8	0.10	0.4 ± 0.1

[a] The titrations were generally performed in duplicates in 50 mM Tris buffer (pH 7.4) and the errors between the runs were <15%. [b] CRR = cross-reactivity = binding constant of a given compound by a MINP receptor normalized to that of the template by the same MINP [c] The binding constant was obtained from fluorescence titration and thus was not compared with the ITC binding data.

The K_a values for **2**, **3**, **4**, and **5** were determined to be 8.0×10^3, 8.7×10^4, 2.9×10^4, and 3.7×10^4 M^{-1}, respectively (Table 1, entries 3–6). Thus, the binding constants for these

other NSAIDs by MINP-**1** were at least an order of magnitude weaker than that for the Naproxen template. In the literature, the specificity of an antibody is represented by its cross-reactivity with ligands analogous to its antigen; the cross-reactivity may be obtained from either ITC binding data[30] or antibody-based assays such as ELISA.[9] The binding constants in our studies translate to cross-reactivity of 0.01, 0.1, 0.03 and 0.04 for **2** (Indomethacin), **3** (Ibuprofen), **4** (Ketoprofen), and **5** (Dichlofenac), respectively.

In the literature, polyclonal antibodies have been prepared for Naproxen.[9] The immunization (of rabbits) was reported to take 25 weeks. Competitive ELISA was then used to determine the specificity of the antibody for both NSAID and other anlogues. The cross-reativity for Ibuprofen and Diclofanac was 0.09 and 0.04, respectively.[9] Thus, the specificity displayed by our plastic antibodies were essentially identical to that exhibited by the antibodies generated through a lengthy and more expensive procedures.

Since all the NSAIDs studied carry the identical carboxylate, the selectivity of our MINP should derive from the size/shape of the binding pocket. We were delighted to see that Ibuprofen and Ketoprofen, two closely related structures of Naproxen could be distinguished so nicely by MINP-**1**. Apparently, the binding pocket was so well formed that even an insertion of a single ketone in the middle of the aromatic moiety (in Ketoprofen) was not tolerated by the binding pocket.

Another feature of our MINP is its controllable number of binding sites. The ITC titration revealed that the number of binding site per particle averaged 0.6–1.1. The number agreed well with our prepration: since the micelle aggreation number was ca. 50 and the [template]/[surfactant] ratio was 1:50 in our MINP prepration,[9] we anticipated a single binding site per particle on average. The number of binding sites obtained also compared

favorably with typical numbers of protein/antibody receptors, as inactive receptors, impurities, and inaccurities in the molecular weight of the materials frequently cause diviation of the binding site from unity, even when the orignial bioreceptor contains a single binding site.[30]

Indomethacin (**2**) was the largest NSAID drug in our study. Because it is generally easier to fit a smaller molecule in a larger binding pocket than vice versa, we were especially curious about the specificity of MINP-**2** for these NSAIDs. As shown in Table 1 (entry 7, see Figure 2b for the titration curve), the binding constant of MINP-**2** for the template itself was $(0.98 \pm 0.05) \times 10^6$ M^{-1}, very similar to the value for Naproxen by MINP-**1**. Because Indomethacin is signficantly larger in size than Naproxen, one would anticipate that the binding of the larger ligand by its correspoinding MINP receptor should be stronger, as a major driving force in the binding should be the expulsion of the water molecules in the binding pocket by the corresponding ligand and a larger guest should expel more water molecules from the (larger) binding pocket.

There could be several possible reasons why the larger Indomethacin did not display stronger binding than the smaller Naproxen. First, Indomethacin contained an amide group in the structure. The amide carbonyl oxygen is an excellent hydrogen-bond acceptor and is expected to be solvated quite well by water prior to its entrance into the binding pocket. Desolvation of the guest costs free energy and is expected to negatively impact the binding affinity. Second, if the amide group was hydrophilic enough to stay near the surface of the micelle during molecular imprinting, the binding pocket obtained from Indomethacin in MINP-**2** could be shallower than that obtained from Naproxen in MINP-**1**. If this is indeed the case, the shallower binding pocket would reduce the hydrophobic driving force for the

binding, as part of the guest molecule might still be exposed to water after the binding. In contrast, a more deeply embedded binding pocket should bury the hydrophobic guest more completely; thus, the smaller but overall more hydrophobic aromatic group in Naproxen might be better shielded from water by its binding pocket. Third, a rigid aromatic group (of Naproxen and the top protion of Indomethacin) has little conformational freedom whereas the tertiary amide bond of Indomethacin could adopt either a trans or cis configuration prior to binding. Since binding will fix the conformation of the guest (by fitting the guest into the pre-formed binding pocket), the loss of conformaitonal entropy will also lower the potential driving force for the binding.

Although the binding for Indomethacin was not signfiicantly stronger than for Naproxen by their corresponding MINPs, it is encouraging to see that MINP-**2** remained highly selective. The cross-reactivity of this MINP was 0.05, 0.08, 0.01 and 0.1 for **1** (Naproxen), **3** (Ibuprofen), **4** (Ketoprofen), and **5** (Dichlofenac), respectively. Thus, similar to MINP-**1**, the highest cross-reactivity for the non-templated NSAIDs was 0.1, similar to what was observed for the natural antibodies.

A close examination of our binding data suggests that a smaller guest indeed can fit into a larger pocket more easily than a larger guest does a smaller pocket. For example, the cross-reactivity of Indomethacin relative to Naproxen in MINP-**1** was 0.01, indicating that the large guest had difficulty fitting into the binding pocket generated by the small guest. The cross-reactivity of Naproxen to Indomethacin in MINP-**2**, however, was 0.05. Thus, although the pocket was quite selective for the NSAIDs studied, relatively speaking, a small guest indeed fitted better to a larger pocket than vice versa.

Conclusion

Traditionally, chemists use molecular synthesis to create discrete, well-defined molecular receptors for molecules of interest.[2,3] However, building concave receptors with guest-complementary binding surfaces require ingenious molecular design, lengthy synthesis, and many times is simply impossible for complex shaped/functionalized molecules or simple molecules lacking proper functional-group handles. As shown in this study, the great similarity and subtle differences among the NSAIDs make it extremely challenging to create specific molecular receptors for them. Although one could turn to biological methods to generate antibodies for the drugs, the procedures involve lengthy immunization and cumbersome purification and the resulting biomolecules are unstable under many conditions. In contrast, our molecular imprinting in cross-linked micelles readily yielded "synthetic antibodies" with antibody-like specificity. Although higher binding affinities (than the current micromolar affinities) would be better, the ease of the synthesis, the diversity of the MINP receptors that can be created, the strong tolerance of the materials for organic solvent and high temperatures due to their high cross-linking density,[16] and the excellent molecular recognition of the materials suggest that MINPs could become attractive substitutes for antibodies in appropriate applications.

Acknowledgement

We thank NSF for partial support of the research.

Experimental Section

General Method

Methanol, methylene chloride, and ethyl acetate were of HPLC grade and were purchased from Fisher Scientific. All other reagents and solvents were of ACS-certified grade or higher, and were used as received from commercial suppliers. Routine ^{1}H and ^{13}C NMR spectra were recorded on a Bruker DRX-400 or on a Varian VXR-400 spectrometer. ESI-MS mass was recorded on Shimadzu LCMS-2010 mass spectrometer. Fluorescence spectra were recorded at ambient temperature on a Varian Cary Eclipse Fluorescence spectrophotometer. ITC was performed using a MicroCal VP-ITC Microcalorimeter with Origin 7 software and VPViewer2000 (GE Healthcare, Northampton, MA).

Syntheses

Typical MINP synthesis. To a micellar solution of surfactant **6** (9.3 mg, 0.02 mmol) in D_2O (2.0 mL), divinylbenzene (DVB, 2.8 μL, 0.02 mmol), **1** in D_2O (10 μL of a solution of 10.1 mg/mL, 0.0004 mmol), and 2,2-dimethoxy-2-phenylacetophenone (DMPA) in DMSO (10 μL of a 12.8 mg/mL, 0.0005 mmol) were added.[31] The mixture was ultrasonicated for 10 min. Compound **6** (4.1 mg, 0.024 mmol), $CuCl_2$ in D_2O (10 μL of 6.7 mg/mL, 0.0005 mmol), and sodium ascorbate in D_2O (10 μL of 99 mg/mL, 0.005 mmol) were then added and the reaction mixture was stirred slowly at room temperature for 12 h. Compound **8** (10.6 mg, 0.04 mmol), $CuCl_2$ (10 μL of a 6.7 mg/mL solution in D_2O, 0.0005 mmol), and sodium ascorbate (10 μL of a 99 mg/mL solution in D_2O, 0.005 mmol) were then added and the solution stirred for another 6 h at room temperature. The reaction mixture was transferred to a glass vial, purged with nitrogen for 15 min, sealed with a rubber stopper, and irradiated in a

Rayonet reactor for 12 h. ^{1}H NMR spectroscopy was used to monitor the progress of reaction. The reaction mixture was poured into acetone (8 mL). The precipitate was collected by centrifugation and washed with a mixture of acetone/water (5 mL/1 mL) three times. The crude product was washed with methanol/acetic acid (5 mL/0.1 mL) five times, and then with methanol (2 mL), followed by excess acetone. The off-white product was dried in air to afford the final MINPs (17 mg, 85%).

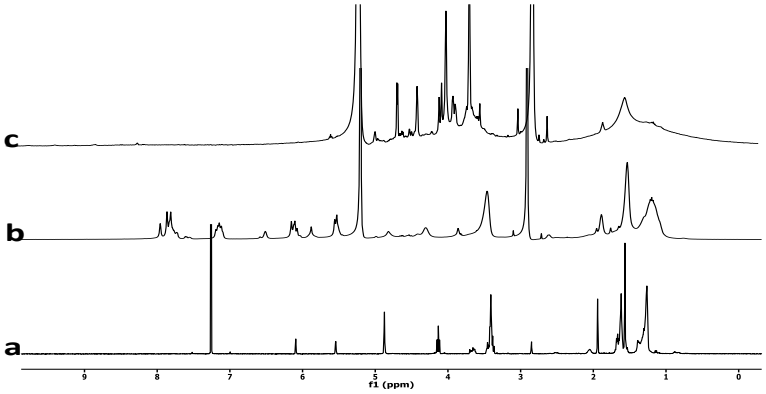

Figure 4. ^{1}H NMR spectra of: (a) **6** in $CDCl_3$, (b) alkynyl-SCM in D_2O, and (c) MINP-**1** in D_2O.

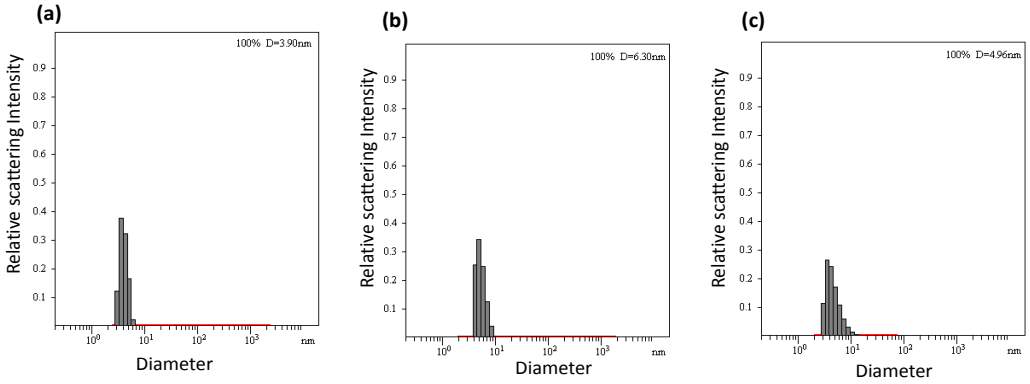

Figure 5. Distribution of the hydrodynamic diameters of the nanoparticles in water as determined by DLS for (a) alkynyl-SCM, (b) surface-functionalized SCM and (c) MINP-**1** after purification.

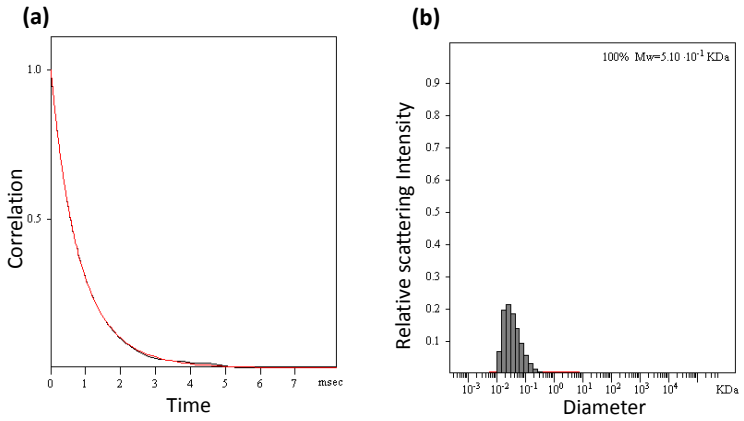

Figure 6. Distribution of the molecular weights of MINP-**1** and the correlation curves for DLS. The PRECISION DECONVOLVE program assumes the intensity of scattering is proportional to the mass of the particle squared.

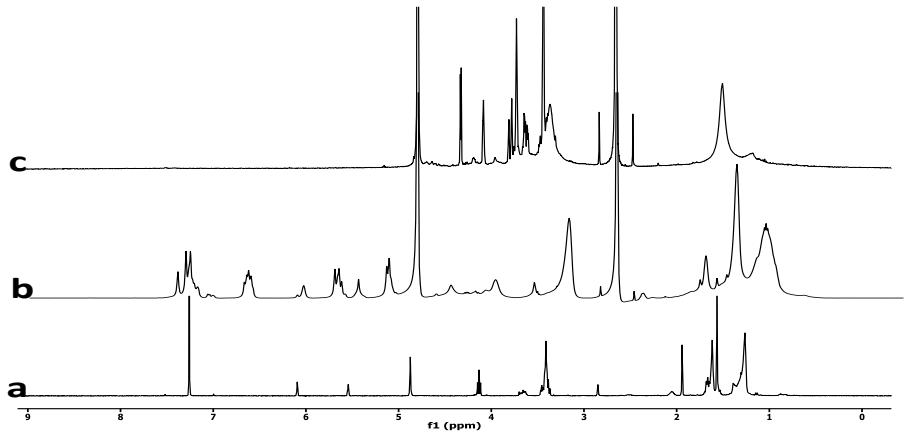

Figure 7. ^{1}H NMR spectra of: (a) **6** in $CDCl_3$, (b) alkynyl-SCM in D_2O, and (c) MINP-**2** in D_2O.

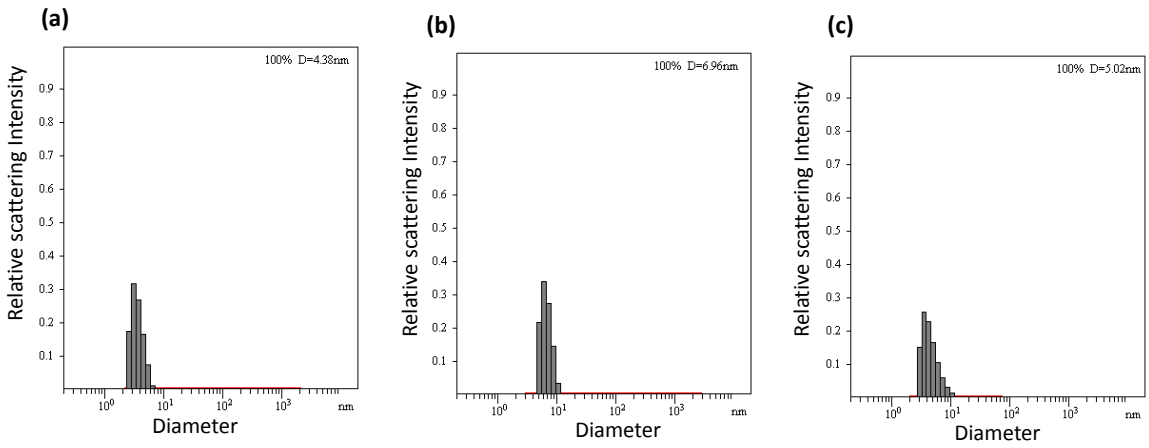

Figure 8. Distribution of the hydrodynamic diameters of the nanoparticles in water as determined by DLS for (a) alkynyl-SCM, (b) surface-functionalized SCM and (c) MINP-**2** after purification.

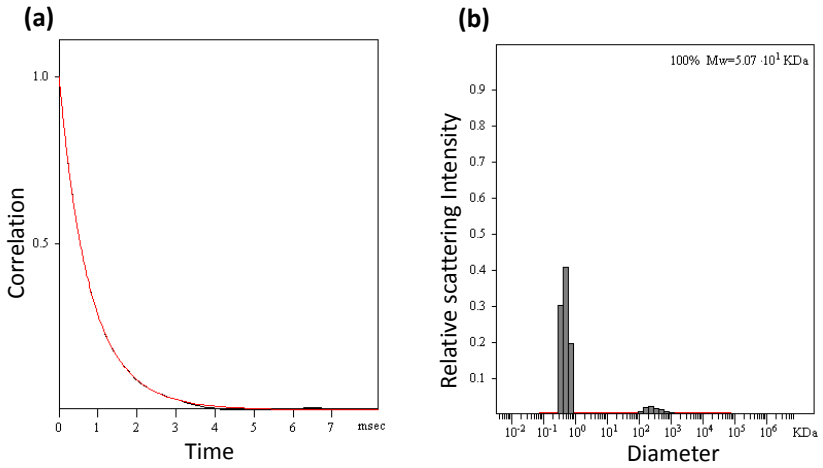

Figure 9. Distribution of the molecular weights of MINP-**2** and the correlation curves for DLS. The PRECISION DECONVOLVE program assumes the intensity of scattering is proportional to the mass of the particle squared.

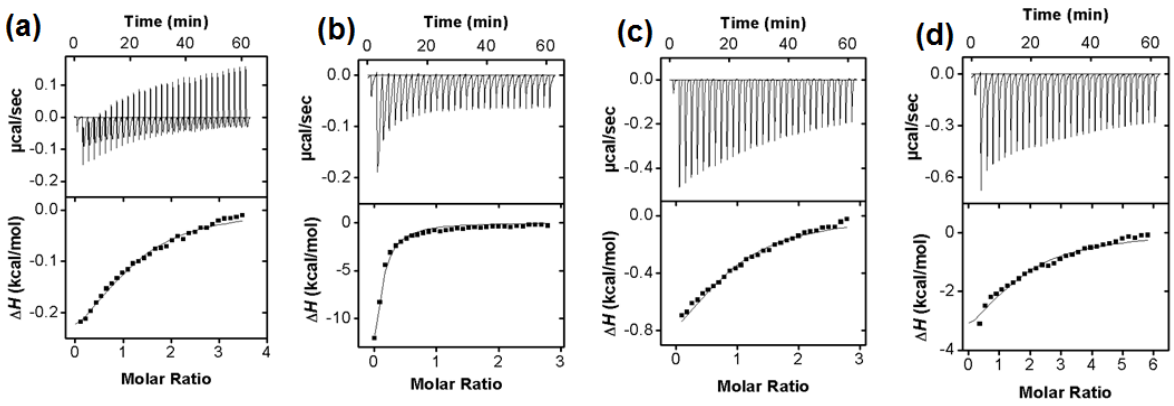

Figure 10. ITC titration curves obtained at 298 K for the binding of (a) **2** (3.0 mM) by MINP-2 (0.2 mM); (b) **3** (1.2 mM) by MINP-2 (0.1 mM); (c) **4** (6.0 mM) by MINP-2 (0.5 mM); and (d) **5** (5.0 mM) by MINP-**1** (0.2 mM); in 50 mM Tris buffer (pH 7.4). The data correspond to entries 3, 4, 5, and 6, respectively, in Table 1. The top panel shows the raw calorimetric data. The area under each peak represents the amount of heat generated at each ejection and is plotted against the molar ratio of MINP to the substrate. The solid line is the best fit of the experimental data to the sequential binding of N equal and independent binding sites on the MINP. The heat of dilution for the substrate, obtained by adding the substrate to the buffer, was subtracted from the heat released during the binding. Binding parameters were auto-generated after curve fitting using Microcal Origin 7.

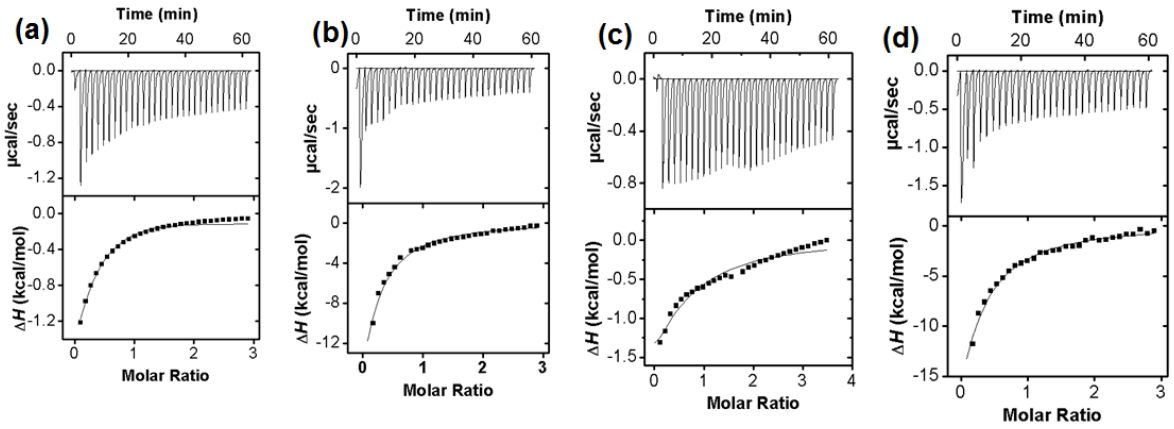

Figure 11. ITC titration curves obtained at 298 K for the binding of (a) **1** (2.5 mM) by MINP-5 (0.2 mM); (b) **3** (5.0 mM) by MINP-5 (0.4 mM); (c) **4** (6.0 mM) by MINP-5 (0.5 mM); and (d) **5** (2.5 mM) by MINP-**2** (0.2 mM); in 50 mM Tris buffer (pH 7.4). The data correspond to entries 8, 9, 10, and 11, respectively, in Table 1. The top panel shows the raw calorimetric data. The area under each peak represents the amount of heat generated at each ejection and is plotted against the molar ratio of MINP to the substrate. The solid line is the best fit of the experimental data to the sequential binding of N equal and independent binding sites on the MINP. The heat of dilution for the substrate, obtained by adding the substrate to the buffer, was subtracted from the heat released during the binding. Binding parameters were auto-generated after curve fitting using Microcal Origin 7.

Notes and References

(1) Janeway, C. *Immunobiology : The Immune System in Health and Disease*; 6th ed.; Garland Science: New York, 2005.

(2) Atwood, J. L.; Lehn, J. M. *Comprehensive Supramolecular Chemistry*; Pergamon: New York, 1996.

(3) Steed, J. W.; Gale, P. A. *Supramolecular Chemistry: From Molecules to Nanomaterials*; Wiley: Weinheim, 2012.

(4) Rekharsky, M. V.; Mori, T.; Yang, C.; Ko, Y. H.; Selvapalam, N.; Kim, H.; Sobransingh, D.; Kaifer, A. E.; Liu, S.; Isaacs, L.; Chen, W.; Moghaddam, S.; Gilson, M. K.; Kim, K.; Inoue, Y. A Synthetic Host-Guest System Achieves Avidin-Biotin Affinity by Overcoming Enthalpy–Entropy Compensation. *Proc. Natl. Acad. Sci. U. S. A.* **2007**, *104*, 20737-20742.

(5) Hogben, H. J.; Sprafke, J. K.; Hoffmann, M.; Pawlicki, M.; Anderson, H. L. Stepwise Effective Molarities in Porphyrin Oligomer Complexes: Preorganization Results in Exceptionally Strong Chelate Cooperativity. *J. Am. Chem. Soc.* **2011**, *133*, 20962-20969.

(6) Cao, L. P.; Sekutor, M.; Zavalij, P. Y.; Mlinaric-Majerski, K.; Glaser, R.; Isaacs, L. Cucurbit[7]Uril-Guest Pair with an Attomolar Dissociation Constant. *Angew. Chem. Int. Ed.* **2014**, *53*, 988-993.

(7) Lewis, A.; Furst, D. E. *Nonsteroidal Anti-Inflammatory Drugs: Mechanisms and Clinical Uses*; 2nd ed.; M. Dekker: New York, 1994.

(8) Liu, Y.; Minami, T.; Nishiyabu, R.; Wang, Z.; Anzenbacher, P. Sensing of Carboxylate Drugs in Urine by a Supramolecular Sensor Array. *J. Am. Chem. Soc.* **2013**, *135*, 7705-7712.

(9) Meulenberg, E. P.; Peelen, G. O. H.; Lukkien, E.; Koopal, K. Immunochemical Detection Methods for Bioactive Pollutants. *Intern. J. Environ. Anal. Chem.* **2005**, *85*, 861-870.

(10) Deng, A.; Himmelsbach, M.; Zhu, Q.-Z.; Frey, S.; Sengl, M.; Buchberger, W.; Niessner, R.; Knopp, D. Residue Analysis of the Pharmaceutical Diclofenac in Different Water Types Using Elisa and Gc−Ms. *Environ. Sci. Technol.* **2003**, *37*, 3422-3429.

(11) Rostovtsev, V. V.; Green, L. G.; Fokin, V. V.; Sharpless, K. B. A Stepwise Huisgen Cycloaddition Process: Copper(I)-Catalyzed Regioselective "Ligation" of Azides and Terminal Alkynes. *Angew. Chem. Int. Ed.* **2002**, *41*, 2596-2599.

(12) Zhang, S.; Zhao, Y. Facile Synthesis of Multivalent Water-Soluble Organic Nanoparticles Via “Surface Clicking” of Alkynylated Surfactant Micelles. *Macromolecules* **2010**, *43*, 4020-4022.

(13) Cho, H.; Zhao, Y. Environmental Effects Dominate the Folding of Oligocholates in Solution, Surfactant Micelles, and Lipid Membranes. *J. Am. Chem. Soc.* **2010**, *132*, 9890-9899.

(14) Li, X.; Zhao, Y. Protection/Deprotection of Surface Activity and Its Applications in the Controlled Release of Liposomal Contents. *Langmuir* **2012**, *28*, 4152-4159.

(15) Peng, H.-Q.; Chen, Y.-Z.; Zhao, Y.; Yang, Q.-Z.; Wu, L.-Z.; Tung, C.-H.; Zhang, L.-P.; Tong, Q.-X. Artificial Light-Harvesting System Based on Multifunctional Surface-Cross-Linked Micelles. *Angew. Chem. Int. Ed.* **2012**, *51*, 2088-2092.

(16) Awino, J. K.; Zhao, Y. Protein-Mimetic, Molecularly Imprinted Nanoparticles for Selective Binding of Bile Salt Derivatives in Water. *J. Am. Chem. Soc.* **2013**, *135*, 12552-12555.

(17) Wulff, G. Molecular Imprinting in Cross-Linked Materials with the Aid of Molecular Templates— a Way Towards Artificial Antibodies. *Angew. Chem. Int. Ed. Engl.* **1995**, *34*, 1812-1832.

(18) Wulff, G. Enzyme-Like Catalysis by Molecularly Imprinted Polymers. *Chem. Rev.* **2001**, *102*, 1-28.

(19) Haupt, K.; Mosbach, K. Molecularly Imprinted Polymers and Their Use in Biomimetic Sensors. *Chem. Rev.* **2000**, *100*, 2495-2504.

(20) Shea, K. J. Molecular Imprinting of Synthetic Network Polymers: The De Novo Synthesis of Macromolecular Binding and Catalytic Sites. *Trends Polym. Sci.* **1994**, *2*, 166-173.

(21) Sellergren, B. *Molecularly Imprinted Polymers: Man-Made Mimics of Antibodies and Their Applications in Analytical Chemistry*; Elsevier: Amsterdam, 2001.

(22) Sellergren, B. Imprinted Polymers with Memory for Small Molecules, Proteins, or Crystals. *Angew. Chem. Int. Ed.* **2000**, *39*, 1031-1037.

(23) Komiyama, M. *Molecular Imprinting: From Fundamentals to Applications*; Wiley-VCH: Weinheim, 2003.

(24) Yan, M.; Ramström, O. *Molecularly Imprinted Materials: Science and Technology*; Marcel Dekker: New York, 2005.

(25) Alexander, C.; Andersson, H. S.; Andersson, L. I.; Ansell, R. J.; Kirsch, N.; Nicholls, I. A.; O'Mahony, J.; Whitcombe, M. J. Molecular Imprinting Science and Technology: A

Survey of the Literature for the Years up to and Including 2003. *J. Mol. Recognit.* **2006**, *19*, 106-180.

(26) Kempe, M.; Mosbach, K. Direct Resolution of Naproxen on a Noncovalently Molecularly Imprinted Chiral Stationary-Phase. *Journal of Chromatography A* **1994**, *664*, 276-279.

(27) Hung, C. Y.; Huang, Y. T.; Huang, H. H.; Hwang, C. C. Synthesis and Molecular Recognition of Molecularly Imprinted Polymer with Ibuprofen as Template. *J. Chin. Chem. Soc.* **2006**, *53*, 1173-1180.

(28) Chen, D.-M.; Fu, Q.; Du, W.; Sun, S.-J.; Huang, P.; Chang, C. Preparation and Evaluation of Monolithic Molecularly Imprinted Stationary Phase for S-Naproxen. *J. Pharm. Anal.* **2011**, *1*, 26-31.

(29) Manesiotis, P.; Osmani, Q.; McLoughlin, P. An Enantio-Selective Chromatographic Stationary Phase for S-Ibuprofen Prepared by Stoichiometric Molecular Imprinting. *J. Mater. Chem.* **2012**, *22*, 11201-11207.

(30) Mohan, S.; Kourentzi, K.; Schick, K. A.; Uehara, C.; Lipschultz, C. A.; Acchione, M.; DeSantis, M. E.; Smith-Gill, S. J.; Willson, R. C. Association Energetics of Cross-Reactive and Specific Antibodies†. *Biochemistry* **2009**, *48*, 1390-1398.

(31) D_2O was used in the prepration to faciliate the monitoring of the reaction progress by ^1H NMR spectroscopy.

CHAPTER 6

RIGIDITY VERSUS AMPHIPHILICITY IN TRANSMEMBRANE NANOPORE FORMATION BY CHOLATE-BASED MACROCYCLES

A paper published in *Supramolecular Chemistry,* **2014**, *26*, 302-311.

Joseph K. Awino and Yan Zhao

Abstract

Amphiphilic macrocycles consisting of cholates and L-tryptophan were prepared by the copper-catalyzed alkyne–azide cycloaddition (CuAAC). The macrocycles helped glucose permeate lipid bilayer membranes. The macrocycle with two cholates was significantly more active in the glucose transport than the one with three cholates. Inclusion of 30–50% cholesterol in the bilayer accelerated the glucose transport monotonously. The unusual cholesterol effect was explained by the hydrophobically driven pore formation, in which the associative interactions of the water molecules inside the macrocycles prompted the macrocycles to stack over one another to avoid unfavorable water–lipid hydrocarbon contact. Fluorescence quenching by water- and oil-soluble quenchers provided additional evidence for the better penetration of the dicholate macrocycle into the bilayers, consistent with the stacking model. Rigidity in the macrocycle structure was hypothesized to be the main reason for the higher transport activity and deeper membrane-penetration of the dicholate macrocycle in comparison to those of the tricholate.

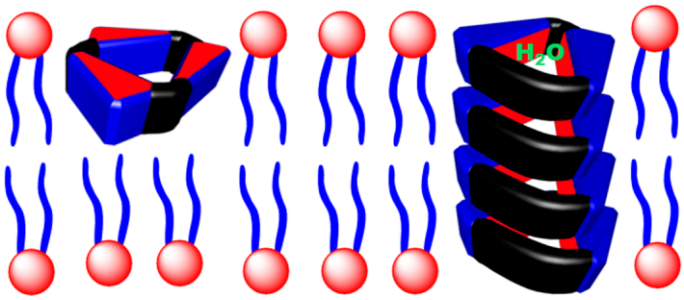

Figure 1. Stacking of macrocyclic oligocholates

Introduction

Controlling the permeability of lipid membranes is a highly important but challenging goal in modern bioorganic chemistry. From the mechanistic point of view, such studies can shed light on biological molecular transport, a fundamental process in numerous functions including signaling and metabolism.[1] Molecular transport across lipid bilayers is also critical to drug delivery, especially when a drug is potent but lacks the necessary pharmacokinetic properties to get inside the targeted cell.

Among various transporters to help hydrophilic molecules permeate lipid bilayers, molecules forming transmembrane (TM) nanopores are particularly interesting. [2] Many pore-forming peptides and proteins exist in nature, enabling processes both vital [1] and hostile (e.g., viral infection) [3] to cells. Because ion conductivity across a nanopore is affected by a polynucleotide moving through the pore, protein nanopores are useful for sequencing DNAs and RNAs, potentially at the single-molecule level.[4] Other applications of TM nanopores include artificial photosynthesis [5] and catalysis. [6]

Chemists have devoted significant efforts toward synthetic nanopore-forming agents. [2] To keep a nanosized pore open in a membrane, the structure must withstand the lateral pressure of the membrane. [7] For this reason, although working extremely well for ion

channels, crown ethers and open chain compounds [8] are often too flexible for nanopore formation. Over the years, a number of designs appeared in the literature, including Ghadiri's cyclic D/L-peptides that self-assembled into TM pores large enough for glucose and glutamic acid to pass through. [9] The β-barrel pores constructed from oligo(phenylene) derivatives by Matile and co-workers proved particularly versatile in structure and function. [6, 10] Other examples include the porphyrin-based nanopores by Satake and Kobuke , [11] the π-stacked aromatic heterocycles by Gong, [12] Fyles' metal-coordinated nanopores, [13] and the guanosine quartet-based giant ion channels by Davis. [14] Recently, Gokel, [15] Iengo and Tecilla, [16] and Hou [17] also constructed TM nanopores with pyrogallol[4]arenes, tetraporphyrin metallacycles, and pillar[n]arenes, respectively.

Our group reported that oligocholate macrocycles such as **1** could self-assemble in lipid membrane by hydrophobic interactions. [18] When amphiphilic macrocycle **1** enters a lipid membrane, it carries a pool of water in its highly hydrophilic interior. These water molecules are "activated" in the nonpolar lipid membrane because they strongly prefer to associate with other water molecules instead of the lipid tails. When the macrocycles exist as monomers, whether at the membrane/water interface or deep inside the membrane, these water molecules are exposed to the lipid hydrocarbon (Figure 2). When they stack into a TM nanopore, however, the water molecules can solvate the introverted hydroxyl and amide groups of the macrocycles and still exchange with the bulk water readily. The exchange of water also may be important to the pore formation, as the entropic cost for trapping a single water molecule can be as high as 2 kcal/mol in the extreme cases. [19]

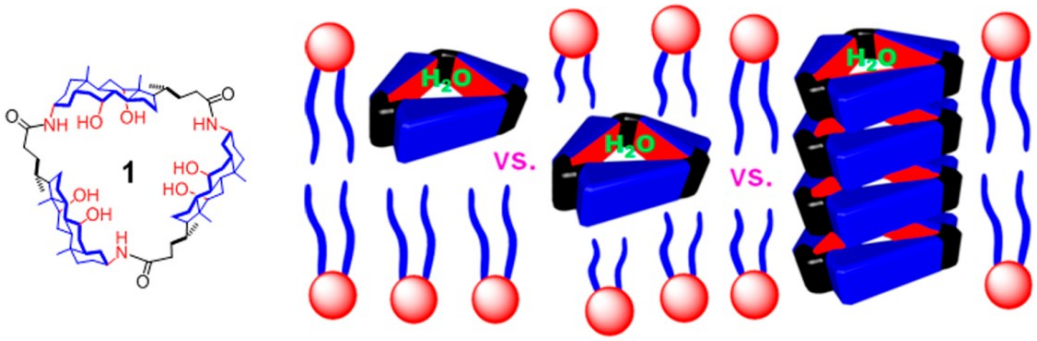

Figure 2. Stacking of oligocholate macrocycle **1** in a lipid bilayer membrane to minimize unfavorable water–lipid hydrocarbon contract. (Reprinted with permission from Ref 20a. Copyright 2013, American Chemical Society, Washington, DC.)

The main evidence for the stacked nanopores came from leakage assays and various control experiments. [20] Appropriately labeled compounds also allowed us to characterize the pore formation by fluorescence and solid-state NMR spectroscopy. [21] In this paper, we synthesized two tryptophan-labeled macrocycles **2** and **3**. We report the surprising finding that the smaller cyclic cholate dimer (**2**) consistently outperformed the larger trimer (**3**) as a pore-forming agent. Both the glucose transport data and fluorescence studies indicate that the dimer penetrates lipid membranes better than the trimer, demonstrating that rigidity is more important than mere amphiphilicity in this class of pore-forming agents.

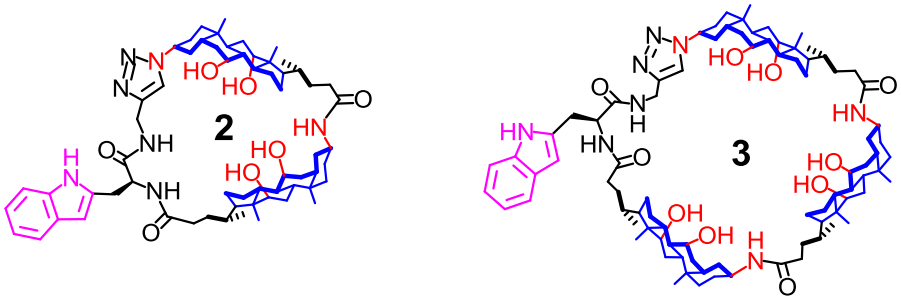

Results and Discussion

Design and Synthesis of tryptophan-labeled oligocholate macrocycles

We initially designed the dicholate macrocycle (**2**) to be a glucose-carrier in membranes. Davis and others have synthesized various cyclic cholate derivatives (cholaphanes, cyclocholamides, and cyclocholates) for binding monosaccharides. [22] Because dicholate **2** had a similar internal size as some of the sugar-binding cyclocholamides, [22a] we reasoned that the compound should be able to bind glucose and shuttle it across a membrane.

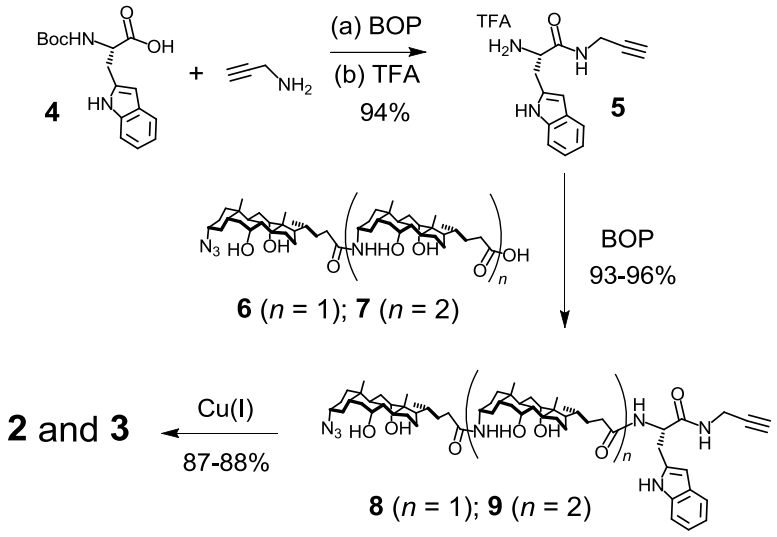

Scheme 1. Syntheses of macrocycles **2** and **3**.

The motivation for building a glucose-carrier came from the realization that, although any nanopore with appropriate size could transport glucose across lipid membranes, [9a, 18] synthetic glucose-carriers are rare. [23] On the other hand, most glucose transporters in nature (e.g., GluT proteins) operate by the carrier mechanism. [24] Carrier-based transporters are considered necessary for the chemical imbalance between the intra- and extracellular media, as a pore (i.e., the alternative mechanism) large enough for glucose probably would have difficulty preventing the passage of smaller molecules and ions (e.g., Na^+) (*24b*).

Scheme 1 illustrates the syntheses of **2** and **3**. In both compounds, L-tryptophan was included as a fluorescent label to probe the location and aggregation of the macrocycles in lipid membranes. For the synthesis, Boc-protected L-tryptophan (**4**) was first coupled to propargyl amine using benzotriazole-1-yl-oxy-tris-(dimethylamino)-phosphonium hexafluorophosphate (BOP). Standard deprotection by trifluoroacetic acid (TFA) yielded compound **5** in high yield. The carboxylic acid derivatives **6** and **7**, synthesized according to previously published procedures, [25] were coupled to **5** using BOP to afford **8** and **9**, respectively. Terminated with an azide on one end and an alkyne on the other, these compounds were cyclized readily under the standard click reaction condition ($CuSO_4$/sodium ascorbate) [26] to afford macrocycles **2** and **3** in good yields. The large difference in the polarity between the cyclized and linear compounds made it straightforward to separate the products from the starting materials.

Transport of glucose across lipid membranes

The pore formation of macrocycle **1** (as well as other analogues) was generally studied through its induced leakage of glucose-filled liposomes. [18, 21a] A number of unusual observations supported the hydrophobically driven stacking model in our earlier work. [18] For example, Hill analysis indicated that four molecules of the cholate macrocycle were involved in the glucose leakage and the height of **1** happened to be roughly 1/4 of the hydrophobic thickness of the membrane. Other evidence includes the correlation between the rigidity of the macrocycle and the transport of glucose, the inactivity of the linear tricholate, an unusual increase of the glucose transport rate with an increase of the membrane hydrophobicity, and a counterintuitive faster translocation of maltotriose over glucose (due to the longer sugar's

templating of the nanopore). When the macrocycles contained a pyrene-labeled side chain, the formation of pyrene excimer scaled with the thickness and hydrophobicity of the membrane, in agreement with the stacking model. [18, 21a] When the oligocholates were labeled with a fluorescent dansyl group, environmentally sensitive emission, red-edge excitation shift (REES), and fluorescence quenching by water- and oil-soluble quenchers consistently supported the better penetration of the cyclic trimer into the hydrophobic core of the membrane than a linear trimer control. [21b] By inserting an ^{15}N, $^{13}C\alpha$-labeled glycine into the cyclic and linear tricholate, we were able to confirm the pore formation additionally using ^{13}C-detected ^{1}H spin diffusion experiments to probe the depth of insertion of the compounds in the membranes, as well as their contact with water molecules. [21c]

As with other studies, [18, 21a] we first employed the liposome leakage assay to examine glucose transport of **2** and **3** across lipid membranes. Briefly, glucose (300 mM) was first encapsulated within POPC/POPG large unilamellar vesicles (LUVs) and the external glucose was removed by gel filtration. ATP, NADP, hexokinase, and glucose-6-phosphate dehydrogenase were then added to the liposomal solution. In the absence of a glucose-transporter, the glucose was physically separated from the extravesicular reagents and enzymes. If a macrocycle transports glucose across the membranes, its addition will trigger the release of glucose, which will be converted by the enzymes while NADP is reduced to NADPH. Because of the fast enzymatic kinetics, the formation of NADPH at 340 nm normally correlates directly with the rate of glucose efflux. [27] The leakage experiments were performed in duplicates and the relative error in the data was generally <20%.

Figure 3a compares the leakage profiles of glucose-filled POPC/POPG LUVs after the addition of 0–5 μM of macrocycle **2** (◆) and **3** (□). Note that the smaller macrocycle (**2**)

consistently outperformed the larger one (**3**) in these assays. At 5 μM, for example, dicholate **2** caused 25% of the 300 mM glucose to leak out of the liposomes at 60 min and tricholate **3** only 15%. Overall, neither compound could compare with the parent tricholate (**1**) that causes complete leakage of glucose at half of the concentration (2.5 μM) [18]

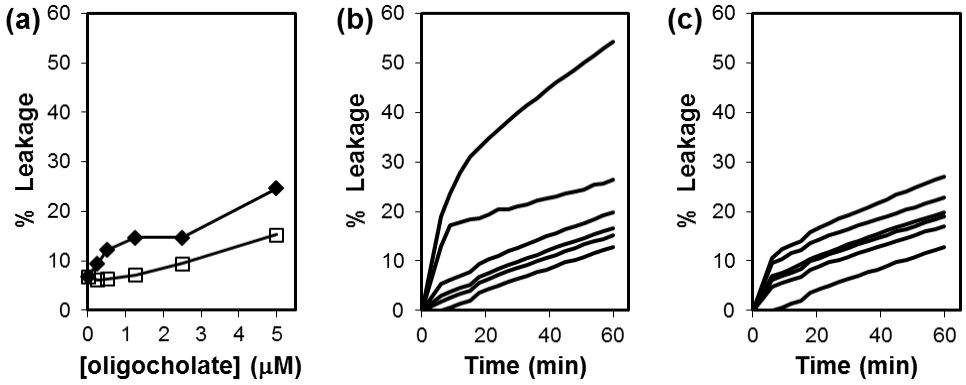

Figure 3. (a) Percent leakage of glucose at 60 min from POPC/POPG LUVs as a function of oligocholate concentration for **2** (◆) and **3** (□). (b, c) Glucose leakage profiles from POPC/POPG LUVs with 50% of cholesterol upon addition of 0, 0.25, 0.50, 1.25, 2.5, and 5.0 μM of macrocycle **2** (b) and **3** (c) from bottom to top. [Phospholipids] = 107 μM. UV-vis spectra were collected every 3 min from 6–57 min and the liposomes were lysed at 60 min upon addition of 1% Triton X-100. The leakage experiments were performed in duplicates and the relative error in the data was generally <20%.

The poor performance of **3** was not surprising. Our previous work indicates that rigidity in the macrocycle was important to the pore formation. [18] Conformationally flexible macrocycles need to flatten out before the stacking could work (Figure 2). In addition, if multiple rotatable bonds are introduced between two cholates—as in the case of **3** by the triazole and tryptophan—one (or more) of the cholates could turn its hydrophilic face outward. As illustrated by Figure 1, the "in–out" amphiphilicity of **1** is necessary for the

macrocycle to pull water molecules into the membrane. Any disruption of such topology is expected to be detrimental to the pore formation.

The poorer performance of **2** compared to the parent macrocycle **1** was not a surprise either. Because of the importance of the "in–out" amphiphilicity to the stacked nanopores, we had thought that it was not possible for **2** to form the TM nanopore, due to its reduced number of amphiphilic cholates (vide infra). If **2** serves as a glucose carrier, its efficiency was expected to be lower than **1**, as a carrier has to move back and forth in order to transport its guest while a nanopore can transport its guest continuously. [28]

What was surprisingly to us was the better performance of **2** over **3**, and the logical question became "What was the mechanism of the transport?" One way to understand the transport mechanism is to study the effect of lipid composition on the transport rate. Cholesterol is known to increase the hydrophobic thickness and the stability [29] of POPC bilayer and decrease its fluidity. [30] Cholesterol-containing bilayers are much less permeable to hydrophilic molecules, glucose included. [31] In our hands, the glucose leakage increased significantly and monotonously after inclusion of 30 mol % (data not shown) and 50 mol % cholesterol for both **2** and **3** (Figure 3b,c). With 5 μM of dicholate **2**, the glucose leakage at 60 min more than doubled with 50% cholesterol in the membranes (compare Figures 3a and 3b).

The unusual faster glucose leakage in the presence of cholesterol is the hallmark of the stacked nanopores. [18] Essentially, although cholesterol makes the membrane more hydrophobic, thicker, and more stable, the higher hydrophobicity of the membrane strengthens the associative interactions of water molecules inside the macrocycles and, in

turn, promotes the pore formation. Glucose leakage becomes faster under such a condition, opposite to the conventional expectation based on the permeability of the membrane itself.

As mentioned earlier, we had thought cyclic dicholate **2** was too small for the stacked nanopores in the beginning of the project. Since the macrocycles rely on the entrapped water molecules to provide the hydrophobic driving force for the stacking, the smaller cavity in **2**, combined with weaker amphiphilicity due to a lower number of the cholates, was anticipated to be detrimental to the pore formation. The cholesterol experiments, however, indicated that **2** clearly did NOT act as a carrier for glucose. The higher leakage rate in cholesterol-containing membranes was completely opposite to the known cholesterol effect on carrier-based transporters, [32] including oligocholate macrocycles [20c] or foldamers [33] that operate by the carrier mechanism.

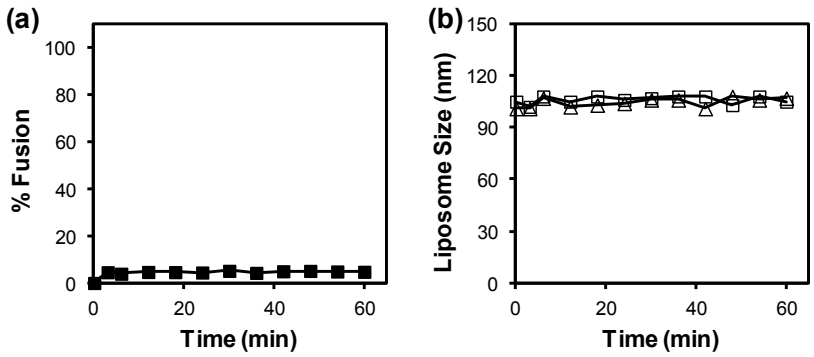

Figure 4. (a) Percent lipid-mixing in the POPC/POPG LUVs upon the addition of **2**. [**2**] = 5.0 μM, [Phospholipids] = 54.0 μM. (b) Size (diameter) of the POPC/POPG LUVs before (□) and after (△) the addition of **2**. [**2**] = 0.29 μM, [Phospholipids] = 2.9 μM.

We also performed lipid-mixing assays to confirm the intactness of the membranes. After all, since glucose can react with the enzymes as long as the two are mixed, glucose would appear to "leak" out of the liposomes if the membrane was disrupted or destroyed. In a lipid-mixing assay, 1 mol % of NBD- and rhodamine-functionalized lipids are included in the

membranes of one batch of liposomes. The labeled and unlabeled LUVs are then incubated together while the fluorescence resonance energy transfer (FRET) from NBD- to rhodamine-functionalized lipids is monitored. [34] If a compound causes fusion or destruction of the membrane, the fluorescent labels will be diluted, lowering the FRET efficiency in the meantime. Figure 4a shows that, even at 10 mol %, twice of the highest tested concentration of **2** in the leakage assays, the liposomes exhibited ≤5% lipid mixing. The result suggests that the lipid bilayers were intact after the addition of the macrocycle. The experiment also ruled out fusion or membrane destruction as the reason for the glucose leakage.

To further confirm the intactness of the membranes, we monitored the size (diameter) of the LUVs by dynamic light scattering (DLS). The liposomes were prepared by the extrusion method using 100 nm polycarbonate filters. [35] Figure 3b shows the size of the liposomes with and without addition of 10 mol % macrocycle **2**. There was essentially no change in size over the entire course of the experiment, with and without **2**. The result excluded any mechanisms that cause vesicle aggregation or membrane fusion, as well as those that destroy the lipid bilayers.

Fluorescence Quenching

The above experiments ruled out carrier-based transport, membrane fusion, or any processes that destroy the lipid bilayers as the reason for the glucose leakage induced by macrocycle 2. The unusual increase of the transport rate with the addition of 30–50% cholesterol was contrary to generic, unspecific disruption or destabilization of lipid membranes but was in line with all the previous studies that supported the stacking model. [18, 20-21] The tryptophan label on the macrocycles allowed us to study the quenching of lipid-solubilized **2** and **3** by

water- and lipid-soluble quenchers. Such experiments could help us determine the location of the fluorophore (i.e., tryptophan) and understand the behavior of the macrocycles, as demonstrated in a previous study. [21b] The basic premise for the study is two-fold. First, the location of the fluorophore (thus the macrocycle) determines its accessibility to the quencher. If the macrocycle stays near the membrane/water interface, it should be accessible to both water-soluble and lipid-soluble quenchers. If the macrocycle penetrates deep into the lipid membrane, its accessibility to the lipid-soluble quencher should increase whereas that to the water-soluble quencher decrease. Second, for an amphiphilic molecule to move into the hydrophobic core of a membrane, it has to bury or hide its hydrophilic groups. Aggregation (via intermolecular hydrogen bonds) [36] and folding (i.e., intramolecular hydrogen bonds for a linear oligocholate) [33, 37] are possible ways to bury the hydrophilic groups. The pore formation in the cyclic oligocholates (Figure 1) fundamentally accomplishes the same. As the macrocycle aggregates inside a bilayer, its quenching behavior should be affected.

Our water-soluble quencher was sodium iodide (NaI) and the lipid-soluble TEMPO. [21b] We only studied the quenching with 50 mol % cholesterol in the bilayers, as such membranes gave the highest glucose transport activities for the macrocycles (Figure 3). To understand the concentration-dependent pore formation, we carried out fluorescence quenching at two different concentrations of the oligocholates, i.e., 0.5 and 5 mol % relative to the phospholipids. As shown by Figures 3b and 3c, at 0.5 mol % concentration, neither **2** nor **3** afforded any significance glucose leakage, suggesting a negligible degree of pore formation. The leakage increased to 55% with 5 mol % concentration of **2**. Thus, some of this macrocycle should be in the aggregated, stacked state.

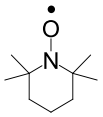

TEMPO

Figures 5a and 5b show the quenching plots of **2** and **3** by NaI at the two concentrations, respectively. Since both compounds could be quenched by the water-soluble quencher, a significant portion of the compounds must be located at the membrane/water interface. All the quenching curves exhibited a downward curvature. The downward curvature rules out combined dynamic (collision-based) and static (binding-based) quenching, which typically shows upward deviation from linearity. [38] Simple dynamic or static quenching generally affords linear Stern–Volmer plots.

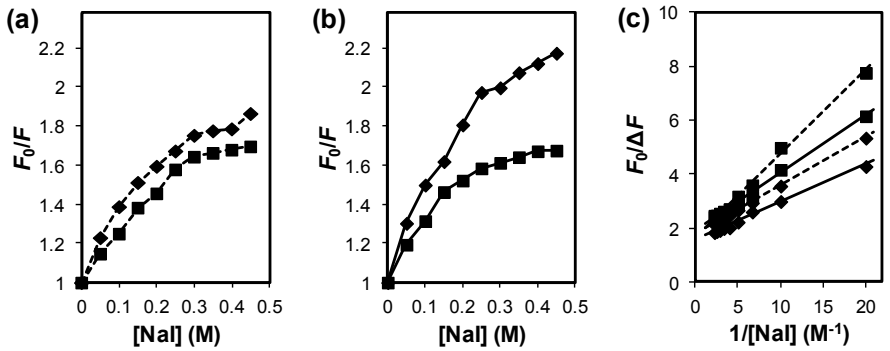

Figure 5. (a, b) Fluorescence quenching of macrocycles **2** (■) and **3** (◆) by NaI. The [oligocholate]/[phospholipids] = 0.5 % (a) and 5% (b). [Phospholipids] = 107 μM. (c) Modified Stern-Volmer plots for macrocycles **2** (■) and **3** (◆). The dashed lines are data obtained with [oligocholate]/[phospholipids] = 0.5 % and the solid lines with [oligocholate]/[phospholipids] = 5%.

Downward deviation from a linear quenching plot is often observed when fluorophores are located in the interior of a protein that is inaccessible to the quencher. [38]

Because the internal fluorophores are shielded from the quencher, the extent of quenching is less than when all the fluorophores are located on the surface, freely accessible to the quencher. Under such a scenario, the quenching data may be analyzed by the modified Stern–Volmer equation,

$$F_0/(\Delta F) = F_0/(F_0 - F) = 1/(f_a K_a[Q]) + 1/f_a,$$

in which F_0 is the initial fluorescence intensity, F the fluorescence intensity after the addition of the quencher Q, f_a the accessible fraction of the fluorophore to the quencher, and K_a the Stern–Volmer quenching constant for the accessible fluorophores. As shown by Figure 4c, all the quenching curves became linear using the modified quenching equation.

We also performed similar quenching experiments using the lipid-soluble TEMPO as the quencher (Figure 6a). At the higher concentration (5 mol % relative to the phospholipids), linear Stern–Volmer plots were obtained; thus, both compounds were fully accessible to TEMPO under this condition. At 0.5 mol % relative to the lipids, downward quenching plots were once again observed and were converted to the linear plots using the modified Stern–Volmer equation (Figure 6b).

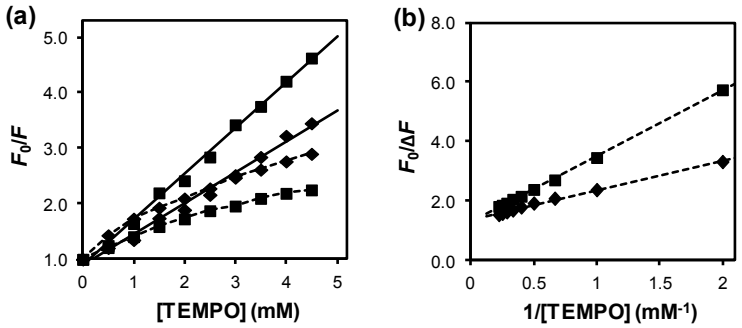

Figure 6. (a) Fluorescence quenching of macrocycles **2** (■) and **3** (◆) by TEMPO. The dashed lines are data obtained with [oligocholate]/[phospholipids] = 0.5% and the solid lines with [Oligocholate]/[phospholipids] = 5%. [Phospholipids] = 107 μM. (b) Modified Stern-Volmer plots for macrocycles **2** (■) and **3** (◆) with [oligocholate]/[phospholipids] = 0.5%.

Table 1 summarizes the quenching data for the two macrocycles. At 0.5 mol %, the accessible fractions of **2** and **3** to NaI were within experimental error—58 and 56%, respectively (entries 1 and 2). Interestingly, an increase in the macrocycle concentration made the accessible fractions (f_a) of the macrocycles go to opposite directions: dicholate **2** went from 58 to 52% whereas tricholate **3** from 56 to 64%. In other words, as more macrocycles entered the lipid membranes, the fraction of the macrocycles at the membrane/water interface increased for **3** but decreased for **2**, assuming that only the macrocycles at the interface were accessible to NaI.

Table 1. Quenching data obtained for compounds **2** and **3**[a]

entry	compound	quencher	f_a	K_a (M^{-1})
1	0.5 mol % **2**	NaI	58%	2.0
2	0.5 mol % **3**	NaI	56%	3.2
3	5 mol % **2**	NaI	52%	2.5
4	5 mol % **3**	NaI	64%	4.6
5	0.5 mol % **2**	TEMPO	79%	360
6	0.5 mol % **3**	TEMPO	75%	752
7	5 mol % **2**	TEMPO	100%	788
8	5 mol % **3**	TEMPO	100%	523

[a] The quenching experiments were performed in duplicates and the relative error was 0–5% for f_a and 0–16% for K_a.

The quenching data so far support the better pore formation of **2** over **3**. As the dicholate macrocycle stacks to form the TM nanopore, some of the macrocycles are located within the hydrophobic core of the membrane and become less accessible to NaI. It is significant that the NaI-accessible fraction of **3** increased at the higher concentration. Not only did the tricholate macrocycle fail to form TM nanopores effectively—evident from the

lower glucose transport activities—more of the compounds seemed to have migrated to the membrane/water interface at the higher concentration (see below for more discussion).

The picture becomes even clearer when we compare the quenching data of NaI and TEMPO. First of all, f_a was significantly higher with TEMPO (75–100%) than with NaI (52–64%). The result probably just reflects that fact that these macrocycles are overall quite hydrophobic molecules and prefer to stay in the nonpolar membrane environment. Even if they are located at the membrane/water interface, they must be still located in a nonpolar environment. [21b] We were not surprised to see the sum of the water-accessible fraction and the oil-accessible fraction being greater than 100%, as fluorophores located at the membrane/water interface should be accessible to both NaI and TEMPO.

Another observation was that the Stern–Volmer quenching constants (K_a) were much larger for TEMPO than for NaI. This difference should simply derive from the different quenching efficiencies of the two compounds. Moreover, the liposome solution was a phase-separated system. Since both the macrocycles and TEMPO were located within the lipid bilayers, their effective concentrations in the membranes were much higher than their concentrations in the entire solution. Note that the quenching constants were calculated based on the solution concentrations.

We also observed that both **2** and **3** became more accessible to TEMPO as their concentrations increased in the membranes—f_a went from 75–79% to 100% (Table 1, entries 5–8). The trend was completely consistent with the NaI-quenching data of **2**, which suggested that more of the macrocycles migrated to the hydrophobic core of the membrane at the higher concentration. The trend was also in line with substantial increase of glucose leakage at the higher concentration (Figure 3b). For tricholate macrocycle **3**, however, the

quenching data of TEMPO and of NaI seemed to contradict each other. How could it be possible for **3** to become more accessible to the lipid-soluble TEMPO and the water-soluble NaI at the same time when its concentration increased in the membrane? We believe the result might have derived from the aggregation of the macrocycle in the membrane. At 0.5 mol % in the lipid membrane, **3** most likely existed as monomers at the membrane/water interface while being embedded in the membrane. The observed accessible fractions to either NaI or TEMPO under such a condition just reflected the location of the fluorophore. At the higher concentration (5 mol %), the significant glucose transport activity (Figure 3c) suggests that some degree of aggregation (pore-formation) was present (as mentioned earlier, carrier-based transport was already ruled out by the unusual cholesterol effect). The accessible fractions (f_a) under this condition, therefore, had contributions from both the monomeric and aggregated species. As long as the two states of **3** were in equilibrium and the aggregated form was accessible to TEMPO, all the macrocycles would appear fully accessible to TEMPO. This is because the macrocycles on the membrane surface could migrate into the membrane by equilibrating with the transiently stacked macrocycles, even if the latter represents a small fraction of the total. Meantime, when the membrane surface is crowded with the macrocycle (due to the latter's high concentration in the membrane), the lipids may not fully shield the macrocycle from water exposure, resulting a higher accessible fraction of to NaI.

Another interesting observation in the quenching experiments was that the Stern–Volmer quenching constants (K_a) for the two macrocycles went to opposite directions with increasing concentrations: K_a more than doubled for **2** but decreased by 30% for **3** (Table 1, entries 5–8). Thus, even though both compounds became more accessible to TEMPO at the

higher concentration, their quenching efficiencies displayed very different trends. We believe that these results provide additional support for the aggregation mentioned above. When **2** aggregated, it apparently followed the stacking model in Figure 2 quite closely and migrated into the hydrophobic core of the membrane. [39] As more of the macrocycles moved deeper into the bilayer, they became more easily quenched by TEMPO, which should be located in the hydrophobic core of the membrane due to its strong hydrophobicity. On the other hand, the situation was quite different when the larger, flexible macrocycle (**3**) aggregated. The pore formation was poor, evident from the lower glucose transport in comparison to that of **2**. Under this condition, the majority of **3** should reside at the membrane/water interface. Even though the macrocycles were accessible to TEMPO, the quenching was inefficient because the fluorophore and the quencher resided at different locations in the membranes and they only saw each other through a rather unfavorable stacking of the macrocycles.

Conclusion

Inclusion of a natural α-amino acid (L-tryptophan) into the cholate macrocycles allowed us to study the pore formation of these compounds by both glucose leakage and fluorescence quenching. The combination of the two techniques elucidated previously unknown structure–activity relationship in the pore-forming macrocycles. In the water-templated stacking model, rigidity of the macrocycle seems to far outweigh its amphiphilicity. Despite one fewer facially amphiphilic cholate group in the structure, dicholate **2** consistently outperformed tricholate **3** in the pore formation, as demonstrated by both the glucose leakage assays and the quenching studies. The fluorescence quenching, in particular, revealed different dynamics and aggregation of the macrocycles in the membrane.

At low concentrations, both macrocycles prefer to stay at the membrane/water interface, possibly to minimize the unfavorable contact between the entrapped water molecules with the lipid hydrocarbon (Figure 2). At higher concentrations, the rigid dimer (**2**) migrates inside the membrane to form the TM nanopore, as a result of the associative interactions of entrapped water molecules. The larger, more flexible trimer (**3**), however, could not do so as easily. Only a small fraction of the macrocycles stacks into nanopores while the majority resides near the surface. The preference for the membrane surface is presumably a result of the flexible structure, which allows macrocycle **3** to turn its hydrophilic face toward water to satisfy its solvation needs without resorting to the stacking.

Acknowledgement

We thank NSF (DMR-1005515) for supporting the research

Experimental Section

General Method

All reagents and solvents were of ACS-certified grade or higher and used as received from commercial suppliers. Millipore water was used to prepare buffers and liposomes. Routine ^{1}H and ^{13}C NMR spectra were recorded on a Varian VXR-400 or on a Varian MR-400 spectrometer. Fluorescence spectra were recorded at ambient temperature on a Varian Cary Eclipse fluorescence spectrophotometer. Compounds 5, [40] 6, [25] and 7 [25] were synthesized according to previously published procedures.

Syntheses

Compound 8. Compound **6** (48 mg, 0.06 mmol), compound **5** (23 mg, 0.07 mmol), and BOP (49 mg, 0.11 mmol) were dissolved in dry DMF (5 mL). DIPEA (0.17 mL, 1.0 mmol) was added. After being stirred for 12 h at 60 °C, the mixture was cooled to room temperature and poured into a 1 M HCl solution (5 mL). The precipitate was collected by suction filtration, washed with water (3 × 20 mL), dried in air, and purified by column chromatography over silica gel using 12:1 CH_2Cl_2/CH_3OH as eluent to afford a white powder (60 mg, 96%). ^{1}H NMR (400 MHz, $CDCl_3/CD_3OD$ = 1:1, δ): 7.87(m, 1 H), 7.86 (m, 1H), 7.61(d, *J* = 7.8 Hz, 1 H), 7.39 (s, 1H), 7.33 (s, 1H), 4.21 (s, 1H), 4.14 (s, 1H), 4.02 (s, 1H), 3.88 (br, 1H), 3.45 (br, 1H), 3.36 (br, 1H), 2.81(br, 1H) , 2.64 (s, 1H), 1.48-2.50 (series of m), 1.38(s, 4H), 0.82 (m, 6H). ^{13}C NMR (100 MHz, $CDCl_3/CD_3OD$ = 1:1, δ): 175.5, 173.2, 136.5, 128.4, 124.6, 122.4, 119.8, 119.4, 112.3, 110.3, 73.9, 73.1, 72.3, 69.1, 68.9, 63.8, 62.6, 59.9, 54.9, 54.6, 54.3, 47.7, 47.4, 47.3, 42.8, 42.6,42.5, 40.4, 40.2, 37.8, 37.2, 36.9,36.8, 36.4, 35.9, 35.8, 35.7, 35.6, 34.9, 34.2, 33.8, 33.6, 33.2, 32.8, 32.6, 32.2, 31.7, 31.5, 29.7, 29.4, 29.0, 28.4, 27.9, 27.7, 27.5, 27.5, 26.5,26.4, 24.1, 23.4, 17.9, 13.2. ESI-HRMS (*m/z*): $[M + H]^+$ calcd for $C_{62}H_{92}N_7O_7$, 1046.7058; found 1046.7053.

Compound 9. Similar procedure as in the synthesis of **8** was followed and afforded a white powder (93 %). ^{1}H NMR (400 MHz, $CDCl_3/CD_3OD$ = 1:1, δ): 7.87 (d, *J* = 7.6 Hz, 1 H), 7.82 (m, 1H), 7.68 (d, *J* = 8.0 Hz, 1 H), 7.61 (d, *J* = 8.0 Hz, 1 H), 7.39 (d, *J* = 8.4 Hz, 1 H), 7.33 (s, 1 H), 4.31(s, 2 H), 4.25 (s, 2 H), 4.19 (s, 2H), 3.98 (s, 1 H), 3.88 (br, 1H), 3.62 (s, 1H), 3.57 (br, 1H), 2.64 (s, 1H), 2.60-1.80 (series of m), 1.63 (s, 9H), 1.29 (s, 6H), 1.06 (s, 6H). ^{13}C NMR (100 MHz, $CDCl_3/CD_3OD$ = 1:1, δ): 174.4, 174.2, 173.8, 172.6, 134.9, 126.7, 122.9, 120.7, 118.8, 117.5, 110.8, 108.5, 73.9, 72.2, 71.4, 70.6, 69.4, 67.4, 67.2, 61.5, 60.9,

58. 2, 54.9, 54.6, 54.3, 45.7, 45.6, 41.2, 41.0, 38.7, 38.6, 35.9, 35.8, 35.7, 35.6, 35.4, 34.9, 34.8, 34.7, 34.6, 34.5, 34.2, 34.1, 33.9, 33.8, 33.7, 33.6, 33.4, 33.2, 32.8, 32.7, 32.6, 32.3, 32.2, 32.1, 32.0, 31.9, 31.8, 31.7, 31.6, 31.5, 31.3, 30.8, 30.6, 30.4, 29.7, 29.4, 29.0, 28.9, 28.4, 28.3, 28.1, 27.9, 27.7, 27.5, 27.3, 26.8, 26.7, 26.5,26.4, 26.3, 26.2, 22.4, 21.7, 16.3, 11.5. ESI-HRMS (*m/z*): $[M + H]^+$ calcd for $C_{86}H_{131}N_8O_{10,}$ 1435.9988; found 1435.9980.

Compound 2. Compound **8** (60 mg, 0.06 mmol), $CuSO_4 \cdot 5H_2O$ (75 mg, 0.3 mmol), and sodium ascorbate (594 mg, 3 mmol) were dissolved in a 2:1:1 mixture of THF/MeOH/H_2O (20 mL). After the reaction mixture was stirred at room temperature for 24 h, it was filtered and the organic solvents were removed by rotary evaporation. The precipitate formed was collected by suction filtration, washed with water (3 × 10 mL), dried in air, and purified by column chromatography over silica gel using 12:1 CH_2Cl_2/CH_3OH as eluent to afford a white powder (52 mg, 87 %). ^{1}H NMR (400 MHz, $CDCl_3$/CD_3OD = 1:1, δ): δ: 7.69 (m, 1H), 7.65 (m, 1H), 7.41 (d, *J* = 7.8 Hz, 1 H), 7.17 (s, 1H), 7.10 (s, 1H), 4.50-4.28 (series of m), 3.88 (br, 9H), 3.36 (br, 1H), 2.81 (br, 1H) , 2.42 (m, 3H), 1.48-2.40 (series of m),1.38 (s, 4H), 0.82 (m, 6H). ^{13}C NMR (100 MHz, $CDCl_3$/CD_3OD = 1:1, δ): 178.6, 178.4, 175.6, 131.3, 130.9, 127.4, 125.9, 125.4, 123.3, 122.7, 122.1, 119.7, 115.2, 114.4, 113.1, 110.7, 76.8, 75.1, 73.9, 71.9, 71.3, 66.0, 65.4, 57.4, 50.6, 50.2, 45.8, 45.5, 45.4, 43.3, 43.1, 42.5, 39.4, 39.2, 38.9, 37.8, 37.2, 36.9, 36.8, 36.4, 35.9, 35.8, 35.6, 34.9, 34.2, 33.8, 33.6, 33.2, 32.8, 32.6, 32.2, 31.6, 31.2, 29.7, 29.4, 29.0, 28.4, 26.9, 26.3, 20.8, 20.7, 16.2. ESI-HRMS (*m/z*): $[M + H]^+$ calcd for $C_{62}H_{92}N_7O_7$, 1046.7058; found 1046.7057.

Compound 3. Similar procedure as in the synthesis of **2** was followed and afforded a white powder (88 %). ^{1}H NMR (400 MHz, $CDCl_3$/CD_3OD = 1:1, δ): 8.13 (m, 1H), 7.90 (m, 1H), 7.45 (s, 1H), 7.21 (d, *J* = 6.8 Hz, 1 H), 7.13 (d, *J* = 6.8 Hz, 2H), 4.50 (s, 3H), 4.06 (m, 3H),

3.65 (br, 1H), 2.81 (br, 1H), 2.42-1.70 (series of m), 1.38 (s, 4H), 0.82 (m, 6H). ^{13}C NMR (100 MHz, $CDCl_3/CD_3OD$ = 1:1, δ): 178.8, 178.3, 178.2, 175.3, 138.6,138.3, 131.3, 130.2, 127.4, 125.4, 122.8, 122.1, 115.3, 113.2, 73.9, 72.2, 71.4, 70.6, 69.4, 67.4, 67.2, 61.5, 60.9, 58.2, 54.9, 54.6, 54.3, 52.4, 51.8, 50.4, 49.9, 45.7, 45.6, 44.1, 43.2, 41.2, 41.0, 38.7, 38.6, 37.9, 37.7, 37.5, 37. 2, 36.8, 36.5, 36.2, 35.9, 35.8, 35.7, 35.6, 35.4, 34.9, 34.8, 34.7, 34.6, 34.5, 34.2, 34.1, 33.9, 33.8, 33.7, 33.6, 33.4, 33.2, 32.8, 32.7, 32.6, 32.3, 32.2, 32.1, 32.0, 31.9, 31.8, 31.7, 31.6, 31.5, 31.3, 30.8, 30.6, 30.4, 27.0, 26.3, 21.1, 21.0, 20.9, 16.2. ESI-HRMS (*m/z*): $[M + H]^+$ calcd for $C_{86}H_{131}N_8O_{10,}$ 1435.9988; found 1435. 9999.

Liposome preparation. Unlabeled POPC/POPG large unilamellar vesicles (LUVs) were prepared according to a literature procedure (*23a*). A chloroform solution of POPC (25 mg/mL, 198 μL) and POPG (50 mg/mL, 10.0 μL) was placed in a 10 mL test tube and dried under a stream of nitrogen. The residue was dried further under high vacuum overnight. Rehydration of the lipids was done using HEPES buffer (10 mM HEPES, 107 mM NaCl, pH=7.4) and allowed to continue for 30 min with occasional vortexing. The opaque dispersion was subjected to ten freeze–thaw cycles. The resulting mixture was extruded twenty-nine times through a polycarbonate filter (diameter = 19 mm, pore size = 100 nm) at room temperature using an Avanti Mini-Extruder. A portion (0.3 mL) of the liposome solution was diluted to 5.0 mL with the HEPES (10 mM HEPES, 107 mM NaCl, pH=7.4) buffer. The concentration of phospholipids in the stock solution was 0.86 mM.

Fluorescence Quenching. A typical procedure for the quenching experiment is as follows. Stock solutions (5.0×10^{-4} M) of **2** and **3** in DMSO were prepared. Aliquots of the above LUV solution (250 μL) and HEPES buffer (1750 μL, 10 mM HEPES, 107 mM NaCl, pH = 7.4) were placed in a quartz cuvette. The concentration of phospholipids in each cuvette was

107 μM. An aliquot (13.0 μL) of the oligocholate stock solution was added via a microsyringe and vortexed gently for 5 s before the initial fluorescence spectrum was recorded. In the case of the water-soluble quencher, aliquots (10.0 μL) of NaI (7 M in the above HEPES buffer that contained 0.1 mM $Na_2S_2O_3$) were added with a Hamilton Gastight syringe. In the case of the lipid-soluble quencher, aliquots (2.0 μL) of TEMPO (0.5 M in ethanol) were added. After each addition, the sample was vortexed gently for 5 s. The fluorescence spectrum was recorded over 10 min at 1 min intervals and averaged. The excitation wavelength was set at 330 nm.

^{1}H NMR of compound **8**

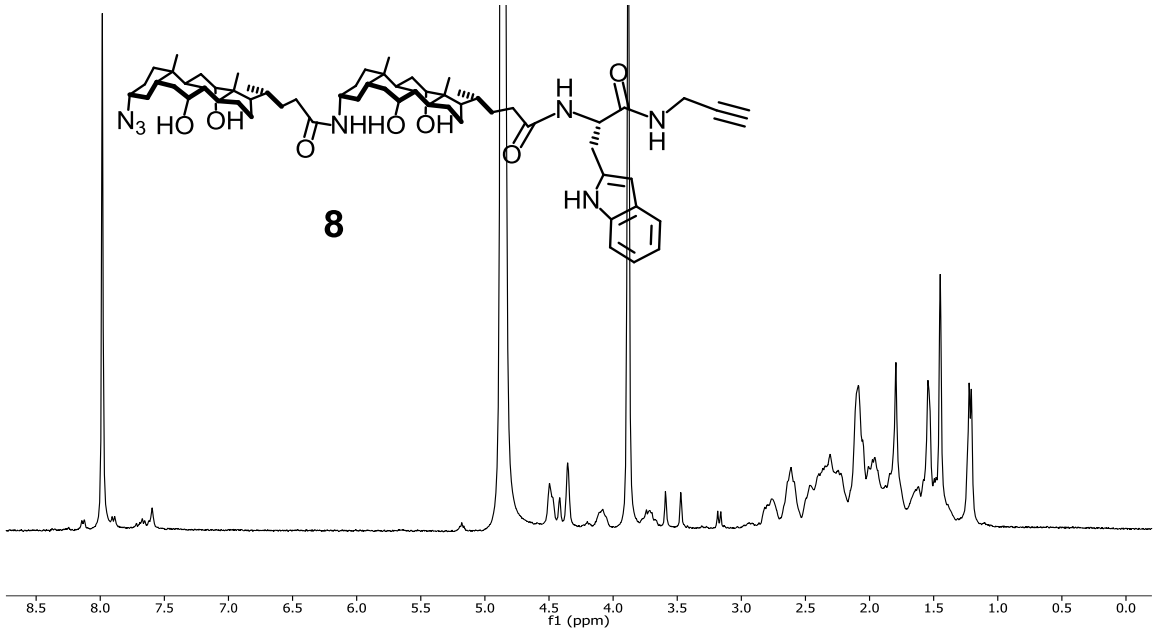

^{13}C NMR of compound **8**

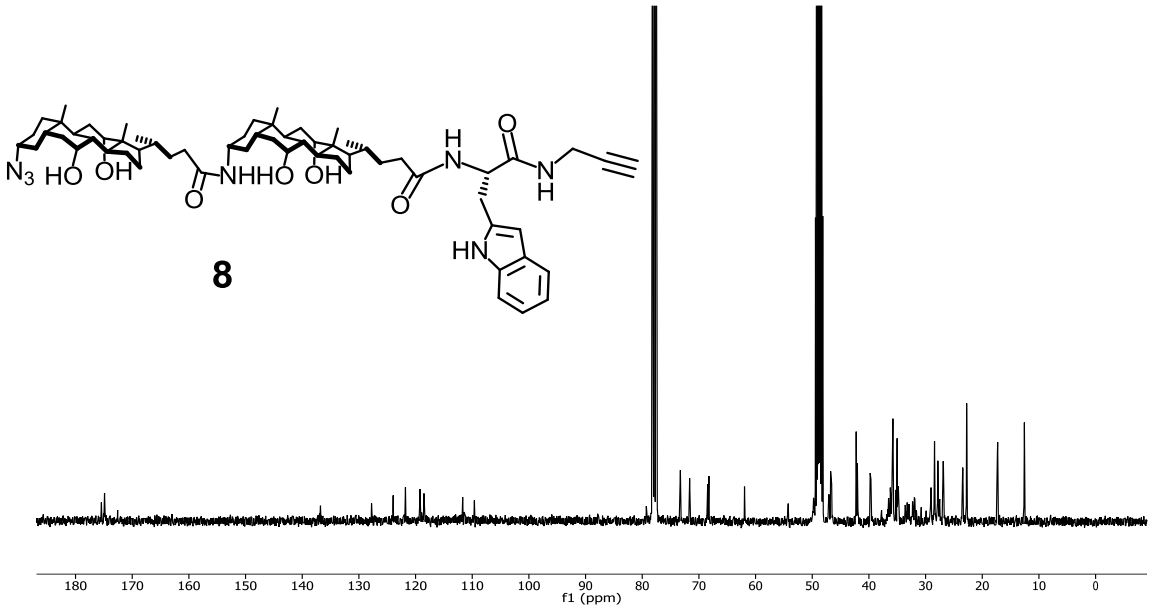

^{1}H NMR of compound **2**

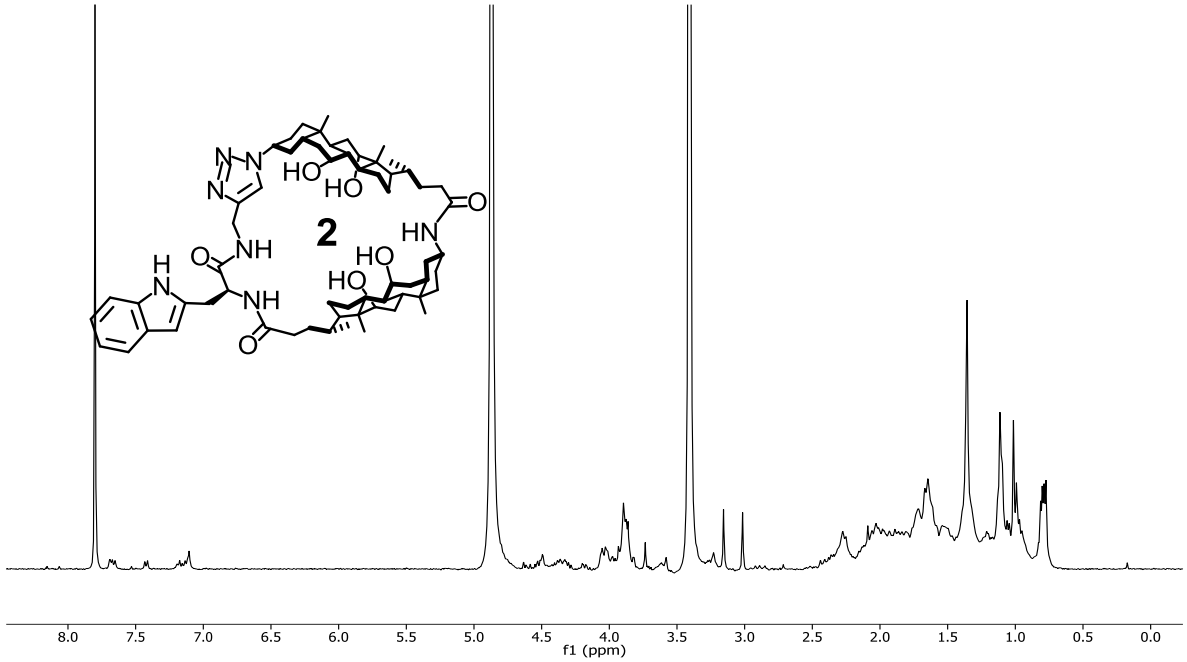

^{13}C NMR of compound **2**

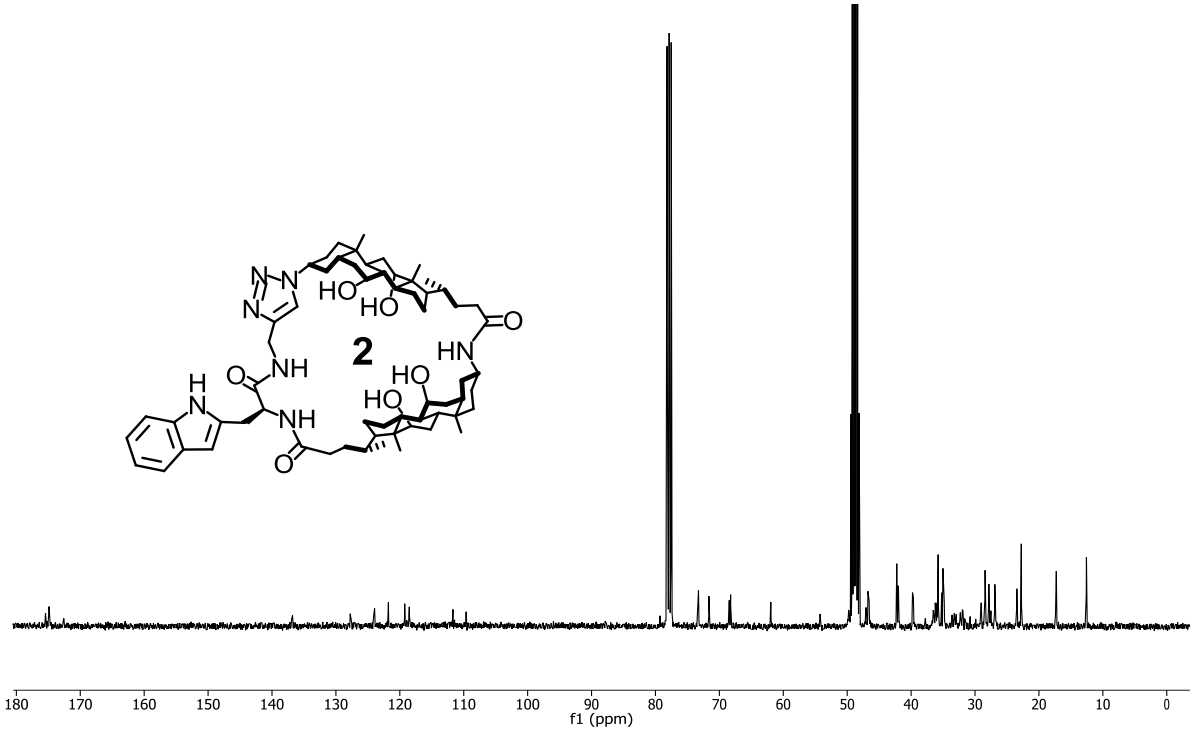

[1] H NMR of compound **9**

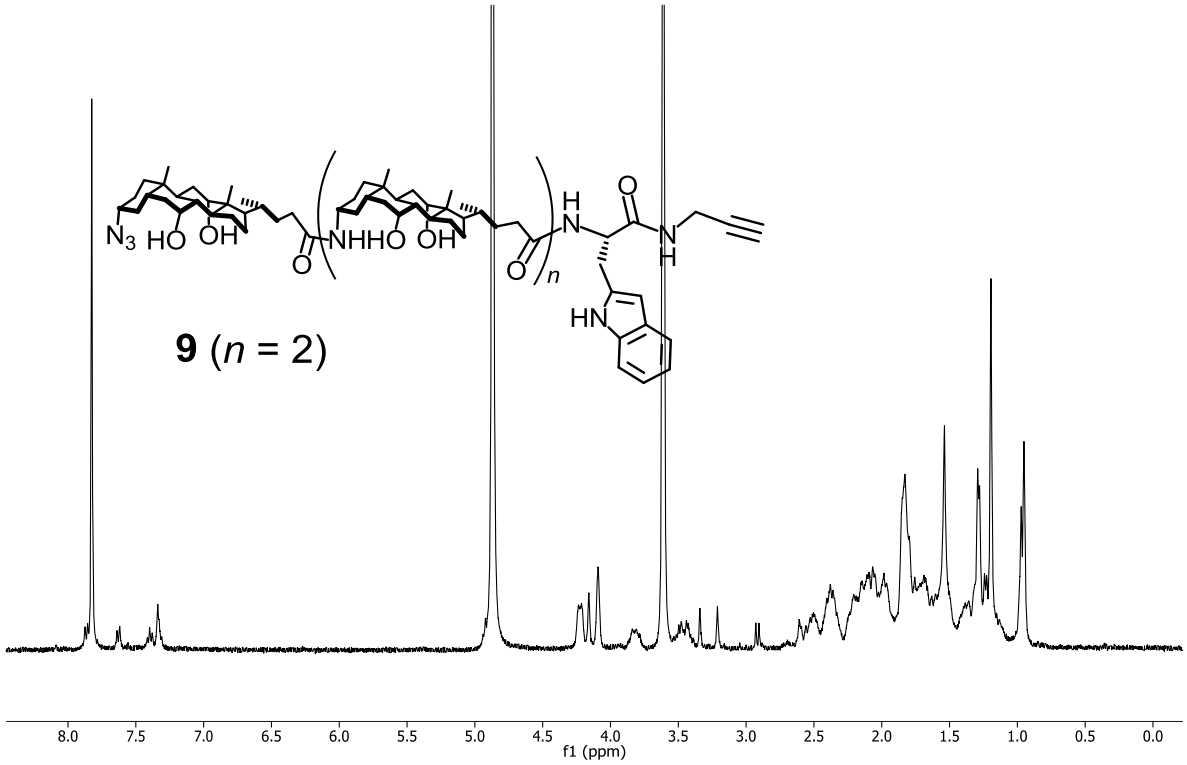

[13] C NMR of compound **9**

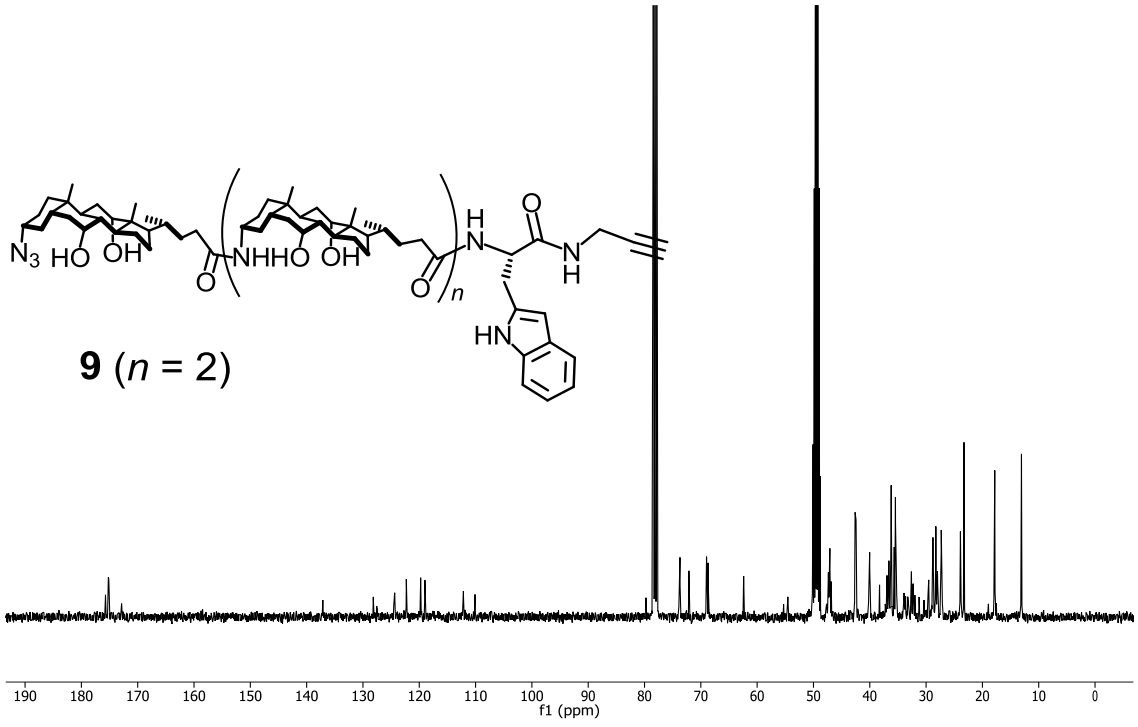

^{1}H NMR of compound **3**

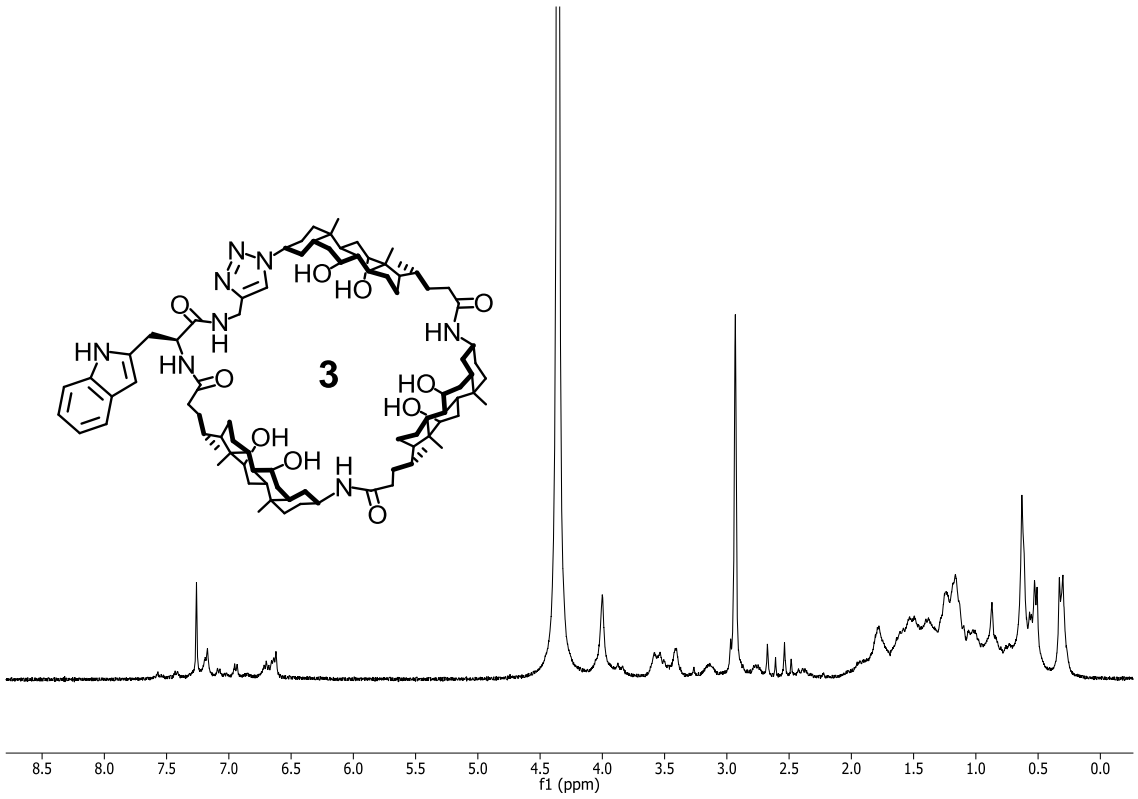

^{13}C NMR of compound **3**

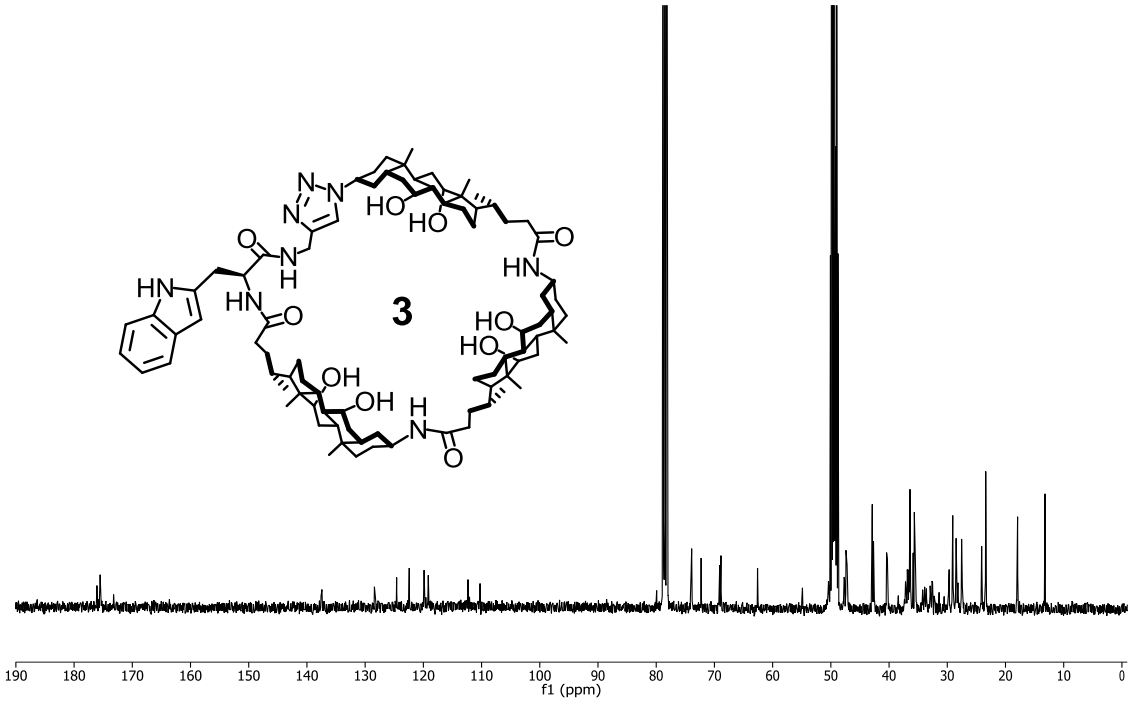

Notes and References

(1) Lee, A. G. *Biomembranes: A Multi-Volume Treatise*; JAI Press: Greenwich, 1995.

(2) (a) Matile, S.; Som, A.; Sorde, N. *Tetrahedron* **2004**, *60*, 6405. (b) Sisson, A. L.; Shah, M. R.; Bhosale, S.; Matile, S. *Chem. Soc. Rev.* **2006**, *35*, 1269.

(3) (a) Menestrina, G.; Dalla Serra, M.; Lazarovici, P. *Pore-Forming Peptides and Protein Toxins*; Taylor & Francis: London ; New York, 2003. (b) Goot, F. G. v. d. *Pore-Forming Toxins*; Springer: Berlin; New York, N.Y., 2001. (c) Tamm, L. K. *Protein-Lipid Interactions: From Membrane Domains to Cellular Networks*; Wiley-VCH: Weinheim, 2005. (d) Gilbert, R. J. C. *Cell. Mol. Life Sci.* **2002**, *59*, 832.

(4) (a) Kasianowicz, J. J.; Robertson, J. W. F.; Chan, E. R.; Reiner, J. E.; Stanford, V. M. *Annu. Rev. Anal. Chem.* **2008**, *1*, 737. (b) Kasianowicz, J. J.; Brandin, E.; Branton, D.; Deamer, D. W. *Proc. Natl. Acad. Sci. U. S. A.* **1996**, *93*, 13770. (c) Akeson, M.; Branton, D.; Kasianowicz, J. J.; Brandin, E.; Deamer, D. W. *Biophys. J.* **1999**, *77*, 3227. (d) Meller, A.; Nivon, L.; Brandin, E.; Golovchenko, J.; Branton, D. *Proc. Natl. Acad. Sci. U. S. A.* **2000**, *97*, 1079. (e) Vercoutere, W.; Winters-Hilt, S.; Olsen, H.; Deamer, D.; Haussler, D.; Akeson, M. *Nat. Biotechnol.* **2001**, *19*, 248. (f) Howorka, S.; Cheley, S.; Bayley, H. *Nat. Biotechnol.* **2001**, *19*, 636. (g) Clarke, J.; Wu, H. C.; Jayasinghe, L.; Patel, A.; Reid, S.; Bayley, H. *Nat. Biotechnol.* **2009**, *4*, 265.

(5) Bhosale, S.; Sisson, A. L.; Talukdar, P.; Furstenberg, A.; Banerji, N.; Vauthey, E.; Bollot, G.; Mareda, J.; Roger, C.; Wurthner, F.; Sakai, N.; Matile, S. *Science* **2006**, *313*, 84.

(6) Sakai, N.; Sorde, N.; Matile, S. *J. Am. Chem. Soc.* **2003**, *125*, 7776.

(7) Som, A.; Matile, S. *Chem. Biodiv.* **2005**, *2*, 717.

(8) (a) Gokel, G. W.; Mukhopadhyay, A. *Chem. Soc. Rev.* **2001**, *30*, 274. (b) Fyles, T. M. *Chem. Soc. Rev.* **2007**, *36*, 335. (c) Koert, U.; Al-Momani, L.; Pfeifer, J. R. *Synthesis-Stuttgart* **2004**, 1129. (d) Gokel, G. W.; Murillo, O. *Acc. Chem. Res.* **1996**, *29*, 425. (e) Jung, M.; Kim, H.; Baek, K.; Kim, K. *Angew. Chem. Int. Ed.* **2008**, *47*, 5755. (f) Li, X.; Shen, B.; Yao, X. Q.; Yang, D. *J. Am. Chem. Soc.* **2009**, *131*, 13676.

(9) (a) Granja, J. R.; Ghadiri, M. R. *J. Am. Chem. Soc.* **1994**, *116*, 10785. (b) Sanchez-Quesada, J.; Kim, H. S.; Ghadiri, M. R. *Angew. Chem. Int. Ed.* **2001**, *40*, 2503.

(10) (a) Sakai, N.; Mareda, J.; Matile, S. *Acc. Chem. Res.* **2005**, *38*, 79. (b) Das, G.; Talukdar, P.; Matile, S. *Science* **2002**, *298*, 1600.

(11) Satake, A.; Yamamura, M.; Oda, M.; Kobuke, Y. *J. Am. Chem. Soc.* **2008**, *130*, 6314.

(12) Helsel, A. J.; Brown, A. L.; Yamato, K.; Feng, W.; Yuan, L. H.; Clements, A. J.; Harding, S. V.; Szabo, G.; Shao, Z. F.; Gong, B. *J. Am. Chem. Soc.* **2008**, *130*, 15784.

(13) Fyles, T. M.; Tong, C. C. *New. J. Chem.* **2007**, *31*, 655.

(14) Ma, L.; Melegari, M.; Colombini, M.; Davis, J. T. *J. Am. Chem. Soc.* **2008**, *130*, 2938.

(15) Negin, S.; Daschbach, M. M.; Kulikov, O. V.; Rath, N.; Gokel, G. W. *J. Am. Chem. Soc.* **2011**, *133*, 3234.

(16) Boccalon, M.; Iengo, E.; Tecilla, P. *J. Am. Chem. Soc.* **2012**, *134*, 20310.

(17) (a) Si, W.; Chen, L.; Hu, X. B.; Tang, G. F.; Chen, Z. X.; Hou, J. L.; Li, Z. T. *Angew. Chem. Int. Ed.* **2011**, *50*, 12564. (b) Chen, L.; Si, W.; Zhang, L.; Tang, G.; Li, Z.-T.; Hou, J.-L. *J. Am. Chem. Soc.* **2013**, *135*, 2152.

(18) Cho, H.; Widanapathirana, L.; Zhao, Y. *J. Am. Chem. Soc.* **2011**, *133*, 141.

(19) Dunitz, J. D. *Science* **1994**, *264*, 670.

(20) (a) Zhao, Y.; Cho, H.; Widanapathirana, L.; Zhang, S. *Acc. Chem. Res.* **2013**, DOI: 10.1021/ar300337f. (b) Cho, H.; Zhao, Y. *Langmuir* **2011**, *27*, 4936. (c) Widanapathirana, L.; Li, X.; Zhao, Y. *Org. Biomol. Chem.* **2012**, *10*, 5077. (d) Widanapathirana, L.; Zhao, Y. *J. Org. Chem.* **2013**, *78*, 4610.

(21) (a) Widanapathirana, L.; Zhao, Y. *J. Org. Chem.* **2012**, *77*, 4679. (b) Widanapathirana, L.; Zhao, Y. *Langmuir* **2012**, *28*, 8165. (c) Wang, T.; Widanapathirana, L.; Zhao, Y.; Hong, M. *Langmuir* **2012**, *28*, 17071.

(22) (a) Davis, A. P. *Chem. Soc. Rev.* **1993**, *22*, 243. (b) Davis, A. P.; Wareham, R. S. *Angew. Chem. Int. Ed.* **1999**, *38*, 2978. (c) Davis, A. P.; Walsh, J. J. *Chem. Commun.* **1996**, 449.

(23) (a) Westmark, P. R.; Smith, B. D. *J. Am. Chem. Soc.* **1994**, *116*, 9343. (b) Westmark, P. R.; Gardiner, S. J.; Smith, B. D. *J. Am. Chem. Soc.* **1996**, *118*, 11093. (c) Cho, H.; Zhao, Y. *Chem. Commun.* **2011**, *47*, 8970.

(24) (a) Silverman, M. *Annu. Rev. Biochem.* **1991**, *60*, 757. (b) Lienhard, G. E.; Slot, J. W.; James, D. E.; Mueckler, M. M. *Sci. Am.* **1992**, *266*, 86. (c) Mueckler, M. *Eur. J.*

Biochem. **1994**, *219*, 713. (d) Manolescu, A. R.; Witkowska, K.; Kinnaird, A.; Cessford, T.; Cheeseman, C. *Physiology* **2007**, *22*, 234.

(25) Zhao, Y.; Zhong, Z. *J. Am. Chem. Soc.* **2005**, *127*, 17894.

(26) Rostovtsev, V. V.; Green, L. G.; Fokin, V. V.; Sharpless, K. B. *Angew. Chem. Int. Ed.* **2002**, *41*, 2596.

(27) Kinsky, S. C.; Haxby, J. A.; Zopf, D. A.; Alving, C. R.; Kinsky, C. B. *Biochemistry* **1969**, *8*, 4149.

(28) Stein, W. D. *Carriers and Pumps: An Introduction to Membrane Transport*; Academic Press: San Diego, CA, 1990.

(29) Nezil, F. A.; Bloom, M. *Biophys. J.* **1992**, *61*, 1176.

(30) Holthuis, J. C. M.; van Meer, G.; Huitema, K. *Mol. Membr. Biol.* **2003**, *20*, 231.

(31) (a) Demel, R. A.; Bruckdor, K. R.; van Deene, L. L. *Biochim. Biophys. Acta* **1972**, *255*, 321. (b) Demel, R. A.; R., B. K.; L., V. L. *Biochim. Biophys. Acta* **1972**, *255*, 321. (c) Papahadjopoulos, D.; Nir, S.; Ohki, S. *Biochim. Biophys. Acta* **1972**, *266*, 561.

(32) Davis, J. T.; Okunola, O.; Quesada, R. *Chem. Soc. Rev.* **2010**, *39*, 3843.

(33) Zhang, S.; Zhao, Y. *Chem. -Eur. J.* **2011**, *17*, 12444.

(34) Struck, D. K.; Hoekstra, D.; Pagano, R. E. *Biochemistry* **1981**, *20*, 4093.

(35) Olson, F.; Hunt, C. A.; Szoka, F. C.; Vail, W. J.; Papahadjopoulos, D. *Biochim. Biophys. Acta* **1979**, *557*, 9.

(36) Zhang, S.; Zhao, Y. *Org. Biomol. Chem.* **2012**, *10*.

(37) Cho, H.; Zhao, Y. *J. Am. Chem. Soc.* **2010**, *132*, 9890.

(38) Lakowicz, J. R. *Principles of Fluorescence Spectroscopy*; 2nd ed.; Kluwer Academic/Plenum: New York, 1999; Chap 8.

(39) The stacked nanopores of **2** was also supported by its strong glucose transport activity (Figure 2), smaller accessible fraction to NaI (Table 1, entries 1 and 3), and a larger accessible fraction to TEMPO (Table 1, entries 5 and 7) with an increase in concentration.

(40) Cordero, F. M.; Bonanno, P.; Chioccioli, M.; Gratteri, P.; Robina, I.; Moreno Vargas, A. J.; Brandi, A. *Tetrahedron* **2011**, *67*, 9555.

CHAPTER 7

CONCLUSIONS

The work presented in this dissertation illustrates a simple but effective method for the design and synthesis of molecularly imprinted nanoparticles (MINPs) that are fully compatible and functional in water. The MINPs were generated from a functionalized tripropargylammonium surfactant that enabled double cross linking on the surface and in the core of the micelle, in the presence of a template and divinylbenzene (DVB) cross linker. The resulting MINPs contained guest-tailored hydrophobic pockets while maintaining a hydrophilic surface by virtue of the sugar-derived ligands incorporated onto the surface during the post-functionalization process. Binding studies were performed using isothermal titration calorimetry and fluorescence spectroscopy to investigate the properties of the nanoparticles. The MINPs utilized recognition properties of an antibody for the antigen, in which the antigen perfectly fits into the antibody's binding site, whereas the other structurally related compounds are discriminated against from binding to the same site. The fundamental principle relies on the imprinting technology in which binding pockets are created with predetermined selectivity and specificity for a given analyte. The nanoparticles resembled natural proteins in water-solubility, hydrophilic surface and hydrophobic core, and in their discrete nanosized structure.

Noteworthy properties portrayed by MINPs include easy purification, complete template removal, high affinity with specific selectivity for the corresponding substrates, ability to functionalize the core, ability to introduce an inhibitory effect on the binding site, sensitivity to pH - for a functionalized core, molecular sensing of an analyte in the presence

of its analogues, and ability to act as monoclonal antibodies for nonsteroidal anti-inflammatory drugs (NSAIDs); among others.

Initial investigation of the binding properties of MINPs involved a templated synthesis of the nanoparticles from bile salt derivative containing dansyl group as the fluorescent probe. Parallel binding studies performed using ITC and fluorescence spectroscopy revealed 1:1 binding with high affinity and selectivity for the corresponding analyte. Altering the ratio of the template to the tripropargylammonium surfactant from 1:50 to 1:25 generated two independent binding sites, each having similar binding affinity and selectivity to the previous one.

Molecular sensing monitored through Förster resonance energy transfer (FRET) requires that the donor-acceptor pair must be within an acceptable distance for effective overlap between the donor emission and acceptor absorption. The average size of MINPs is 2.5 nm in radius, including the hydrophilic surface. In our endeavors to explore this application of MINPs as biomimetic sensors in water, we installed polymerizable dansyl groups into the core of the nanoparticles during an imprinting process that involved the use of a naphthyl group as the template. The resultant MINPs were able to detect the presence of the analyte from amongst other substrates that were very closely related to the analyte in shape and structure. This remarkable property portrayed by MINPs ascertains the superiority of its design over the traditional methods that have previously been used.

To fine tune the binding, the imprinted pocket needs to be functionalized, preferably through covalent imprinting. Efforts were made toward this goal. Covalent imprinting was used to install an acid-functionalized hydrophobic pocket by carrying out the imprinting process in the presence of a photolabile *o*-nitrobenzyl derivative as a template. Controlled

release of the template was monitored by fluorescence for a period of time before complete removal was acquired. Amide coupling reaction between an aminonaphthalene and the acid-functionalized hydrophobic pocket incorporated the naphthyl group into the imprinted core, inhibiting the original analyte from accessing the binding site. Inhibition of the binding pocket is a common phenomenon in enzymatic catalysis and this property of MINPs is likely to broaden the understanding and application of MINPs as catalytic enzymes.

Homogeneity of the binding pockets, typical to monoclonal antibodies, is an important characteristic for efficient molecular recognition. The MINPs presented here were investigated for their ability to respond to various NSAIDs as the antigens, with their monoclonal hydrophobic binding pockets tailored for either naproxen or indomethacin. The MINPs displayed high selectivity for their corresponding templates, while registering very low cross reactivity ratios for those NSAIDs bearing close resemblance to the analyte.

In this regard, we have raised the first synthetic antibodies that bear the closest resemblance to their natural counterparts in function and properties. Further work is necessary to understand how these molecules could be utilized in biological systems as a step toward practical application in an attempt to substitute them for their natural counterparts.